Charge Transfer Processes of Atomic Hydrogen Rydberg States near Surfaces

Mark G. B. Dethlefsen

Merton College

University of Oxford

A thesis submitted for the degree of Doctor of Philosophy

Trinity Term 2013

Charge Transfer Processes of Atomic Hydrogen Rydberg States near Surfaces

Mark G. B. Dethlefsen, Merton College

A thesis submitted in partial fulfilment of the requirements
for the degree of Doctor of Philosophy of the University of Oxford

Trinity Term, 2013

Abstract

When approaching a metal surface, the electronic structure of Rydberg atoms or molecules is perturbed by the surface potential and at close enough distances resonant ionisation of the Rydberg electron into the conduction band of the surface can occur. It is possible to interfere in this process and steer the ionisation distance by making use of the polarisability of the Rydberg orbital in the presence of electric fields. The resulting ions from the surface can extracted via electric fields and subsequently detected via well established ion detection schemes. The question of how this charge-transfer process is affected by different properties of the surface (both electronic and structural) represents the main aspect of the work presented in this thesis.

At first, the charge transfer of atomic hydrogen Rydberg atoms with a flat gold metal surface is investigated. While such a surface might appear homogeneous, stray fields are present in its vicinity due to local variations in the surface work function. The surface ionisation process as a function of applied electric field is therefore measured experimentally and the results are compared with classical Monte-Carlo simulations (which include stray field effects). This way the possibility to utilize Rydberg states as a probe of the magnitude of such stray fields is demonstrated. To investigate the effect the surface structure can have on the ionisation process, the interaction of Rydberg atoms with surfaces covered by nanoparticles is investigated. Surface ionisation is measured at a 5 nm nanoparticle monolayer surface and it is shown that population transfer between surface- and vacuum-oriented Rydberg states occurs. In addition, results are presented, which suggest a dependence of the ionisation process on the relative size of Rydberg orbital and nanoparticle. Furthermore, charge transfer between a Rydberg state and discrete electronic states at the surface vacuum interface are investigated by performing experiments with a Cu(100) band-gap semiconductor surface. By analysing surface ionisation as a function of collisional velocity ionisation rates can be determined and are subsequently compared with theoretical predictions. The potential of identifying resonant ionisation is thereby demonstrated. Last, a new method to produce $2s$ atomic hydrogen via mixing of the $2s$ and $2p$ state in an electric field is proposed and first experimental results are presented, thus demonstrating viability of the idea.

The experiments presented in this thesis represent the most in depth analysis of the charge-transfer process between atomic hydrogen Rydberg states and a range of different surfaces to date. As such, they demonstrate the potential of utilizing the unique properties of Rydberg states and their applicability as surface probes. In addition, these results pave the way for further experiments involving thin films or the phenomenon of quantum reflectivity.

Acknowledgements

Numerous people contribute to the success of such an extensive peace of work and all them deserve my deepest gratitude. First and utmost my thanks belong to my supervisor, Prof. Tim Softley for his never ending patience when reading and correcting this thesis and for giving me helpful guidance and support throughout my PhD. I also need to thank the whole Softley group (past and present members), for their friendship, help and for some great times inside and outside of the lab. Working with you guys was both amazing and rewarding. I would also like to thank Tertia Softley for her great hospitality at great group dinners and barbecues.

But there are several people in the Softley group, I am particular indebted to. Mark F for teaching me everything I know about optics and lasers and for his help and advise in the field of data analysis. Eric not just for starting the project and building the experimental setup but also for setting the background for my own work. Jemma and Sashi for spending time with me in the lab and helping me solve many experimental problems. Mike for bringing a new drive to the project with all his great (and sometimes crazy) ideas and Chris for always giving a helping hand when needed.

I would also like to thank all my wonderful friends in Oxford which made my time here special and memorable. Mathias, Phil, Erica, Mat, Tim, Will, Kat, Chris, James, Martin, Emanuel, Mai, Masa and Marc A.

Special thanks go to SiuSiu for her amazing support throughout my PhD, without her this work would not have been possible. Besides her cooking skills, it was her never ending love and her amazing patience with me which gave me the strength to finish my PhD.

Lastly, I would like to thank my family for their support and encouragement not just throughout my PhD but my whole life.

To no extent is this a complete list and I am almost certain that I forgot someone. But whoever that might be, feel certain that you also hold my gratitude and try not to be (too) offended...

Contents

Chapter 1

Introduction

A Rydberg state is a quantum state of an atom or molecule whose energies follow the well known Rydberg formula and can be described using hydrogen like wavefunctions. In general these states exist for every neutral atom or molecule excited to a high enough principal quantum number and they naturally occur in a range of environments such as the interstellar medium and in plasmas. Rydberg states possess many interesting properties such as a large electron to core separation, a high polarisability by electromagnetic fields and a weak binding energy. While interacting with a surface, Rydberg states can be perturbed by and undergo charge transfer to the surface which opens the door for many interesting possible applications. This thesis aims to investigate the possibility to use Rydberg states as surface probes utilizing both experimental and theoretical approaches.

As mentioned above, the term 'Rydberg state' strictly speaking refers to a quantum state and not to a physical entity and the correct term to use would be Rydberg atom or molecule. However, for reasons of readability the two terms are used interchangeable in this thesis. It needs to be noted that all units in this thesis are atomic units unless stated otherwise.

1.1 Motivaton

Due to their size and polarisability different properties of Rydberg atoms and molecules can easily be perturbed by a range of external methods. This possibility of external control makes them an interesting target for a range of existing or potential applications in chemistry or physics. Rydberg atoms form commonly in plasmas due to the recombination of electrons with ions [1]. In addition, they are believed to play an important role in determining the properties of a plasma in the surface-plasma boundary region [2] and studying Rydberg-surface interactions can therefore give important information to further understand the processes involved. Rydberg states also play a role in some surface modification techniques like high-energy ion sputtering in which several electrons are transferred from the surface into high lying Rydberg states and subsequently stripped from the atom close to the surface [3]. Another interesting concept involving Rydberg states is 'Rydberg matter' as proposed by Manykin and Holmlid [4, 5]. It assumes the generation of circular Ryderg states, which are emitted from a surface, in planar clusters in a process somewhat similar to Bose-Einstein condensation. So far the only suggested way to remove the condensation energy from the system and to avoid ionisation is for this condensation to occur near the surface which can act as a heat sink [6]. Gaining a better understanding of the ionisation behaviour of Rydberg states near surfaces might shed more light onto this controversial idea. Furthermore, different Rydberg species are present in abundance in the interstellar medium where they possess a long lifetime due to low collision rates. In the past they have been used as radiation sources in astrophysics [7] though interest in them has somewhat decreased in recent years.

There are several possible applications which make use of the interesting properties of Rydberg states and for many of those, a closer understanding of the Rydberg-surface interaction is essential. Nguyen et al. suggested that it should be possible to use Rydberg atoms to deposit patterns on a nanometre scale using standing wave laser fields [8] or inhomogeneous electric fields [9, 10] to guide them. Another field in which Rydberg states might be of interest is quantum computing. Different atom-chip experiments have been proposed and performed using trapped Rydberg states [11, 12, 13, 14] and recently Saffman et al. demonstrated that it is possible to build a CNOT logic gate out of two Rubidium atoms using the Rydberg blockade mechanism [15, 16]. Also, the collisions of highly excited atoms with adsorbates on surfaces might offer a chance to investigate and to control chemical reactions. An in-depth understanding of the interaction of Rydberg states with surfaces is of great importance to many, if not all, of these possible applications and this field of study has therefore attracted a considerable amount of interest in the last few years.

The interactions of Rydberg states with surfaces have been extensively studied experimentally and theoretically. However most of the theoretical studies focused on atomic hydrogen as it represents the most tractable system quantum-mechanically due to its quantum mechanical simplicity and the high symmetry of the hydrogen-atom – surface system [17, 18]. A wide range of theoretical methods have been employed including classical over-the-barrier ionisation [19] and classical trajectory approaches [20, 21], semi-classical calculations [22, 23, 24], perturbation theory [25, 26, 27], scattering theory [28], non-perturbative complex-scaling methods [29, 30, 31], time dependent-close coupling methods [32, 33] as well as time-dependent wave packet propagation calculations [34, 35, 36, 37]. Due to the experimental difficulties associated with hydrogen atoms, experimental studies have so far mainly been performed using alkali metal atoms [38, 39, 40, 41, 42, 43], Xenon and other rare gases [44, 45, 46, 47] or hydrogen molecules [48, 49, 50, 51]. Only recently, the first experimental results studying the interactions of atomic hydrogen Rydberg states with metal surfaces have been published, for the first time linking theory directly with experiment [37, 52]. Further experiments utilising H-atoms might therefore help to explain differences between theory and experiment and lay the ground for some of the possible applications.

1.2 Rydberg states

In a Rydberg atom or molecule one electron has been excited to a high energy orbit. Classically, this increase in principal quantum number equates to an increase in orbital radius, the size of which scales with n^2. For high enough principal quantum numbers the Rydberg electron sees the ion core as a single point charge, making it possible to approximate the Rydberg state as a hydrogenic system using hydrogenic wavefunctions. Only in the case of electrons with low angular momentum, which penetrate deep into the core regions, or in the presence of electromagnetic fields does this approximation break down.

Under field-free conditions, the excited electron wave function outside the core region, can be described using the principal quantum number n, the angular momentum quantum number l and the magnetic quantum number m_l. The energy of a Rydberg state (in a.u.) relative to the ionisation threshold to which the series converges to is given by [53]:

$$E_{nlm_l} = -\frac{1}{2(n-\delta_l)^2} \tag{1.1}$$

where δ_l is the l-dependent quantum defect which represents a phase shift in the hydrogenic wavefunction, accounting for the shielding (or the lack thereof) of the Rydberg orbital from the 'core' region. Essentially, it represents a scaling parameter which smoothly matches the hydrogenic wavefunction onto the core wavefunction. The quantum defect is greatest for $l = 0$ as these states 'penetrate' deepest into the core region, and it gradually tends towards zero with increasing angular momentum (the exact values depend on the specific atom or molecule).

Rydberg states have many interesting properties. Their orbit radius scales with n^2 resulting in relatively small binding energies for high principal quantum numbers. Due to the large distance from the ion core they possess a long lifetime with respect to different decay mechanisms such as spontaneous emission ($\propto n^3$), black body radiation ($\propto n^2$) or autoionisation and predissociation. In addition they exhibit a high polarisability that scales with n^7 making Rydberg states easily perturbed by external fields [54].

These properties result in a very long-range interaction with metal surfaces. The large radius and weak binding energy mean that charge transfer can occur relatively far from the surface (the ionisation distance is ~ 100 nm for an $n = 20$ atomic hydrogen Rydberg state) while the high polarisabilty means that the properties of a Rydberg state are easily influenced by surface characteristics. Therefore Rydberg states represent interesting and intriguing systems to probe surface interactions such as charge-transfer in surface scattering experiments.

Rydberg states can easily be prepared and their properties influenced to a high degree of accuracy by using a combination of spectroscopic methods and electromagnetic fields. The orbit size can be controlled by choosing different principal quantum numbers and it is possible to control the orientation of the Rydberg electron (pointing towards the surface or towards the vacuum) through external electric fields applied during the excitation process.

1.3 Lifetime of Rydberg states

As mentioned above, one of the key features of Rydberg atoms and molecules is their surprisingly long lifetime. While atoms or molecules in high-n Rydberg states are actually energetically unstable with respect to the electronic ground state, they are often very stable kinetically on typical experimental timescales. An expression for the lifetime of an atom excited into a quasi-hydrogenic Rydberg state with the quantum numbers n and l has been calculated by Chang [55]:

$$\tau = 93n^3 \left(l + \frac{1}{2} \right)^2 . \tag{1.2}$$

In general, there are different decay mechanisms contributing to this overall lifetime. These mechanisms can be separated into two different groups: radiative and non-radiative decay pathways. Radiative decay processes represent the main pathway for the de-excitation for Rydberg atoms or molecules. There are two different contributions to this process, namely spontaneous emission and black body radiation (BBR) and both of them will be described in the following paragraphs.

The non-radiative decay pathways include processes such as auto-ionisation and pre-dissociation. While these mechanisms can have a notable impact on the lifetime for molecular Rydberg states they are not present for atomic hydrogen. As this thesis exclusively deals with Rydberg states of atomic hydrogen they will therefore not be discussed in detail.

1.3.1 Spontaneous emission

As the name indicates, spontaneous emission is a process at which the Rydberg atom emits a photon and thereby decays into a state with lower energy. Classically this process is only possible when the Rydberg electron is passing through the core region. As the time that a Rydberg atom spends within this region depends on the eccentricity of the Rydberg orbital, this contribution to the decay rate depends strongly on the angular momentum quantum number l.

The radiative lifetime of a Rydberg state $|n, l\rangle$ is the inverse of the total radiative decay rate, which can be obtained by summing up the Einstein Coefficients $A_{n'l',nl}$ of all possible transitions to lower energy states states $|n', l'\rangle$ [53]:

$$\tau_{n,l} = \left(\sum_{n',l'} A_{n'l',nl} \right)^{-1} . \tag{1.3}$$

This thesis only deals with atomic hydrogen and as such, this lower lying state will by definition always be another Rydberg state. For other atoms or molecules however, $|n', l'\rangle$ could also be another excited state or the electronic ground state. The Einstein Coefficient can be calculated as [53]:

$$\begin{aligned} A_{n'l',nl} &= \frac{-2e^2\omega_{n'l',nl}^2}{\hbar c^3} \bar{f}_{n'l',nl} \\ \text{with } \omega_{n'l',nl} &= \frac{E_{n',l'} - E_{n,l}}{\hbar} \end{aligned} \tag{1.4}$$

with $\omega_{n'l',nl}$ being the angular frequency and $\bar{f}_{n'l',nl}$ the m_l independent oscillator strength:

$$\bar{f}_{n'l',nl} = \frac{2\omega_{n'l',nl}}{3} \frac{l_{\max}}{2l+1} |\langle n', l'|r|n, l\rangle|^2 \tag{1.5}$$

where $l_{\max}$ is the larger of l or l'.

From Equations 1.4 and 1.5 follows that the radiative lifetime has a strong dependence on the angular frequency ($\propto \omega_{n'l',nl}^3$) and therefore the spontaneous emission decay rate is usually dominated by the highest angular frequency. In general, the most probable transition is the one to the lowest energy state with $l' = l - 1$, due to the usual selection rule of $\Delta l = \pm 1$ (except for an $|n, s\rangle$ state). For $n \to \infty$ and $n >> l$ the frequency of the highest frequency transition approaches a constant and the transition probability depends only on the radial matrix element $|\langle n', l'|r|n, l\rangle|^2$. As only those parts of the Rydberg state wavefunction which spatially overlap with the wavefunction of the lower energy state contribute to the matrix element, this term scales with n^{-3} due to the normalisation of the Rydberg state wavefunction. The lifetime of a Rydberg state $|n, l\rangle$ is thus proportional to [53]:

$$\tau_{n,l} \propto n^3. \tag{1.6}$$

It should be noted that this reasoning is not applicable for a Rydberg state with $l \approx n$ due to the lack of overlap between the wavefunctions involved. For this state the lifetime scales with approximately $\tau_{n,l} \propto n^5$.

1.3.2 Black body radiation

The second contribution to the radiative decay of Rydberg states is their interaction with black-body radiation (BBR). This interaction can lead to de-excitation of the Rydberg state but also to transitions between high lying states and may even lead to ionisation [56, 57, 58, 59].

The lifetimes of high lying Rydberg states are strongly affected by black-body-radiation due to the small level spacings in this energy region and also due to the large transition dipole matrix elements between Rydberg states leading to a redistribution of an initial population. In addition, the black-body radiation also affects the spontaneous emission decay rate. To estimate the rate of a BBR induced transition it is useful to express the radiation field in the form of number of photons per mode of radiation field ($\bar{n}$) which is derived from Planck's radiation law for energy density and is given as [53]:

$$\bar{n} = \frac{1}{e^{h\nu/kT} - 1}. \tag{1.7}$$

For low frequencies this reduces to ($h\nu << kT$):

$$\bar{n} \simeq \frac{kT}{h\nu} \tag{1.8}$$

As shown in the previous chapter, the spontaneous emission rate is defined by the Einstein Coefficient $A_{n'l',nl}$. The stimulated emission rate $K_{n'l',nl}$ can be calculated by simply multiplying the spontaneous emission rate by $\bar{n}$ [53]:

$$\begin{aligned} K_{n'l',nl} &= \bar{n} A_{n'l',nl} \\ &= \frac{-2\bar{n} e^2 \omega_{n'l',nl}^2}{\hbar c^3} \bar{f}_{n'l',nl}. \end{aligned} \tag{1.9}$$

Because of the frequency term in $\bar{n}$, the frequency dependence of black body radiation is significantly different from the spontaneous emission, meaning that the two processes favour different final states. Low frequency transitions to nearby energy states (lower or higher in energy) are thereby most favourable for BBR while high frequency transitions to low lying states are most likely for spontaneous emission. Analogous to the lifetime with respect to spontaneous emission, the lifetime of a Rydberg state $|n, l\rangle$ with respect to black-body-radiation can be calculated by summing up the transition probabilities to all possible final states $|n', l'\rangle$ [53]:

$$\tau_{n,l}^{\mathrm{BBR}} = \left(\sum_{n',l'} \frac{-2\bar{n} e^2 \omega_{n'l',nl}^2}{\hbar c^3} \bar{f}_{n'l',nl} \right)^{-1}. \tag{1.10}$$

In the low frequency limit Equation 1.10 can be re-written as:

$$\tau_{n,l}^{\mathrm{BBR}} = \left(\sum_{n',l'} \frac{-2KT e^2 \omega_{n'l',nl}}{\hbar^2 c^3} \bar{f}_{n'l',nl} \right)^{-1}. \tag{1.11}$$

This summation implicitly includes the continuum. Using the summation rule Equation 1.11 can be written as [18]:

$$\begin{aligned}\sum_{n',l'} \omega_{n'l',nl} \bar{f}_{n'l',nl} &= \frac{2}{3n^2} \\ \tau_{n,l}^{\mathrm{BBR}} &= \left(\frac{-4kTe^2}{3\hbar^2 c^3 n^2} \right)^{-1} .\end{aligned} \tag{1.12}$$

The lifetime with respect to black-body-radiation therefore scales with n^2. Comparing this value to the n^3 dependence with respect to spontaneous emissions it becomes evident, that BBR will be the dominant factor regarding the lifetime of hydrogen atoms excited to high lying Rydberg states even for low angular momentum states.

1.4 Rydberg states in electric fields - The Stark effect

It has already been mentioned that Rydberg states possess a large polarisability and are therefore highly susceptible to external electric fields. This so-called Stark effect leads to significant deviation from the Coulombic $1/r$ potential and lifts some of the degeneracies present in the field-free case [60]. It is important to understand this effect as the interactions of Rydberg atoms or molecules with surfaces are of a similar nature (see section 1.6). In addition, under the normal experimental conditions for the work presented in this thesis, a homogeneous electric field is usually applied during laser excitation in order to control the polarisation of the Rydberg electron wavefunction.

In a homogeneous electric field F the Schrödinger equation for the hydrogen atom takes on the following form:

$$
\begin{aligned}
H\Psi &= (H^0 + H^1(F))\Psi = E\Psi \\
H^0 &= -\frac{1}{2}\nabla^2 - \frac{1}{r} \\
H^1 &= -\hat{\mathrm{F}} \cdot \hat{\mu} = -F\mu_z = +Fr\cos\theta
\end{aligned}
\tag{1.13}
$$

were H^0 is the field-free Hamiltonian and H^1 describes the perturbing Stark effect. $\hat{\mu}$ is the dipole moment operator and μ_z its z-component. Solving the Schrödinger equation in spherical coordinates for the field-free case (only H^0) leads to the well known hydrogenic wavefunction $\Psi_{nml_l} = |nlm_l\rangle = R_{nl}(r)Y_{lm_l}(\theta\phi)$ with $R_{nl}(r)$ being the radial wavefunction of the hydrogen atom and $Y_{lm_l}(\theta\phi)$ a spherical harmonic. Both sets of functions are well defined by the quantum numbers n, l and m_l and the energies are given by Equation 1.1 (with $\delta_l = 0$). Therefore, the energies of the different Rydberg states only depend on the principal quantum number n and possess an electronic degeneracy of n^2.

Upon application of an electric field this degeneracy is lifted and the eigenstates of the complete Hamiltonian can be expressed as linear combinations of the basis functions $|nlm_l\rangle$. It can be shown that in this case states with $m' = m$ and $l' = l + 1$ are coupled by the electric field [18]. Therefore only the magnetic quantum number m_l is preserved and the angular momentum quantum number l is no longer a 'good' quantum number.

It is also possible to solve the Schrödinger equation in parabolic coordinates [18]. The resulting wavefunctions can still be described with the quantum numbers n and m_l but the angular momentum quantum number l is replaced by the parabolic quantum numbers n_1 and n_2. These new quantum numbers are related to n and m_l by

$$
n = n_1 + n_2 + |m_l| + 1. \tag{1.14}
$$

For simplicity, a new quantum number k is defined with $k = n_1 - n_2$, which can take $n - m$ integer values ranging from $-(n - |m_l| - 1)$ to $(n - |m_l| - 1)$ in steps of two.

The energies of the different Stark states of the hydrogen atom together with their dependence on the electric field have been calculated by Bekenstein et al.[61]:

$$\begin{aligned}
E_{nkm_l} = &-\frac{1}{2n^2} + \frac{3}{2}Fnk - \frac{1}{16}F^2n^4\left(17n^2 - 3k^2 - 9m_l^2 + 19\right) \\
&+ \frac{3}{32}F^3n^7k\left(23n^2 - k^2 + 11m_l^2 + 39\right) \\
&- \frac{1}{1024}F^4n^{10}\left(5487n^4 + 35182n^2 - 1134m_l^2k^2 + 1806n^2k^2\right. \\
&\left.-3402n^2m_l^2 - 3093k^4 - 549m_l^4 + 5754k^2 - 8622m_l^2 + 16211\right) \\
&+ O\left(F^5\right) + ... \qquad (1.15)
\end{aligned}$$

From this it becomes evident that the n^2 degeneracy at zero-field is lifted in an electric field. To first order, the Stark splitting is linear and only depends on the electric field strength F and the parabolic quantum number k. At larger electric fields, higher order terms increase in importance which leads to a deviation from the linear behaviour. The energy of Stark states with a positive k are shifted to higher energy (so called 'blue-shifted' states) while states with a negative k are shifted to lower energies ('red shifted'). Figure 1.1 shows the calculated Stark energies of atomic hydrogen in the range $n = 8$ to $n = 10$, $m_l = 0$ as a function of applied electric field using Equation 1.15. For the range shown in this figure, this so called Stark map is dominated by the linear component of the Stark effect.

For the extreme red- and blue-shifted states the wavefunctions are highly polarised along the electric field axis. This gives rise to very high dipole moments for these states which can be used to decelerate or trap Rydberg states [9, 12, 62, 63]. This dipole moment can be derived from the gradient of energy versus field of a Stark state and to first order can therefore be estimated as $\frac{3}{2}nk$ (see Equation 1.15). In effect, the

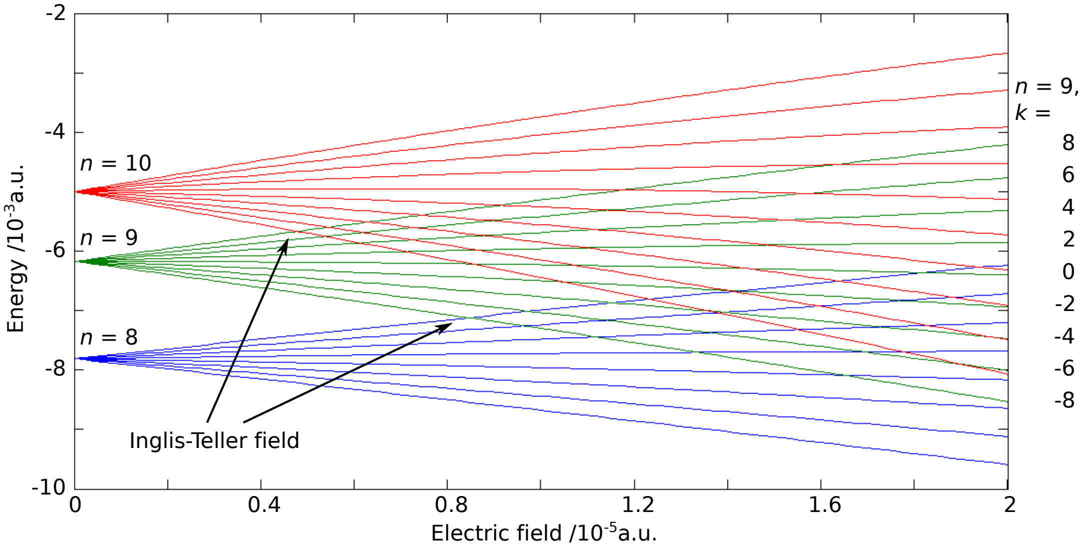

Figure 1.1: Calculated Stark map for principal quantum numbers in the range $n =$ 8 - 10 for the $m_l = 0$ case. The energies were calculated using Equation 1.15. The different k states of the $n = 9$ manifold are labelled and Inglis-Teller limits are shown.

gradient is non-zero and almost constant at all fields (assuming a linear Stark effect) and therefore a hydrogen Rydberg atom can be considered to have a permanent dipole moment. There are two exceptions to this assumption. Firstly, mid-manifold Stark states ($k = 0$) are symmetric around the field axis and therefore do not possess a dipole moment. Also, low l Rydberg states of atoms and molecules other than hydrogen do not show a linear Stark effect, which makes it more difficult to estimate their dipole moment. An example of the electronic wavefunctions for the $n = 8$ Rydberg states is shown in Figure 1.2. The polarisation of the electronic wavefunctions with respect to the electric field is clearly visible.

At large enough electric fields, the so called Inglis-Teller field, the extreme red- and blue shifted Stark states of neighbouring Rydberg states cross (see arrows in Figure 1.1) and the field of the first crossing can be approximated as $F_{IT} \approx \frac{1}{3}n^{-5}$ a.u. In hydrogenic systems (ignoring spin-orbit coupling) there is no coupling between different parabolic eigenfunctions with the same magnetic quantum number m_l. Therefore crossings of

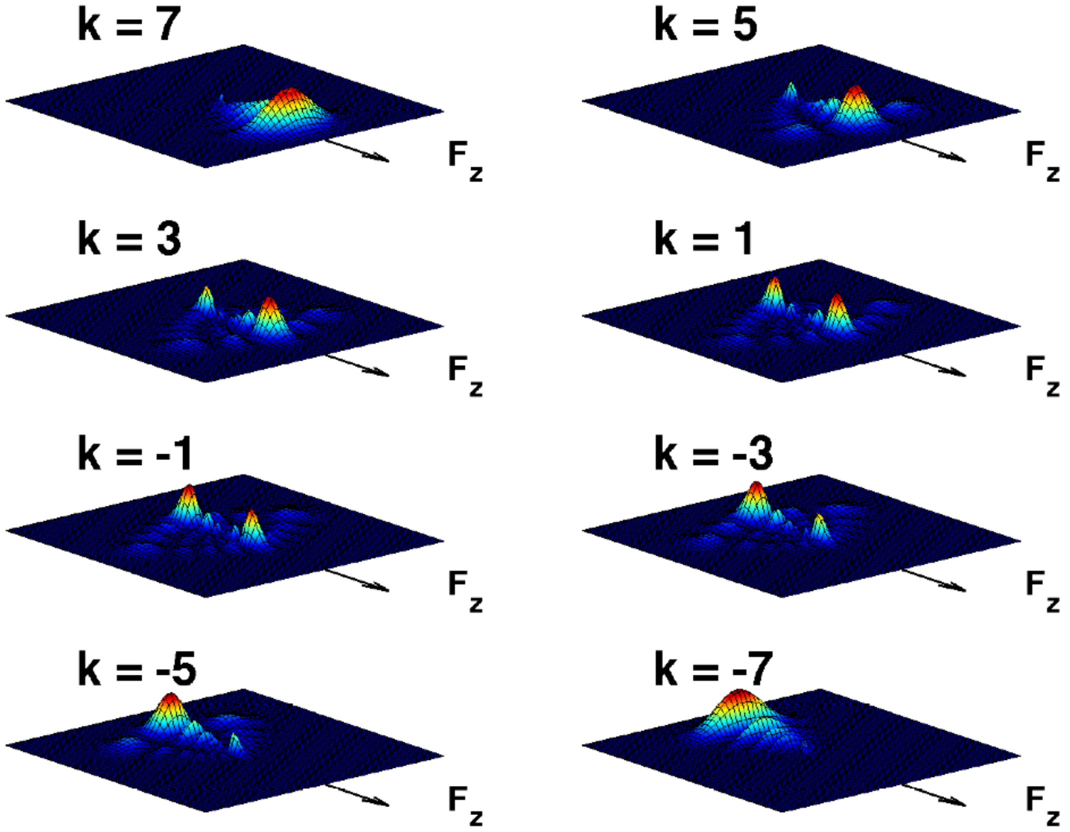

Figure 1.2: Calculated parabolic wavefunctions for the $n = 8$, $m_l = 0$ Rydberg states of atomic hydrogen as described by Gallagher [53]. The electric field is applied along the z-axis. The change in polarisation in accordance with a change of parabolic quantum number is clearly visible.

neighbouring Stark manifolds are traversed diabatically without any interactions of the states involved.

However, for non hydrogenic systems the Stark map is more complex due to the Rydberg electron penetrating into the core region which in turn leads to a loss of the spherical symmetry of the system. In this case the wavefunctions are only separable in parabolic coordinates and coupling between different principal quantum number n (and same m_l) can occur. Contrary to the hydrogenic case, neighbouring n-manifolds now cross adiabatically (avoided crossings) beyond the Inglis-Teller limit which results in changes in some of the characteristics of the electronic wavefunctions involved. The direction of the dipole moment is reversed when a Rydberg state passes through a crossing and red-shifted states become blue shifted or *vice versa*. This mixing-behaviour is of importance in the interaction of non-hydrogenic systems with surfaces as will be seen in Section 1.7. Figure 1.3 shows a calculated Stark map in the range n = 13 - 15 of xenon demonstrating the effect of avoided crossings [37]. Due to the non-zero quantum defect for low l states, these states are parenthetically separated from the higher l main parts of the manifold at zero field and exhibit a quadratic Stark effect at low fields.

1.5 Field ionisation

In an electric field the Coulomb potential for (Stark-) Rydberg states is given by:

$$V = -\frac{1}{r} + Fz \tag{1.16}$$

assuming that the field is applied along the z-axis. Figure 1.4 a) shows a 3D dimensional view of the calculated potential surface using Equation 1.16 which possesses a saddle point along the field axis (blue line) at $z = -1/\sqrt{F}$ with a height

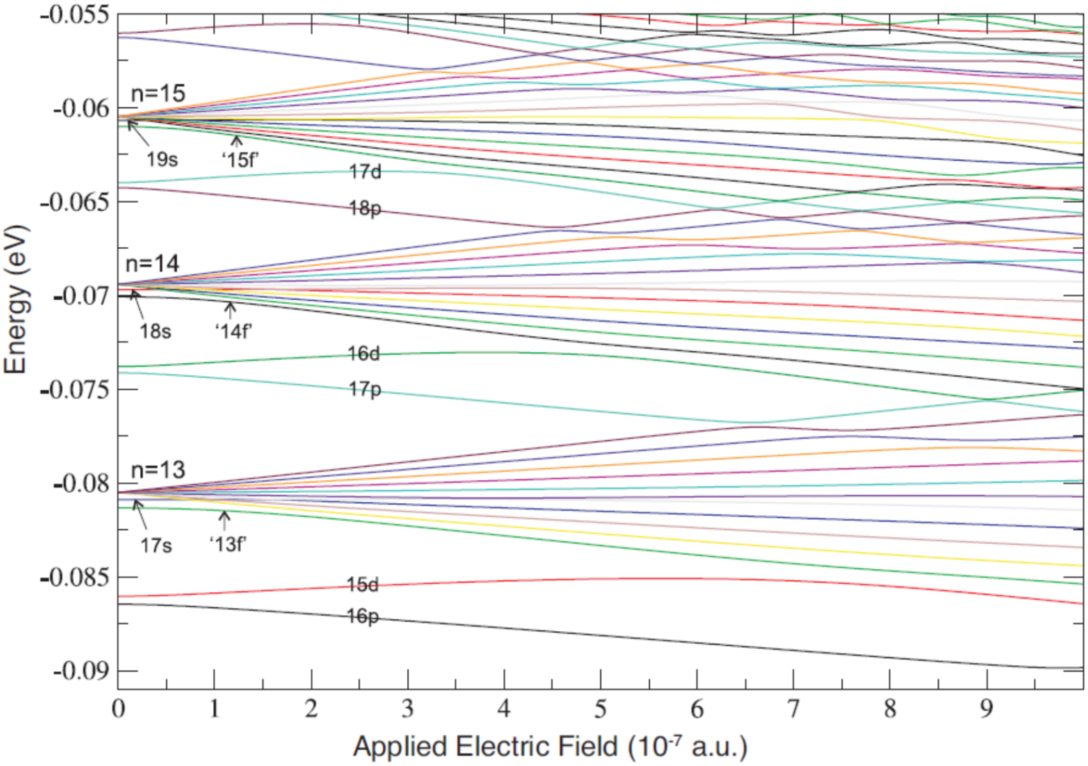

Figure 1.3: From [37]. Calculated Stark map of Xenon in the range n = 13 - 15, demonstrating the effect of avoided crossings on the energies of the Stark states.

of $V_{\text{saddle}} = -2\sqrt{F}$. The different contributing parts to the overall potential along the z-axis (blue line) are shown in Figure 1.4 b). Both the field-free $-1/r$ potential (green dashed line) and the electric field (red dotted line) are shown together with the resulting overall potential. Due to the presence of the potential barrier all Stark states have a finite lifetime with respect to tunnelling through the barrier. In addition to this, the barrier height and width depend on the electric field strength. From a pure classical point of view it can be assumed that at large enough electric fields the energy of a given Stark state lies above the saddle point energy. In this case, the Rydberg electron is no longer confined by the potential and 'over-the-barrier' (OTB) ionisation occurs. From Equation 1.15, it can be derived that the energy of the most red-shifted state ($m_l = 0$) of a given Stark-manifold lies above the saddle point for a field of

$$F \sim \frac{1}{9n^4}. \tag{1.17}$$

With increasing parabolic quantum number k the energy of the Stark states of a given n-manifold increases. Blue-shifted states would therefore be expected to ionise at lower electric fields than red-shifted states of the same manifold. Once again using Equation 1.15 the electric field needed to ionise the most blue-shifted state of a given manifold can be calculated as:

$$F \sim \frac{11 - 4\sqrt{7}}{9n^4}. \tag{1.18}$$

However, in order to get a more realistic picture of the ionisation process it is important to consider the electron polarisation of the red- and blue-shifted Stark states with respect to the saddle point. For red-shifted states the electron density 'points' towards the saddle point and Equation 1.17 gives a good estimate of the field required. For blue-shifted states however, the electron density is mainly located away from the

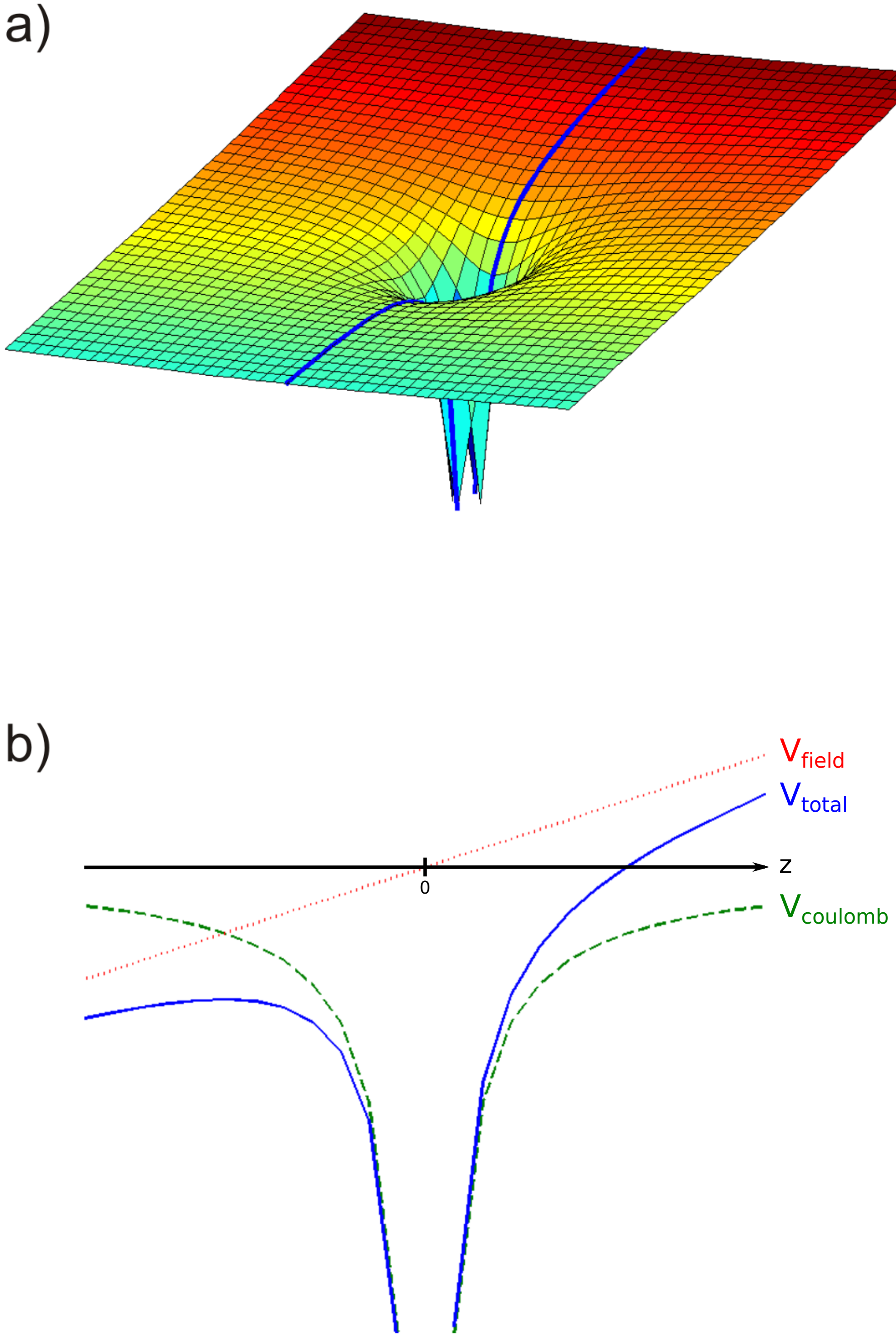

Figure 1.4: a) Calculated potential energy surface for a hydrogen atom in an electric field using Equation 1.16. The blue line marks the field (z) axis. b) Breakdown of the different components of the potential energy (along z-axis). blue line: full potential, green line: $1/r$ Coulomb potential, red line: contribution of the electric field.

saddle point. These states are therefore kinetically more stable which results in the requirement for an electric field to be approximately two times as big as the field needed to ionize a red-shifted state for ionisation to occur on a reasonable experimental time-scale. The field ionisation rate of a hydrogenic Rydberg state has been approximated by Kolosov [64]:

$$\begin{aligned} \Gamma = \frac{(4R)^{2n_2+m_l+1}}{n^3 n_2!(n_2+m_l)!} \exp[-\frac{3}{2}R - \frac{1}{4}n^3 F(34n_2^2 \\ + 34n_2 m_l + 46n_2 + 7m_l^2 + 23m_l + \frac{53}{3})] \qquad (1.19) \\ \text{with} \quad R = (-2E_{nm_lk})^{3/2}/F. \end{aligned}$$

E_{nm_lk} is the fourth-order perturbative Stark energy as given by Equation 1.15. The predicted ionisation rates from this equation vary widely across a Stark manifold. Figure 1.5 shows a calculated Stark map of the $n = 20$, $m_l = 0$ Stark manifold. The open circles represent the electric fields of the different Stark states of the same principal quantum number at which the ionisation rate reaches $10^5\,\mathrm{s}^{-1}$. This value corresponds to a lifetime in the electric field of about 10 μs, the time-scale of a typical Rydberg-surface experiment as performed in this thesis. For comparison, the classical ionisation limit, which only takes into account the height of the potential barrier is also shown (green dotted line).

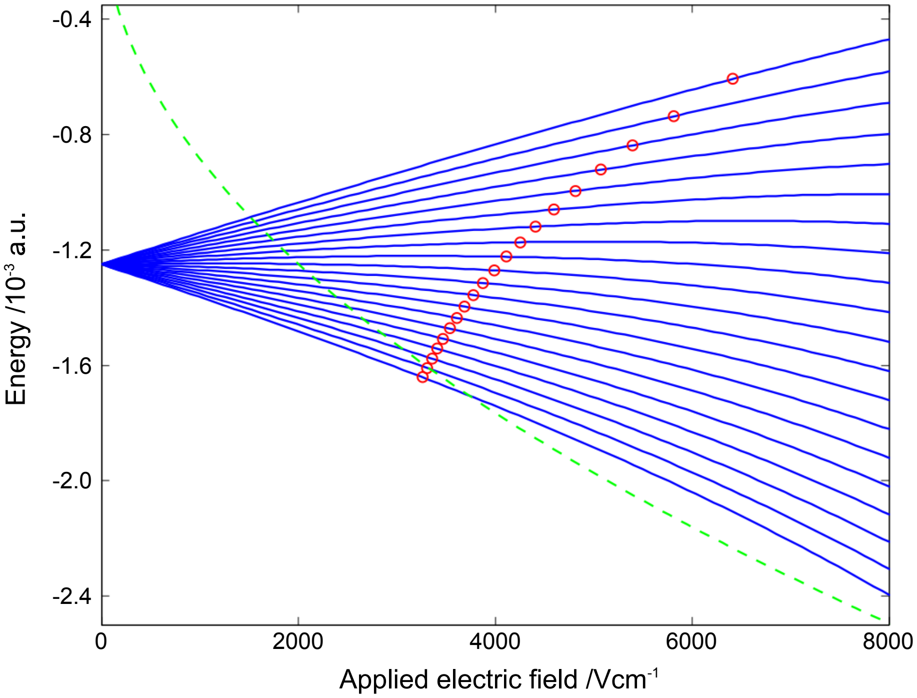

Figure 1.5: Calculated Stark map for the n=20, m_l=0 manifold. Green line: classical ionisation limit (field at which energy of the Stark state lies above the saddle point. Red circles: field at which the ionisation rate calculated by Equation 1.20 exceeds 1×10^{-5} s^{-1}.

1.6 Surface interactions

The interaction of Rydberg states with a metal surface shows some resemblance to the interaction with an electric field as discussed in the previous section. It can be described using a surprisingly simple classical image charge model, with the surface boundary acting as the image plane. In this approach, fictitious image charges of the Rydberg electron as well as the ion core (of opposite sign) are located within the surface at the same distance from the surface-vacuum boundary as the real Rydberg state outside. While these image-charges are not real particles they do, to a certain extent, represent the shifts in the electron distribution in the surface due to the fluctuating charge distribution in the Rydberg state. This leads to a Van-der-Waals type interaction in which the proton, image proton, electron and image electron are considered as point charges. The system possesses cylindrical symmetry and the model works well for long-range interaction (see Section 1.6.1 for small atom-surface separations) as the assumption of point-charges is reasonable in this case. Figure 1.6 presents the geometry of this model-system and the different contributions to the overall potential are shown.

Due to the cylindrical symmetry cylindrical coordinates (ρ and θ) are used:

$$\begin{aligned} x &= \rho \cos\theta \\ y &= \rho \sin\theta. \end{aligned} \tag{1.20}$$

The different contributions to the overall potential are the Coulomb interaction between the proton and the electron (V_c), the interaction of the proton with its own image charge ($V_\mathrm{pp'}$) and with the image charge of the electron ($V_\mathrm{pe'}$) as well as the interaction of the electron with its image charge ($V_\mathrm{ee'}$) and with the image charge of

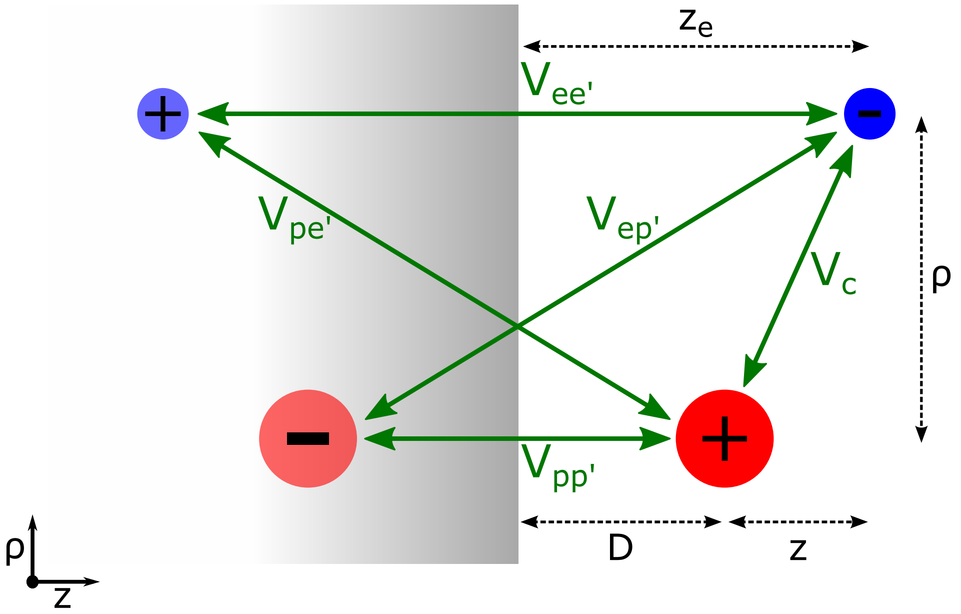

Figure 1.6: Classical interaction between an atom (proton=red, electron=blue) and its image charges (with opposite sign) within the surface showing the different interactions contributing to the potential.

the proton ($V_{\text{ep'}}$).

$$
\begin{aligned}
V_{\text{c}} &= -\frac{Ze^2}{r} \\
V_{\text{pp'}} &= -\frac{\beta Z^2 e^2}{4D} \\
V_{\text{ee'}} &= -\frac{\beta e^2}{4(D+z)} \\
V_{\text{ep'}} = V_{\text{pe'}} &= \frac{\beta Z e^2}{\sqrt{\rho^2 + (2D+z)^2}}
\end{aligned}
\tag{1.21}
$$

with D being the proton surface separation, Ze the ion-core charge, ρ and z the electron coordinates in the ion-core frame and $D + z = z_e$ is the distance of the electron from the surface. β describes the electric shielding of the image charges by the surface and can be given as:

$$\beta = \frac{\epsilon_p - 1}{\epsilon_p + 1} \tag{1.22}$$

where ϵ_p is the dielectric constant of the surface. For a perfect metal surface $\beta = 1$.

Using atomic units and for a hydrogen atom $Z = e = 1$. At the asymptotic limit the overall one-electron potential is thus given as (including a possibly present additional electric field F):

$$\begin{aligned} V_{\text{tot}} =& V_{\text{c}} + V_{\text{surf}} + V_{\text{field}} \\ =& V_{\text{c}} + V_{\text{pp'}} + V_{\text{ee'}} + V_{\text{ep'}} + V_{\text{field}} \\ =& -\frac{1}{\sqrt{z^2+\rho^2}} - \frac{1}{4D} - \frac{1}{4(D+z)} + \frac{1}{\sqrt{\rho^2+(2D+z)^2}} + V_{\text{field}} \end{aligned} \tag{1.23}$$

using

$$\begin{aligned} \lim_{D\to\infty} V_{\text{surf}} =& V_{ee'} + V_{pp'} + V_{ep'} \\ =& -\frac{1}{4z_e} - \frac{1}{4D} + \frac{1}{\sqrt{(D+|z_e|)^2+\rho^2}} \\ =& -\frac{1}{4(D+z)} - \frac{1}{4D} + \frac{1}{\sqrt{(D+|D+z|)^2+\rho^2}} \end{aligned} \tag{1.24}$$

Binomially expanding Equation 1.24, it can be shown that the dominant force between surface and Rydberg state is attractive [37]. It can also be seen that for $D^2 >> r^2$ hydrogenic spherical wave-functions $|nlm_l\rangle$ with $\Delta l = 0, \pm 2$ and $\Delta m_l = 0$ are coupled by the Van-der-Waals perturbation. Similar to the Stark effect, this leads to the lifting of the n^2 degeneracy of the n-manifolds and a strong polarisation of the electron eigenfunctions with respect to the surface [37]. Red-shifted states are thereby oriented towards the surface while blue-shifted states are pointing towards the vacuum. The effect of this polarisation on the surface interaction will be discussed in more detail in Chapter 2.2.1.

1.6.1 The Jellium Model

Equation 1.24 is only valid in the asymptotic limit of $\lim_{z\to\infty} V_{\text{surf}}$ due to a singularity in $V_{ee'}$ at $z = -D$. In order to correctly model the Rydberg-state – surface interaction at close proximity a simple Jenning-Jones one-electron pseudo potential [65] treating the metal as a Jellium can be used. In this model the electrons are assumed to move freely within a background of fixed charge density, representing the ion cores in the metal. The overall potential can thus be given as:

$$V_{\text{ee'}}(z, D) = \begin{cases} \frac{-1+\exp[-\alpha((D+z)-z_0)]}{4((D+z)-z_0)} & \text{if } (D+z) > z_0 \\ \frac{V_0}{A\exp[B((D+z)-z_0)]+1} & \text{otherwise} \end{cases} \tag{1.25}$$

$$\text{with} \quad A = -1 - 4V_0/\beta, \quad B = -2V_0/A$$

with V_0 being the bulk potential of the surface, z_0 the image plain of the surface and β is surface specific interpolation parameter. For an aluminium surface these parameters are $z_0 = 0.7$, $V_0 = -0.574$ and $\beta = 1.25$. The resulting potential with all its different components is shown in figure 1.7.

1.6.2 Classical charge transfer

Similar to the potential of a hydrogen Rydberg state in an electric field the surface interaction potential exhibits a potential barrier with the saddle point lying on the surface normal. The height and the width of this potential barrier depends on the distance of the Rydberg atom from the surface and they both decrease with decreasing distance from the surface as can be seen in Figure 1.8. The position of the saddle point

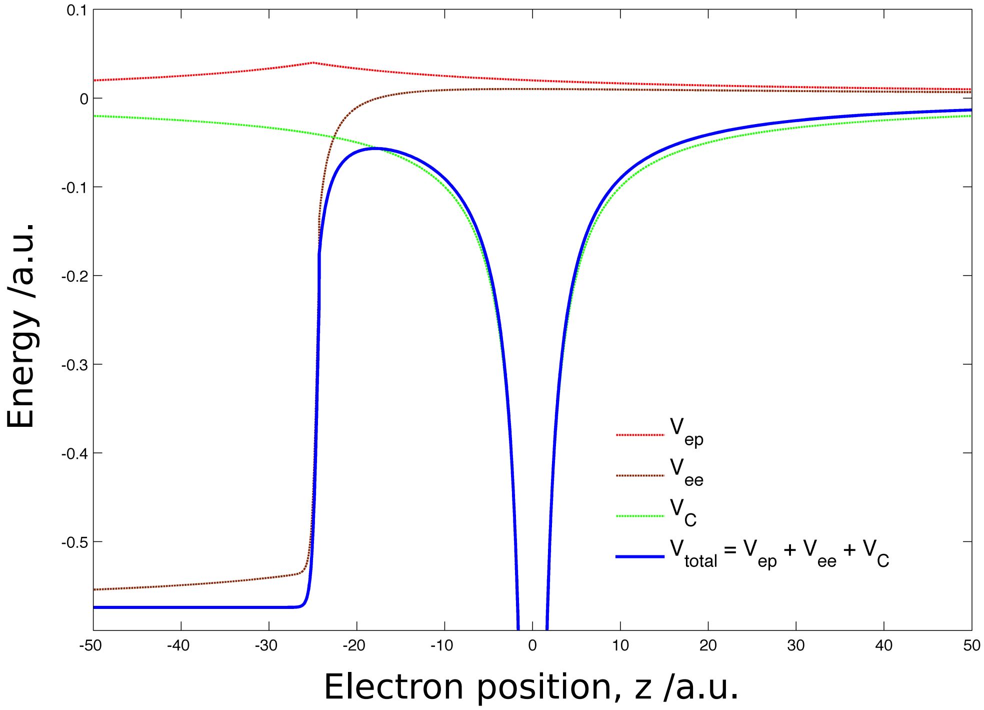

Figure 1.7: Plot of the total electronic potential, $V_texttotal$, an electron exhibits in the presence of an aluminium surface. The potential is calculated using the Jellium model (1.25) and the different contributions to the total potential, $V_textee', V_textep', V_textc$, are shown. The surface is located at an electron coordinate of z = -25 a.u. (with respect to the ion-core).

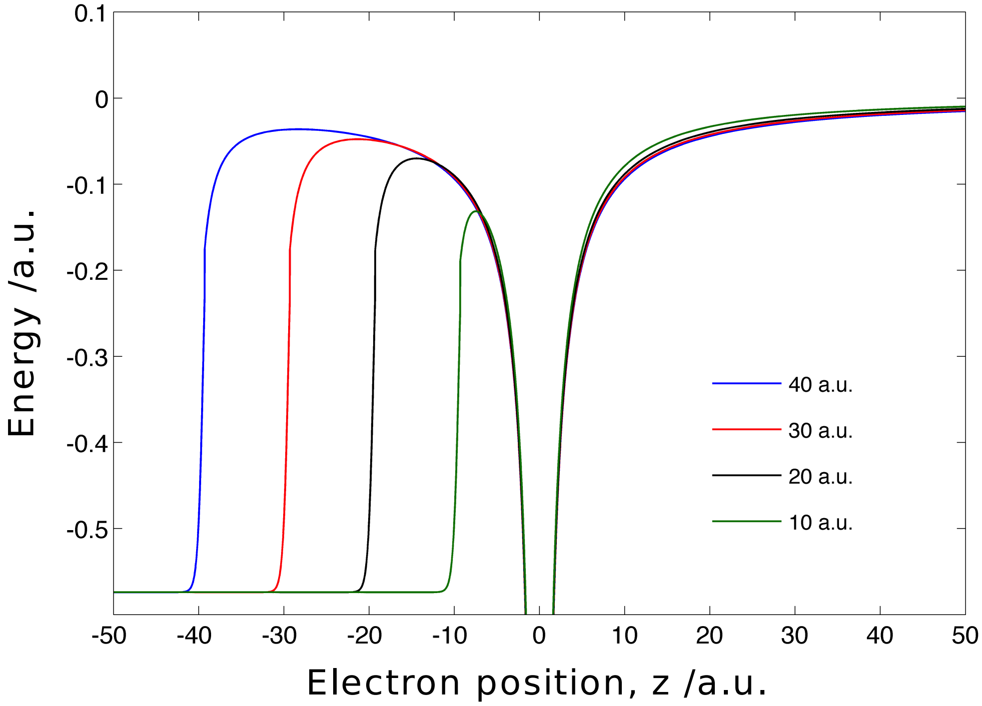

Figure 1.8: Plot of the total electronic surface potential as a function of the distance of the Rydberg state from the surface, calculated using Equation 1.25 . The relationship of barrier height and width is shown by plotting the potential for a range of distances (D = 10, 20, 30, 40 a.u.).

is given by [21]:

$$z_{\text{saddle}}(D) = -\left(1 - \sqrt{\frac{4\sqrt{5}}{7}}\right) D \approx -0.69D \tag{1.26}$$

and the barrier height is

$$E_{\text{saddle}} = -\frac{7\sqrt{5+4\sqrt{2}}}{4D\left(1+2\sqrt{2}\right)} - \frac{1}{4D} \approx -\frac{1.7422}{D}. \tag{1.27}$$

Ignoring quantum mechanical effects such as tunnelling, the Rydberg state energy must be above the saddle point energy for charge transfer into the conduction band of the surface to occur (over-the-barrier ionisation). From Equation 1.15 can be seen that to first order the energy of a Rydberg state scales with n^{-2}. It is thus possible to derive the general ionisation distance in zero field as a function of principal quantum number squared: $D_{\mathrm{OTB}} \approx 3.48n^2a_0$. For a Rydberg state with a principal quantum number $n = 30$ this corresponds to an ionisation distance of $\sim$ 170 nm. It should be noted that this ionisation distance is only valid in zero-field and does not include the perturbation of the energy of the Rydberg state as it approaches the surface. Such perturbations significantly complicate the system and an extension of the OTB-model including the effects of an electric field will be discussed in Chapter 2.

1.7 Previous experimental studies of Rydberg state surface interactions

The interaction of Rydberg states with surfaces has been studied extensively both theoretically and experimentally. The aim of most of these experiments was to gain a greater understanding of the effect the surface has on the level structure of the Rydberg state, to comprehend the origins of energy level perturbations and as a more distant possibility, to see whether these states are suitable to probe the energy structure or the physical structure of the surface. In the following sections I will highlight some of the progress that has been made in this area to date.

1.7.1 Charge transfer experiments

The first experiments which investigated the charge transfer of Rydberg states to surfaces were performed by Fabre et al. [40]. In these experiments sodium Rydberg states (Na(n,d)) were created by laser excitation and these states were then passed through a thin gold foil with micrometer sized slits. The transmission of Rydberg atoms as a function of principal quantum number n was monitored at different angles of the foil in the molecular beam, thereby effectively varying the size of the slits. Measuring the transmission rates allowed for a direct observation of the physical size of the Rydberg atoms, as this number directly relates to the number of atoms which do not undergo surface ionisation when colliding with the foil. Modelling the Rydberg states as hard spheres and the gold foil as a 'sieve' resulted in an average surface ionisation distance of $\sim 4.5n^2a_0$. This number differed noticeably from the theoretically predicted value of $\sim 3.5n^2a_0$ (see section 1.6.2) and it was suggested that patch electric fields due to adsorption of sodium atoms on the gold surface might be responsible for the observed discrepancies.

A first in depth study of the interaction of Rydberg states with metal surfaces was published by Dunning and co-workers at Rice University in 1988 [43]. In their experiments they investigated the ionisation behaviour of K(nd) Rydberg states at a grazing incidence angle on a flat gold metal surface. After ionisation, the resulting ions keep flying towards the surface due to their initial velocity and the now purely attractive proton - image-proton interaction. To prevent neutralisation at the surface an electric field was applied to repel the ions and they were subsequently detected via a position-sensitive detector. Assuming conservation of energy the electric field F_{min} needed to repel an ion depends on the distance from the surface as well as the collisional velocity of the ion and is given as:

$$\vec{F}_{\mathrm{min}}(D_i, T_\perp) = Z_c \left[\frac{1}{2D_i} + \sqrt{\frac{T_\perp}{D_i}} \right]^2 \tag{1.28}$$

where Z_c is the charge of the particle ($Z_c = 1$ for a proton), $T_\perp$ is the kinetic energy component perpendicular to the surface and D_i is the distance at which the ion is formed. Alternatively it is possible to rearrange Equation 1.28 so it gives the minimum ionisation distance D_{min} for which detection of an ion is possible at a given field $\vec{F}$:

$$D_{\text{min}}(\vec{F}, T_\perp) = \frac{T_\perp + \sqrt{(\vec{F}/Z_c)} + \sqrt{T_\perp^2 + 2T_\perp\sqrt{F\vec{/}Z_c}}}{2(F\vec{/}Z_c)}. \tag{1.29}$$

Equations 1.28 and 1.29 demonstrate how extraction field and ionisation distance are related: the field needed to repel the ion from the surfaces increases when the ionisation distance decreases. By measuring the detected ion signal as a function of electric field it is possible to gain information about the distance from the surface at which ionisation occurred. In the asymptotic limit of $T_\perp \to 0$ and using the over-the-barrier ionisation assumption that D_i scales with n^2 (see section 2.1 for details) it can be shown that

$$\lim_{T_\perp \to 0} \vec{F}_{\text{min}}(D_i, T_\perp) = \frac{Z_c}{4D_i^2} \sim\propto n^{-4} \tag{1.30}$$

To analyse the surface ionisation behaviour Gray et al. analysed the ion detection probability as a function of applied electric field, so called surface ionisation profiles. These traces show some distinct features (see Figure 1.9 for typical profiles) and will be explained in more detail in Section 3.2.2. With increasing electric field, smaller and smaller ionisation distances can be probed leading to a characteristic increase of signal with applied field until a maximum is reached. After this maximum, the signal drops to zero once the field ionisation threshold is reached, as field-ionised atoms or molecules are detected in a different channel. The detected traces are either normalised to 1 or more commonly, normalised to the integrated field ionisation signal to convert the signal to a detection probability. The results obtained in the experiments by Gray et al. showed an increase in the detected ion signal at electric fields that (via Equation 1.29) corresponded to an ionisation distance of approximately $(4-5)n^2a_0$, which is in good agreement to the results obtained by Fabre at al. However a not insignificant number of ions could be detected at lower fields indicating that some of the Rydberg atoms were ionised further away from the surface than expected. This behaviour was explained by assuming that over the course of the experiment potassium atoms were deposited on the surface leading to patch fields which in turn lead to an increase and spread in ionisation distance.

The same group therefore repeated the experiments using less reactive xenon atoms incident on an Au(111) surface for principal quantum numbers in the range $n = 13 - 20$ [44] . This time they determined the ionisation distance as a function of principal quantum number as $(4.5 \pm 0.9)n^2a_0$, once more in good agreement with previous experiments. More importantly though, no more ionisation at greater distances from the surface could be observed.

In further experiments Dunning et al. also investigated possible effects of the electron polarisation on the ionisation of Rydberg states [66, 67, 68]. They took advantage of the Stark effect and excited xenon atoms in the presence of an electric field allowing the selective population of the most red- $(k = -(n-1),\ m_l = 0)$ and blue-shifted $(k = +(n-1),\ m_l = 0)$ Rydberg states of a range of principal quantum numbers. As described in section 2.2.1, significantly different ionisation behaviour can be expected, as for the red-shifted case the electron cloud points towards the surface while for the blue-shifted states it points towards the vacuum. However, in these experiments, no significant differences in the surface ionisation profiles for red- and blue-shifted states could be observed, indicating that all Stark states of a given manifold ionised at similar distances from the surface, as shown in Figure 1.9. The observed onset of the signal for blue-shifted states corresponds to an ionisation distance from the surface of approximately $Z_i \sim 4.5n^2a_0$. However, these were expected to ionise at a significantly smaller distance of approximately $Z_i = 1.2n^2a_0$ in turn leading to a much higher extraction field required to repel the resulting ions from the surface [69, 31]. This rather unexpected observation was explained by suggesting that avoided crossings between Stark manifolds of neighbouring Rydberg states in non-hydrogenic atoms and molecules lead to loss of distinct electron polarisation. As explained in section 1.6 the surface interaction has a similar effect on the Rydberg state as an applied electric field. However, due to the different symmetry of the system and also due to the non-hydrogenic nature of the xenon atom, Rydberg states with the same magnetic quantum number (here: $m_l = 0$) may undergo avoided crossings at a close enough distance to the surface (beyond the Inglis-Teller-limit). Whenever a Rydberg state crosses adiabatically through one of these crossings the electron polarisation 'flips' from red- to blue-shifted (or vice versa). The atom undergoes multiple crossings on its approach to the surface, but due to the fact that red-shifted states ionise at greater distances, the ionisation dynamics of all Stark states are dominated by the ionisation behaviour of red-shifted states, independent of the original orientation.

Subsequently, Dunning and co-workers used rate equations to model their experimental results [70, 45]. While experimental surface ionisation profiles showed an exponential increase of detected ion signal with electric field, this increase occurred at a much slower rate than expected from atomic hydrogen calculations. By repeating the experiments at different incident angles of the molecular beam they concluded that these differences were due to surface inhomogeneities (e.g. surface deposits or local variations in crystal structure). While AFM measurements confirmed that the gold surface was atomically flat as expected, Kelvin-Probe-microscopy revealed variations in the surface potential on the scale of $\sim \pm 60 - 70$ V with domain sizes ranging from ~ 50 nm to ~ 250 nm. These results indicate that the patch charges might stem from changes in the surface work function possibly caused by adsorbates present on the surface or by 'buried' surface defects. By including these stray fields into relatively simple over-the-barrier ionisation simulations Dunning and co-workers were able to model their experimental results with a high level of accuracy [46, 47]. These findings are of special interest to

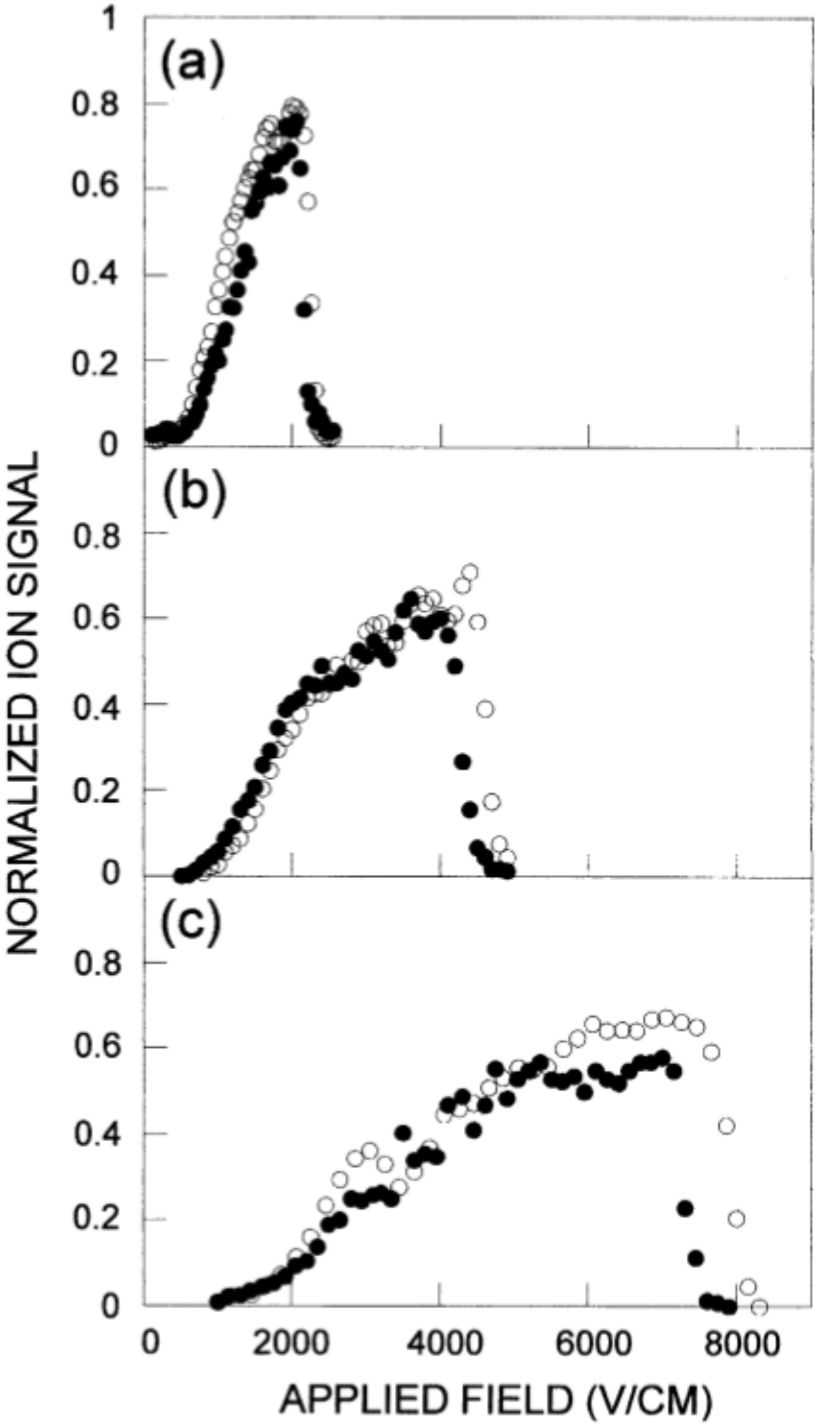

Figure 1.9: From [68]. Previous experimental results showing the surface ionisation signal as a function of electric field of the most red- (open circles) and blue-shifted Stark states (filled circles) of the $n = 20$ (a), 17 (b) and 15 (c), $m_l = 0$ Xe manifolds. Only minimal differences between the surface ionisation signals for red- and blue-shifted states can be seen.

this thesis as some of the work presented here is performed with flat gold surfaces, similar to those in the experiments by Dunning et al., and should therefore be affected by the same (or similar) patch fields.

Other experiments investigating the interaction of Rydberg states with gold metal surfaces were performed by Softley et al. in Oxford [48, 49, 50]. In their experiments hydrogen molecules (H_2) were used instead of rare gases, adding an additional degree of complexity to the system. Rydberg hydrogen molecules can possess different core rotational quantum states N^+. While states with different N^+ are usually not coupled by homogeneous electric fields, only small field perturbations or the interaction with a surface are enough lift this restriction and allow for population transfer between these states to occur. In their experiments, Softley et al. employed a laser excitation scheme using two perpendicularly oriented laser beams to create H_2 Rydberg states with a core rotational quantum number of $N^+ = 2$. They observed that the ionisation behaviour was dominated by avoided crossings of Stark states of the $N^+ = 2$ and the $N^+ = 0$ (no core rotation) core rotational states. Figure 1.10 demonstrates how this coupling between the two core rotational states leads to a population transfer, from an initially populated $N^+ = 2$ state with principal quantum number n, to a state with an effectively higher principal quantum number v_0 which is associated with the $N^+ = 0$ channel (rotational to electronic energy transfer). This 'increase' in principal quantum number in turn leads to an increase in ionisation distance. The experimentally detected ionisation distance scaled with $D_i \sim (3-5)v_0^2 a_0$ which is in good agreement with previous studies using rare gases [48, 49]. In addition, resonances were visible in the recorded surface ionisation profiles, which could be associated with electric fields corresponding to avoided crossings in the Stark map between states of different core rotational quantum numbers (see Figure 1.11) [50]. Investigations making use of the polarisation of Stark states were also carried out. But similar to the

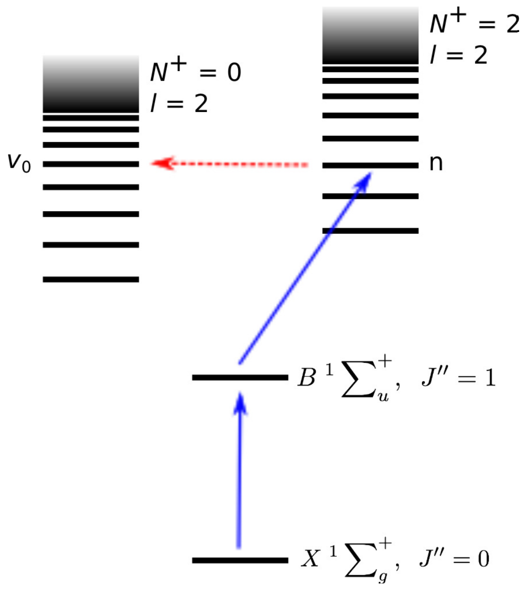

Figure 1.10: Schematic of the population transfer between Rydberg state of H_2 with different core rotational quantum numbers N^+. An electron is excited to Rydberg states with a principal quantum number n ($N^+ = 2$) in a 2 laser - 2 photon excitation scheme via the B $^1\sum_u^+$ state (blue lines). In the presence of an electric field, crossings with Rydberg states with a core principal quantum number $N^+ = 0$ occur which possess a higher principal quantum number v_0 ($v_0 > n$). Population transfer into these states takes place (red dotted line) and the $N^+ = 0$ hence becomes the dominant channel in the ionisation process. While experimentally it is possible to excite both $l = 0$ and $l = 2$ states, only the $l = 2$ states are shown here for clarity.

results of Dunning et al. the surface ionisation was found to be dominated by avoided crossings of neighbouring manifolds leading to the loss of polarisation.

In order to probe the effect of polarisation of the electronic wavefunctions of the Rydberg state has on the surface ionisation dynamics and to allow for a direct comparison of experimental and theoretical results, So et al. excited hydrogen atoms in the presence of an external electric field [37, 36]. The experimental setup used was analogous to earlier experiments performed with hydrogen molecules, but by using hydrogen atoms the investigated system could be significantly simplified. As stated earlier, H-atoms tend to pass through energy crossings diabatically, without any change of polarisation. In Figure 1.12 a) surface ionisation profiles of different Stark states of the $n = 23$

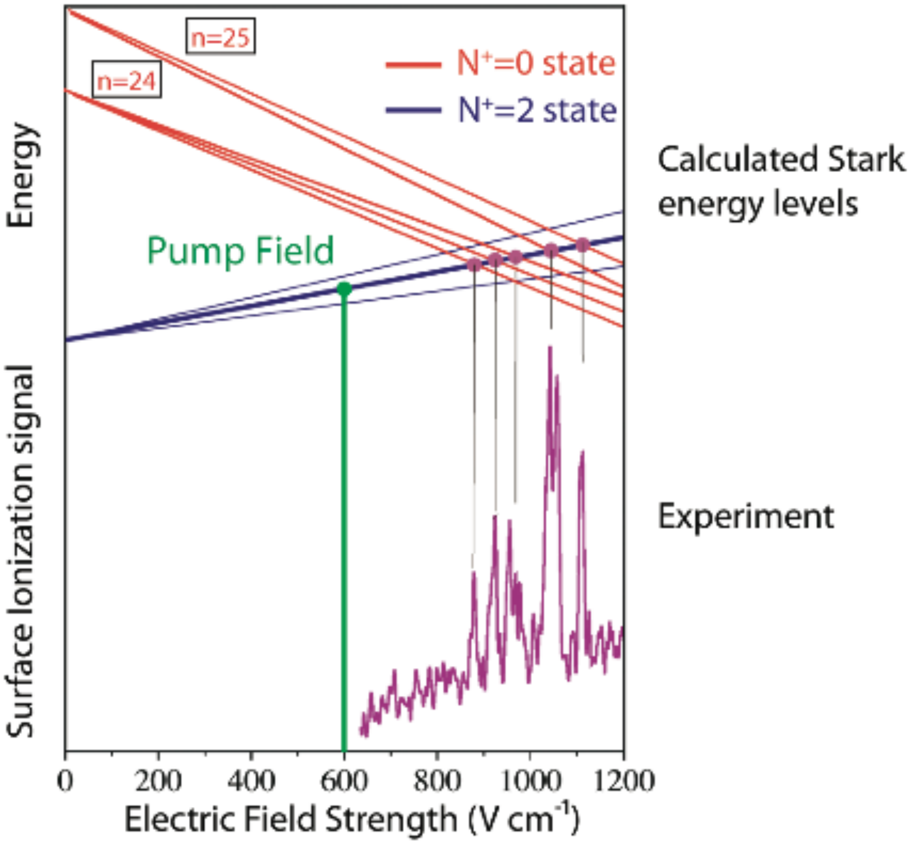

Figure 1.11: From [50]. Example of energy-level crossings of an initial state $N^+ = 2$, $n = 17$ (blue lines) with levels of the $N^+ = 0$, $n = 24, 25$ manifolds (red lines) and a comparison with the observed resonances in the surface ionization profile for that state (purple).

Rydberg manifold are presented. Contrary to earlier experiments [67, 68, 48, 49] red- and blue-shifted states now showed distinctly different surface ionisation profiles. The onset as well as the high-field cut-off for red-shifted states appeared at significantly lower fields than for blue-shifted states, indicating that these states ionise further away from the surface. In order to model the results, an over-the-barrier ionisation model which was convoluted with a Gaussian spread of ionisation distances ($\sigma = 2.5n^2$) and shifted by a factor of $1n^2$ was used (see chapter 2.3.1 for more details). The ionisation distance was thus determined to be $\sim 3.5n^2$ a.u., which is in good agreement with theoretical predictions. Figure 1.12 b) shows the surface ionisation profiles for the most red-shifted Stark states for a range of principal quantum numbers (full lines) and the theoretical model (dotted lines). The effect of collisional velocities was also investigated in the same work. It could be shown that, in accordance with theory [31], the detection efficiency within the rising part of the surface ionisation profile increases when the velocity of the Rydberg state is decreased.

In related experiments it was shown by Softley and co-workers that it is possible to detect electrons originating from the surface ionisation process induced by the Rydberg state surface interaction [71, 37, 51]. This could be achieved by reversing the ion-extraction field and detecting the electrons via a backscattering mechanism (no electron flux into the metal) as proposed by So et al. [36]. As with previous experiments using ion-detection it could be shown that the surface ionisation dynamics depend strongly on the species involved. Under these conditions, H_2-molecules showed the same mixing of states with different core rotational quantum numbers N^+ as described above, while experiments with atomic hydrogen demonstrated that for this species polarisation of the electronic wavefunctions can be retained upon approach of the surface (though the relative intensity of the surface ionisation profiles of Stark states of a given n-manifold was reversed).

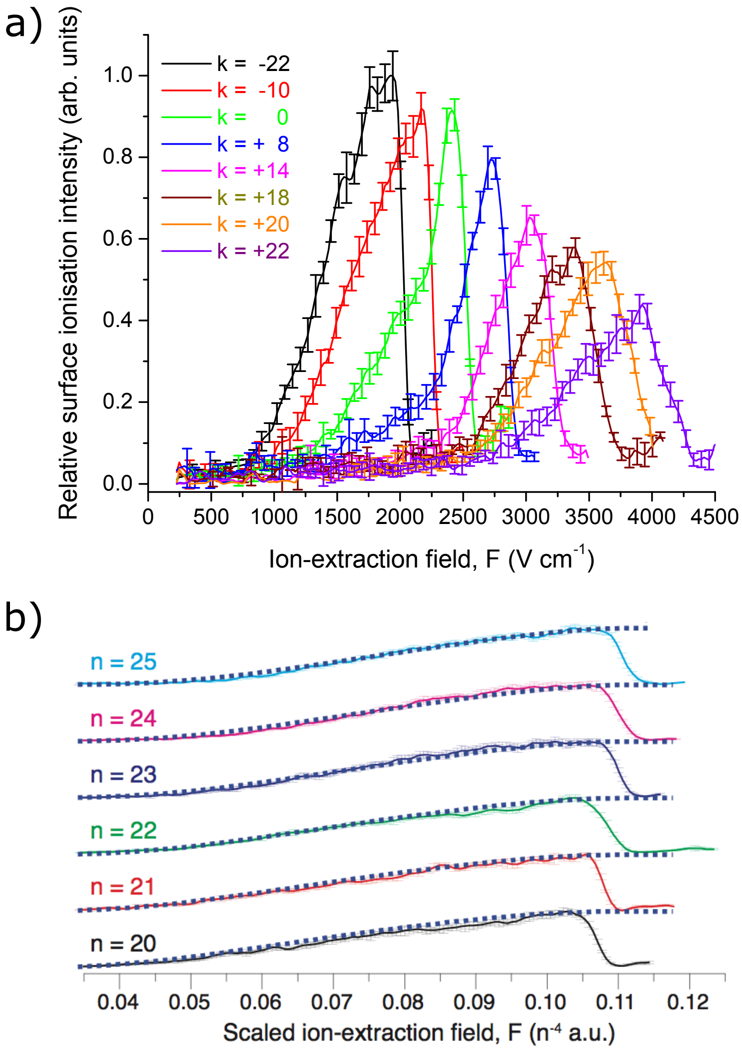

Figure 1.12: From[37]. a) surface ionisation profiles of different Stark states of the $n = 23$ Rydberg state of atomic hydrogen. The effect of electron polarisation can be seen by the shift of onset and cut-off of the individual profiles. b) surface ionisation profiles of the most red-shifted Stark states for a range of principal quantum numbers (full lines) together with the results using the theoretical model described in the text (dotted lines).

One of the aims of this thesis is to investigate how surface properties influence the surface ionisation behaviour. Dunning et al. were the first to study this question by investigating the surface ionisation of xenon Rydberg atoms at semiconductor surfaces [72, 45, 73]. Both n- and p-type doped Si(100) surfaces were investigated and significant differences in the onset of the detected ion signal were observed and were attributed to stray fields created by changes in the surface potential in the order of $\sim \pm 100\ mV$ with length scales of approximately $\sim 1\ \mu m$. As a possible origin for these stray fields it was suggested that over the course of the experiment a thin layer of SiO_2 might have grown on the surface.

A more in-depth analysis of the interaction of Rydberg states with doped silicon surfaces was recently performed by Ganeshalingam et al. [74] in the group of Prof. Softley in Oxford. In this work a closer look was taken at the effects the type of dopant (p- or n-type) as well as the dopant concentration can have on the ionisation behaviour. Both of these parameters were expected to be of importance due to their expected effects on the ionisation process. In order to simulate the system the dopant atoms were modelled as fixed charges in the surface layer in a background of opposite charge. Then a so-called ionisation surface was calculated, a 2-dimensional map of the distances from the surface at which ionisation occurs. Essentially, the dopant resulted in a corrugation of this ionisation surface, the magnitude of which depends on dopant kind and concentration (see Figure 1.13 a). In the experiments both molecular as well as atomic hydrogen were used and the results for both species essentially followed the same trends: n-type semiconductor surfaces generally resulted in an increased detection efficiency of the surface ionisation profile over p-type semiconductors and the detection efficiency decreased with increasing dopant concentration (see Figure 1.13 b and c). These results could be backed up by Monte-Carlo trajectory simulations, which qualitatively confirmed experimental observations.

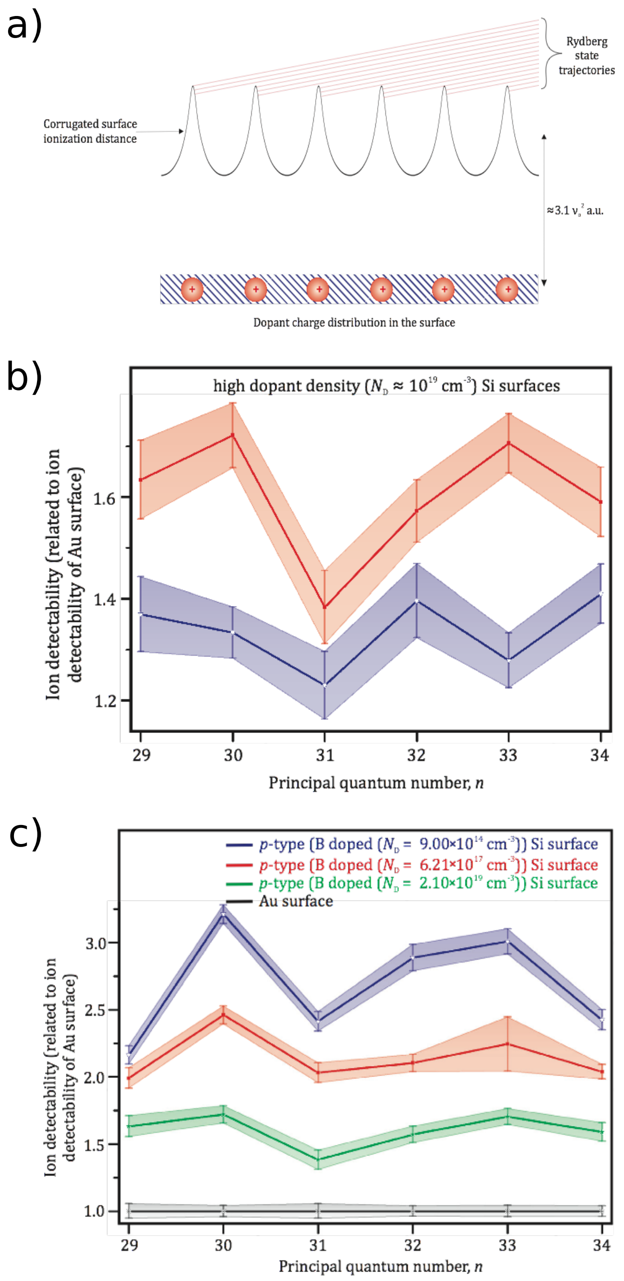

Figure 1.13: Results from [74]. a) schematic of the corrugated ionisation surface resulting from the dopant in the surface. Due to the shallow impact angle of the Rydberg states (red lines) this leads to ionisation at greater then expected distances from the surface. b) comparison of the detection efficiency of p- (blue line) and n-type (red line) semiconductors as a function of principle quantum number. c) comparison of the effect of dopant concentrations on detection efficiency (observed at a p-type surface) as a function of principle quantum number.

So et al. also investigated the interactions of atomic hydrogen Rydberg states with a single crystal Cu(100) surface [37]. Cu(100) is a band-gap semi-conductor for which the projected surface band-gap lies in the experimentally accessible energy range of Rydberg states. Wave-packet-propagation (WPP) calculations predicted that the image charge interaction of an electron with such a surface can lead to the emergence of so called 'surface-states' and 'image states' within the band-gap which themselves form a pseudo-Rydberg series. While charge-transfer from the Rydberg states to the copper should be inhibited in the band-gap region, resonant ionisation can be expected at certain electric fields where the Rydberg energy matches that of a surface or image state. Figure 1.14 a) shows the calculated energies of these image states (grey dotted lines) as well as the energies of hydrogen Rydberg states with a parabolic quantum number of $k \simeq 0$ (full lines). The energy of the image states was increased by the author by a shift of 5×10^{-5} a.u. in order to approximate perturbations effects of the incoming ion core potential. Figure 1.14 b) shows the ratio of the integrated surface signal detected for the Cu(100) surface compared with the bulk gold surface as measured by So et al. An enhanced detection efficiency was observed for those Rydberg states that are in resonance with image states. However, the observed error for these experiments was quite large and more work is therefore required. Together with the results from Ganeshalingam et al. the results by So et al. demonstrate the possibility to utilize Rydberg states to probe surface properties, thereby laying the ground-work for this thesis.

1.7.2 Theoretical investigations

In recent years there have been several theoretical investigations focusing on the interaction of Rydberg states with surfaces, employing a range of theoretical methods. This section aims to provide a short overview of the work undertaken and results achieved

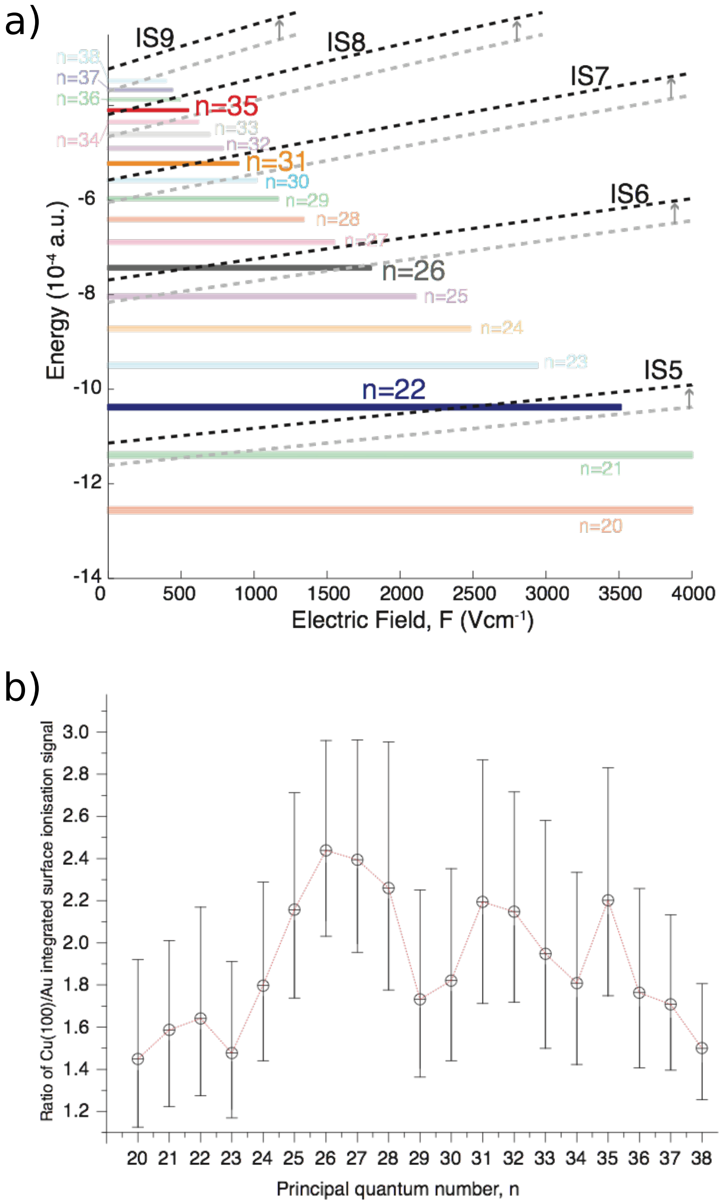

Figure 1.14: From [37]. a) Stark map of the mid-manifold Stark states ($k \sim 0$) of atomic hydrogen (coloured full lines) and the energies of the Cu(100) image states (grey dotted line). The energy of the image states is shifted by 5×10^{-5} a.u. to approximate perturbations due to the presence of the Rydberg state. b) ratio of the integrated surface ionisation signal of Cu(100) compared with bulk Au. An enhanced detection probability can be observed for principal quantum numbers that have crossings with image states.

to date.

Nordlander et al. have used a complex scaling approach to calculate the ionisation behaviour of atomic Rydberg states near a Jellium type metal [29, 30, 75, 31] and also near impurity-covered [76] and corrugated metal surfaces [77]. In this method the Schrödinger equation is solved by extending the coordinates into the complex plane and subsequently diagonalising the (non-Hermitian, complex) Hamiltonian. Results obtained for metallic surfaces showed a lifting of the l degeneracy of a given principal quantum number manifold, level broadening near the surface and adiabatic level crossings, leading to a polarisation of the electronic wavefunction in a range of orientations [29, 75]. The calculations also included the effect of an externally applied electric field on the Rydberg state, though in this particular case only the effect of the field on the ion after charge transfer to the surface was considered (see section 2.2.3 for the effect of the field on the charge transfer process) [30, 31]. The effect of the surface itself on the charge transfer process was also studied by investigating impurity-covered and corrugated surfaces, resulting in the conclusion that both of these modification can have great effect on the ionisation dynamics of Rydberg states.

Wille and co-workers performed an extensive theoretical investigation of Rydberg atoms and ions near metal surfaces trying to derive universal scaling behaviours using a range of quasi-classical and quantum mechanical methods [78]. They were thus able to define a range of scaling parameters regarding transition rates, ionisation distance (‘classical threshold distance’) and also transition matrix elements.

The interaction of xenon Rydberg states with metal surfaces using wave-packet propagation theory was first studied by Sjakste et al. [35]. In their work, they investigated the effect an external electric field can have on the polarisation of the electronic wavefunction and how this, in turn, affects the surface ionisation of Stark states. They were able to explain theoretically the loss of polarisation during the surface interaction observed by Hill et al. [44] and Lloyd et al. [48] for xenon and molecular hydrogen respectively. This time-dependent method is an improvement over other methods used previously as it allowed the inclusion of dynamically distinguishable adiabatic and non-adiabatic effects.

So et al. used a similar wavepacket approach to calculate the interaction of atomic hydrogen Rydberg states near Cu(111) and Cu(100) band-gap semiconductor surfaces [36]. This work was based on first theoretical investigations by Borisov and co-workers who studied the interaction of H^- near Cu(111) [34]. As mentioned in section 1.6, putting a charge in front of a metal surface leads to the emergence of an image charge within the metal. In turn, this leads to a Coulombic potential just outside the metal and the formation of bound energy states within this potential, the so called surface and image states. For the most part, these states are resonant with either the valence or conduction band and they are effectively not populated. For Rydberg states with energies in the band-gap however, surface ionisation predominantly occurs via the image and surface states, leading to resonance effects which might also be detected experimentally.

1.7.3 Other noteworthy experiments

Besides studying the charge transfer between a Rydberg state and a surface it can also be of interest to study the long-range interactions as described in section 1.6. Due to the large distance it is possible to assume a Van-der-Waals type interaction:

$$V_{\mathrm{VDW}} = -\frac{1}{16D^3}(r^2 + z^2) \tag{1.31}$$

with D being the surface separation and (r, z) the electron coordinates.

This idea was first investigated by Hinds and co-workers [38]. In their experiments they sent a beam of Cs and Na Rydberg atoms between two gold plated mirrors. Only those atoms that fly centrally through the 'tunnel' could exit the setup undisturbed while all others were deflected towards one of the two mirrors by the Van-der-Waals interaction. By measuring the transmission rate as a function of principal quantum number and mirror separation the magnitude of the deflection and thus the VDW force could be determined and the results were found to be in good agreement with theoretical calculations. In a similar experiment the same group also measured the width of the $3p$ to ns ($n = 10 - 13$) transition, broadened by the surface interaction, and results were once again found to be in good agreement with theoretical predictions [79, 39]. However small deviations from theoretical predictions could be found in both experiments and were explained with the presence of patch fields due to the polycrystalline nature of the two gold surfaces. These fields were found to scale with D^{-2} as can be expected for such fields [80, 81, 82]. This once again demonstrates the possibility to extract information about surface by studying Rydberg state – surface interactions.

Another one of the suggested applications of Rydberg states lies in the field of quantum computing. For this sort of application it is essential to gain precise control over quantum states, population and coherence lifetime and all of these parameters are influenced by the presence of a surface. Tauschinsky et al. therefore recently studied the energy shifts and change in linewidth of ultra-cold rubidium atoms trapped on an atom-chip [14]. Using electromagnetically induced transparency (EIT) these changes were investigated as a function of distance (10 - 200 μm) from the surface for the $5p - nd_{\frac{3}{2},\frac{5}{2}}$ and $5p - ns_{\frac{1}{2}}$ ($n = 22 - 35$) transitions. However, no significant broadening of the energy levels could be detected as the corresponding electric fields needed to induce these changes scaled with a much lower factor then expected ($D^{-0.7}$ instead of D^{-3}). It was assumed that this might be due to the deposition of Rb atoms on the chip underneath the trap, with each adsorbed atom acting as an electric dipole oriented perpendicular to the surface.

1.8 Aim and outline

Understanding the interaction of Rydberg states with surfaces at close proximity is essential for several of the proposed applications (e.g. quantum computing). Past experimental and theoretical studies have demonstrated the possibility to use Rydberg states as probes of the electronic and physical structure of surfaces. Different target atoms and molecules have been used in the past but experiments using atomic hydrogen are of special interest as they allow an easy and direct comparison of theoretical models with experimental results. Only recently, first investigations making use of this effect have been published and more work is needed to further understand charge-transfer processes near surfaces.

The work presented in this thesis aims to further increase the understanding of the interaction of Rydberg states with surfaces, mainly by experimental means. Charge-transfer processes are studied at a range of different surfaces thereby varying the physical properties of the surface. The results are then compared with theoretical models to quantitatively compare experiments with theory.

Chapter 2 focuses on the theoretical background of the interaction of Rydberg states with surfaces. In particular the classical over-the-barrier ionisation process and the effect of size and polarisation of the Rydberg state with respect to the surface are explained in detail. Furthermore, different theoretical modelling techniques used to simulate and explain experimental results are presented. Chapter 3 introduces the experimental setup with all its components and variables. Modifications to the setup are highlighted and their purpose is explained.

The following chapters present experimental results together with their interpretations. In Chapter 4 the interaction of H-atoms with a bulk gold surface is revisited showing the effect of the modifications made to the experimental setup with respect to earlier results. Chapter 5 investigates the charge transfer between H-atoms and gold nanoparticle covered surfaces of varying particle sizes and densities. Chapter 6 presents further investigations of Rydberg states interacting with a Cu(100) surface. As an extension to previous studies, these experiments investigate the effect of collisional velocity on the charge transfer process with the aim to uncover possible resonance effects between the Rydberg states and surface or image-states of the surface. A novel way to produce $2s$ Rydberg states via mixing of the $2s$ and $2p$ states in an electric field is presented in Chapter 7. Chapter 8 finally summarises the experimental results and their interpretations and gives an outlook to future experiments.

Chapter 2

Theoretical Techniques

Experimental results presented in this thesis are mainly analysed with methods based on the *over-the-barrier* (OTB) ionisation approach. This chapter therefore explains the general idea of this method and its implementations. In addition the effects of the physical and electronic structure of the surface on the ionisation behaviour are investigated from a theoretical point of view.

2.1 Classical over the barrier ionisation

Classical over-the-barrier ionisation of a Rydberg atom or molecule near a metal surface occurs, when the energy of the electron lies above the saddle-point of its confining potential. It is therefore no longer bound to the ion core and moves into the conduction band of the surface. At this point, the ionisation probability rises from 0 to 1 instantaneously in the form of a step function. In a way, quantum mechanical ionisation is an extension of classic ionisation whereby the Rydberg electron wavefunction can also tunnel resonantly through the barrier into an empty energy level of the surface. As the efficiency of this process depends on the width of the potential barrier, the tunnelling probability drops off exponentially with an increase in Rydberg state to surface separation. Both the quantum mechanical and the classical approach result in almost identical ionisation probabilities as a function of distance, suggesting that tunnelling effects are actually quite small [30, 77, 36, 35]. Strictly speaking, this is not true for blue-shifted states, as will be discussed later in this section. As described in section 1.6 ionisation occurs at a Rydberg atom – surface separation of approximately $3.5n^2a_0$ in a field-free environment. However, these assumptions do not take into account that the energy of a Rydberg state in the presence of a metal surface is perturbed by the image-charge interaction which in turn will affect the OTB ionisation distance. Also, kinetic effects as described in Section 1.5, play a similarly important role in the surface ionisation and result in significant differences between the classical model and experimental results. Only a quantum mechanical calculation for the electron is therefore capable of exactly predicting the surface ionisation behaviour.

It is important to point out again, that the over-the-barrier approach can only reliably be used for the most red shifted Stark state of a given n-manifold ($k = -(n-1)$). Only for this case is the electron density mainly located at the saddle-point side of the potential and ionisation can occur quasi instantaneously once the Rydberg state energy lies above the saddle-point energy. The more positive the parabolic quantum number k becomes the further the electron density shifts to the opposite side of the saddle-point and kinetic effects become increasingly important. This leads to the observation that even though the energy of the state lies above the saddle-point, the Rydberg electron stays trapped in the potential until the Rydberg state reaches a significantly shorter distance from the surface.

2.1.1 The energy of a Rydberg state in the presence of a surface

As mentioned in the previous chapter, it is possible to estimate the effect of the surface potential on a Rydberg state using perturbation theory. Taking into account that in the experiments presented in this thesis the Rydberg states interact with the surface in the presence of an electric field and making use of the cylindrical symmetry of both the electric field and the surface potential (see Equation 1.24) it is most convenient to work in the parabolic hydrogen basis set (parabolic coordinates). The first order perturbation energy shift in a field-free environment can be given as [83]:

$$\begin{aligned}\Delta^1 E^{\mathrm{surf}}_{nm_lk} &= -\frac{1}{16D^3}\langle nm_lk|(\rho^2+z^2)|nm_lk\rangle \\ &= -\frac{n^2}{64D^3}(8n^2+8-4m_l^2+12k^2) \qquad (2.1)\end{aligned}$$

This energy shift is always negative and the Van-der-Waals interaction thus always results in a lowering of the total energy of the Rydberg state. Taking equation 2.1, the energy of Stark states in the presence of an electric field F at a distance D can, to the first order, be expressed as:

$$E_{nm_lk}(F,D) \approx E^{\mathrm{Stark}}_{nm_lk}(F) - \frac{n^2}{64D^3}(8n^2+8-4m_l^2+12k^2) \qquad (2.2)$$

where $E^{\mathrm{Stark}}_{nm_lk}(F)$ is the Rydberg Stark energy as given by equation 1.15. Though equation 2.2 is derived from perturbation theory and as such only delivers a numerical approximation of the exact energy it still provides a simple analytical form for the energy of a Rydberg state near a surface. It has been shown that this approach gives a reasonable approximation of the more correct Rydberg energy as calculated by other methods such as complex scaling [37].

2.1.2 The saddle-point energy

Combining equations 1.23 and 1.24 results in the overall one-electron potential of a Rydberg state near a metal surface. This potential possesses a barrier with a finite width between the ion-core and the surface and tends towards infinity on the vacuum side. The height and width of the barrier decreases both with a decrease in Rydberg atom – surface separation and with an increase in electric field. This facilitates charge transfer to surfaces both classically via over-the-barrier ionisation as well as quantum mechanically via tunnelling. The position of the saddle point of the barrier for a hydrogen atom in zero field is given analytically as [21]

$$z_{\text{saddle}} = -\left(1 + \sqrt{\frac{-5+4\sqrt{2}}{7}}\right) D \approx -0.693673D \tag{2.3}$$

with z_{saddle} being the distance of the saddle point from the nucleus and D the Distance of the Rydberg state from the surface. The barrier height at the saddle point is given as:

$$E_{\text{saddle}} = -\frac{7\sqrt{5+4\sqrt{2}}}{4D(1+2\sqrt{2})} - \frac{1}{4D} \approx \frac{-1.7422}{D} \tag{2.4}$$

Upon the addition of an electric field F the position of the saddle point is shifted towards the nucleus as follows [21]:

$$z_{\text{saddle}} = -0.693673D + 0.044466FD^3 + 0.006259F^2D^5 + 0.000220F^3D^7 + O(F^4) \tag{2.5}$$

and the barrier height is lowered approximately linearly with increasing electric field:

$$E_{\text{saddle}} \approx \frac{-1.7422}{D} - 0.693673FD \tag{2.6}$$

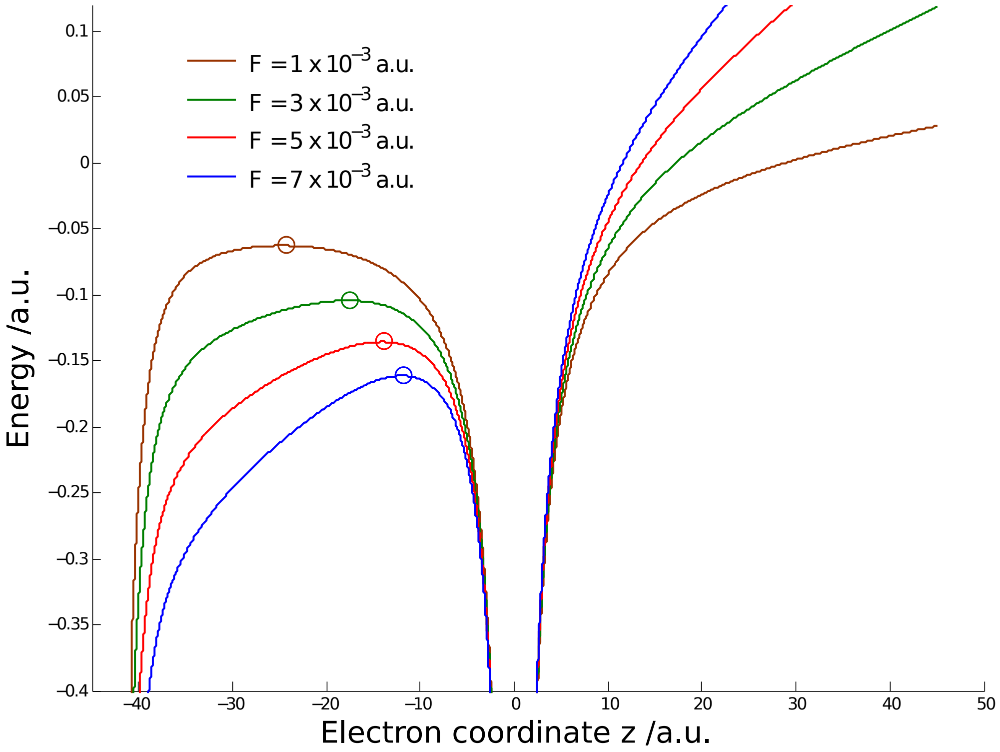

Figure 2.1: Plot of the total one-electron potential $V_{\text{tot}} = V_{\text{c}} + V_{\text{surf}} + V_{\text{field}}$ of a hydrogen atom near a metal surface for different electric fields F. The distance D from the surface is set to a constant 40 a.u. The saddle-point position and energies are calculated by equations 2.5 and 2.6 and marked by circles in the same colour as the corresponding electric field. The decrease in barrier height and width with increasing electric field is clearly visible.

Figure 2.1 shows the effect of an increasing electric field on the barrier between a Rydberg state and a metallic surface at a distance of 40 a.u.

From a classical point of view ionisation occurs at a distance D from the surface at which, for a given external field F, the energy of the Rydberg states is equal to the energy of the saddle point of the one-electron potential. In zero field that corresponds to an ionisation distance of $D_{\text{OTB}} \approx 3.48n^2a_0$. The cumulative ionisation probability $\Upsilon(D, F)$ at a Rydberg atom – surface separation D and an electric field F is thus given as:

$$\Upsilon(D, F) = h(D_{\text{OTB}}(F) - D) \tag{2.7}$$

where $h(D_{\mathrm{OTB}}(F) - D)$ is a Heaviside step function with the 'step' being located at $D = D_{\mathrm{OTB}}$.

2.1.3 Ion detection probability

In the experiments presented in this thesis the surface ionisation process is typically observed by detecting the resulting ions. This can be achieved by applying an external electric field which counteracts the attractive proton - image-proton interaction and repels the ion from the surface. From equation 1.28 it follows, that for a given ionisation distance and collisional velocity there is a critical field F_{min} which is needed to detect the ion. For every initial state σ it is therefore possible to define a critical ion detection field $F^{\sigma}_{\mathrm{crit}}(T_{\perp})$. The OTB approach predicts the surface ionisation detection probability to be a step function which steps from zero to unity at the critical ion detection field, $S_{\sigma}(F, v_{\perp}) = h(F - F^{\sigma}_{\mathrm{crit}}(v_{\perp}))$. Experimentally, the Rydberg atoms will not approach the surface with exactly one single velocity but rather with a velocity distribution $f(v_{\perp})$. Including this, the ion detection signal becomes:

$$S_{\sigma}(F, v_{\perp}) = \int_0^{\infty} h(F - F^{\sigma}_{\mathrm{crit}}(v_{\perp}))f(v_{\perp})\mathrm{d}v_{\perp} \tag{2.8}$$

It is possible to define a lower limit to the critical ion detection field and the corresponding ionisation distance by combining equations 1.30 and 2.6:

$$F^{\mathrm{lim}}_{\mathrm{crit}} = \frac{{E_{\mathrm{saddle}}}^2}{(1.7422 \times 2 + 0.693673/2)^2} = \frac{{E_{\mathrm{Ryd}}}^2}{14.6784} \tag{2.9}$$

If the effects of an electric field and a surface are not taken into account and by using equation 1.1 to calculate the energy of the Rydberg state, the lower limit critical detection field is given as

$$F_{\mathrm{crit}}^{\mathrm{lim}} = 0.017n^{-4} \tag{2.10}$$

corresponding to an ionisation distance of $3.82n^2$ [35]. This relationship has been used in previous experimental studies to model the interaction of Xe atoms with surfaces [70, 46]. However, it was shown by So et al. that this scaling of ionisation distance ($\propto n^2$) and applied external extraction field ($\propto n^{-4}$) is not strictly valid as the effects of velocity and the Rydberg energy shift due to the surface interaction (see equation 2.1) need to be taken into account [37]. For the range of hydrogen Rydberg states studied in this thesis it was shown that the critical scaled extraction field varies linearly with n and the ionisation distance (for the most red shifted state) has a non-linear dependence ranging from $\sim (3.9 - 4.5)\ n^2 a_0$.

The experiments presented in this thesis cover Rydberg states in the range $n \approx 25 - 35$ with collisional velocities in the range $v_\perp \approx 300 - 950\ \mathrm{m\,s^{-1}}$. For these states, the critical extraction field can be empirically fitted by adding an n^{-3} dependence to equation 2.10:

$$F_{\mathrm{crit}}(n, T_\perp) = \frac{0.017}{n^4} + \frac{\sqrt{T_\perp}}{3.174^{\frac{3}{2}} n^3}. \tag{2.11}$$

2.2 Interaction of atomic hydrogen with metal surfaces

It was mentioned in Section 1.4, that the interaction of Rydberg states with surfaces in many ways resembles the effect of an electric field as it leads to a lifting of the l-degeneracy. However, there are important differences between the two effects and this section aims to explain how the charge-transfer of a Rydberg state near a metal surface depends on the different properties of the Rydberg state.

2.2.1 Rydberg orbital dimension and polarisation

For simplification, the effect the Rydberg orbital dimension has on the charge transfer process is first discussed without including an externally applied electric field. As mentioned in the previous section, ionisation or charge transfer occurs when the Rydberg state energy lies above (or near) the saddle-point energy. In turn this leads to a dependency of the charge transfer process on the principal quantum number, which in a classical picture relates to an increase in the physical dimension (or size) of the Rydberg state orbital. In accordance with results from the classical OTB model the most probable ionisation distance of the most surface oriented states scales with the Rydberg dimension n^2. This effect has been confirmed independently by theoretical [78, 36] as well experimental studies [44, 48, 52].

The interaction of a Rydberg atom or molecule with the surface leads to an effect similar to that of an electric field (c.f. the Stark effect): the l-degeneracy is lifted and a splitting in states with a range of energies can be observed. The lowest energy states thereby possess the shortest lifetime (largest width), are polarised towards the surface and therefore ionise furthest away from it. The lifetime of these states increases (decrease of width) with increasing energy as the electron polarisation slowly shifts towards the vacuum. In turn this leads to a decrease in ionisation distance as has been shown in a range of theoretical studies [29, 30, 36]. Figure 2.2 a) shows a comparison of ionisation rates of the $n = 4$ Rydberg atom approaching a metal surface with collisional velocity of $3\,\mathrm{x}10^{-4}$ a.u. (taken from [37]) calculated both via wavepacket and complex scaling calculations. As can be expected, states which are oriented towards the surface ionise at a greater distances while vacuum oriented states ionise closer to the surface, over a wider range of distances. It should be noted however, that due to changes in

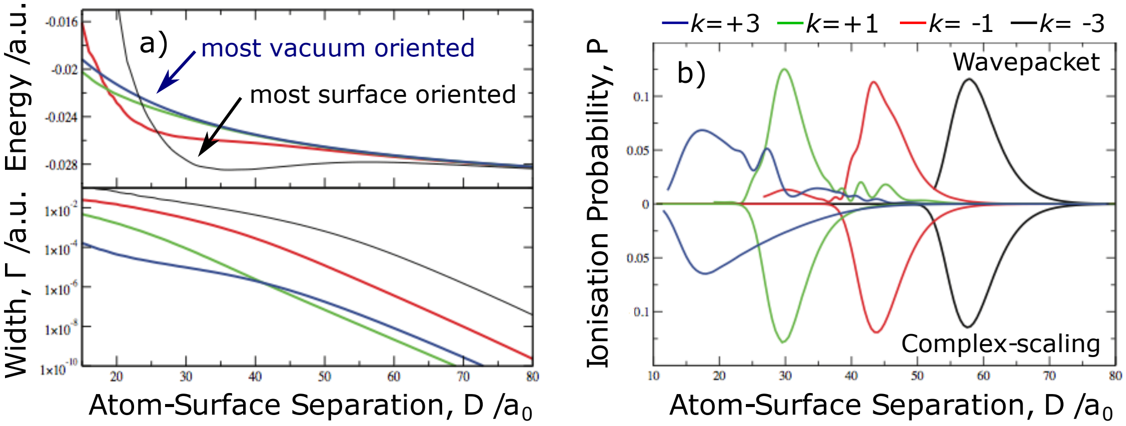

Figure 2.2: From [37]. Energies, widths and ionisation rates of the $n = 4$, $m_l = 0$ Rydberg states near a Jellium type surface without an external electric field. a) Energies and width as a function of atom-surface separation, calculated using complex scaling theory. The state independent proton – image proton $V_{pp'}$ contribution is not included. b) ionisation probability of the same states as a function of atom-surface separation using both wavepacket propagation calculations [36] and complex scaling theory [29].

electron polarisation at avoided crossings, it is only possible to experimentally observe this effect for atomic hydrogen [52].

Figure 2.2 a) shows the energies of the different states of the $n = 4$ Stark-manifold as a function of electric field. The different energy curves can be explained by the surface potential as explained in the previous chapter (Figure 1.7, Equation 1.25). Due to the nature of the potential, vacuum-oriented states are mainly affected by the long range part of the Jellium potential which is dominated by the electron-image proton interaction ($V_{ep'}$). This contribution depends on both the atom and the electron coordinate and increases with decreasing distance which in turn leads to an increase in energy scaling roughly with $\sim 1/(4D)$ (see Equation 1.23). With increasing polarisation of of the electronic wavefunction towards the surface the attractive contributions of the surface potential is probed in more detail. This is dominated by the attractive electron - image electron interaction which lowers the energy of the Rydberg state. Together with the also present repulsive electron - image proton potential this leads to a slightly more complex behaviour for surface oriented states. Initially the energy increases as the potential is dominated by $V_{ep'}$ but it subsequently decreases when $V_{ee'}$ is starting to be probed. At very close distances $V_{ep'}$ becomes very repulsive and once more dominates the overall potential leading to a rise in energy. As already mentioned in the previous chapter, the contribution of $V_{pp'}$ is identical for all states and is attractive at all distances.

2.2.2 Collisional velocity

The effect of the collisional velocity on the detection efficiency has already been described in Sections 1.7 and 2.1.3. However, the collisional velocity also affects the properties of a Rydberg state as it approaches the surface.

When not interacting with a surface (but in the presence of an electric field), Rydberg states possess a cylindrical symmetry and no interaction of states with the same magnetic quantum number m_l is possible. Including the image-charge interaction with a surface breaks this symmetry which in turn allows for mixing of states with the same m_l to occur. At zero (applied) external electrical field (or very low fields) the different states of a given n-manifold are energetically fairly close together. This is especially true for vacuum oriented states, which are now very likely to encounter avoided crossings. As the number of states increases with the principal quantum number the number of crossings increases accordingly.

At a crossing of two states the polarisation of the Rydberg orbital might either be ‘flipped’ from red- to blue-shifted (or vice versa) or some intermediate mixing might occur depending on the electronic wavefunctions involved and on the strength of the coupling between them. This can lead to a variation of the ionisation probability as a function of atom surface separation as observed in previous results [44, 48]. Figure 2.3 shows a comparison of the ionisation probabilities of the different states of the $n = 10$

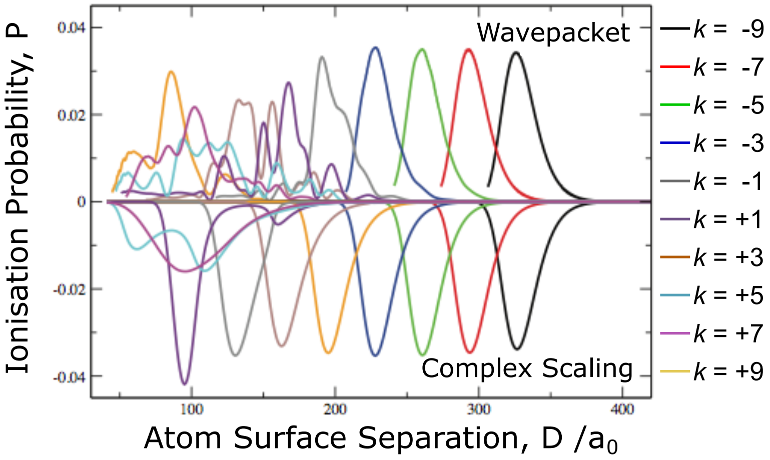

Figure 2.3: From [37]. Ionisation probabilities of the different states of the $n = 10$, $m_l = 0$ hydrogen Rydberg state near a Jellium surface as a function of Rydberg state surface separation, determined using wavepacket propagation (positive axis) and complex scaling calculations (negative axis). No external field is applied and the collisional velocity of the Rydberg state is $3\,\mathrm{x}\,10^{-4}$ a.u. (= 656 $\mathrm{m\,s^{-1}}$). States that ionise furthest from the surface are oriented towards it. The electron polarisation shifts more and more towards the vacuum with decreasing ionisation distance.

manifold calculated via wavepacket propagation and complex scaling theory, taken from [37]. For the most surface oriented states both methods are in good agreement. However, with increasing polarisation towards the surface (smaller ionisation distance), distinct differences appear and in some cases states even seem to have exchanged completely, e.g. the $k = +9$ state (yellow line) changes from most vacuum shifted (wavepacket results) to mid-manifold (complex scaling).

In the complex scaling approach [30] all crossings between states of the same manifold are assumed to be traversed adiabatically which means the electron polarisation of a given state is 'flipped' at every crossing. However, the Landau-Zener avoided crossings model [84] states that the behaviour at the crossing depends on the off-diagonal matrix elements in the adiabatic basis set ($\approx$ size of the gap of the avoided crossing, ΔE) as well as how fast the crossing is traversed (c.f. the collisional velocity of the Rydberg state). This effect is demonstrated in Figure 2.4 which depicts the two possibilities to traverse energy level crossings for two arbitrary electronic states $|1\rangle$ and $|2\rangle$. For

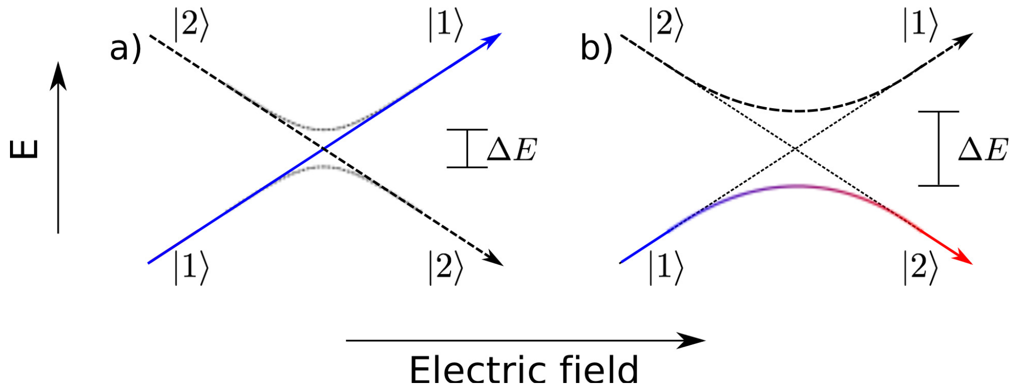

Figure 2.4: Comparison of diabatic (a) and adiabatic (b) behaviour at energy level crossings. The energy of two elecronic states is shown as a function of electric field. How the energy crossing between the two states is traversed depends on the energy gap (ΔE) between the two states at the crossing as well as the velocity (v) at which the crossing is traversed. For large ΔE and v the crossing is traversed diabatically while for small ΔE and slow v adiabatic behaviour is dominant.

small energy differences ΔE and high velocity v (for the work presented here this relates to whether the Rydberg state is moving fast enough) the crossing is traversed diabatically without (or with minimal) change to the polarisation of the electronic wavefunction. At slow enough collisional velocities however and for a large enough ΔE, adiabatic behaviour dominates, leading to changes in the wavefunction. In addition, intermediate behaviour (bifurcation) is also possible. Static calculations such as the complex-scaling approach assume that all crossing are traversed adiabatically [29, 30, 31]. Dynamic wavepacket propagation calculations [85, 36, 37] on the other hand include non-adiabatic behaviour and therefore give a more accurate picture of the interactions described in this thesis (at an increased computational cost).

2.2.3 The effect of external electric fields

All the experiments presented in this thesis were carried out in the presence of an externally applied electric field. This can either be an extraction field the aim of which is to repel the ion following surface ionisation or a Stark field in order to pick a specific polarisation of the Rydberg state on excitation (or both fields simultaneously).

As mentioned in the previous section, at low or zero electric field, avoided crossings appear on approach to the surface predominantly for blue-shifted states of a given n-manifold due to the high density of states. With increasing field, the Stark effect (see Section 1.4) leads to increased level splitting thus reducing the amount of crossing. In addition, with increasing electric field the applied electric field first becomes equal to and subsequently bigger than the image charge field at the surface ionisation distance. This effectively introduces an extra symmetry which decreases the level interaction and results in a stronger contribution of diabatic effects [37].

It has been shown for lower principal quantum numbers that even in the presence of weak electric fields, wavepacket propagation and complex scaling calculations result in nearly identical ionisation probabilities as a function of Rydberg state surface separation [37]. The range of fields present in the experiments carried out for this thesis are therefore expected to be sufficiently high to only consider non-adiabatic ionisation dynamics as individual states are far enough apart to possess a single Gaussian like ionisation probability.

2.3 Modelling approaches

The overall aim of this thesis is to gain a better understanding of how the physical properties of the surface can influence the ionisation behaviour of Rydberg atoms or molecules. In order to understand and interpret the experimental results presented in later chapters theoretical models need to be developed, which take into account all the experimental variables. This section therefore introduces the theoretical calculations which were carried out in order to simulate experimental results.

2.3.1 Metal surfaces

As mentioned in chapter 1.7 it is possible to simulate the experimentally obtained surface ionisation profiles of the most red-shifted Stark states ($k = -(n-1)$) of the hydrogen atom by using a semi-empirical model based on the classical over-the-barrier ionisation model. In this model surface ionisation is assumed to occur around a mean ionisation distance $\mu(F)$ which depends on the applied external electric field. Ionisation thereby occurs over a range of distances around $\mu(F)$ with a standard deviation σ. The cumulative ionisation probability as a function of distance from the surface (D) and electric field (F) is given as:

$$\Upsilon(D, F) = 1 - \frac{1}{2}\left[1 + \mathrm{erf}\left(\frac{D - \mu(F)}{\sqrt{2\sigma^2}}\right)\right] \tag{2.12}$$

The ion detection probability is found in the same way as in Equation 2.8: by calculating the critical field required to detect the resulting ions and comparing this field to the currently applied ion extraction field. To accurately model experimental results, the mean ionisation distance is then shifted by a factor δ from the classical OTB ionisation distance D_{OTB}:

$$\mu(F) = D_{\mathrm{OTB}} - \delta \tag{2.13}$$

In order to match the width of the simulated surface ionisation profiles to previous experimental results, the standard deviation of ionisation distances is set to $\sigma = 2.5\ n^2 a_0$ and a shift of $\delta = 1.0 n^2 \mathrm{a}_0$ is applied (see Figure 1.12) [37]. The surface ionisation profiles obtained this way are in excellent agreement with the experimentally obtained results. Furthermore this model is capable of describing the effect of changing the collisional velocity. Figure 2.5 a) demonstrates how the simulated surface ionisation profile changes from the pure OTB approach when the above changes are implemented.

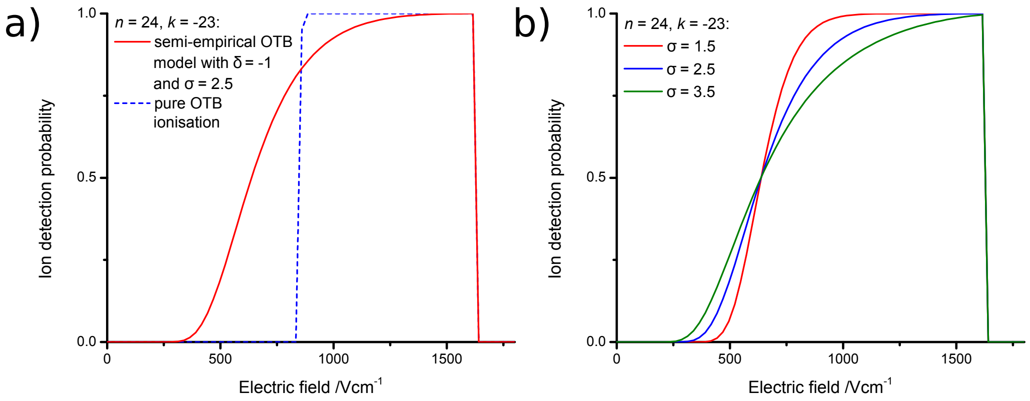

Figure 2.5: Semi-empirical over-the-barrier ionisation model: a) effect of introducing a range of ionisation distances and shifting the ionisation distance by $\delta = 1\ n^2 a_0$ for $n = 24, k = -23$. b) effect of ionisation width parameter σ. The bigger σ the more 'stretched' the surface ionisation profile becomes, meaning ionisation occurs over a wider range of distances.

Instead of a step-function, ionisation now occurs over a range of distances. In figure 2.5 b) the effect of the standard deviation parameter σ is demonstrated by varying it between $\sigma = 1.5$ and 3.5. It can be seen that with an increase in σ ionisation occurs over a wider range of distances resulting in a 'stretched' surface ionisation profile.

It is worth noting that in this model the width of the ionisation signal is solely modelled as a variation of ionisation distance due to the non-instantaneous nature of the ionisation event. While most likely present, this effect is probably not large enough to solely account for the experimentally observed spread and the current implementation might therefore be accounting for a range of other effects impacting on the shape of the surface ionisation profile such as the presence of stray/inhomogeneous fields.

2.3.2 Monte-Carlo trajectory simulations

Monte-Carlo trajectory simulations were carried out as part of the theoretical calculations described in the next section. In such simulations all important experimental conditions (e.g. Rydberg atom beam, surface properties, extraction field, ...) are modelled and subsequently ionisation distances and detection probabilities for a fixed number of ions are sampled. Every trajectory starts at a random position x_0/y_0 above the surface at the fixed distance of $z_0 = 35\ n^2a_0$ which is deemed large enough to only exhibit minimal interaction with the surface. The initial direction of the Rydberg state is also chosen randomly while its velocity v and impact angle θ are chosen from a model distribution representing the incoming molecular beam (see Section 3.1.1 for the experimental velocities and impact angles). Interaction of the Rydberg state with its image charge and surface fields can lead to perturbations of the trajectory as well an acceleration or deceleration and these effects are included in the Rydberg atom trajectory calculations.

The Rydberg atom is considered to be ionised once it crosses a pre-computed ionisation surface for the corresponding applied electric field. This ionisation point subsequently acts as a starting point for ion trajectory calculations. The calculations are carried out using MATLAB's$^{\text{TM}}$ ODE 45 differential equation solver (based on the Runge-Kutta algorithm [86]). Again, the effects of image-charge, surface fields and now additionally the extraction field are included in the calculations. The calculation for every ion is terminated either when the Rydberg state crashes into the surface ($z = 1$, not detected or when the ions flies away from the surface with a velocity greater then 1000 $\mathrm{m\,s^{-1}}$ which results in an ion detection event being recorded.

It should be noted that all Monte-Carlo trajectory simulations carried out are based on the purely classical over-the barrier ionisation approach and as such they are unable to completely describe the ionisation process. For example quantum mechanical effects like tunnelling are not considered but also kinetic lifetime effects as discussed in Section 1.5 are not included. As such, this method is only suitable to model the surface interaction of the most red-shifted Stark states ($k = -(n-1)$). To get a more general picture of the Rydberg state - surface interaction more complicated theoretical methods, such as wave-packet-propagation theory [37], need to be used. The model also does not include the effect of inhomogeneous fields (e.g. close to the surface), which can result in m_l mixing. The amount of this mixing can be estimated by carrying out perturbation theory calculations [87] and might be included in theoretical calculations at a later time.

2.3.3 Patch fields and surface roughness

While the modelling approach presented in the previous section can be tuned to result in excellent agreement with experimental data (examples given later) it does not necessarily explain why ionisation occurs over such a wide range of distances from the surface. Past experimental work by Hinds and co-workers [38, 79], Tauschinsky [14] and co-workers , Gray et al. [43] and Dunning et al. [73, 46] all showed that the interaction of Rydberg states with surfaces can easily be influenced by local surface fields. The observed fields are believed to stem from local changes in the surface work function and might possibly be due to adsorbates on the surface, surface defects or the polycrystalline nature of the surface [82, 81, 88]. Such fields are assumed to be typical for surfaces created by evaporation deposition and this type of surface is used for some of the experiments presented in this thesis.

Pu et al. recently suggested that the spread in ionisation distance might be predominantly due to such fields present near the surface [47]. As mentioned in section 1.7 these stray fields are able to extend far into the vacuum and scale strongly with distance from the surface ($\sim D^{-2}$). The charge transfer for Rydberg states studied in this thesis ($n = 25 - 35$) occurs at distances from the surface of $\sim 100 - 350$ nm and might therefore be influenced by these fields as the OTB ionisation distance is dependent on the electric field (see section 2.1). In addition, the detection efficiency of charged particles varies with electric field as can be seen from equation 1.28.

Earlier work by So et al. showed that ionisation did indeed occur over a wide range of distances from the surface but these results could not be completely explained with the stray fields measured by Pu et al. [37]. However, recent modifications to the experimental setup make it worthwhile to re-investigate this effect (see section 3.1.4 for details on the modifications).

The stray field potential

In order to gain an idea of the magnitude and domain sizes of the stray fields, Dunning and co-workers measured the potential variations of a (nearly) atomically flat evaporated gold surface using Kelvin-probe spectroscopy [47]. Using the results obtained in these measurements and embedding them in trajectory simulations they were able to reproduce experimental surface ionisation profiles of xenon with a high degree of accuracy. The surface potentials of the gold surface used for the work presented in this thesis have not been measured but, as it was produced in a similar fashion to that used by Dunning and co-workers, patch fields of the same order of magnitude and domain size can be expected. It therefore seems reasonable to incorporate the potentials measured by Pu et al. into the Monte-Carlo trajectory simulations that were described in Section 2.3.2.

Unfortunately, the original data as measured by Dunning and co-workers was not available for use and the magnitude of the surface potentials and domain sizes had to be extracted directly from the figure published in [47]. While overall this should result in the same patch fields a decreases in resolution from 512 × 512 to only 245 × 245 data points both spanning an area of 1 μm leads to small but noticeable differences. Figure 2.6 shows both the original data as published in [47] (a) as well as the reproduced data (b). While the extracted surface potential appears to be in good agreement with the original data, slight differences can be seen. It was shown in [37] that the lower resolution results in a slightly lower mean stray field but it was deemed that this difference does not significantly alter the results obtained with the trajectory simulations.

Taking the reconstructed surface potential, one now needs to calculate the resulting stray fields originating from the surface. This can be done by making use of the fact that the surface fields provide boundary conditions for Laplace's equation in three dimensions:

$$\frac{\partial^2\phi}{\partial x^2}+\frac{\partial^2\phi}{\partial y^2}+\frac{\partial^2\phi}{\partial z^2}=0. \tag{2.14}$$

For $z > 0$ and assuming that $\phi(z \to \infty) = 0$ this differential equation is satisfied by linear combinations of periodic functions of the form [47]:

$$\begin{aligned}\phi(x,y,z) &= \sum_i\sum_j\left[A_{i,j}\cos\left(k_{x,i}x+k_{y,i}y\right)+B_{i,j}\sin\left(k_{x,i}x+k_{y,i}y\right)\right]\exp\left(-k_z(i,j)z\right)\\ &= \sum_i\sum_j \mathrm{Re}\left\{\left(A_{i,j}+\mathrm{i}B_{i,j}\right)\exp\left[-\mathrm{i}\left(k_{x,i}x+k_{y,i}y\right)\right]\right\}\exp\left(-k_z(i,j)z\right)\\ &= \sum_i\sum_j \mathrm{Re}\left\{C_{i,j}\exp\left[-\mathrm{i}\left(k_{x,i}x+k_{y,i}y\right)\right]\right\}\exp\left(-k_z(i,j)z\right) \qquad (2.15)\end{aligned}$$

where $k_{i,j} = \sqrt{k_{xi}^2+k_{yj}^2}$. The values for $\phi(x,y,0)$ right at the surface can be taken from the reconstructed surface potential (see Figure 2.6) and the complex coefficients $C_{i,j}$ can be calculated using a 2D Fourier transform

$$C_{i,j}=\frac{1}{N^2}\sum_n^{N-1}\sum_m^{N-1}\phi\left(\frac{nL}{N},\frac{mL}{N},0\right)\exp\left[2\pi\mathrm{i}\left(\frac{ni+mj}{N}\right)\right], \tag{2.16}$$

$$i,j=0,1,...,(N-1).$$

Combining Equations 2.15 and 2.16 it is possible to calculate the potential for every point above the surface by taking the real component of the inverse 2D Fourier

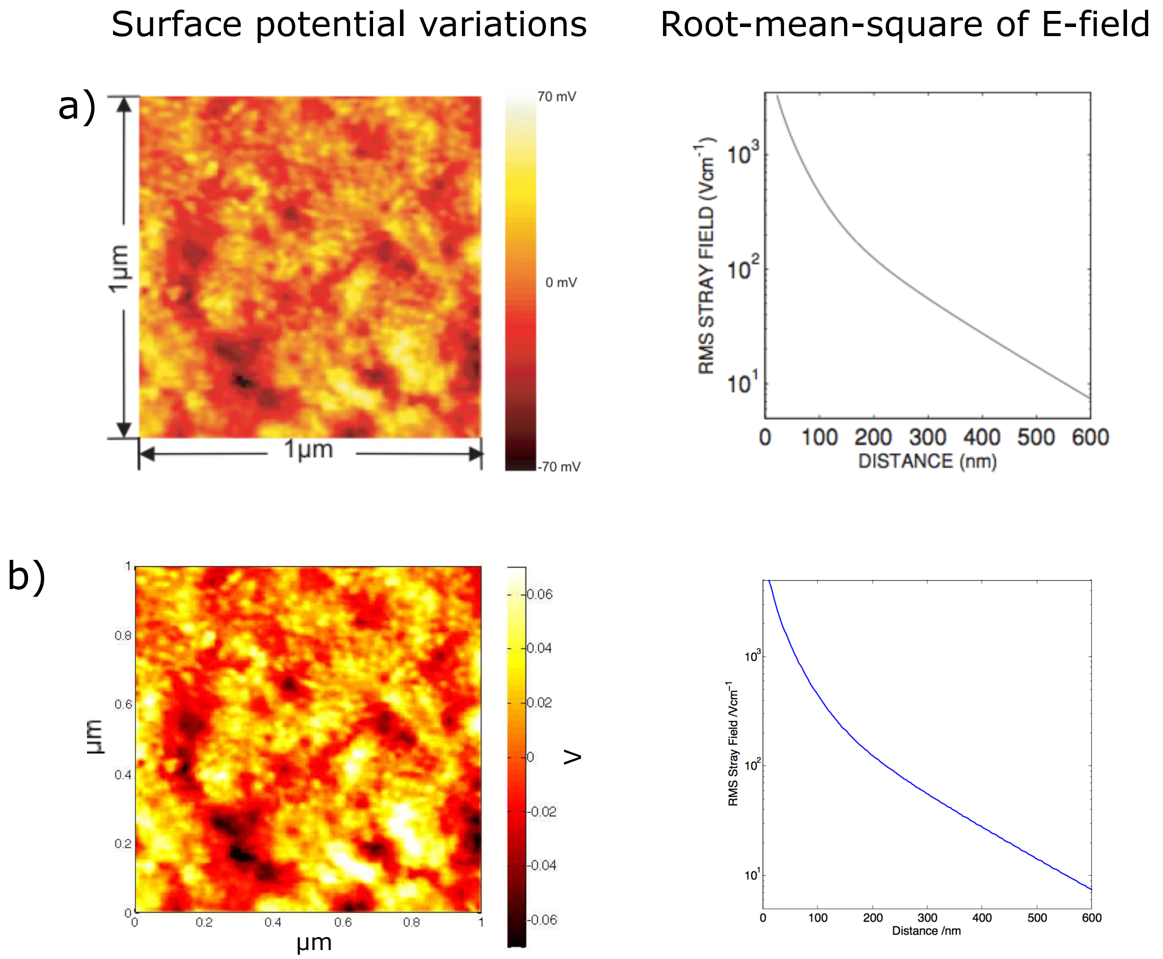

Figure 2.6: Stray electric fields present at deposited flat gold surfaces. a) results obtained by Dunning and co-workers (Reprinted Figure with permission from [47]. Copyright 2010 by the American Physical Society). Left image: measured surface potentials using Kelvin-probe spectroscopy (512 × 512 data points). Right image: root mean square of the resulting electric field. b) reconstructed results as used in this thesis. Left image: reconstructed surface potential (245 × 245 data points). Right image: resulting root-mean-square field. Slight differences between original and reconstructed data can be seen, the reason for which is explained in the text.

transform

$$\phi(x,y,z) = \mathrm{Re}\left\{\sum_{i=0}^{N-1}\sum_{j=0}^{N-1} C_{i,j}\exp\left[2\pi\mathrm{i}\left(\frac{\mathrm{i}x+\mathrm{i}y}{L}\right)\right]\exp\left[-k_z(i,j)z\right]\right\} \tag{2.17}$$

where $k_z(i,j) = \frac{2\pi N}{L}\sqrt{i'^2+j'^2}$ and $i' = \mathrm{mod}(0.5+\frac{i}{N},1)$, $j' = \mathrm{mod}(0.5+\frac{j}{N},1)$, mod(a,b) being the modulus after division.

The images on the right of Figure 2.6 show the root-mean-square (RMS) deviation of the stray electric fields calculated by the above method. The difference between the original data from [47] (a) and the reconstructed data (b) now becomes evident in the form of a slightly smaller RMS for the reconstructed data used in this work ($\sim$ 2 V cm^{-1} at a distance of 600 nm).

Ionisation in the presence of stray fields

All the stray field calculations presented in this work were carried out for the most-red shifted Stark states of a given n-manifold. This is due to the fact that only for these states is the over-the-barrier ionisation approach approximately valid (see Section 2.2.1).

The main effect of the patch fields is the generation of a strongly corrugated ionisation surface which unsurprisingly shows some resemblance to the measured stray fields below it. This corrugation leads to a range of different ionisation and detection distances depending on the position of the ion above the surface which, on average, are larger then the unperturbed distances. In turn this leads to a broadening of the critical detection field and therefore to a broadening of the detected surface ionisation profile (see section 3.2). This is a distinct difference from the step function predicted by ‘pure’ OTB theory as explained in section 2.1.

The ionisation surface is pre-computed before running trajectory simulations in order to decrease computational cost. It is created by calculating the distance from the surface at every point (x, y) for a given electrical field F and principal quantum number n at which ionisation occurs. As explained above, ionisation occurs when the energy of the most red-shifted Stark state is higher than the saddle-point energy. Due to the inhomogeneity of the patch fields on the surface this saddle-point does not necessarily lie along the z-axis and its position and energy is found numerically via a search procedure. Figure 2.7 a) and b) show the ionisation surfaces for the most red-shifted Stark state of an $n = 26$ Rydberg state at two applied electric fields of $0\ \mathrm{V\,cm^{-1}}$ and $900\ \mathrm{V\,cm^{-1}}$. The corrugation (mapping the surface potentials) is visible and it can be seen that the ionisation surface shifts further away from the surface with an increase in electric field. In order to demonstrate the spread of ionisation distances resulting from this corrugation histograms of ionisation distances for the same applied electric fields are presented in Figure 2.7 c) and d). It can be seen that applying an electric field not only leads to an increase in ionisation distance but also leads to a spread of the distances at which ionisation occurs.

Comparing this calculated spread of ionisation distances to the experimental results of So et al. shows relatively good agreement, with the experimentally detectable ionisation occurring for distances ranging from 2.5 to about 6.0 $n^2\mathrm{a}_0$ [37]. It should be noted, that for high applied electric fields, ionisation is theoretically possible at even greater distances from the surface ($\sim 8\,n^2\mathrm{a}_0$) but it is impossible to observe this experimentally via surface ionisation profiles.

Due to the z-component of the surface potential decaying faster for low frequency components (see Equation 2.17), the effect of the corrugation also depends on the size of the Rydberg orbital and therefore on the principal quantum number . This is demonstrated in Figure 2.8 a) and b) which shows the ionisation surface at zero electric field for the most red-shifted Stark states of the $n = 20$ and $n = 28$ Rydberg

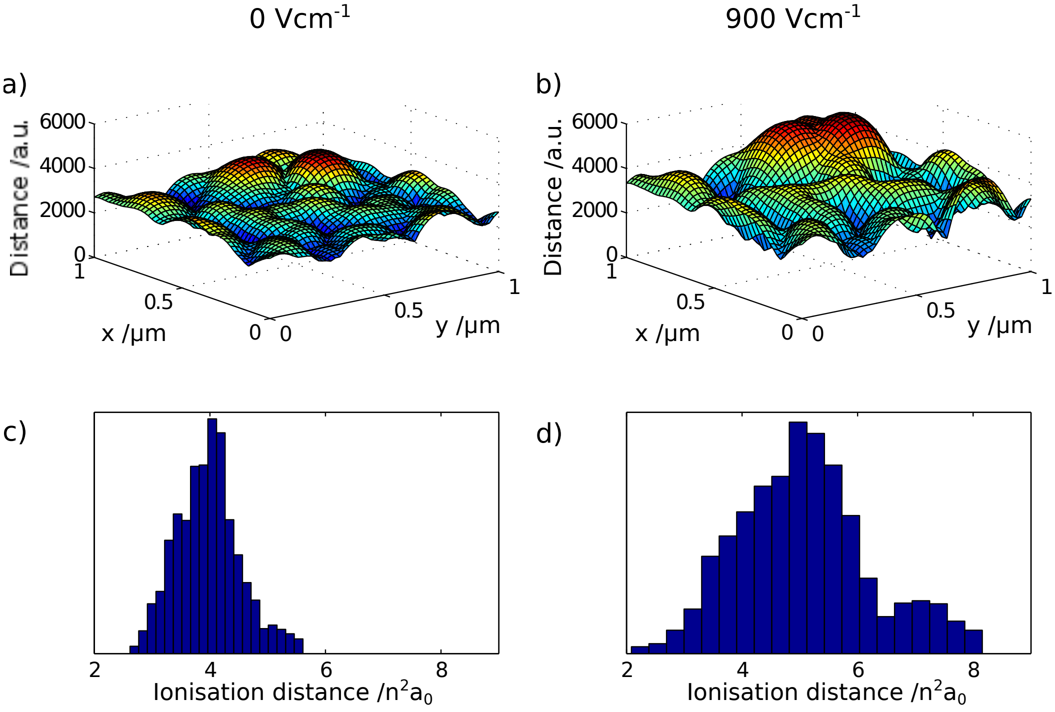

Figure 2.7: Images a) and b) show the calculated ionisation surfaces for the most red-shifted Stark states of the $n = 26$ manifolds at two different applied electric fields of $0\ \mathrm{V\,cm^{-1}}$ und $900\ \mathrm{V\,cm^{-1}}$. The dependence of the ionisation distance on the applied electric fields is visible, with the ionisation surface shifting further away from the surface as the field increases. c) and d) show histograms of the ionisation distances at the corresponding electric fields (distance scaled by n^2). This demonstrates how patch fields lead to a spread of ionisation distance and how applying an electric field results in a spread and shift of the ionisation distance.

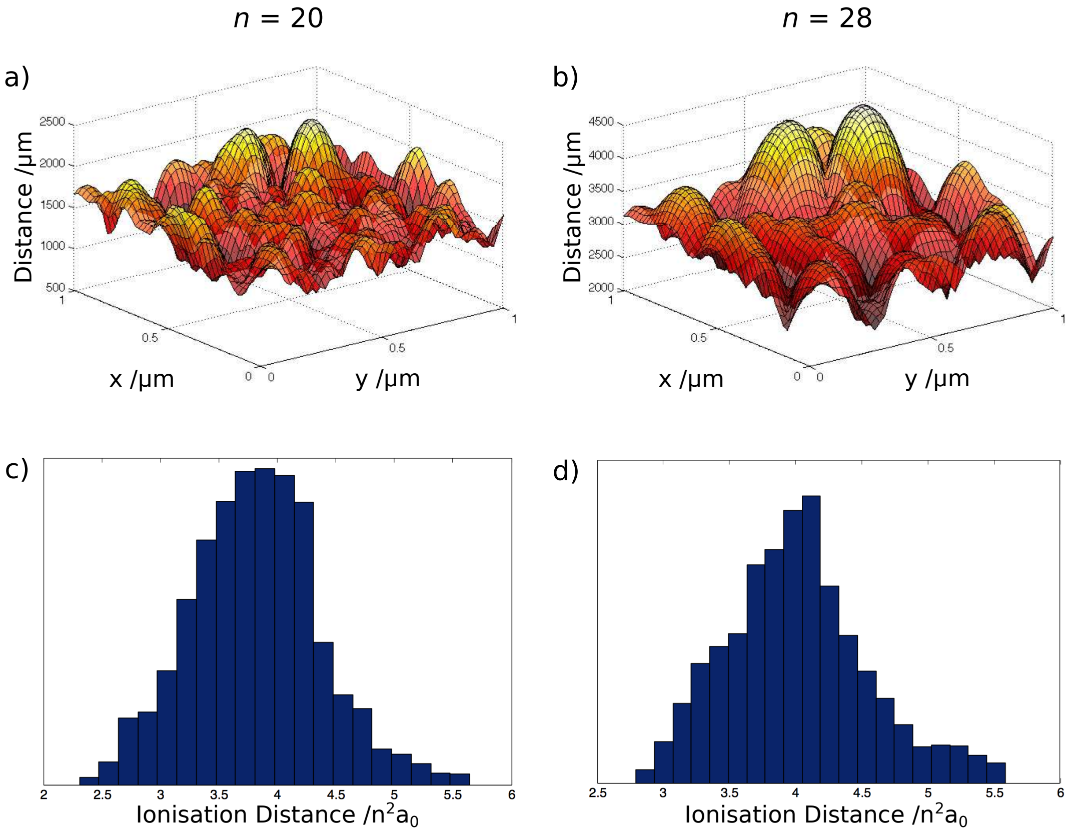

Figure 2.8: Images a) and b) show the calculated ionisation surfaces for the most red-shifted Stark states of the $n = 20$ and $n = 28$ manifolds at an applied electric field of $0\,\mathrm{V\,cm^{-1}}$. The dependence of the ionisation distance on the principal quantum number can be seen and the effect of the stray fields on the ionisation surface is visible. c) and d) show histograms of the ionisation distances (distance scaled by n^2), confirming that the ionisation distance scales approximately with n^2.

manifolds. The corresponding histograms of ionisation distance are shown in c) and d). The 'uneven' spread of ionisation distances can be explained by the fact that the saddle-point for a given Rydberg hydrogen atom does not necessarily lie on the z-axis and the ionisation distance is therefore dominated by the effect of the most positive surface potential in its near vicinity.

Monte-Carlo-Trajectory Simulations

After creating a 'database' of ionisation distances of all applied electric fields of interest for a given state it is possible to perform Monte-Carlo trajectory simulations (see

Section 2.3.2). For every electric field in the surface ionisation profile, a fixed number of trajectories are calculated (usually around 200). Trajectories are given a random (x, y) starting position above the surface (fixed distance) as well as an initial velocity and impact angle. Ionisation is deemed to occur when the atom crosses the ionisation surface and a detection event is recorded if the applied electric field is strong enough to repel the ion from the surface. By plotting detection efficiency vs. electric field a surface ionisation profile can be modelled. Figure 2.9 a) shows simulated surface ionisation profiles for the $n = 28$, $k = -27$ Rydberg state with a total velocity of $v = 2535\ \mathrm{m\,s^{-1}}$ and two different impact angles of 10° (blue lines) and 15° (red lines). The dashed lines show the calculations based on the corresponding unperturbed OTB ionisation distances for comparison. As expected, the inclusion of the patch fields into these calculations leads to a spread of the simulated ionisation profile as well as a shift towards lower extraction fields (corresponding to a larger ionisation distance). A detailed comparison with experimental results will be presented in Chapter 4.

Changing the impact angle of the approaching Rydberg atom has two different effects. Firstly, a decrease in impact angle corresponds to a decrease in collisional velocity $(v_\perp)$ and thereby in kinetic energy of the atom. From Equation 1.28 can be seen that this in turn leads to an increase in extraction probability. However broadening of the minimum detectable distance can also be observed as the ion has a higher probability of moving towards more attractive local field regions, which hinders detection. The second effect of changing the impact angle is a matter of surface sampling. Prior to ionisation, the Rydberg state trajectory traverses a larger part of the surface before its intersection with the ionisation surface and it is thus more likely to ionise at one of the ‘peaks’ of the ionisation surface, corresponding to a larger ionisation distance. On average the effects lead to an increase in the average ionisation distance and thereby to an increase in detection efficiency.

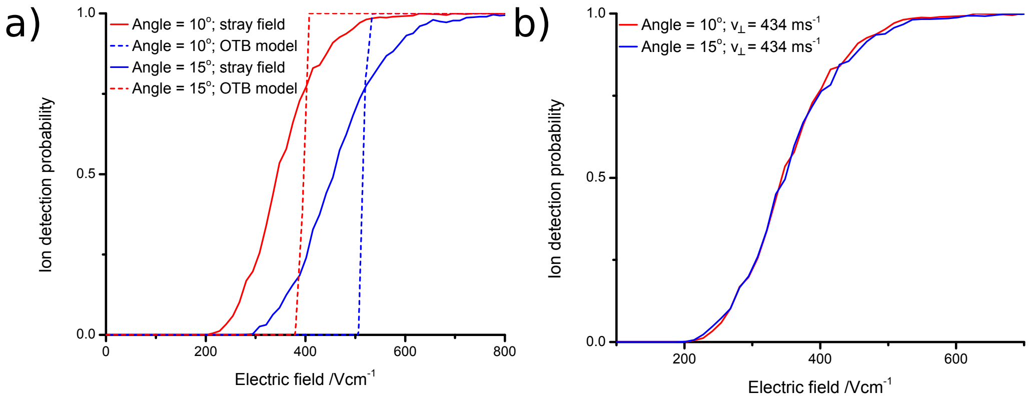

Figure 2.9: Monte-Carlo trajectory simulations for the $n = 28$, $k = -27$ Rydberg states including the effect of surface patch charges as a plot of fraction of detected ions vs. electric field. a) trajectory simulations for Rydberg states with an initial velocity of $v = 2500\ \mathrm{m\,s^{-1}}$ at two different impact angles of 10° (red full line) and 15° (blue full line). As comparison the results for the pure OTB surface ionisation (no surface fields) are shown in corresponding dotted lines. b) comparison of the effect changing the collisional velocity by changing the impact angle and by changing the total velocity. Red line: 15° and $v = 1677\ \mathrm{m\,s^{-1}} \rightarrow v_\perp = 434\ \mathrm{m\,s^{-1}}$. Blue line: 10° and $v = 2500\ \mathrm{m\,s^{-1}} \rightarrow v_\perp = 434\ \mathrm{m\,s^{-1}}$.

This effect is demonstrated in Figure 2.9 b) which shows surface ionisation profiles of the $n = 28$, $k = -27$ Rydberg state. The full lines represent trajectory simulations for Rydberg states with a final collisional velocity of $v_\perp = 440\ \mathrm{m\,s^{-1}}$. This can be achieved either by simulating Rydberg H atoms with an initial velocity of $2500\ \mathrm{m\,s^{-1}}$ and an impact angle of 10° (blue line) or by decreasing the velocity to $1677\ \mathrm{m\,s^{-1}}$ and increasing the impact angle to 15° (red line). While both profiles are quite similar, it can be seen that for the high field part of the surface ionisation profile the smaller impact angle results in a slightly higher detection efficiency and thus in a slightly larger ionisation distance. As mentioned above, this can be explained by the fact that Rydberg states with a lower impact angle tend to sample a larger area of the surface and are thus more likely to ionise at the ‘hills’ of the ionisation surface (see Figure 2.7).

It is possible to tune the empirical model explained in Section 2.3.1 in such a way

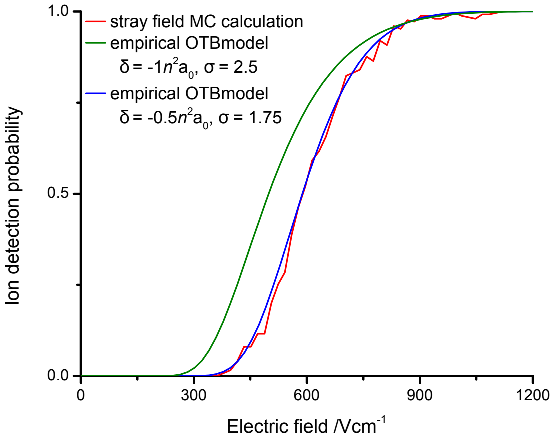

Figure 2.10: Comparison of the stray-field Monte-Carlo trajectory simulations (red line) with the semi-empiracel model for the $n = 26$, $k = -25$. Two different simulated profiles obtained with the semi-empirical model are shown: one with the same fitting parameters used by So et al. [37] (green line) and one using fitting parameters chosen to make the profile fit the Monte-Carlo results.

that it duplicates the results obtained with the Monte-Carlo trajectory simulations. This is demonstrated in Figure 2.10 which show the Monte-Carlo trajectory simulation results for the $n = 26$, $k = -25$ state (red line) together with results from the empirical model. Two different parameter sets are used for the empirical model, the parameters needed to obtain a good fit of the results of So et al. (green line) [52] as well as a set of parameters leading to maximum overlap between the Monte-Carlo model and the empirical model (blue line, $\delta = -0.5n^2\mathrm{a}_0$, $\sigma = 1.75$). The lack of overlap between the empirical model using the fitting parameters from So et al. with the stray field results indicate that the previously observed experimental results can not simply be explained by the presence of stray fields near the surface. A closer look at this will be taken in Chapters 3 and 4.

2.3.4 Band-gap semiconductors

So far only free-electron metal surfaces for which charge transfer to the conduction band is always possible have been considered. This somewhat simple picture does not describe how the surface ionisation process might be altered if, instead of a band structure, a discrete level structure would be present at the surface or if the band would be split into a conduction and a valence band with an energy gap in between. Band-gap semiconductors thus provide an intriguing target to test the possibility of using Rydberg states as probes for the electronic structure of a surface as charge transfer should be prohibited for energies that fall in the band-gap region.

First theoretical studies involving charge transfer of H^- ions near a Cu(111) surface were performed by Borisov et al. [34]. While the energy of the H^- ion lies within the projected band-gap, a range of image and surface states could possibly be populated due to the image charge interaction of an electron outside a surface. The calculations thus successfully demonstrated the possibility to observe charge-transfer to the metal via these states.

More recently, So et al. investigated the interaction of hydrogen atom Rydberg states with Cu(100) where the energy of the band gap corresponds to the experimentally accessible range of Rydberg states [37]. In this work the electronic structure of the surface was calculated using the one-electron potential of Chulkov et al. [89] and the interaction of the surface with Rydberg states of low principal quantum numbers n ($n \leq 10$) were simulated using wave-packet propagation calculations [36, 37]. These theoretical results were then scaled up to make them comparable with experimental results. While some correlation between image state energy and detection efficiency could be observed additional work on this topic is needed and the results of such will be presented in Chapter 6. This section explains the theoretical background of the interaction of Rydberg states with band-gap semiconductors and gives a summary of the experimental results obtained to date.

The electronic structure of Cu(100) semiconductors

Both Cu(100) and Cu(111) possess a projected band gap (though at different energies) in the direction of the surface normal $\vec{z}$ (for a definition of the coordinate system used see Figure 1.6). However within the band-gap exist a range of discrete energy levels called surface and image states. Their wavefunctions tend towards zero in both the direction of the vacuum as well as the direction of the bulk metal and they are therefore confined to the metal vacuum interface.

Surface states arise from the cleavage of the bulk metal and are localised at the surface atomic layer and their wavefunction decays exponentially towards the vacuum [90, 91]. Image states however originate from the attractive Coulomb potential of an electron outside a metal with its mirror image and the surface barrier created by the band-gap [92]. They are located in the vacuum region of the interface, behind the image plane z_{im} and form a hydrogen-like Rydberg series with the ‘nuclear charge term’ set to $Z = \frac{1}{4}$:

$$E_n^{\mathrm{IS}} = -\frac{1}{16} * \frac{1}{2(n+a)^2} \tag{2.18}$$

where n is the image state index (analogous to the principal quantum number) and a is the surface dependent quantum defect parameter. For Cu(111) this parameter is approximately equal to $a \approx 0.02$ while for Cu(100) it is $a \approx 0.24$ [89, 93]. The 1D wavefunction of these image states is of the form [93]:

$$\Psi_n^{\mathrm{IS}}(z_e) = z_e R_{n,l=0}(z_e/4) \tag{2.19}$$

with $R_{n,l=0}$ being the normalised hydrogenic radial wavefunction (s-wave). Due to their rather large decay lengths the image state wavefunctions can extend far into the vacuum:

$$\langle z_e \rangle_n^{\mathrm{IS}} = 6(n+a)^2 a_0 \tag{2.20}$$

and significant overlap with the Rydberg state function of an incoming atom is possible. In turn this should lead to strong resonant effects in the charge transfer process, especially compared to resonant effects with the surface states which are located within the surface.

On an uncorrugated surface an electron can move quasi-freely parallel to the surface ($\vec{\rho}$). This forms a 2D continuum of energies for the image and surface states:

$$E_n^{\mathrm{IS,SS}}(k_\parallel) = E_n^{\mathrm{IS,SS}} + \frac{k_\parallel^2}{2\mu} \tag{2.21}$$

where $k_\parallel$ is the electron momentum parallel to the surface and μ is the effective mass of an electron ($\mu \simeq 1$) [94].

Figure 2.11 shows the calculated band gap structure of Cu(111) and Cu(100) together with the energies of the corresponding image and surface states as a function of electron momentum parallel to the surface. The energies of a pure Jellium model surface are also shown for comparison. The copper potentials are calculated following the work of Chulkov et al. [95] and the figure is taken from [37]. At this time it should be pointed out that surface and image states whose energies lie in the bulk part of the potential (grey shaded area) are called ‘resonances’ instead of ‘states’. They are very broad and short lived due to their strong coupling to either the valence or conduction bands. The figure also shows the energies of hydrogen Rydberg states (green lines) and states with energies close to a predicted surface or image state are marked in orange. It can be seen that only for a Cu(100) surface does the experimentally accessible range of hydrogen Rydberg states lie within the band gap. The experimental studies presented in Chapter 6 will therefore only focus on this surface.

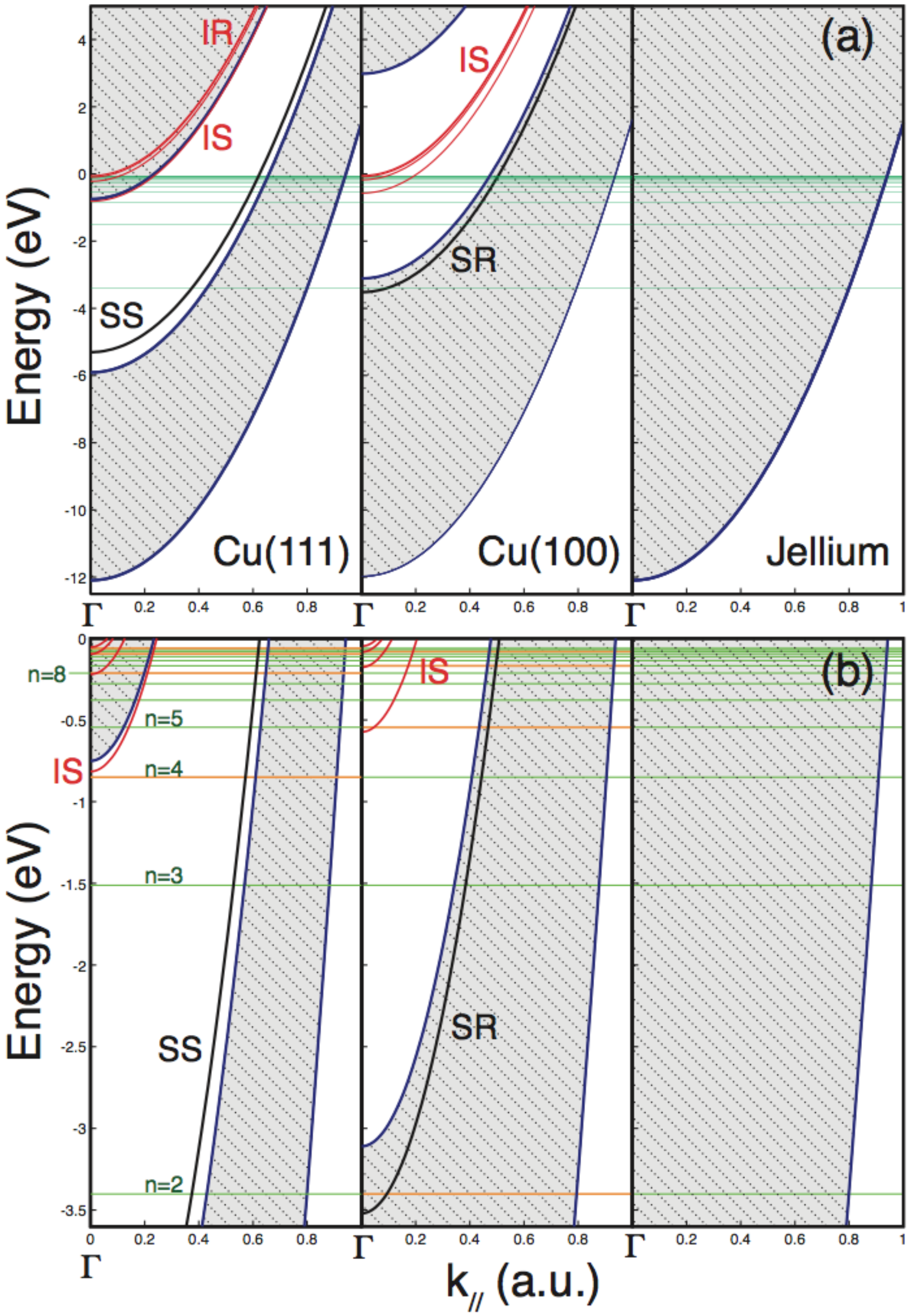

Figure 2.11: From [37], based on [95]. a) Energies of the electronic states in Cu(111), Cu(100) and a Jellium model surface as a function of electron momentum parallel to the surface ($k_{\|}$). The grey shaded area corresponds to the 3D bulk states, surface states (SS) and surface resonances (SR) are shown as full black lines, image states (IS) and resonances (SR) as full red lines and the hydrogen atom Rydberg energies are depicted as green lines. b) zoomed in part of a), focusing on the Rydberg states with energies in the proximity of a surface or image state are marked in orange.

Charge transfer to surface and image states

So et al. performed wavepacket propagation (WPP) calculations in order to theoretically study the charge transfer behaviour of hydrogen Rydberg states near Cu semiconductor surfaces [37]. It should be noted that these calculations are computationally far more challenging than classical over-the-barrier ionisation calculations and this complexity scales exponentially with principal quantum number. Therefore, only low principal quantum number states in the range $n = 2 - 10$ were investigated and only the field free case as well as the most red-shifted Stark states ($k = -(n-1)$) were considered.

Figure 2.12 a) shows ionisation rates for the most red-shifted Stark state of an $n = 5$ Rydberg atom as a function of atom surface separation for Cu(100), Cu(111) and a Jellium surface. In this case, the Rydberg energy lies within the band-gap for both copper surfaces. For Cu(111) it is nearly degenerate with one of the image states which leads to a resonant enhancement of the ionisation rate at a distance similar to those observed with a Jellium model surface. However, there is no overlap with surface or image states of the Cu(100) surface leading to a suppression of surface ionisation. Figure 2.12 b) shows snapshots of the electronic wavefunction extracted from the WPP calculation for the most red-shifted Stark state of the $n = 4$ Rydberg atom at a distance of approximately $4\,n^2\mathrm{a}_0$. The resonance effect for the Cu(111) case (middle) can clearly be seen, while especially for the Cu(100) surface only minimal ionisation takes place (note that Rydberg atom and surface are moving towards each other in these images). From this image it can also be deduced, that the electron flux tends to be directed into the surface when its energy is in resonance with the bulk or an image state (Jellium, Cu(111)) but is directed more parallel to the surface when off-resonance (Cu(100)).

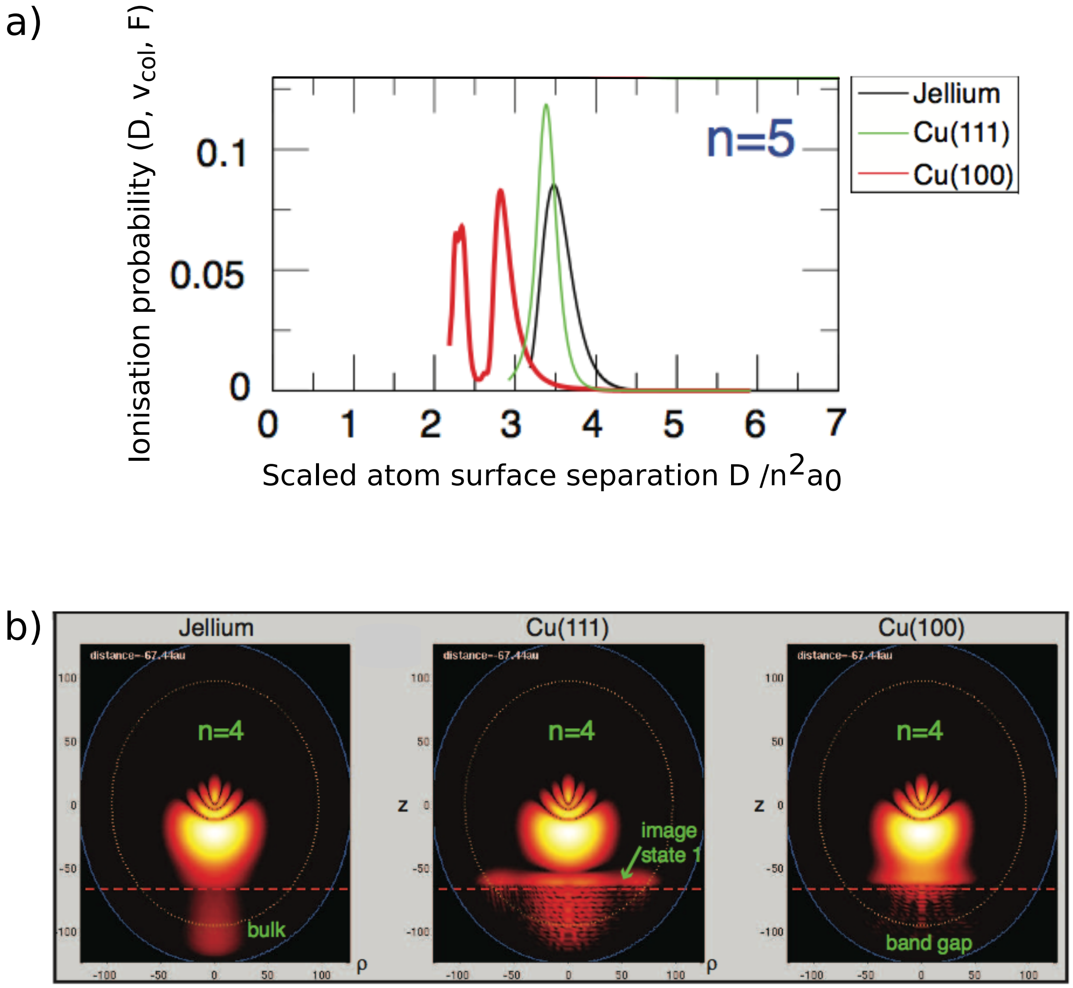

Figure 2.12: From [37]. a) ionisation rate for the most red-shifted Stark state of a $n = 5$ hydrogen Rydberg atom near Jellium, Cu(100) and Cu(111) surfaces as a function of distance as calculated by WPP calculations. b) snapshots of the electronic wavefunctions of the most red-shifted Stark state of a $n = 4$ Rydberg atom on its approach to the surface, extracted from the WPP calculations for all three surfaces at a distance of approximately $4\,n^2 a_0$.

From theory to experiment - previous experimental results

So et al. also studied the interaction of hydrogen Rydberg states with Cu(100) experimentally. While it is computationally not feasible to use WPP calculations to simulate experimental results it is nonetheless possible to make some predictions for the experimentally accessible range of principal quantum numbers. For example, by using Equations 2.18 and 2.21 it is possible to calculate the energies of the image states in the experimentally accessible range. Combining these results with the energy of a field-free Rydberg state or a Stark state at a given electric field (see Equation 1.15), it is possible to identify possible candidates which may show resonance effects.

Figure 2.13 shows the energies of the image states of Cu(100) (dotted lines) overlapped with the energies of (a) the most red shifted ($k = -(n-1)$) and (b) the most centre-manifold Stark states ($k = 0$ or -1) of atomic hydrogen as a function of electric field for the principal quantum numbers in the range $n = 20-38$ (bold, coloured). The length of the bold lines representing the Stark states roughly depicts the approximated/expected field range of the surface ionisation signal from onset to field ionisation. For both cases specific electric fields can be identified at which the overlap between the energy of a Stark state and an image states occurs. Overall, the mid-manifold states are of greater interest experimentally due to the nature of the experiment which requires a varying electric field. Only these states either possess a single crossing with an image state or no crossing at all for a wide range of fields (Figure 2.13 b) making it possible to identify resonance effects in the surface ionisation profiles. On the contrary, red-shifted states vary greatly in energy as the electric field changes and every state will be resonant with an image state sooner or later (Figure 2.13 a), making the analysis of gathered data more complicated.

Experiments were performed by measuring the ratio of the integrated surface ionisation profiles taken with a Cu(100) surface with those taken with a Jellium type gold surface.

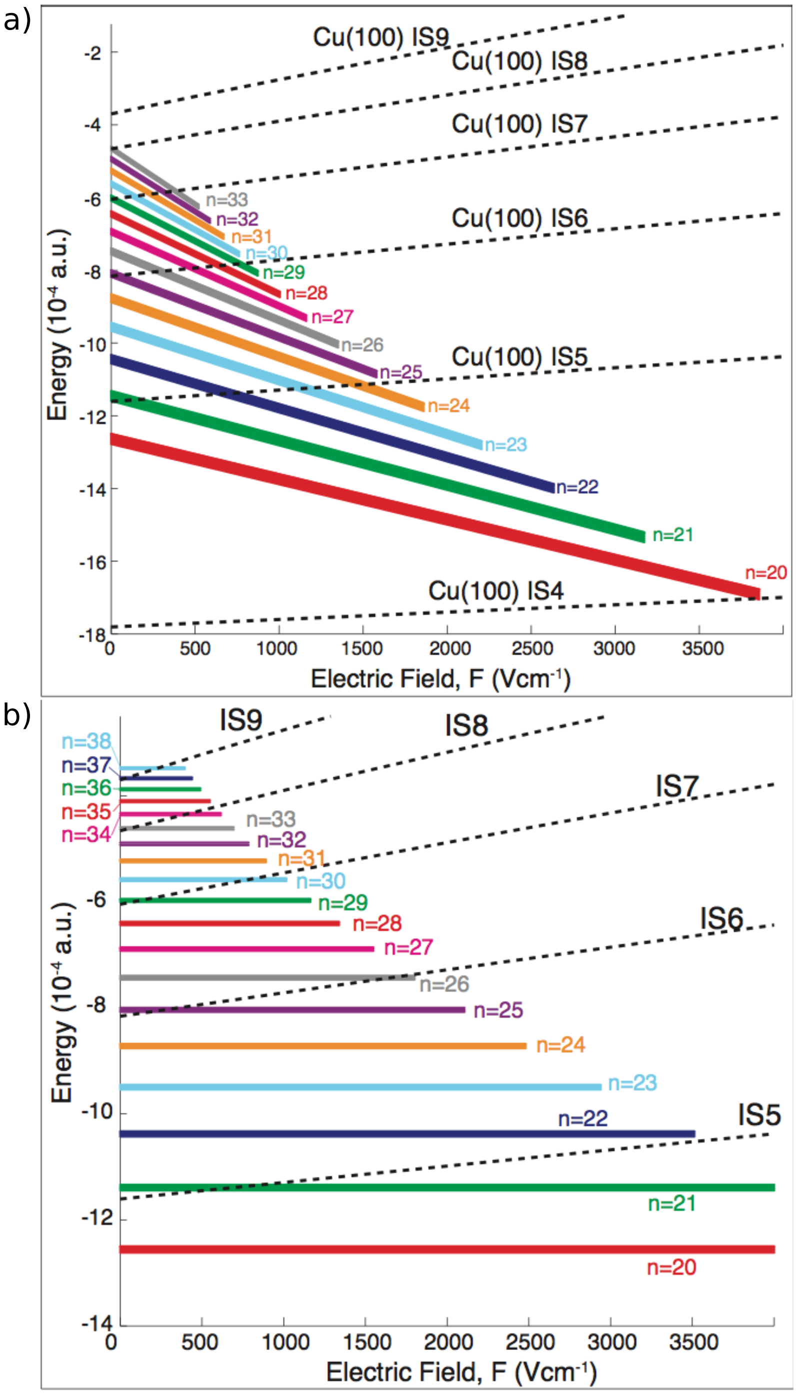

Figure 2.13: From [37]. Overlap of the energies of the image states of Cu(100) (black, dotted lines) with the energy of H-atom Rydberg states in the range $n = 20 - 38$ (full coloured lines) as a function of electric field. The length of full lines approximately represents the electric field range for which a surface ionisation profile for the corresponding state can be detected. a) energies of the most red shifted Stark states of hydrogen: $k = -(n-1)$. b) mid-manifold Stark states: $k = 0$ or -1.

These experiments were performed for both, the most red-shifted as well as centre-manifold Stark states in the range $n = 20 - 38$. As could be expected, the results of the $k = -(n-1)$ Stark states delivered inconclusive results (results not shown). The results for the $k \simeq 0$ states are presented in Figure 2.14 a). In this case, significant variations of the ratios of the integrated signal can be seen for a range of principal quantum numbers investigated, with local maxima occurring at $n = 22, 26, 31, 35$. Comparing these results with Figure 2.14 b), which shows again the overlap of the Rydberg state energies with the Cu(100) image state energies (grey, dotted lines) it becomes evident that the energies of all the states with enhanced detection efficiency appear just above one of the image states. An even better agreement can be achieved by shifting the energy of the image states up by a factor of 5×10^{-5} a.u. (black, dotted lines) which is a reasonable assumption to make as perturbation effects due to the presence of the Rydberg states are not included in calculating the image state energies.

It should be noted however, that the observed experimental error of the integrated signal ratios are of a similar size as the height of the detected peaks themselves. Therefore, the presented results did not deliver definite proof of resonance effects due to the interaction of the Rydberg atom with image states of the Cu(100). The results thus only present potential evidence for the presence of resonance effects and further investigations are needed to confirm this assumption. Such experiments will be presented in Chapter 6. Nonetheless, this early work represents a further example for the possibility to use Rydberg states as surface probes.

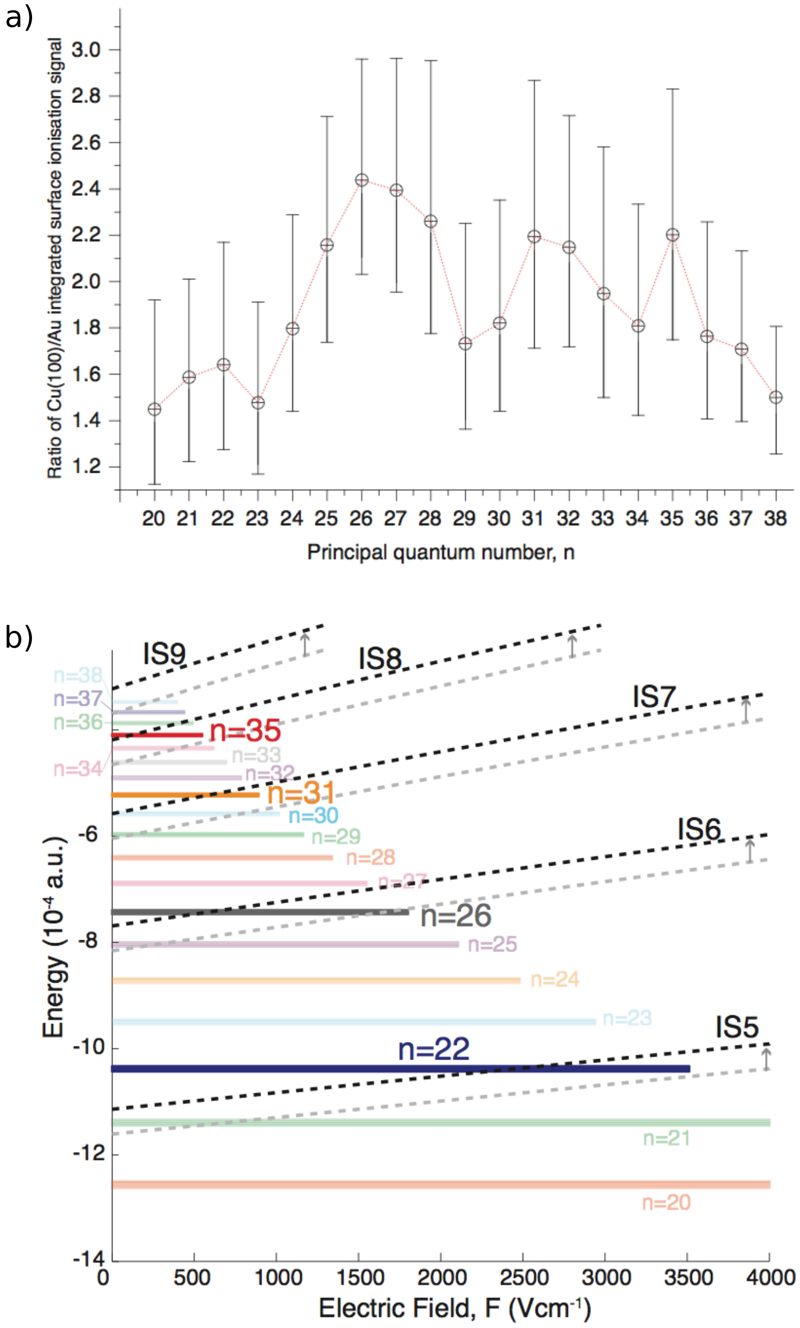

Figure 2.14: From [37]. a) ratio of the integrated surface ionisation profiles for the Cu(100) surface over a jellium type gold surface for mid-manifold Stark states ($k = -n + 1$) for principal quantum numbers in the range $n = 20 - 38$. b) overlap of the energies of the image states of Cu(100) (grey, dotted lines) with the energy of mid-manifold Stark states ($k = 0$ or -1) in the range $n = 20 - 38$ (full coloured lines) as a function of electric field. The energies of the image states a shifted up by 5×10^{-5} a.u. as explained in the text (black, dotted lines).

Chapter 3

Experimental techniques

In this chapter the experimental setup used to record the data presented in this thesis is described in detail and recently added modifications are highlighted. Furthermore experimental techniques and data analysis techniques are explained. The experimental results obtained in this way will be shown in the following chapter.

3.1 Experimental setup

The experimental results shown in this thesis were acquired on an experimental setup which has been described in detail elsewhere [37]. In the following paragraphs this setup is introduced, and modifications made to the ion detection system will be explained. A sketch of the whole setup, including surface analysis facilities is shown in Figure 3.1 a) and a detailed schematic of the surface interaction region is presented in Figure 3.1 b).

3.1.1 H-atom molecular beam

The hydrogen source used in this experiment is based on work by Merkt and co-workers [96]. H-atoms are created by photodissociation of either pure ammonia or ammonia

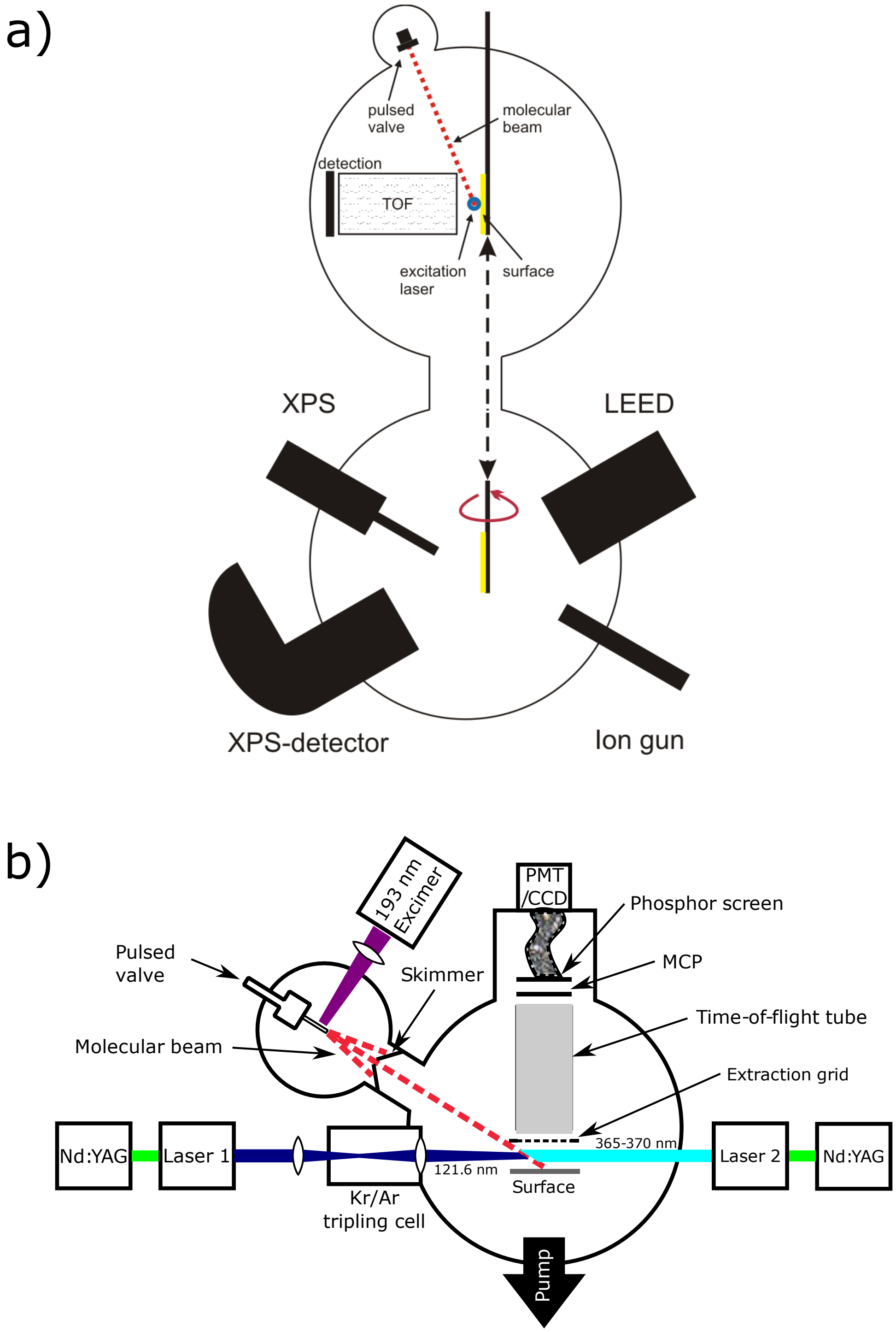

Figure 3.1: a) schematic diagram of the experimental setup used in this thesis showing both the surface interaction and surface analysis chambers. The ability to move the surface in between the two chambers is highlighted. b) in detail diagram of the surface interaction chamber showing the photodissociation, laser excitation and detection regions. A detailed description of the different components can be found in the text.

atoms seeded in a rare gas molecular beam ($\sim$ 20% ammonia). A face plate with a 1 mm aperture is mounted in front of a solenoid pulsed valve (General Valve, Series 9) operating at 10 Hz with a pulse width of $\sim$ 100 µs. A 15 mm long, 1 mm diameter glass capillary (Vitrocom CV1012S) is attached to the front of the faceplate. It is in this capillary that the photo-dissociation of the ammonia ($NH_3 \rightarrow NH_2 + H$) takes place, using a weakly focused (fused silica spherical lens, f = 200 mm) ArF excimer laser (GAM Ex5, 10Hz, $\sim$ 8 ns pulse width) operating at 193 nm with an energy of $\sim$ 4 - 6 mJ/pulse. The ideal backing pressure was found to be $\sim$ 800 mBar for the pure ammonia and $\sim$ 2 Bar for the seeded beam. The molecular beam is allowed to expand for approximately 3 cm after the end of the capillary before flying through a 1 mm diameter skimmer and subsequently travels for another $\sim$ 46 cm before reaching the surface-interaction region.

On approaching the surface (1 inch diameter), the hydrogen atoms are excited into Rydberg states using a two-laser excitation scheme (see Section 3.1.2). The surface is mounted on an xyz-translational stage as well as a rotational stage. It is thereby possible to control the excitation position relative to the surface as well as the incidence angle of the beam (and with that the velocity component perpendicular to the surface). Another way to control the impact velocity is by seeding in different rare gases and adjusting the time delay between dissociation and excitation lasers.

As the distance between the position of photodissociation of the ammonia and the laser excitation is known (49 ± 0.8 cm) it is possible to determine velocities by monitoring the field-ionisation signal as a function of Rydberg excitation delay from the photo-dissociation laser. It can thus be shown that by using different seeding gases and adjusting the delay it is possible to freely choose H-atom velocities in the range of $v = 600 - 3000\,\mathrm{m/s}$ [37]. This technique relies on the fact that the average beam velocity is heavily influenced by the molecular weight of the seeding gas and that the spatial spread of the H-atoms in the direction of the molecular beam at the time of excitation is greater than the original spread during photodissociation. It is also possible to relate the velocity-spread σ of the H-atom cloud at the laser excitation point to a temperature T via $\sigma = \sqrt{kT/m}$. The translational temperature of the beam can thus be determined to be 80 K for the pure ammonia beam and ranges from $\sim$ 20 – 40 K for the different seeded beams depending on the chosen seeding gas. Figure 3.2 shows the measured velocity distributions for the different gas mixes. These were obtained by varying the time delay between photodissociation and laser excitation of the hydrogen atoms. The resulting high-n Rydberg states are then field-ionised and the integrated ion-signal is plotted against velocity. Even though these distributions are fairly wide this does not cause any experimental problems given the short pulse length ($\sim$ 5 ns) of the two excitation lasers, coupled with the large distance from the gas source to the excitation volume. It is therefore possible to excite a relatively narrow velocity distribution with a standard deviation of $\sim$ 1% [37].

Even though it is in principle possible to use a range of seeding gases, the overall signal intensities decrease significantly when the seeding gas becomes heavier. Therefore all experiments presented in this thesis were performed either with pure ammonia or using helium as seeding gas. Assuming an incident angle (α) of $\sim 15^\circ$ and tuning the excitation laser delay to the maximum of the corresponding velocity distributions, leads to velocity components perpendicular to the surface of $v_\perp \approx 650\ \mathrm{m\,s^{-1}}$ for the un-seeded NH_3 and $v_\perp \approx 390\ \mathrm{m\,s^{-1}}$ for ammonia seeded in helium ($v_\perp = sin(\alpha) \cdot v$). It should be noted that the exact velocity depends on the exact laser alignment on a given day. By adjusting the delay of the excitation laser, acceptable signal levels can be detected (and thus experiments can be performed) for molecular beam velocities between $v = 1500\ \mathrm{m\,s^{-1}}$ and $v = 4500\ \mathrm{m\,s^{-1}}$ (see Figure 3.2), correlating to collisional velocity of approximately $350\ \mathrm{m\,s^{-1}}$ and $1150\ \mathrm{m\,s^{-1}}$.

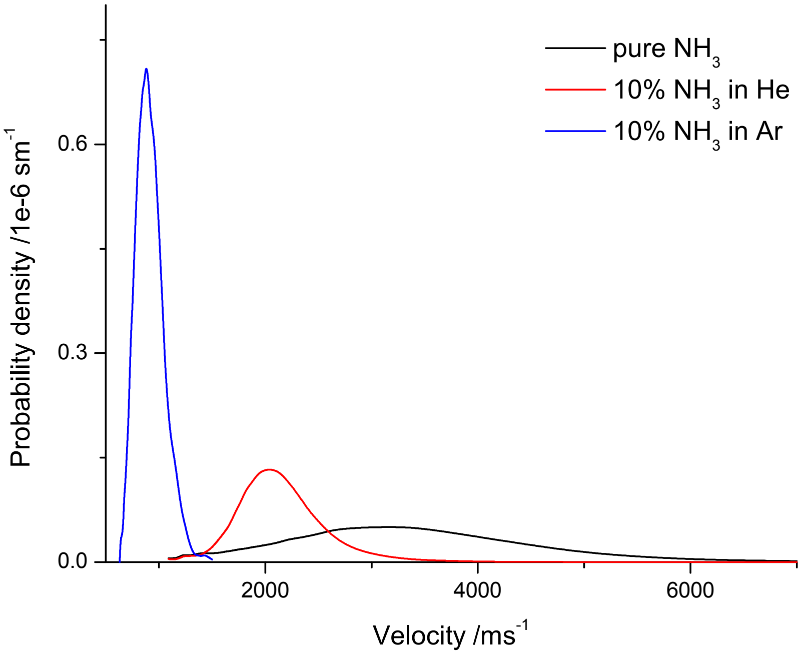

Figure 3.2: Velocity distributions of an atomic beam of hydrogen atoms seeded in different rare gases. The hydrogen atom concentration is given as a function of the amount of ammonia in the seeding gas. In addition, the velocity distribution for an unseeded beam is also shown. The molecule hydrogen is produced from via laser dissociation and the velocity distribution is measured by varying the time delay between photodissociation and laser excitation of the hydrogen atoms (see text for details).

The source chamber is pumped by two turbo pumps backed by rotary pumps, one in the region of the pulsed valve (Pfeiffer Vacuum, TUM521, 833 MHz) and one after the skimmer (Pfeiffer Vacuum, TUM071P, 1500 MHz). An additional rotary backed turbo pump is mounted in the main chamber behind the surface (Pfeiffer Vacuum, TUM521, 833 MHz). This leads to base pressure in the source chamber of $\sim 1\times10^{-8}$ mbar which increases to $\sim 1\times10^{-6}$ mbarr for experiments using pure ammonia and $\sim 8\times10^{-5}$ mbar for experiments using seeded beams. In the surface-interaction chamber the base pressure is $\sim 4 \times 10^{-9}$ mbar which increases to $\sim 7 \times 10^{-9}$ mbar for pure ammonia and $\sim 1 \times 10^{-8}$ mbar in the seeded case. The bottom chamber, containing the surface analysis equipment, is pumped by a rotary backed turbo pump (Pfeiffer Vacuum, TUM262, 1000 MHz) and can be separated from the main chamber by a gate valve. After baking the pressure in this chamber is in the range $\sim 5 \times 10^{-11}$ mbar when separated from the main chamber, rising to $\sim 5 \times 10^{-10}$ mbar with the two chambers connected.

3.1.2 Laser excitation

At a distance of approximately 1 mm from the surface the hydrogen atoms are excited to Rydberg states in the range n = 20 - 30 by two-colour resonant two-photon laser excitation via the $2p$ state. The Lyman-α radiation (λ = 121.6 nm) for the first excitation step is generated by frequency tripling of the doubled output of a Nd:YAG (Continuum Surelite 3, frequency doubled to 532 nm, $\sim$ 430 mJ/pulse) pumped Sirah dye laser (Sirah Cobra-Stretch, Pyridine 2 laser dye, $\sim$ 13 mJ/pulse). The frequency tripling is performed by focusing the laser beam into a rare-gas cell containing a mixture of krypton and argon (partial pressures: Kr 205 mBar, Ar 590 mBar) using a fused-silica spherical lens (f = 200 mm). The resulting VUV radiation is refocused into the vacuum chamber using a LiF spherical lens (f = 150 mm). Assuming a conversion efficiency of about $10^{-6} - 10^{-7}$ this leads to an estimated photon density of the VUV light of about $10^{9} - 10^{10}$ photons/pulse [97]. As the LiF lens provides different focal lengths for the VUV and UV it is ensured that only the Lyman-α radiation is focused into the interaction region. Transitions to the high-lying Rydberg states is achieved by the frequency doubled output of a second Nd:YAG (Continuum Surelite 3, 532 nm, $\sim$ 430 mJ/pulse) pumped dye laser (Sirah Cobra-Stretch, Styrol 8, $\sim$ 5 mJ/pulse) tunable in the range 365 - 370 nm. The second laser is not focused into the vacuum chamber to avoid power broadening which can otherwise be observed.

Figure 3.3 shows the range of accessible Rydberg states by plotting the integrated field ionisation signal (see Section 3.1.3) as a function of second laser wavelength. For $n < 20$ the applied electric field ($\sim$ 4000 V/cm) becomes too small to ionise the Rydberg state so the integrated surface ionisation signal (see Section 3.2) is shown instead. Variations in line intensities are mainly due to variations in laser power over time and the limited tuning range of the laser dye. While this represents the ultimate limit of Rydberg states that can be detected with this setup, the range of states usable to study charge transfer experiments is considerably lower. This is due to a decrease in the signal to noise level, caused by a combination of UV radiation and strong electric fields, as well as the high density of states at high principal quantum numbers. The range of principal quantum numbers investigated in this thesis is thus limited to approximately $n = 25$ to $n = 35$.

The intermediate $2p$ state possesses a hyperfine structure due to the spin-orbit interaction ($^2\mathrm{P}_{\frac{1}{2}}$ - $^2\mathrm{P}_{\frac{3}{2}}$) and the energy difference between these two states is 0.365 cm^{-1} which is a similar magnitude compared to the linewidth of the VUV photon after frequency tripling ($\sim$ 0.3 cm^{-1}). Therefore both intermediate states will be populated during the intermediate process. However it is possible to tune the first excitation laser in such a way that predominately one intermediate state is populated which

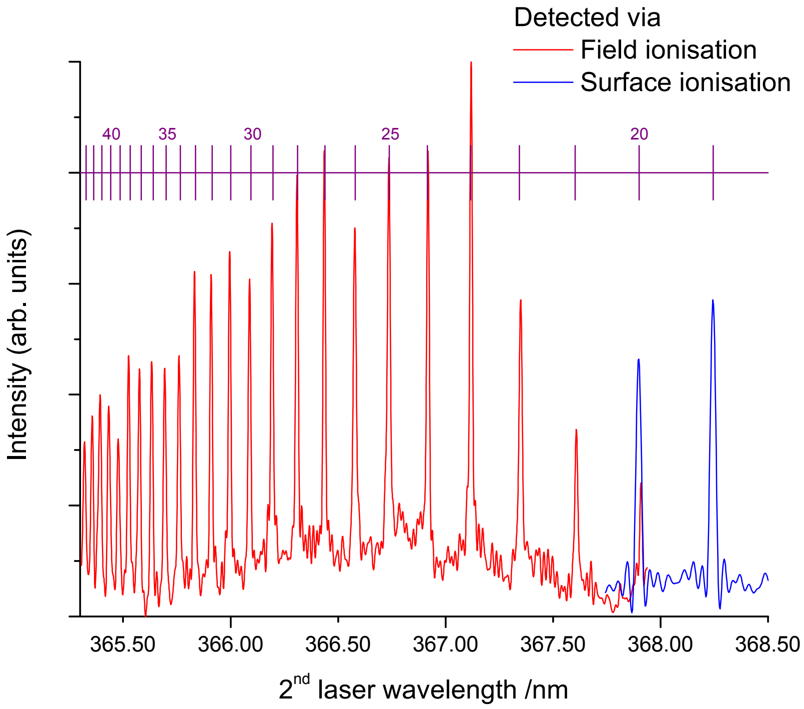

Figure 3.3: Based on [37]. Field ionisation signal as a function of applied 2nd laser wavelength for Rydberg states in the range $n = 19 - 44$ (red line). For low principal quantum numbers (n = 19, 20) the applied electric field is too low to effectively field ionise the Rydberg states and the integrated surface ionisation signal is shown instead (blue line).

significantly simplifies the resulting spectrum. For the experiments presented in this thesis the laser was tuned such as to maximise population in the ${}^2\mathrm{P}_{\frac{3}{2}}$ state.

Due to selection rules during excitation in an electric field it is possible to populate states with different magnetic quantum numbers m_l depending on laser polarisation relative to the electric field axis. In theory, there are three different possibilities, $m_l = 0$ (both parallel with the electric field), $m_l = \pm 1$ (one parallel, one perpendicular) or $m_l = 0, \pm 2$ (both perpendicular). However, in practice imperfect laser polarisations can lead to the excitation of a mixture of different m_l states (with one m_l value being predominant). For this work, laser polarisations for both lasers were chosen to be perpendicular to the electric field axis. It should be noted that even though all states should possess $m_l = 0$ as well as $m_l = \pm 2$ character, the most red and blue shifted Stark states must possess pure $m_l = 0$ character due to the admixture of $l = 0$ functions and because the largest k values occur for $m_l = 0$ (see Equation 1.14).

In order to control the polarisation of the Rydberg state with respect to the surface, an electric field can be applied to the surface prior to laser excitation. This field leads to a lifting of the l-degeneracy and the emergence of polarised Stark states. The amount of the energy-splitting of the individual states depends on the strength of the applied field and the observed spectrum possesses a contribution from both intermediate $2p$ states and different m_l values depending on the quality of the laser alignment. Figure 3.4 shows the field ionisation signal as a function of 2nd laser wavelength for principal quantum numbers in the range $n = 22 - 24$ at a range of different Stark fields. This nicely demonstrates how the optimum Stark field for a given Stark manifold needs to be chosen individually in a way that maximises the splitting between different Stark states without overlapping states of neighbouring n-manifolds. A fully resolved Stark spectrum for the $n = 29$ Rydberg state at a Stark field of 76 V/cm is shown in Figure 4.5, demonstrating the ability to selectively populate different Stark states of a chosen

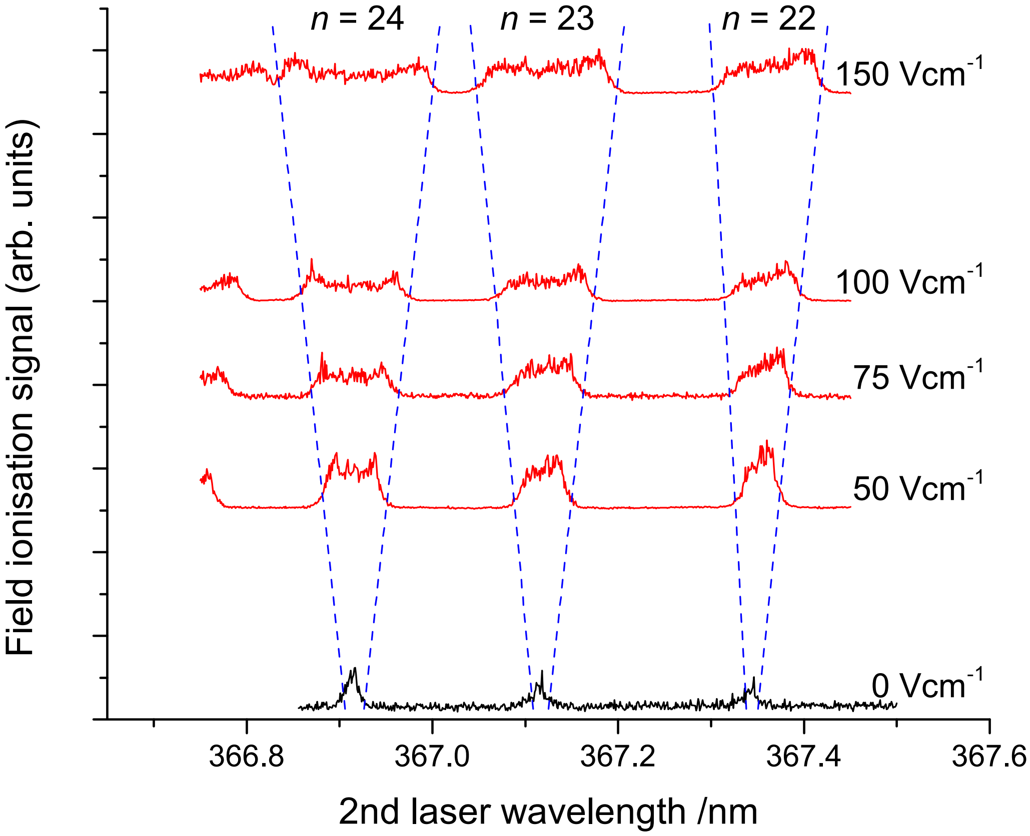

Figure 3.4: Field ionisation signals as a function of 2nd laser wavelength for Rydberg states in the range of n = 22 - 24 for a range of applied Stark fields. The laser polarisation is chosen to predominantly populate $m_l = 0$ states. The increasing spread of Stark states with increasing field is visible (blue dashed lines).

Rydberg manifold.

3.1.3 Ion detection

Approximately 500 ns after excitation a pulsed electric field is applied to either the 1 inch diameter surface or to a mesh (Precision Eforming nickel mesh 86.1% transmission) of the same size situated right opposite the surface at a distance of approximately 1 cm. This field is meant to either field ionise and subsequently detect the Rydberg states or to extract the surface-ionised H-atoms. Depending on the direction of the applied field it is possible to either detect electrons or protons. The extracted protons or electrons subsequently fly through a second mesh (Precision Eforming nickel mesh

86.1% transmission) which is held at a constant voltage equal to the one applied to the front multi channel plate (MCP) allowing for all protons stemming from surface ionisation to arrive at the detector at roughly the same time (independent of extraction voltage).

Subsequently the ions or electrons fly down a $\sim$ 12 cm long time of flight (TOF) tube before reaching the MCP detector (Burle [MCP 18/12/10/5 I 40:1 MS], 18 mm active diameter) and the resulting electrons hit a phosphor screen (P-47 coating). For ion detection the front plate is held at a voltage of $\sim$ -1300 V, the backplate is grounded and the phosphor screen is set to +3000 V. For electron detection the front plate is set to ground, a voltage of +1300 V is applied to the back plate and the phosphor screen is set to +3800 V. The fluorescence coming from the phosphor screen is optically coupled into a flexible fibre optic (Beam Imaging Solutions, HRBIS-1000 series probe head, viewable area: 9.1 mm × 6.6 mm) and can either be detected using a photomultiplier tube (PMT) or can be viewed directly with a charge-coupled device (CCD) camera. The signal from the PMT is amplified by a 3 stage fast amplifier (SR – 445 Quad 350 MHz pre-amplifier, Stanford Research Systems), detected by an oscilloscope and recorded via custom-made LabVIEW^{TM} programs.

The whole detection unit is mounted on the same rotational stage as the surface. This way the plane of the extraction mesh and the detector is always kept parallel to the surface when the later rotates, thus guaranteeing that the applied extraction field is always homogeneous.

3.1.4 Modifications

While some experiments were performed with the setup explained above most results presented in this thesis were obtained using a modified ion-detection unit. Due to the rather small size of the fibre-optic view-port coupled to the phosphor screen the actually detectable area is only $\sim$ 60 mm^2 compared to a surface diameter of 2.4 cm. Therefore only a small portion of the actual field and surface ionisation signal can be detected. This leads to two problems: signal strength and detection efficiency both depend strongly on laser alignment and the undetected area of the MCP ($\sim$ 75%) might be subjected to a strong but undetected ion signal, significantly reducing its lifetime. Modifying the detection setup also offered a chance to solve an unrelated problem, namely the fact that the surface to mesh separation was to small too allow easy and straightforward access to the surface analysis chamber via the vertical manipulator. Instead, the whole chamber needed to be opened and the detection cage be moved out of the way.

To solve these issues a modified detection unit was designed, incorporating ion lenses to focus a larger fraction of the H$^+$ ions onto the detector. Figure 3.5 shows a computer aided design (CAD) drawing of this new setup. Overall the new design is similar to the old setup in that it comes with two meshes as well as a TOF tube (10 cm long) but it additionally contains a cover in front of the MCP to protect its 'blind' parts, a motor to move the front mesh forwards and backwards and most importantly the two lens plates to increase the detectable surface area.

The addition of ion optics which are mounted in front ('Optic 1') as well as behind the TOF tube ('Optic 2') required changes to the voltages that are applied to the different components of the detection cage. While it is in theory possible to apply the pulsed ion extraction field to either the surface or the extraction mesh, the surfaces studied in this thesis require the field to be applied to the mesh. However this limits the highest voltage that can be applied to $\sim$ -2500 V (depending on laser alignment) as ions originating from the laser hitting the surface and other ionisation processes get pulled into the detection region at high applied electric fields. This sets a new lower limit to the experimentally accessible range of principal quantum numbers we

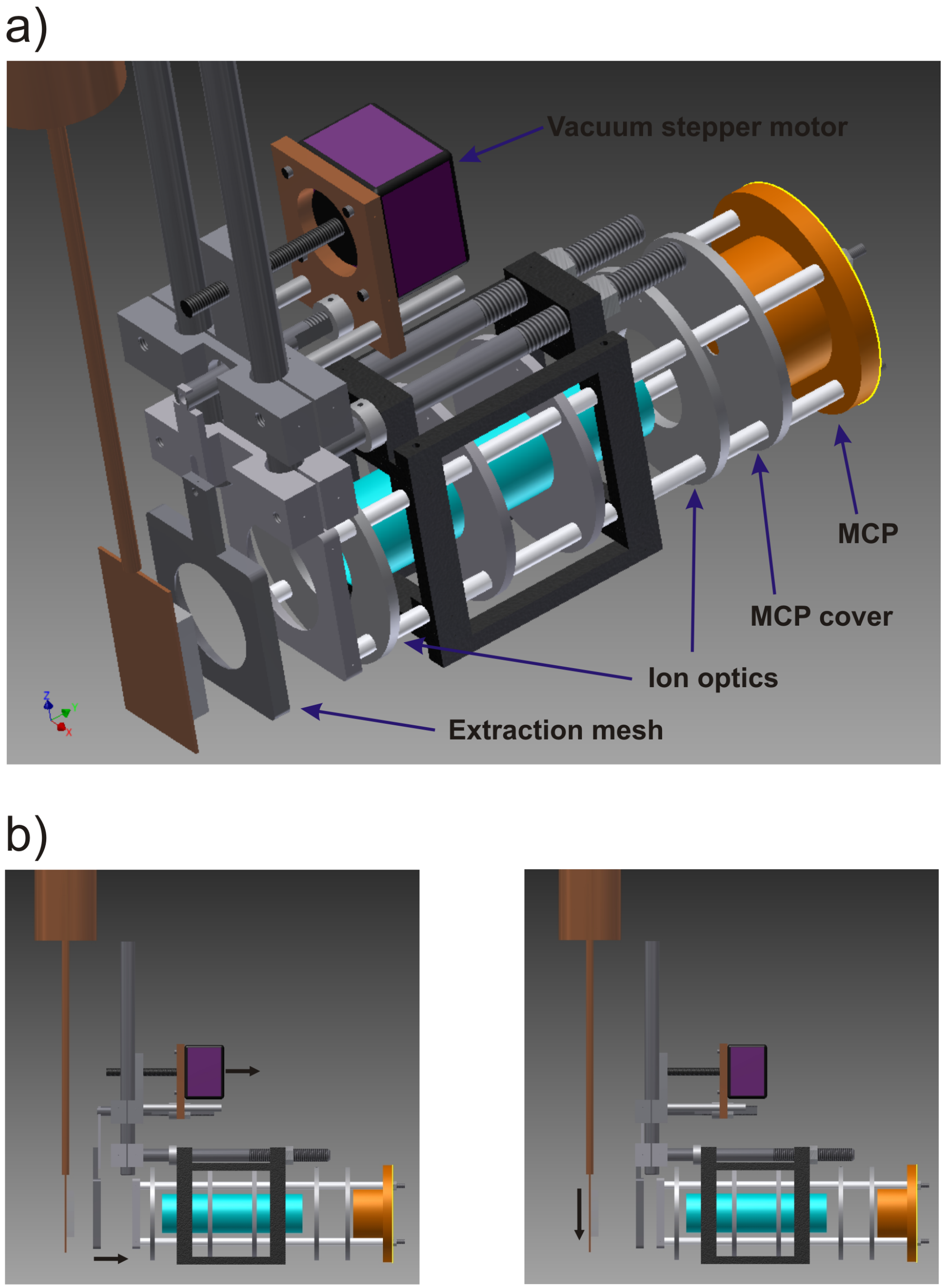

Figure 3.5: CAD drawings of the modified detection cage: a) Schematic of the detection cage. b) Principle of operation of the vacuum stepper motor. Retracting the motor leads to retraction of the front mesh, resulting in extra space that allows the surface to be transferred to the surface analysis chamber.

are able to study to $n = 23$ for red-shifted Stark states and to $n = 28$ if the most blue-shifted Stark states are investigated. The surface is now either grounded or a small positive voltage is applied (20 - 200 V) to enable excitation of specific Stark states. Two centimetres after passing the first mesh, the extracted ions fly through a second mesh which is set to a constant -1300 V. The purpose of this 2nd region of acceleration is the same as in the old setup; it ensures that arrival times at the detector for ions originating from surface ionisation are roughly independent of the applied extraction field. The same voltage of -1300 V is applied to the flight tube and the MCP cover.

As the velocity of the ions still varies somewhat with extraction field, focusing voltages need to be chosen carefully, as the focal point of the ion optics is velocity dependent. Figure 3.6 shows Simion^{TM} [98] simulations of ion trajectories for different extraction and focusing voltages, in which the voltages have been optimised for detection efficiency. Initial ion velocities and position were chosen to mimic closely experimental conditions during laser excitation. While the simulations indicate that it should be possible to adjust focusing voltages in a way to keep ion detection efficiencies approximately constant over the range of extraction voltages used in this thesis, experimental results showed that it is more convenient to scan the first optic linearly with extraction field and keep the second optic at a constant value of -300 V. The detected ion signal as a function of voltage applied to the first optic for different extraction voltages is shown in figure 3.7 a). It can be seen from the different curves that with increasing extraction voltage the maximum detection efficiency shifts to more negative voltages applied to optic 1 (less actual focussing, keeping in mind that ions fly at a 'background' of -1300 V). Figure 3.7 b) shows the absolute value of the optimal voltage applied to optic 1 versus extraction voltage for a range of values. This relationship between the values appears to be roughly linear as can be shown by performing a linear fit through the data points (red line in figure 3.7). The resulting straight line equation can be used to scan the focusing voltage together with the extraction voltage. While the same calibration can be used on a day to day basis it can be shown that this behaviour depends on laser alignment (and thereby on the position above the surface where the Rydberg states are created and where they ionise) and therefore a new calibration is needed after major alignment changes.

3.1.5 Surface analysis facilities

The aim of the work in this thesis is to investigate how surface properties influence the Rydberg state - surface interaction. In order to better understand and characterize the investigated surfaces the setup is equipped with surface analysis facilities. A schematic of the available equipment is shown in figure 3.1 a).

There are three different instruments in the surface analysis chamber. An X-ray photoelectron spectrometer (XPS) consisting of an x-ray source (TX 400/2, PSP Vacuum Technologies) and a hemispherical detector (RESOLVE, PSP Vacuum Technologies) allows element-specific analysis of the surface. Figure 3.8 shows an exemplary XPS spectrum of one of the gold surfaces used in the H-atom gold surface experiments using an aluminium filament. All expected valence electron spectral lines for bulk gold can be seen except the $4s$ line (plotted as detected electrons vs binding energy). This is probably due to the low signal to noise ratio which can be explained by the relatively large distance between the x-ray source and the surface. The doublet structure that is visible for some peaks ($4d$ + $4f$) is due to spin-orbit coupling in the ionic final state.

In addition to that, the chamber is also equipped with a low energy electron diffraction unit (LEED) (BDL 800-IR, PSP Vacuum Technologies) in order to analyse the crystal structure of the surface and an ion gun (ISIS 3000, PSP Vacuum Technologies) for surface cleaning or deposition techniques. LEED needs a vacuum on the order of 1×10^{-10} mBar to work. This requires baking of both the main and the surface analysis

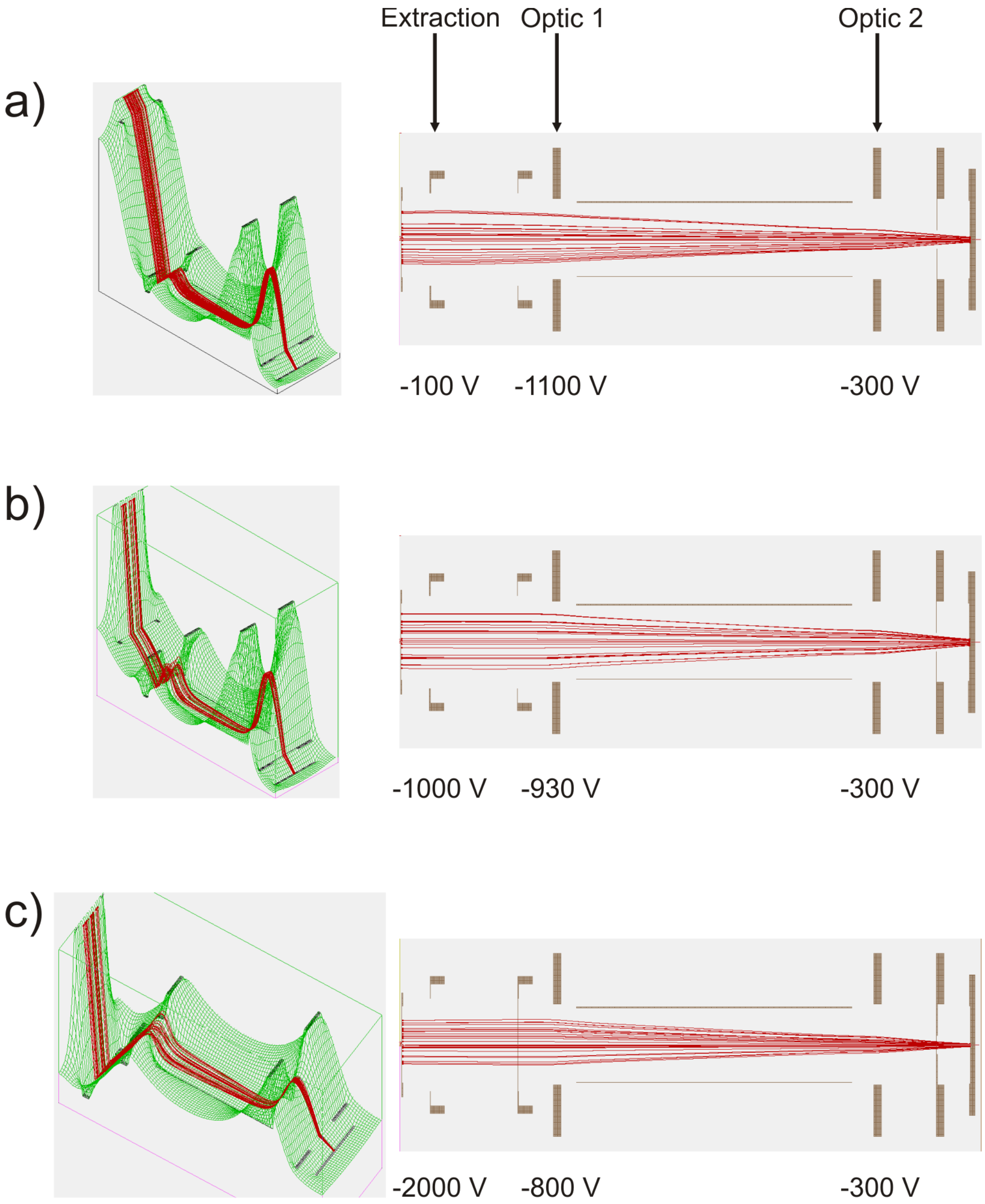

Figure 3.6: Simion ion trajectory calculations [98] for the modified detection setup at different detection voltages. Both the potential energy surface (left) and a cut through the setup are shown. 25 sample trajectories (red lines) with random starting position at 1 mm from the surface are shown for each extraction voltage. The surface is always set to a potential of 0 V, second mesh, flight tube and MCP cover are set to -1300 V. a) Extraction = -100 V, Optic 1 = -1110 V. b) -1000 V, -930 V. c) -2000 V, -800 V.

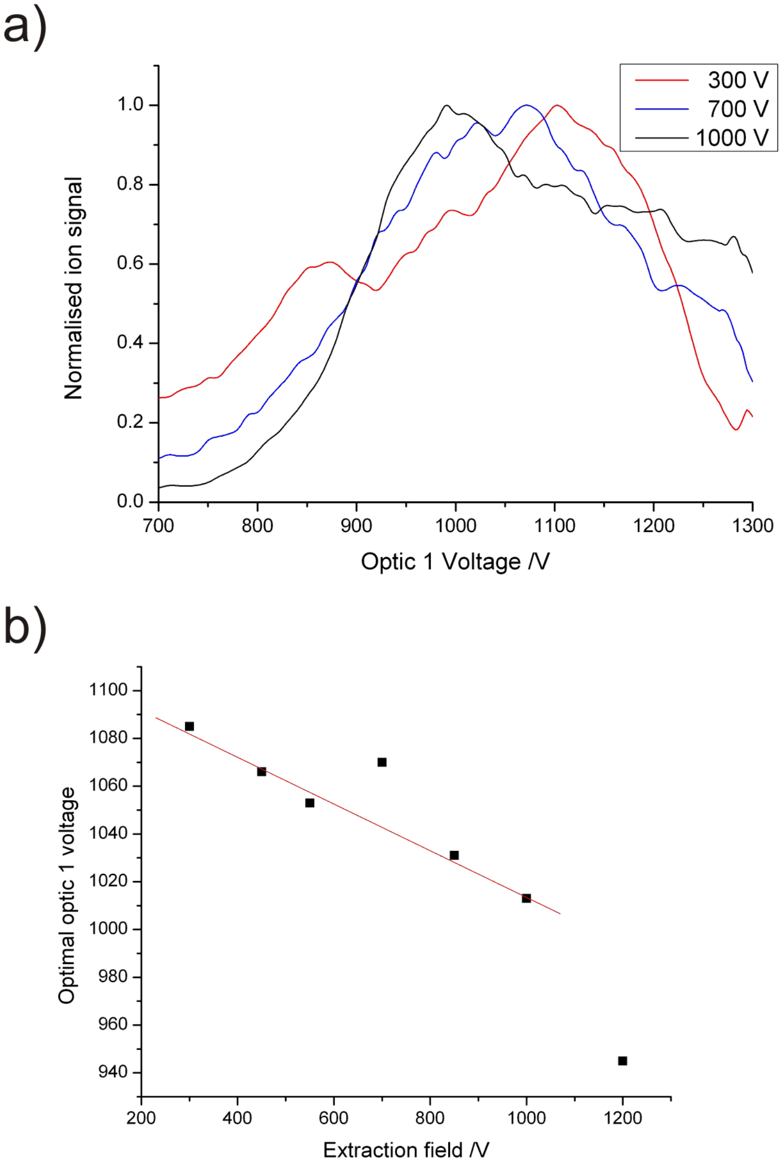

Figure 3.7: Calibration of ion optics: a) Normalised field ionisation signal as a function of applied optic 1 voltage. Optic 2 is held at a constant voltage of -300 V. b) Linear fit to the optimal Optic 1 voltage for a range of extraction voltages.

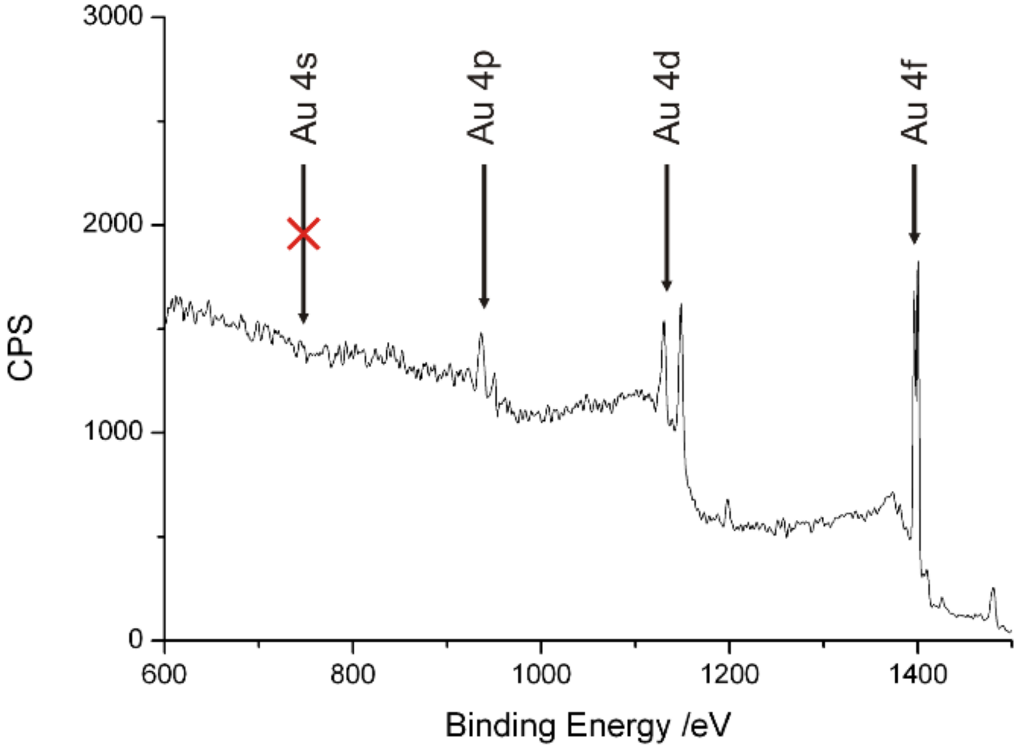

Figure 3.8: XPS spectrum of a bulk gold surface using the setup explained in section 3.1.5. All valence electron lines except the 4*s* peak can be identified. This is probably due to the low signal to noise ratio which can be explained by the relative big X-ray source - surface separation.

chamber and the pressures needed have not yet been achieved and this equipment has therefore not yet been used.

3.2 The surface ionisation signal

This section explains how ions are detected on the MCP detector and how the recorded data is subsequently analysed in the form of a surface ionisation profile. Differences due to introduction of the ion optics are pointed out.

3.2.1 Time of flight profile

Field ionisation and surface ionisation occur at different heights above the surface and at different lateral positions. This difference translates to the detector and allows the two signals to be temporally and spatially separated. Figure 3.9 a) shows an image of the detected ion signal obtained with the CCD camera at an intermediate extraction field, at which both field ionisation and surface ionisation can occur to illustrate this difference. The field ionisation appears as a line at the top of the image (red square) the width of which is mostly determined by the overlap of the two lasers and is roughly 1 mm in length. The surface ionisation signal (green square) is more spread out and lies below the field ionisation signal region which is due to the spread of the excited atoms in the molecular beam after laser excitation (atoms excited further away from the surface travel longer and are found lower). With the introduction of the ion optics the spatial resolution is lost as all ions are focused towards the centre of the MCP as can be seen in figure 3.9 b). While this might be a drawback in some cases it allows monitoring of a greater part of the surface.

Another factor that can influence the time-of-flight profile is the collisional velocity. While the temporal position of the field-ionisation signal is approximately independent

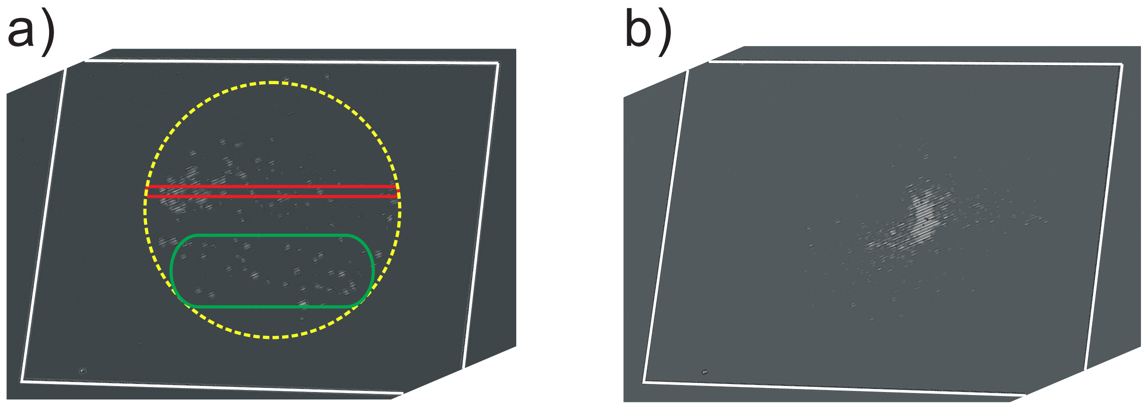

Figure 3.9: CCD camera images of field and surface ionisation signal. The white squares show the borders of the viewport. a) spatial separation of field (red square) and surface ionisation signal (green square) at an extraction field where both processes are possible (no ion focussing). The yellow circle represents the detectable area behind the MCP cover. b) field ionisation signal with ion optics turned on (see text).

of the seeding gas (∼ 1 μs after laser excitation), a shift of the surface ionisation signal to later times in the TOF traces can be observed for heavier gases [37] (unseeded: 2 – 3μs, helium: ∼ 5 μs). The detected surface ionisation profile has a width of ∼ 2 μs which can again be explained with the diameter of the excitation laser beam of ∼ 1 mm and the subsequent spread of the gas cloud on approach to the surface. Temporal separation of the surface and field ionisation signals also depends on the excitation height above the surface as was nicely demonstrated by So et al. [37].

3.2.2 Surface ionisation profile

In a typical experiment the extraction voltage applied to the mesh opposite the surface is scanned in small increments (5 - 10 V) from field ionisation all the way down to 20 V. At every step the field ionisation peak in the TOF profile is integrated and plotted against the electric field (made up of extraction voltage scaled by distance and Stark field). The resulting curve is called a surface ionisation profile.

Figure 3.10 shows the origins of the profile and explains its characteristic shape. Ac-

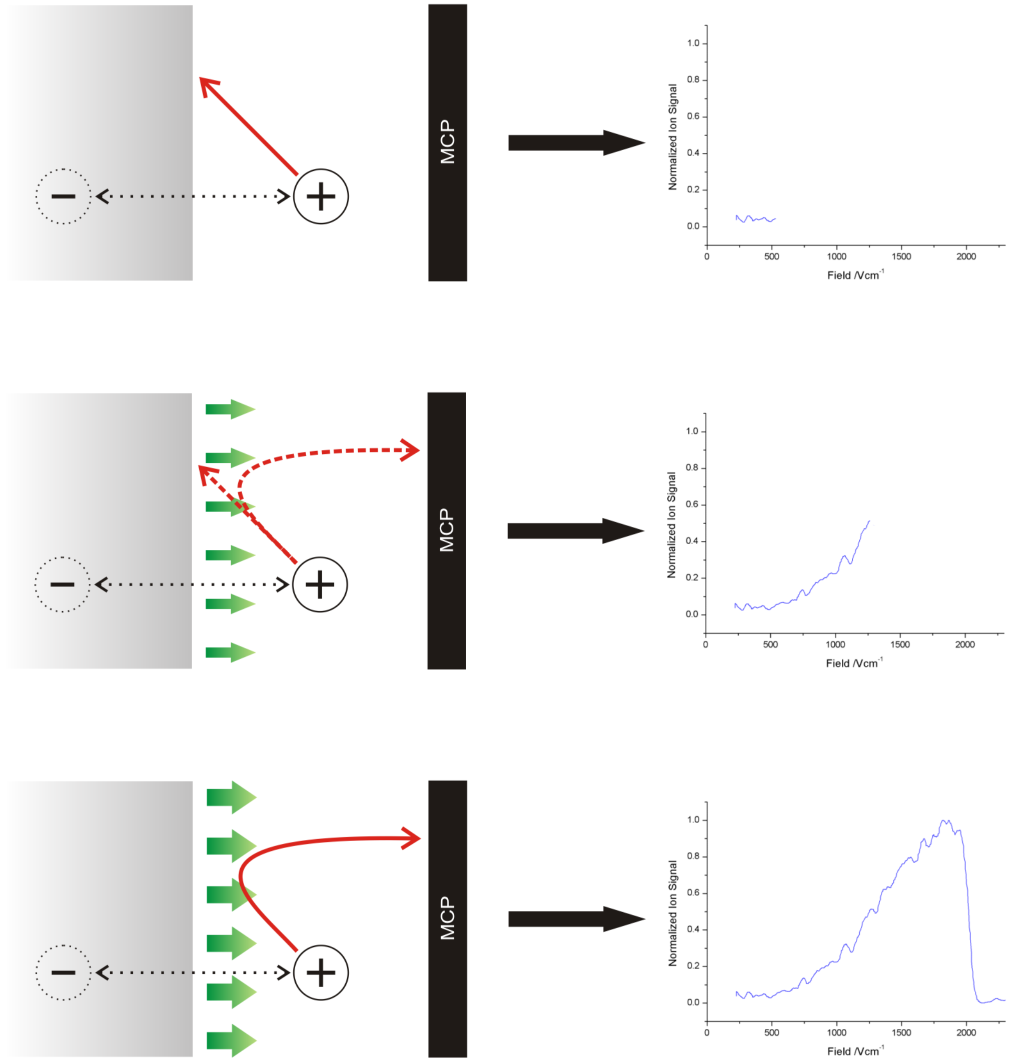

Figure 3.10: Origin of the surface ionisation profile. a) With no (or a very small) extraction field applied the attractive forces between ion-core and surface are too strong and ionised atoms are accelerated towards the surface by their image charge where they eventually neutralise. b) If a small electric field is applied only ions created relatively far away from the surface can be detected. The minimum distance that can be probed at a given field is given by Equation 1.29. c) With an increase in electric field, smaller distances from the surface can be probed and the amount of detected ions increases. The high field cut-off is due to the onset of field ionisation which is detected in a different channel.

cording to equation 1.28, each applied extraction field relates to a minimum ionisation distance. For Rydberg atoms ionising at smaller distances, the field is too low to overcome the effects of kinetic energy combined with the now purely attractive image-charge interaction and the ions collide with the surface where they are neutralised. At very low applied electric fields (depending on n) only ions originating at very large distances from the surface (several $n^2\mathrm{a}_0$) can be repelled, meaning that no or only a few ions can be detected in the surface ionisation gate of the according TOF profile. With increasing field, the minimum ionisation distance that can be probed decreases, which leads to an increase of detected ions with field until the field becomes large enough to ionize the Rydberg state directly (high-field cut-off). In order to determine an overall detection efficiency, the surface ionisation profile is normalised by the size of the field ionisation signal measured by applying a field at a time just before it hits the surface. The size of this signal is roughly proportional to the amount of Rydberg atoms reaching the surface.

3.3 Surface preparation

This section deals with the preparation of some of the different surfaces studied in this thesis. The surfaces investigated in Section 5.1 were prepared in the group of Eah at the Rensselear Polytechnic Institute, New York. Other surfaces used were prepared in-house and the protocols for their preparation are given in this chapter. All the chemicals used were bought from Sigma-Aldrich and used as received unless otherwise stated.

3.3.1 Gold nanoparticle preparation

Gold nanoparticles in the range from $\sim$ 3 - 10 nm diameter were prepared following the procedure described by Eah and co-workers [99] which is based on the Brust method

[100] and will be described in detail in the next paragraph. Other nanoparticles with a greater diameter (15 - 200 nm) were bought from BBI Life Sciences and residual thiols were removed prior to usage by centrifuging and re-dispersion.

A 50 mM solution of $AuCl_4^-$ was made up by dissolving $HAuCl_4 \cdot 3\ H_2O$ in water containing the same amount of HCl. In parallel a 50 mM solution of $NaBH_4$ and NaOH is created. 100 μL of the gold solution is mixed with 10 g of water and stirred vigorously. To that, 300 to 700 μL of the $NaBH_4$ solution are added, depending on the nanoparticle size desired (see table 3.1 for details) and a spontaneous colour change from yellow to red can be observed. Subsequently the mixture is heated at the boiling point of water for 3 minutes and then cooled down in a water bath. The nanoparticles are then transferred into an organic solvent. First 5 g of acetone are added to facilitate the transfer, followed by 10 g of hexane containing 0.5 - 1.0 μM of 1-dodecanethiol (DDT). The DDT molecules form a stabilising monolayer around the nanoparticles and allow them to be transferred in the organic phase. The solution is mixed for 30 seconds and then left to allow the two phases to separate again to encourage phase transfer. No additional cleaning of the nanoparticle solution is needed as all by-products conveniently remain in the aqueous phase.

Table 3.1: Relationship between $HAuCl_4/NaBH_4$ ratio and size of the resulting gold nanoparticles.

$HAuCl_4$ 50mM [μL]	$NaBH_4$ 50 mM [μL]	Ratio	Nanoparticle diameter [nm]
100	300	1:3	3.5
100	400	1:4	4
100	500	1:5	4.5
100	600	1:6	5

Gold nanoparticles in solution have a strong, red colour due to a plasmon resonance effect and UV-Vis spectroscopy therefore provides a good tool for measuring nanoparticle sizes. Figure 3.11 a) shows absorption curves as a function of wavelength for nanoparticles of different sizes both for commercially obtained and self-prepared nanoparticles. The absorption of a nanoparticle solution peaks at around 525 nm, with the exact value depending on the size (smaller size = adsorption peak at smaller wavelength). In principle, we only know the size of the commercial nanoparticles, which hence can be used as calibration tools for the self produced nanoparticles. As shown in [101], the absorption at the position of plasmon resonance (A_{PR}) scaled by the absorption at 450 nm (A_{450}) correlates with the log of the diameter as shown in Figure 3.11 b). A linear fit through the commercial nanoparticles of known sizes (red squares) was performed (dashed black line), while the size of the size of the self-prepared nanoparticles (blue circles) could then be inferred from the fitting parameters.

3.3.2 Gold nanoparticle surface preparation

Several different approaches to deposit nanoparticles on flat surfaces can be found in the literature [99, 102, 103, 104, 105, 106, 107, 108, 109, 110]. Two of these techniques were used to prepare the nanoparticle surfaces used in the experiments presented in this thesis; spin-coating on APTMS functionalised surfaces (sub monolayer coverage) and drop-casting via the Eah method (monolayer coverage).

Sub-monolayer coverage

In order to create surfaces with a sub-monolayer coverage, a mix of spin-coating and dropcasting methods was employed and only commercial nanoparticles were used (BBI Solutions). These nanoparticles were prepared via the Turkevich method [111], are stabilised by citrate ions and come in the form of an aqueous solution. Firstly, any excess of citrate ions, which also acts as reducing agent during the nanoparticle synthesis, need to be removed by centrifuging the nanoparticle solution and re-dispersion of the nanoparticles in de-ionised water. To make sure all residual citrate ions are removed,

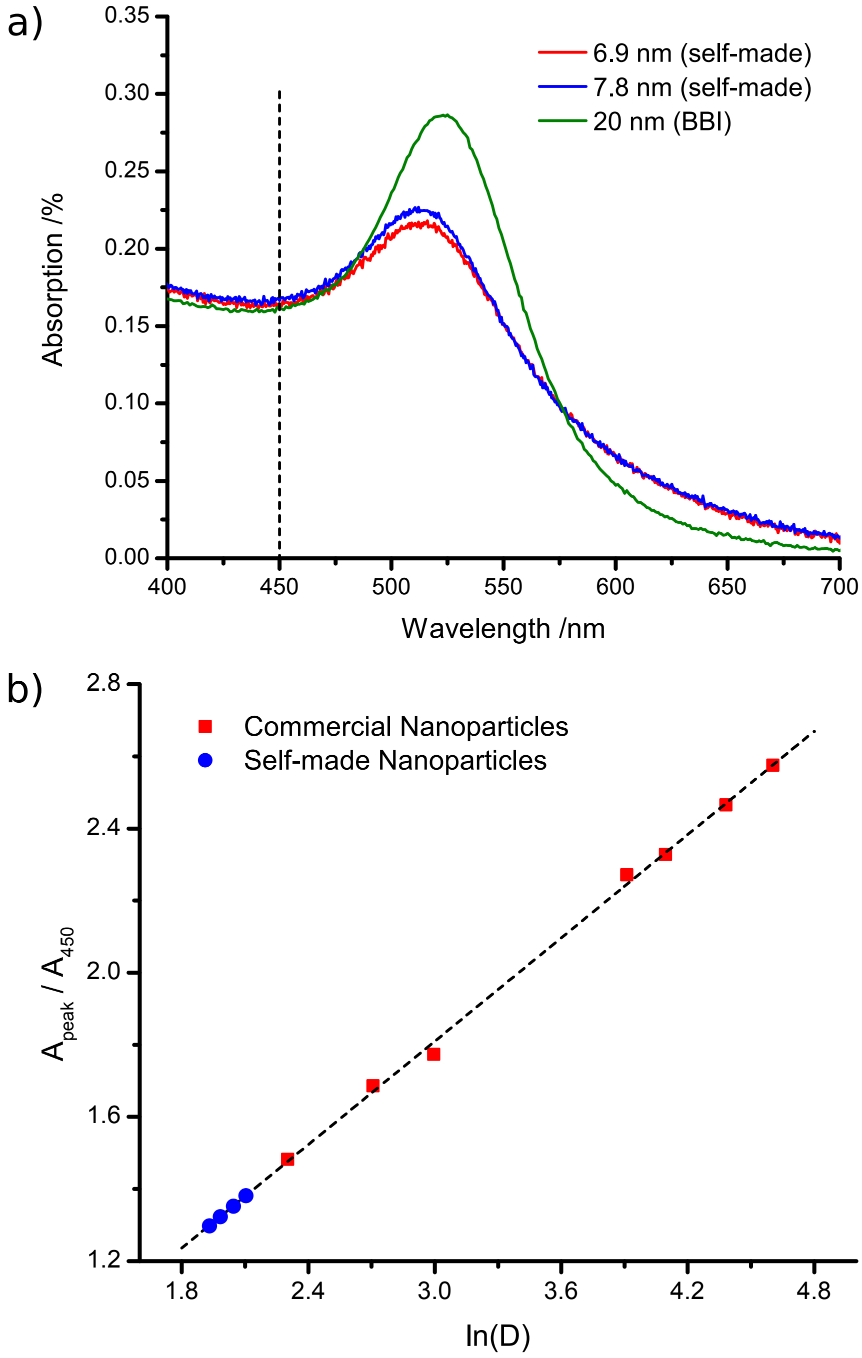

Figure 3.11: UV-Vis absorption of aqueous nanoparticle solutions. a) UV-Vis spectra for Au nanoparticles of different sizes. b) Absorption at the wavelength of the plasmon resonance (A_{PR}) over absorption at 450 nm (A_{450}) as a function of the natural logarithm of the nanoparticle diameter, $\ln(D)$, for self-prepared and commercial Au nanoparticles. The commercial nanoparticles were used as calibration via a linear fit (black dashed line).

Table 3.2: Parameters (g-force and time) for centrifuging gold nanoparticles. Reprinted with permission from Cytodiagnostics Inc. (www.Cytodiagnostics.com).

Size /nm	g-force	Time /min
15	17,000	30
20	4,500	30
45	2,000	30
60	1,125	30
80	600	30
100	400	30

the procedure is performed two times. Table 3.2 shows the centrifugal force and time needed to separate nanoparticles and solvent [**?**] .

Silicon wafers possess a non-polar surface and therefore can only be wetted by a non-polar solvent. As the citrate protected nanoparticles are only soluble in polar solvents, it is not possible to deposit them directly onto the silicon wafer. However, it was shown that this problem can be overcome by functionalising the surface of the silicon wafer with an organosilane polymer such as (3-aminopropyl)-trimethoxysilane (APTMS), essentially creating a polar surface for the nanoparticles to attach to [105, 106, 112]. A schematic of this modification of the surface is shown in Figure 3.12. Prior to functionalisation, the surface is cleaned by immersing it in concentrated nitric acid for about 30 minutes, then rinsed with water and acetone, UV-irradiated for 10 minutes, once again rinsed and finally dried in a nitrogen flow. The surface is then immersed in a solution of 2% APTMS in methanol for about 12 hours leading to the formation of an APTMS monolayer. Finally the surface is rinsed with water and methanol and subsequently dried in a nitrogen flow.

Nanoparticles can than be deposited on the surface either by spin-coating or by drop-casting. In the drop-casting technique, a small amount of the (aqueous) nanoparticle solution is put on the surface and left to evaporate, leaving behind the nanoparti-

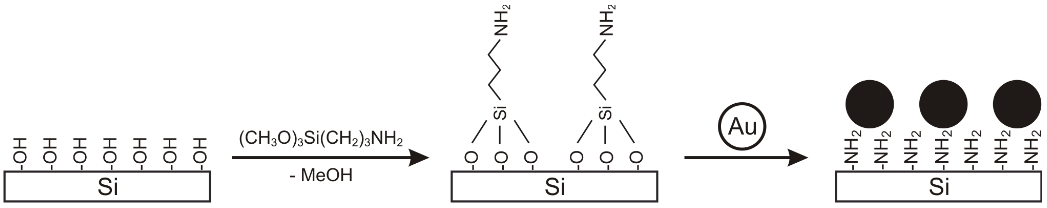

Figure 3.12: Schematic of the deposition of gold nanoparticles on an APTMS coated surface.

cles [109]. The density of nanoparticles on the surface can be tuned by controlling the concentration of nanoparticles in solution and by varying the amount of solution deposited on the surface. This way, it should, in theory, be possible to deposit a densely packed monolayer on the surface. However, it was impossible to repeat the experiments described in [109] and clustering of nanoparticles was observed at high nanoparticle densities.

Figure 3.13 presents AFM images of APTMS modified surfaces covered with nanoparticles of different sizes and particles density. As a general trend, it can be observed that the nanoparticle density decreases with an increase in nanoparticles size. This is due to the fact that the precursor solutions before formation of the nanoparticles always start with the same concentration of Au salt. In this way, the nanoparticle solutions always contain a similar amount of gold, either in the form of many small or fewer and bigger particles. Surfaces prepared via this method were used in the experiments presented in Section 5.2. The highest-achieved coverage of approximately 160 NP/μm was measured for a surface with nanoparticle with a diameter of 20 nm. Trying to further increase the nanoparticle density lead to the formation of nanoparticle clusters. Whether these observed agglomerations are caused by the commercial nanoparticles (all the experiments cited used ‘freshly prepared’ nanoparticles) or by other experimental limitations (such as nanoparticle size) is so far unknown.

Another possible method to deposit nanoparticles on a surface is the spin-coating

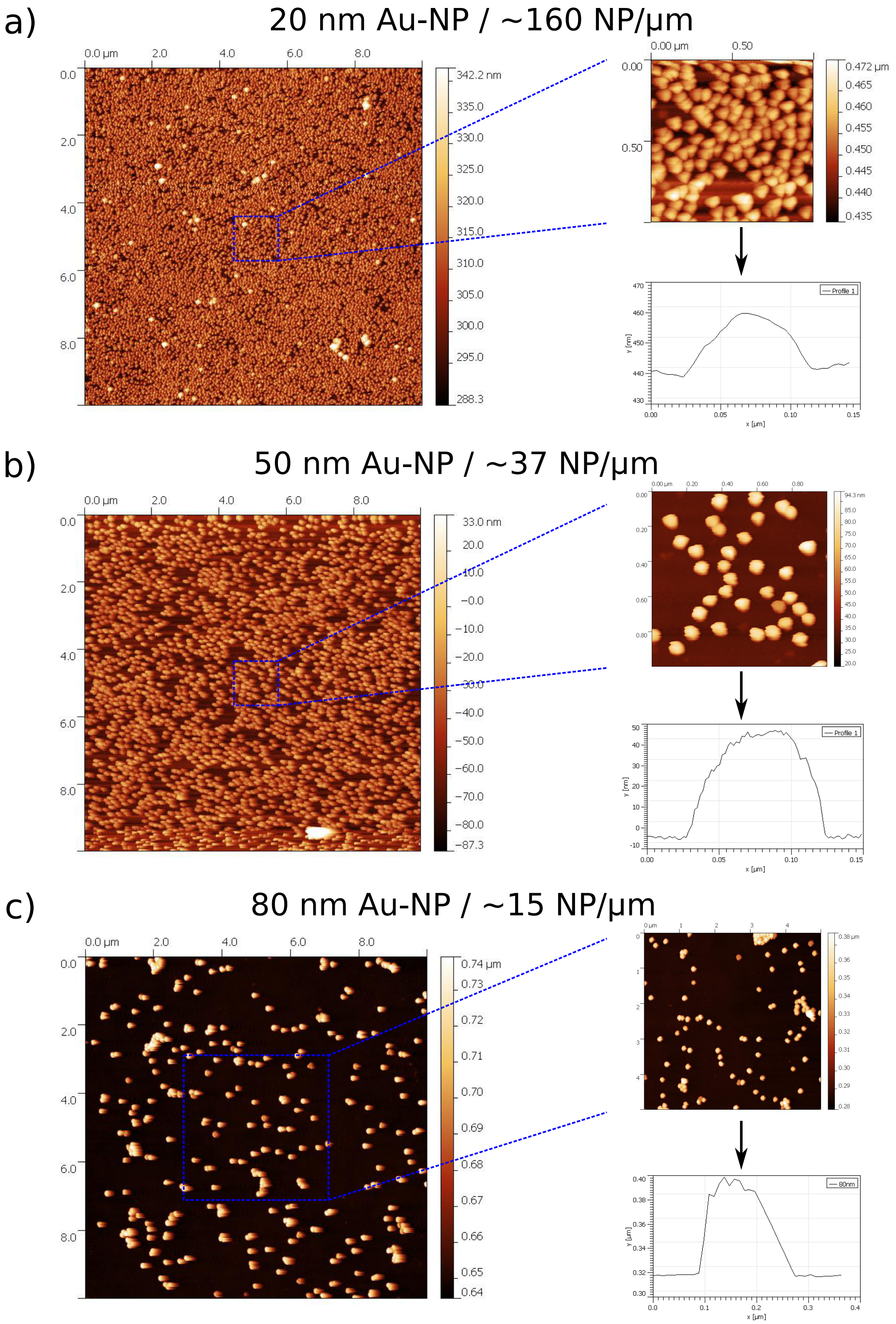

Figure 3.13: Atomic force microscopy images of nanoparticle covered surfaces. The surfaces were prepared by drop-casting of solution containing gold nanoparticles of different sizes on APTMS functionalised surfaces. Cross-sections across single nanoparticles are also shown, confirming the size of the nanoparticles.

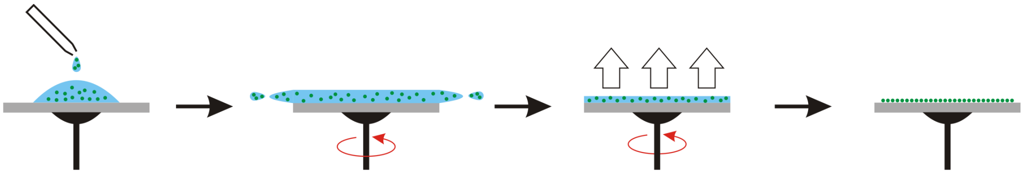

Figure 3.14: Mechanism of the spin-coating process. A droplet of the nanoparticle containing liquid is deposited on the surface. The surface starts spinning which leads to evaporation of the solvent, allowing the nanoparticles to be deposited on the surface.

technique [104, 113]. For this method the silicon wafers were again functionalised with APTMS. The spin-coating mechanism itself is depicted in Figure 3.14. A droplet of nanoparticle solution is deposited on the surface. The surface than starts spinning at a controlled velocity of approximately 500 rpm. The nanoparticle solution is spread out over the surface, forming a thin film (the thickness of the film depends on the chosen speed) while excess liquid is removed from the surface by centrifugal force. The remaining liquid evaporates during the spinning cycle leaving behind a layer of evenly distributed nanoparticles. However, it proved difficult to generate high densities of nanoparticles as large parts of the precursor solution is lost during the spinning-process.

It should be possible to increase the coverage by repeating spin-coating deposition cycles together with mobilising the nanoparticles on the surface [108]. Figure 3.15 a)-c) shows AFM images of the deposition of 50 nm nanoparticles via this method after one (a), three (b) and six deposition cycles (c), demonstrating that the nanoparticle density indeed increases from cycle to cycle (the surface was immersed in a 5 mM dodecanethiol solution for 24h in between spin-coating cycles). However, this method once again does not lead to the formation of a closed monolayer but the particle density on the surface seems to approach an upper limit as shown in Figure 3.15 d).

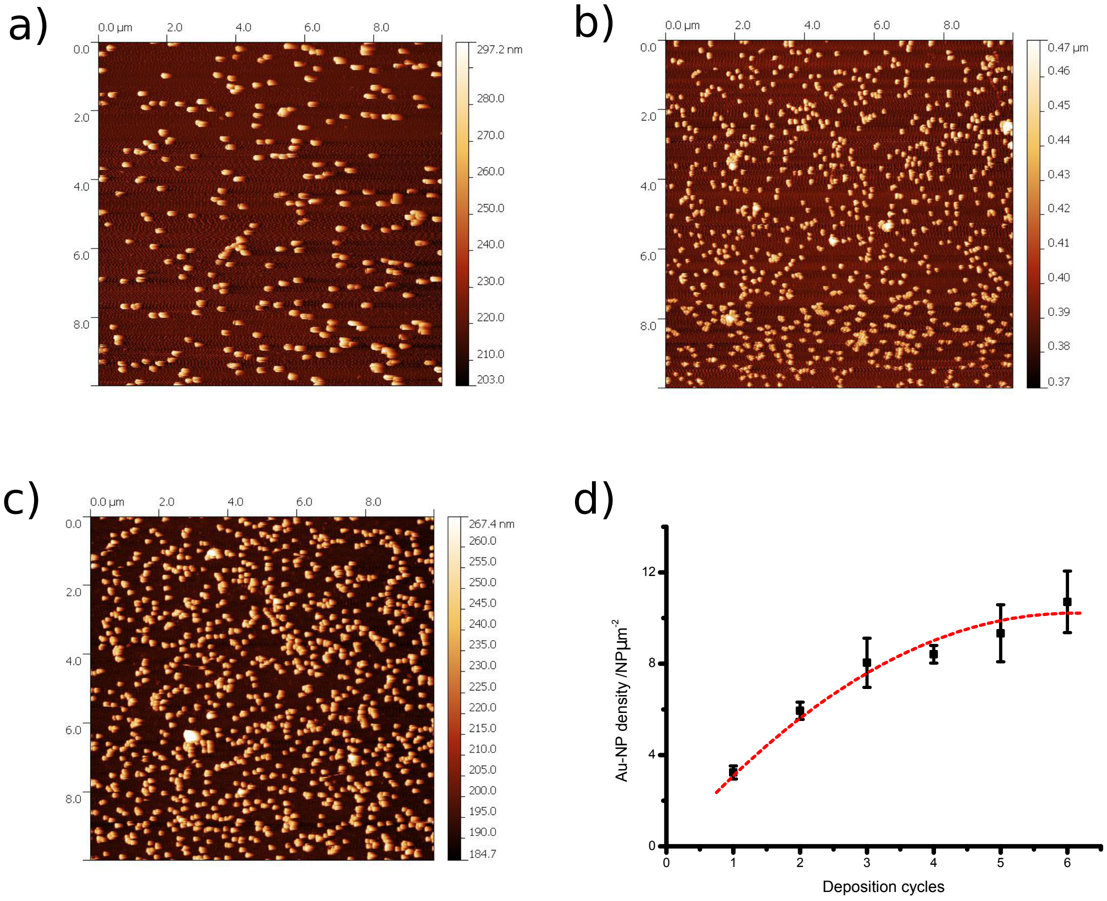

Figure 3.15: Deposition of 50 nm gold nanoparticles via repeated spin-coating. AFM images after one (a), three (b) and six (c) deposition cycles. In between cycles, the surface is immersed in a dodecanethiol solution for ∼ 24h. d) nanoparticle density as a function of deposition cycles.

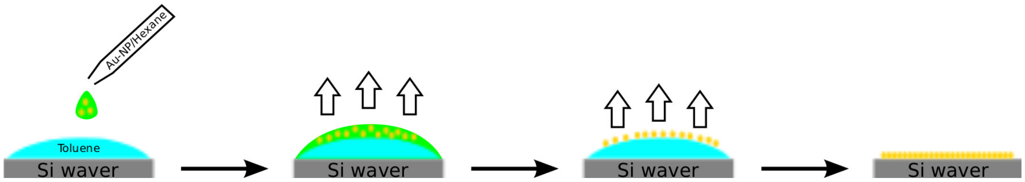

Figure 3.16: Schemtatic of the modified drop-casting method designed by Eah et al.: A droplet of a gold nanoparticle/hexane solution is deposited on top of a toluene film which in turn covers a substrate (e.g. Si wafer). The hexane quickly evaporates, leaving behind the nanoparticles which form a single layer on top of the toluene film. While the toluene slowly evaporates, the nanoparticles are deposited on the substrate.

Monolayer Coverage

This section presents a method to produce surfaces covered by gold nanoparticle forming a closed monolayer and is explained in detail in the work of Eah et al. [99, 102]. For this procedure, nanoparticles produced via the method described in the previous section are used (hexane as a solvent). The mechanism of the method is shown in Figure 3.16. First, the silicon wafer on which a monolayer is to be deposited is cleaned as described in the previous section using both strong acids and UV radiation to destroy organic molecules present on the surface and is subsequently rinsed with deionized water, acetone and hexane. A few drops of toluene are deposited on the wafer such that the whole surface is well covered. On top of that $\sim$ 100 - 200 µL of the hexane solution containing the nanoparticle solution is deposited (the exact amount depends on surface size and nanoparticle concentration). Hexane evaporates $\sim$ 4x quicker than the toluene and as the nanoparticles are insoluble in toluene, they are left floating on the surface of the droplet. Subsequently, the toluene slowly evaporates leaving behind the nanoparticles as a densely packed monolayer on the Si wafer.

Figure 3.17 a) and b) presents an AFM image of a surfaces prepared via this method at different magnifications. These images show an almost flat surface which only occasionally possesses small holes, thus confirming that it is possible to reliably reproduce the results published by Eah et al. [102]. Image c) shows a cross section along the line labelled as '1' further demonstrating the flatness of the surface. The profile also demonstrates that the holes on the surface are small defects where only one or two nanoparticles appear to be missing. For the experiments presented in Section 5.1 surfaces produced by the Eah group themselves (via this method) were used. However, the self-produced surfaces here will be used in future experiments.

3.3.3 Gold surface preparation (bulk-metal)

The gold bulk-metal surface was prepared using an in-house surface facility. Gold (99.99%, Alfa Aesar) was deposited on a 1 inch polished Si-wafer (Compart Technology Ltd) using metal-vapour deposition at a growth rate of approximately 1 nm/s. In order to improve adhesion of gold to the wafer a 5 nm thick layer of chromium was deposited beforehand. The resulting gold layer has a thickness of $\sim$ 200 nm and exhibits a mean roughness less than 1 nm as was shown by AFM [48].

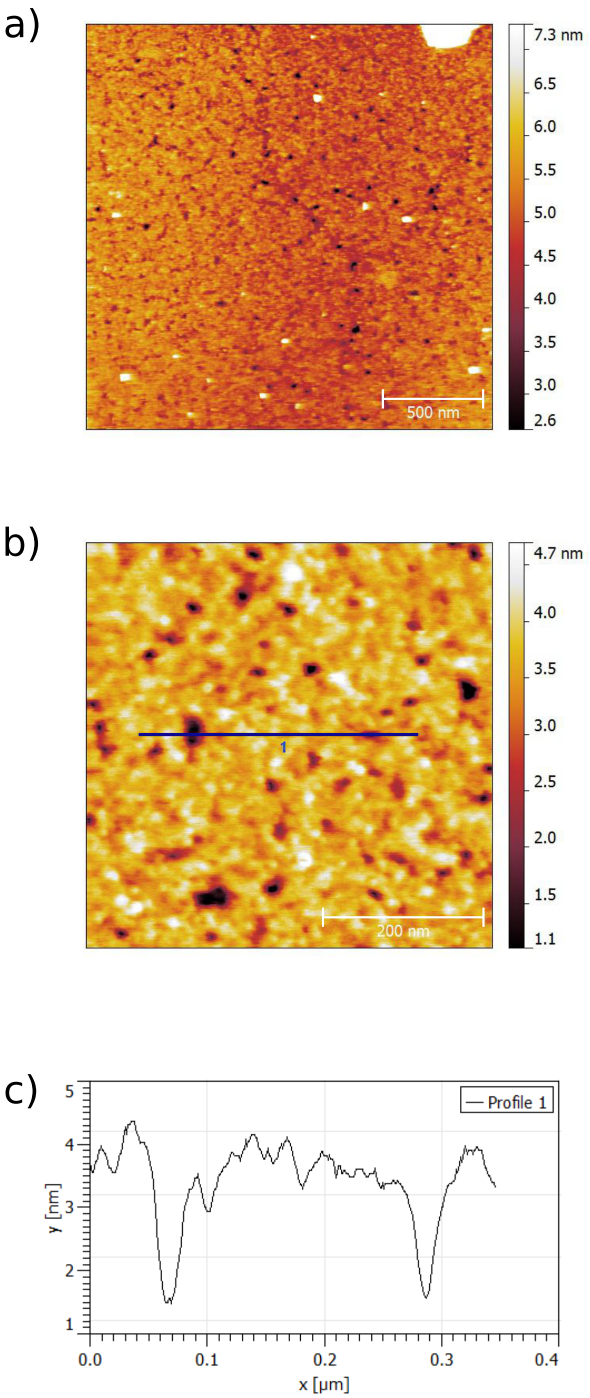

Figure 3.17: Si wafer covered by a 5 nm gold nanoparticle monolayer produced via the method originaly devised by Eah et al. in [102]. a) and b) AFM images of different magnification, demonstrating the flatness of the surface. c) cross section along the line labelled as '1' in b).

Chapter 4

Experimental study of the H-atom gold surface interaction

As mentioned in section 1.7, the interaction of atomic hydrogen Rydberg states with a gold surface has recently been studied by So et al. [37, 52]. In the last chapter the deficiencies of the experimental setup used to obtain these results were explained and modifications which were made in order to overcome these experimental restrictions were introduced. This chapter deals with the experimental results obtained with this modified setup and compares them to theoretical models as well as the earlier results.

4.1 Rydberg state dimension

Figure 4.1 shows the surface ionisation profiles for the most red-shifted Stark states ($k = -(n-1)$, $m_l = 0$) for selected Rydberg states in the range $n = 25 - 35$ as a function of applied ion extraction field. The peak heights are normalised to the field ionisation peak, integrated when positioned right at the beginning of the surface ionisation gate of the time of flight profile (see Section 3.2.2). This gives a reasonable measure of the number of Rydberg atoms that reach the surface. Error

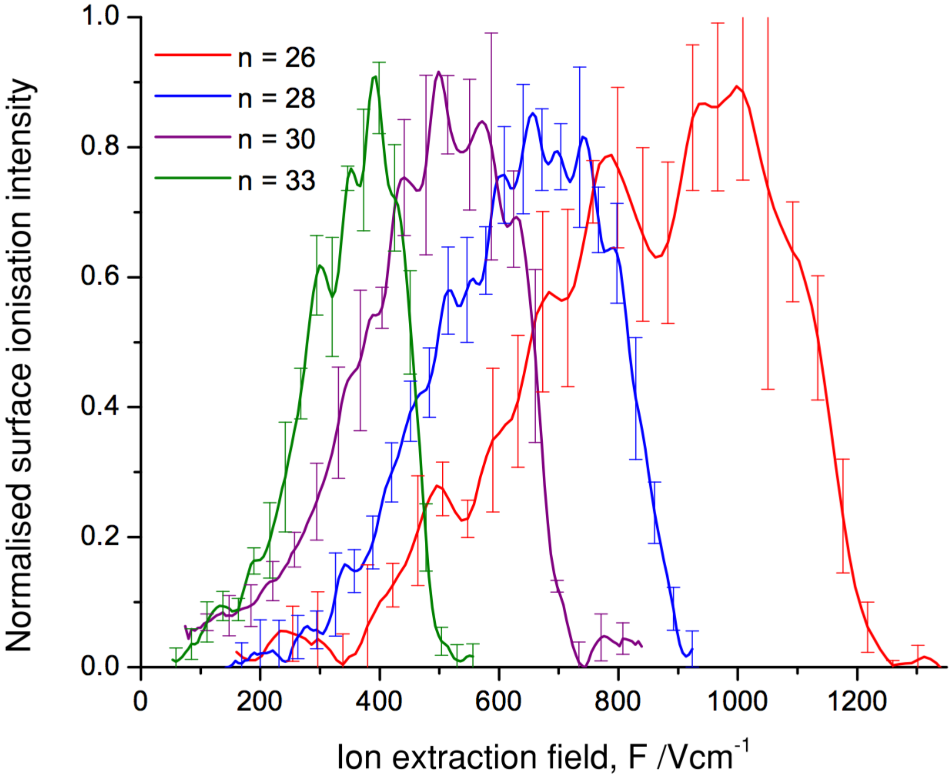

Figure 4.1: Surface ionisation signal as a function of applied electric field for the most red-shifted Stark states of Rydberg states with the principal quantum numbers $n = 26, 28, 30, 33$. The collisional velocities of the incident Rydberg states is $v_\perp \approx$ 650 $\mathrm{m\,s^{-1}}$, the velocity of an un-seeded beam of H-atoms with an incident angle of 15°, excited 180 µs after the photodissociation of NH_3 (see chapter 3 for details).

bars associated with the data points are also shown and for simplicity, the number of error bars is reduced to 25 per trace. The surface ionisation signal gradually increases with the increase of electric field, as closer distances to the surface are probed. The cut-off at high fields represents the electric field at which a given Rydberg state is field ionised, for which the ions are detected in a different channel. With increasing principal quantum number, the onset of the surface ionisation profiles gradually moves to lower field, which indicates that ionisation occurs at greater distances from the surface as is expected from past experiments and theoretical data.

As mentioned at the beginning of this chapter, the same experiments (without using ion-optics) have been performed before but with a question about the variability of ion detection efficiency with field [52]. Ion-trajectory simulations (Simion08) have shown that the introduction of ion-optics increases the ion-detection probability and is expected to improve the consistency of detection probability with applied field (see section 3.1.4). Figure 4.2 shows normalised selected surface ionisation profiles for the most red-shifted Stark states for Rydberg states in the range $n = 26-33$ as a function of applied electric field. The collisional velocities for both sets of data were set to $v_\perp = 656\ \mathrm{m\,s^{-1}}$. Results recorded with both the modified (full red lines) and the old experimental setup (blue, dashed lines) are shown. Both sets of data are normalised to unity, rather than being plotted as the fraction of ions detected, to make the different results more comparable. For the case of the modified setup the rate at which the signal increases with electric field is roughly similar to the increase observed with the old setup. However, the detection efficiency at lower fields is noticeably higher, making it appear as if the whole profile is shifted towards lower fields. The high field cut-off of the profile is mostly unchanged although it is not as clearly defined for the modified setup. Another important difference lies in the maximum of surface ionisation signal. For the old experimental setup, the detected signal continuously increases together with the electric field until field ionisation of the Stark state occurs. The results acquired with the modified setup on the other side, show a saturation effect of the signal before the high field cut-off, indicating that the maximum detection probability is achieved.

It has been shown before that a semi-empirical modification of the classical over-the-barrier ionisation model can be used to simulate the experimental surface ionisation profiles with a high degree of precision (see section 2.3.1). This model uses a set of parameters (shift of ionisation distance $\mu(F)$, ionisation width σ) which can be adjusted to make the simulated curve fit experimental results. Both parameters are dependent on the principal quantum number n and for previous results the best fit was

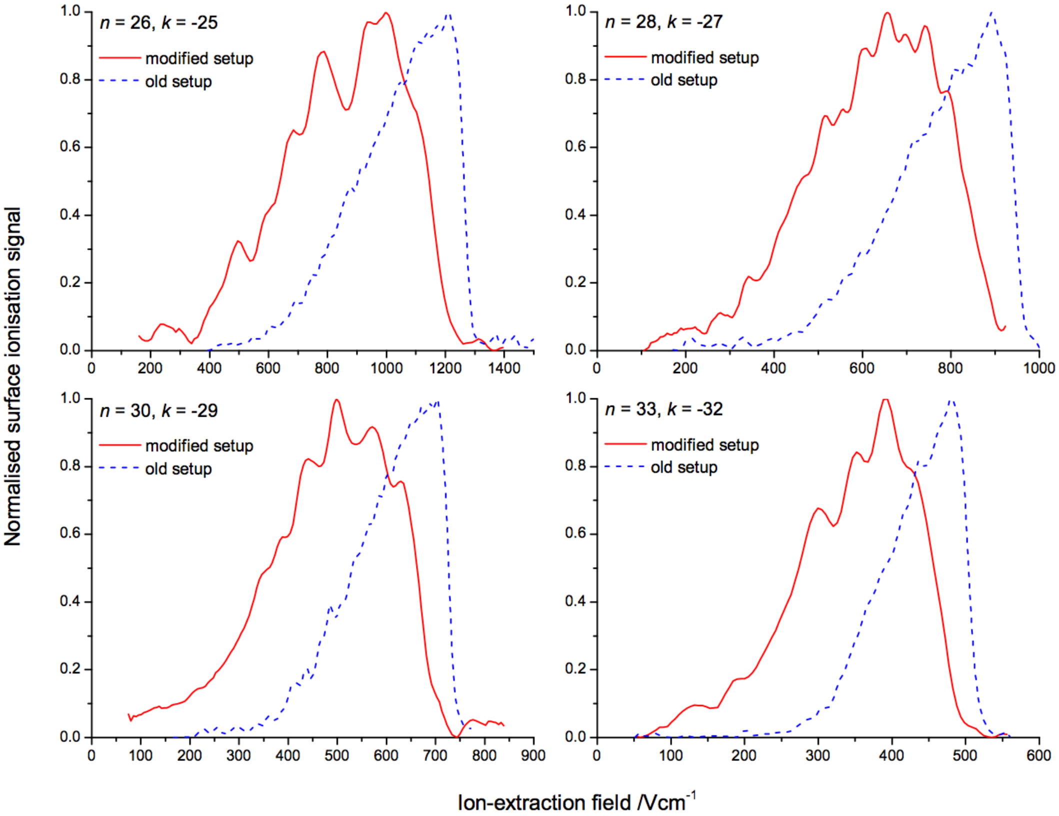

Figure 4.2: Comparison of surface ionisation profiles of the most red-shifted Stark states ($k = -(n-1)$) of the $n = 26, 28, 30, 33$ manifolds. Surface ionsiation profiles measured with the modified experimental setup are shown as full red lines, surface ionisation profiles recorded with the old setup as dashed blue lines. For both sets of data, the collisional velocity is $v_\perp = 656\ \mathrm{m\,s^{-1}}$ and the incident angle is 15°.

achieved by shifting the classical OTB ionisation distance $\mu(F)$ towards the surface such that $\mu(F) = D_{\mathrm{OTB}} - 1n^2$ and assuming a width of ionisation of $\sigma = 2.5n^2\mathrm{a}_0$. However, looking at Figure 4.2, it can be expected that those parameters will have to be adjusted in order to fit experimental results obtained with the new experimental setup.

Figure 4.3 shows the same surface ionisation profiles as displayed in Figure 4.1 but the individual traces are normalised to one, assuming a detection efficiency of 100% (full lines). As expected, a variation of the semi-empirical parameters is necessary to obtain a decent fit of experimental results (dashed lines). Overall, the fitting parameters can be 'reduced' to an ionisation spread of $\sigma = 1.75n^2\mathrm{a}_0$ and a shift of ionisation distance of $-0.5n^2$. As a comparison, the fit obtained by using the semi-empirical parameters from previous experiments is also shown (dotted lines).

Another possible way to simulate the experimental surface ionisation profile has been presented in Section 2.3.3. While including the surface patch fields in Monte-Carlo type trajectory simulations did not result in good agreement with earlier experiments [37], it is worth revisiting this modelling approach. Figure 4.4 therefore shows the same set of surface ionisation profiles as a function of electric field as presented in Figure 4.2 together with simulated surface ionisation profiles. In order to emphasise the interesting part of the spectrum and make different principal quantum numbers n comparable, the surface ionisation profiles are plotted against an ion extraction field which is scaled by $n^{-4}\mathrm{a}_0$ (see section 2.1 for a detailed explanation of the scaling behaviour). Overall there appears to be good agreement of experimental results and the theoretical model. Of the results presented here, only the highest principal quantum number ($n = 33$) shows some deviation of experimental and theoretical results, it appears as if the profile appears is shifted to slightly higher fields. As mentioned in Section 2.3.3, the patch fields 'used' for the calculations in this thesis were recon-

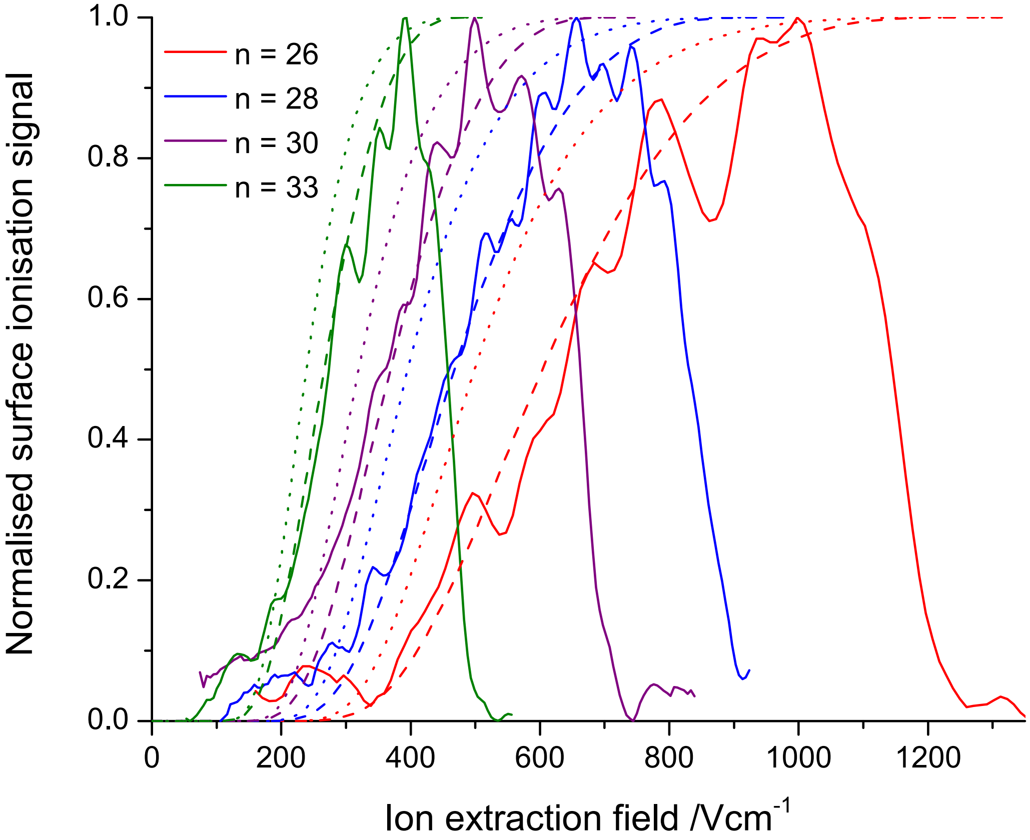

Figure 4.3: Surface ionisation signal as a function of applied electric field for the most red-shifted Stark states of Rydberg states with the principal quantum numbers $n = 26, 28, 30, 33$ an incident angle of 15° and a collisional velocity of $\sim$ 690 m s^{-1} (full lines). The experimental results are fitted using the empirical OTB model as described in Section 2.3.1 using a spread of ionisation distance of $1.75n^2\mathrm{a}_0$ and a shift of the OTB ionisation distance of $\mu(F) = D_{\mathrm{OTB}} - 0.5n^2$ (dashed lines). For comparison, fits obtained with parameters from earlier work by So et al. are also shown (dotted lines) [52].

structed using the surface potentials extracted from data published by Pu et al. [47] and these fields showed some deviation to the original data at large distances. It is therefore feasible to assume that for the case of high principal quantum number the effect of the stray fields on the surface ionisation process of Rydberg states might be underestimated for the results shown here, resulting in the observed discrepancies.

The results presented in this section demonstrate that at least part of the spread and shift of ionisation distance with respect to the OTB model observed by So et al. [37] can be explained by limitations of the previously used experimental setup. The modifications introduced in the present work therefore provide a way to better capture the surface ionisation process of the H-atom Rydberg states. Using surface patch fields to explain the spread in ionisation distance and width furthermore demonstrates the possibility to use Rydberg states as a probe of surface properties.

4.2 Stark polarisation

Varying the principal quantum number is not the only way to tune the surface ionisation distance. As explained in Section 2.2.1 it is possible to control the polarisation of the Rydberg electron wavefunction by exciting the Rydberg state in the presence of an electric field. This sections aims to demonstrate the effect of electron polarisation on the surface ionisation by exciting different Stark states of a given n-manifold and investigating the resulting surface ionisation profiles.

Figure 4.5 shows the Stark spectrum of the $n = 29$, $m_l = 0$ manifold at a Stark field of 76 $\mathrm{V\,cm^{-1}}$. The Stark states studied in this section are marked by vertical full red lines ($k = -28$, 0, +16). It should be noted that the achieved resolution is considerably better in the middle of the spectrum. This is due to two effects. For one, the polarisation of the two excitation lasers is not perfectly aligned with the electric

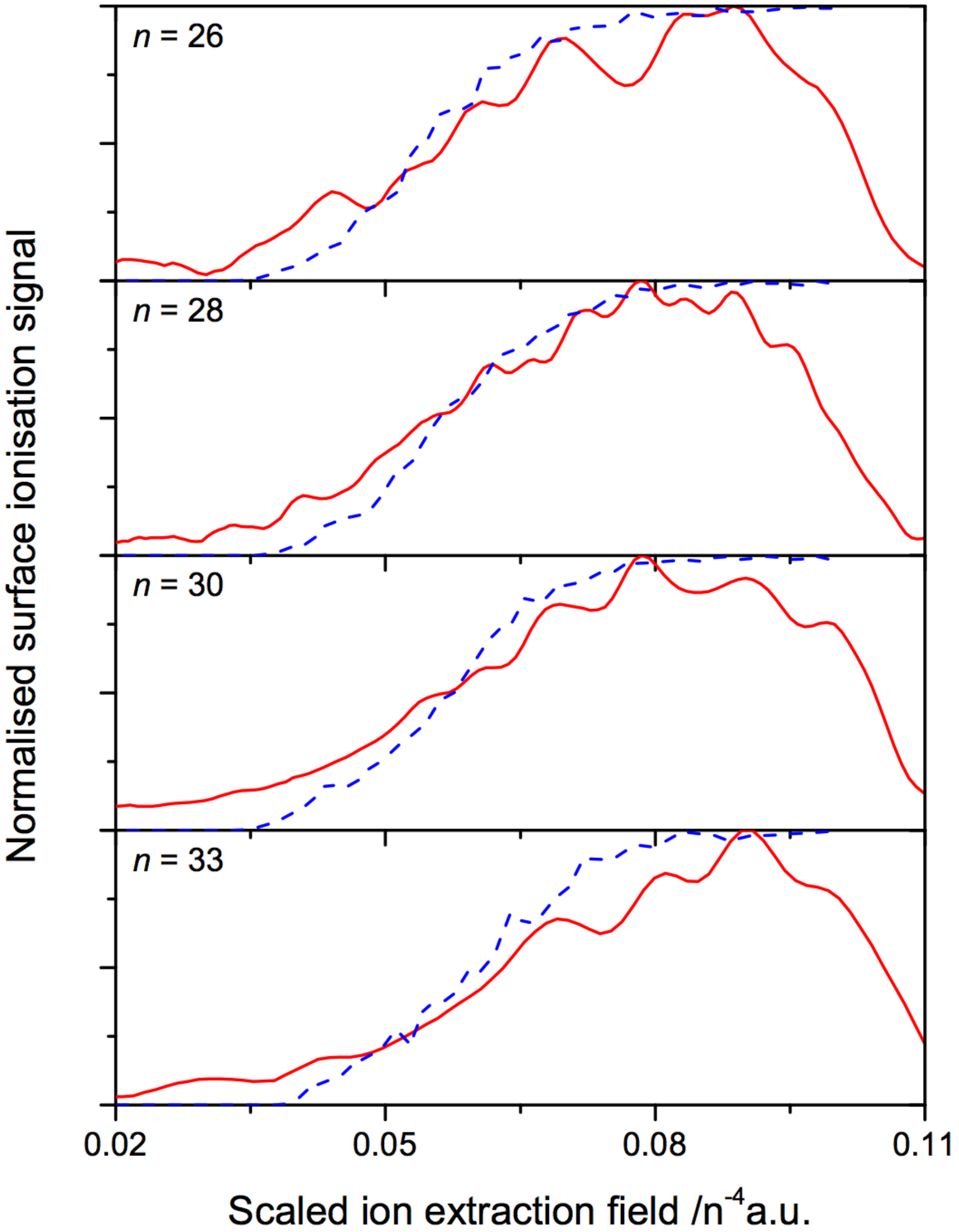

Figure 4.4: Surface ionisation signal as a function of applied electric field for the most-red shifted Stark states of Rydberg states with the principal quantum numbers $n = 26, 28, 30, 33$ with an incident angle of 15° and a collisional velocity of $\sim 690\ \mathrm{m\,s^{-1}}$ (full red lines). The electric field is scaled by n^{-4} to make different profiles comparable. The blue dotted lines are obtained by Monte-Carlo trajectory simulations taking into account the effect of surface patch charges as explained in Section 2.3.3. Overall, good agreement between experimental and simulated results can be observed.

field, resulting in the excitation of $m_l = 1$ states in addition to $m_l = 0, 2$ states. Also, the mid-manifold states do not vary as much in energy with electric field and are thus less susceptible to field inhomogeneities, which lead to line broadening for the extreme red- and blue-shifted states. The corresponding surface ionisation profiles of the three highlighted states are shown in Figure 4.6. The peak heights are normalised to the integrated field ionisation signal measured at the beginning of the surface signal gate. With increasing parabolic quantum number k, the onset of the surface ionisation signal gradually shifts to higher fields, as has been observed in earlier experiments. This can be seen as an indication that the electron wavefunction becomes increasingly polarised towards the vacuum as k increases and is in good agreement with theoretical predictions as discussed in section 2.2.1.

On moving from red- to more blue-shifted states, the maximum surface ionisation signal decreases. Theory predicts that it should be impossible to detect the most blue shifted Stark states of the Rydberg-state manifolds investigated here as the field needed to detect ions resulting from surface ionisation is higher than the field needed to directly field-ionise the state. Indeed it was not possible to detect the $k = -28$ surface ionisation for the $n = 29$ manifold shown here and the same is true for the extreme red-shifted states of other principal quantum numbers (not shown here). This finding is in good agreement with previous experimental results where it was only possible to detect a weak surface ionisation signal for the most blue-shifted states of principal quantum numbers lower than the ones investigated in this thesis [37].

It is possible to use Equation 1.29 together with the detected surface ionisation profiles to estimate the distance from the surface (or range of distances) for which ionisation occurs for a given state. Figure 4.7 shows relative surface ionisation profiles (normalised to the integrated field ionisation signal) of the $k = -28$ and $k = +10$ Stark states of the $n = 29$, $m_l = 0, 2$ manifold. The x-axis has been converted to an esti-

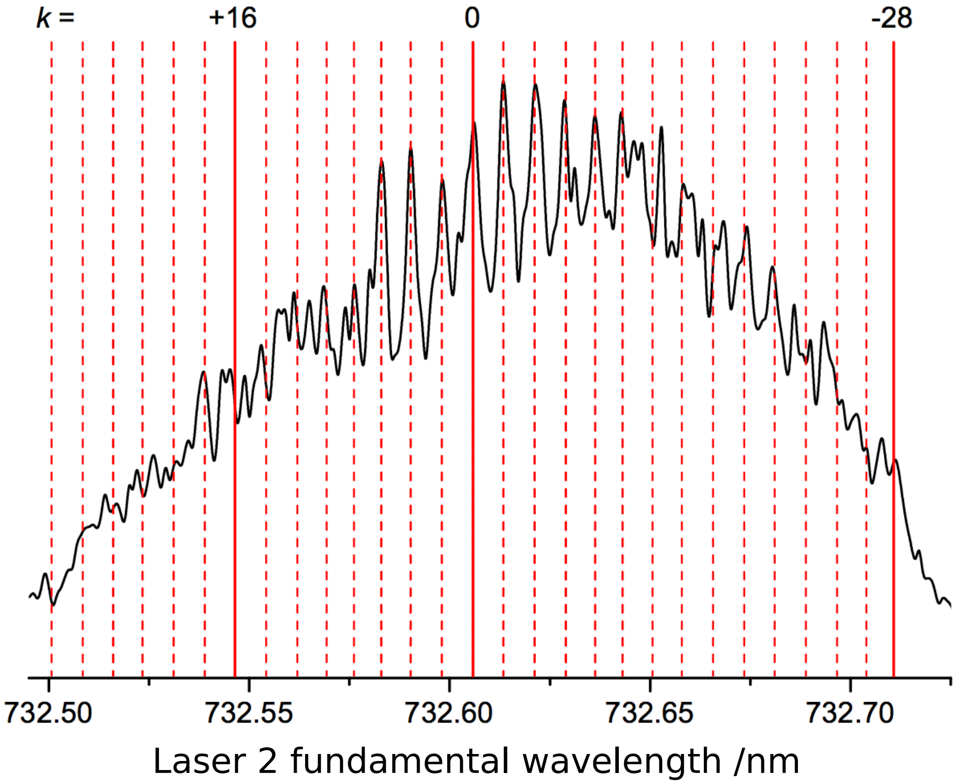

Figure 4.5: Field ionisation spectrum of the $n = 28$ Stark states as a function of the fundamental wavelength of laser 2 (see Section 3). The applied Stark field is 76 V cm^{-1}. Due to the choice of laser polarisation, mainly the $m_l = 0, \pm 2$ are populated. The vertical red dashed lines show the calculated Stark splitting using Equation 1.15. The Stark states investigated in this section ($k = -28$, 0, +16) are shown as full red lines.

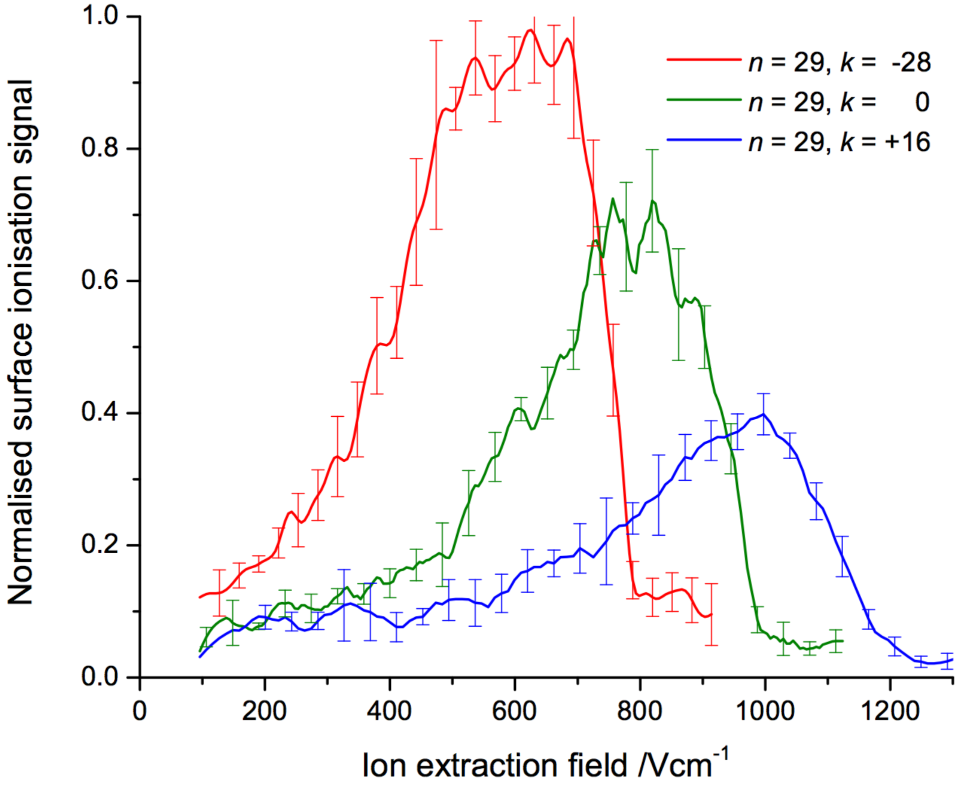

Figure 4.6: Normalised integrated surface ionisation signal of the $k = -28, 0, +16$ Stark states of the $n = 29$ manifold as a function of applied electric field. The collisional velocity is chosen as $v_\perp = 690\ \mathrm{m\,s^{-1}}$. As expected, red shifted states are detected further away from the surface and possess a higher detection efficiency compared to blue shifted states.

mated minimum detected ionisation distance in atomic units and is scaled by the size of the Rydberg state, n^2. It becomes evident, that the surface ionisation of the most red-shifted states can be detected over a fairly wide range of ionisation distances, far away from the surface, while the blue-shifted, $k = +16$ state ionises at a significantly shorter distance. To get a better feel for the exact detectable ionisation distances, it is possible to extract ionisation rates from the detected surface ionisation profiles. This can be done by fitting the experimental data via a sigmoidal function and subsequently multiplying this function with respect to the distance. Dividing the result by the collisional velocity results in an ionisation rate as is shown in Figure 4.7, underneath the surface ionisation profiles. From this it becomes evident, that the most red-shifted states ionise over a fairly wide range of distances of approximately $(2.5 - 4.0)n^2\mathrm{a}_0$, in good agreement with previous results . The blue-shifted, k = +16 state ionises most rapidly at a significantly shorter distance from the surface ($(1.5 - 2.2)n^2\mathrm{a}_0$), again as anticipated.

4.3 Conclusions

The results presented in this chapter cover the interaction of Rydberg states with a bulk-metal gold surface. This was done by exciting H-atoms in the presence of an electric field with different polarisation of their electron wavefunctions with respect to the surface. Subsequently, charge transfer between the Rydberg state and the surface occurs and the resulting ions are extracted via an electric field. The ions are detected via a MCP – phosphor screen – PMT position sensitive detection setup and are analysed in the form of surface ionisation profiles. Experiments were performed using a modified detection setup compared to the results presented by So et al. [37], allowing for a higher detection efficiency and thus a more complete picture of the surface ionisation process.

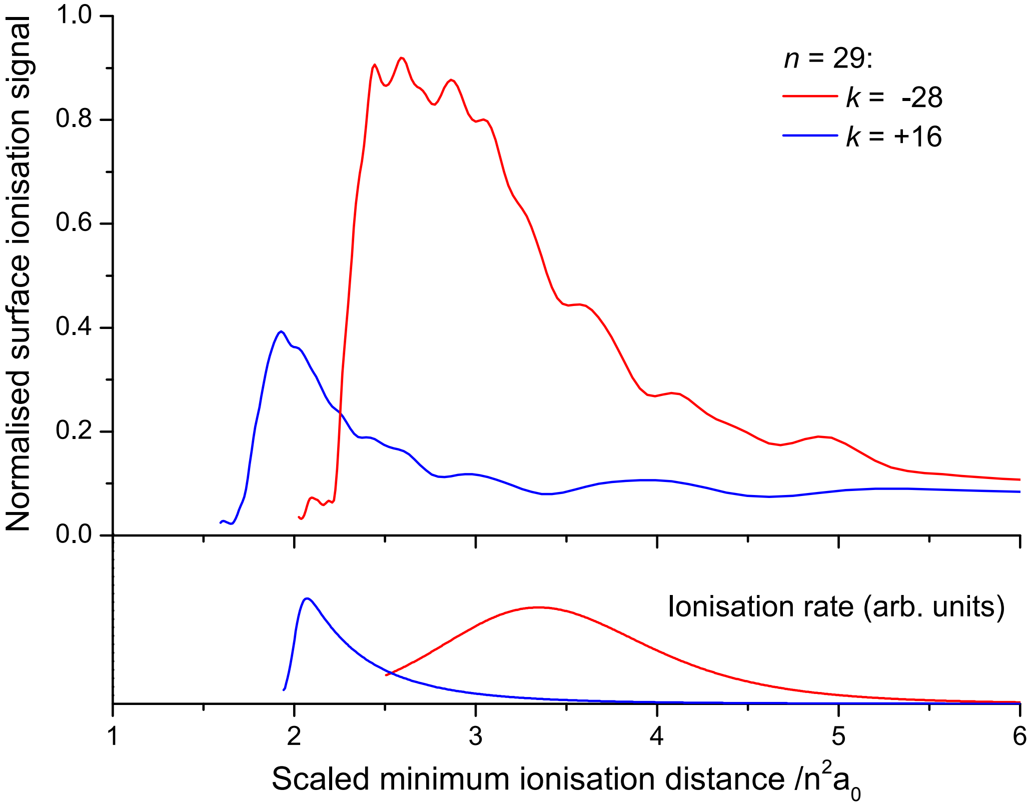

Figure 4.7: Top: relative surface ionisation signal of the $k = -28$ and $+16$, Stark states of the $n = 29$ manifold as a function of a scaled minimum ionisation distance, calculated by Equation 1.29. It is assumed that the Rydberg states approach the surface with an impact angle of 15° and a velocity of $v = 2666\ \mathrm{m\,s^{-1}}$ resulting in a collisional velocity of $v_\perp = 690\ \mathrm{m\,s^{-1}}$. Bottom: ionisation rate derived from the surface ionisation signal for both the blue- and the red-shifted Stark states as explained in the text.

First, the effect of the size of the Rydberg state on the surface ionisation process was investigated by studying the surface ionisation dynamics for the most red-shifted Stark states for a range of principal quantum numbers. The observed ionisation profiles show the expected behaviour: an increase in principal quantum number leads to an increase in ionisation distance, confirming the expectation that the ionisation distance roughly scales with n^4. Compared to previous results obtained with the same setup before its modification, the detection efficiency as a function of electric field has increased, almost reaching one just before the field ionisation cut-off. This saturation of the signal indicates that all detectable ions do indeed reach the detector as is predicted by theory.

The effect of polarisation of the electron wavefunction with respect to the surface was also investigated. Therefore, surface ionisation profiles of the different Stark states of a given principal quantum number manifold were recorded. The profiles show distinct different behaviour in that the ionisation of the most red-shifted state appears at the lowest ion extraction field and possesses the highest detection efficiency. With increasing parabolic quantum number, the surface ionisation profiles shift to higher applied electric fields and the detection efficiency decreases. These results confirmed previous experiments, demonstrating that there is no adiabatic population transfer between neighbouring Stark manifolds and that the ionisation distance increases together with the parabolic quantum number. Ionisation distances range from approximately $3.5\,n^2\,\mathrm{a}_0$ for the most red-shifted state to $<\ 2\,n^2\,\mathrm{a}_0$ for blue-shifted states.

Two different classical methods are employed with the aim to simulate the obtained surface ionisation profiles, the empirical over-the-barrier model first presented by So et al. [37] and Monte-Carlo trajectory simulation including the effects of stray fields based on the work of Pu et al. [47]. The empirical model can be tuned to give good agreement with the experimental results but the parameters needed to achieve this high quality fit are different from the ones needed in previous experiments. Monte-Carlo trajectory simulations incorporating the effects of stray-fields due to patch-charges on the surface have been used before to model the interaction of atomic hydrogen Rydberg states with gold metal surfaces. The results obtained with the modified experimental setup show a very good fit of the experimental results, thus demonstrating the possibility to use Rydberg states as a probe for surface fields.

Chapter 5

Charge transfer at Au nanoparticle surfaces

Nanoparticles represent an interesting target to further investigate the charge transfer of Rydberg states. They can be produced from a range of materials (e.g. metals, semiconductors, composite materials ...) and can be almost freely scaled in size. In addition, some nanoparticles are known to possess a metal to insulator transition, usually depending on the size of the particle [114, 115]. For gold nanoparticles, this transition occurs at around 1.5 nm (Au_{55} cluster) though larger particles of around 5 nm still show distinct differences in their electronic structure compared to bulk metal [116]. It might therefore be of interest to investigate, whether such a transition can be observed in a typical Rydberg charge transfer experiment. A similar metal to insulator transition can be observed for deposited nanoparticles which are in contact with each other. Here the resistance across the nanoparticle cluster depends on the distance between different particles, a parameter that can be tuned by varying the length of the capping molecules used in the synthesis process [117]. Furthermore, high n Rydberg states may easily posses diameters on a micron or sub-micron scale. It might therefore be of interest to investigate the effect of changing the size of a nanoparticle. How would the charge-transfer process change if the nanoparticles are either smaller or bigger than the Rydberg state orbital radius? Or is it possible to observe the aforementioned transition from metal to insulator by analysing charge transfer behaviour?

In this chapter experiments are presented, which investigate the charge transfer between Rydberg states of atomic hydrogen and gold nanoparticles of different sizes deposited on a surface. The aim of these experiments was to gain a general understanding of the ionisation behaviour of the Rydberg atoms near a monolayer nanoparticle surface as well to investigate the effect of the relative size of the nanoparticle (with respect to the size of the Rydberg orbital) on the ionisation process. Gold nanoparticles of different sizes were therefore deposited on silicon wafers following procedures explained in Section 3.3. Surfaces with a sub-monolayer coverage were produced in house via a range of different methods while surface with a monolayer coverage were produced by the group of Sangh-Kee Eah at Rensselaer Polytechnic Institute (NY, USA).

5.1 Charge transfer at a Au monolayer surface

The experiments presented in this section were all performed with 5 nm nanoparticles deposited on a round 1 inch SiO_2 wafer. Figure 5.1 a) shows an atomic force microscopy (AFM) image of such a surface produced by the Eah group. It can be seen that the surface is almost entirely covered by nanoparticles without showing signs of agglomeration, though ‘holes’ in surface are occasionally visible. A cross-section measured along the line labelled as ‘1’ is presented in Figure 5.1 b). This further demonstrates that the surface is flat with differences in height < 0.5 nm and shows that the holes correspond to approximately a single nanoparticle. It should be noted that this picture does not show the surface used for the experiments presented here but rather one produced in parallel to the investigated surface. This is due to the

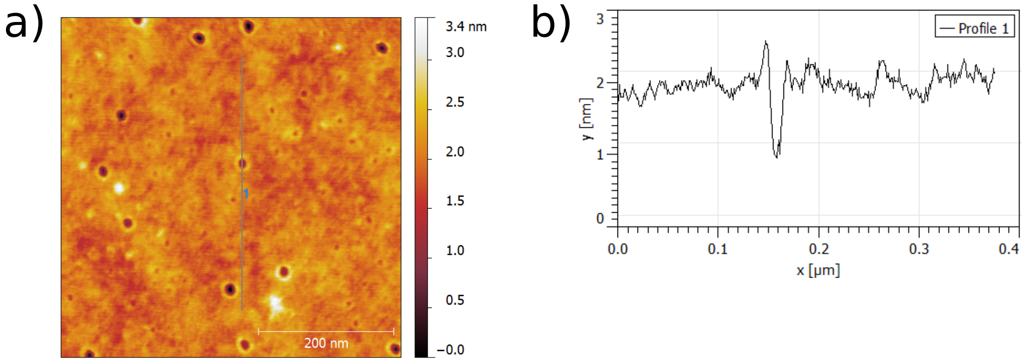

Figure 5.1: a) atomic force microscopy image of a monolayer gold nanoparticle surface prepared analogously to the surface used in the experiments described in this chapter. b) cross-section along the line labeled as 1 in a), showing that the surface is indeed almost completely covered by a monolayer.

destructive nature of the available departmental AFM setup.

5.1.1 Rydberg state dimension

Figure 5.2 shows the normalised surface ionisation signal as a function of applied electric field for the most red-shifted Stark states ($k = -(n-1)$) for a range of principal quantum numbers ($n = 24 - 34$). The Rydberg states approach the Au monolayer surface with a collisional velocity of 430 $m\,s^{-1}$. In general, the detected surface ionisation profiles show the same trends as observed with a bulk Au surface. The high field cut-off appears at the predicted electric fields (see Equation 1.20) and with increasing principal quantum number (and thus orbital radius) the onset of the signal shifts to lower fields. However, the profiles do show some distinct differences from those obtained with a bulk Au surface. Overall, the onset of the surface ionisation signal appears at lower than expected fields, rises quickly afterwards and saturates at fields considerably below the field ionisation limit.

In order to gain a better understanding how exactly surface ionisation profiles measured with a nanoparticle surface differ from those measured with a bulk gold surface, the two systems are shown together in Figure 5.3. This plot again shows the nor-

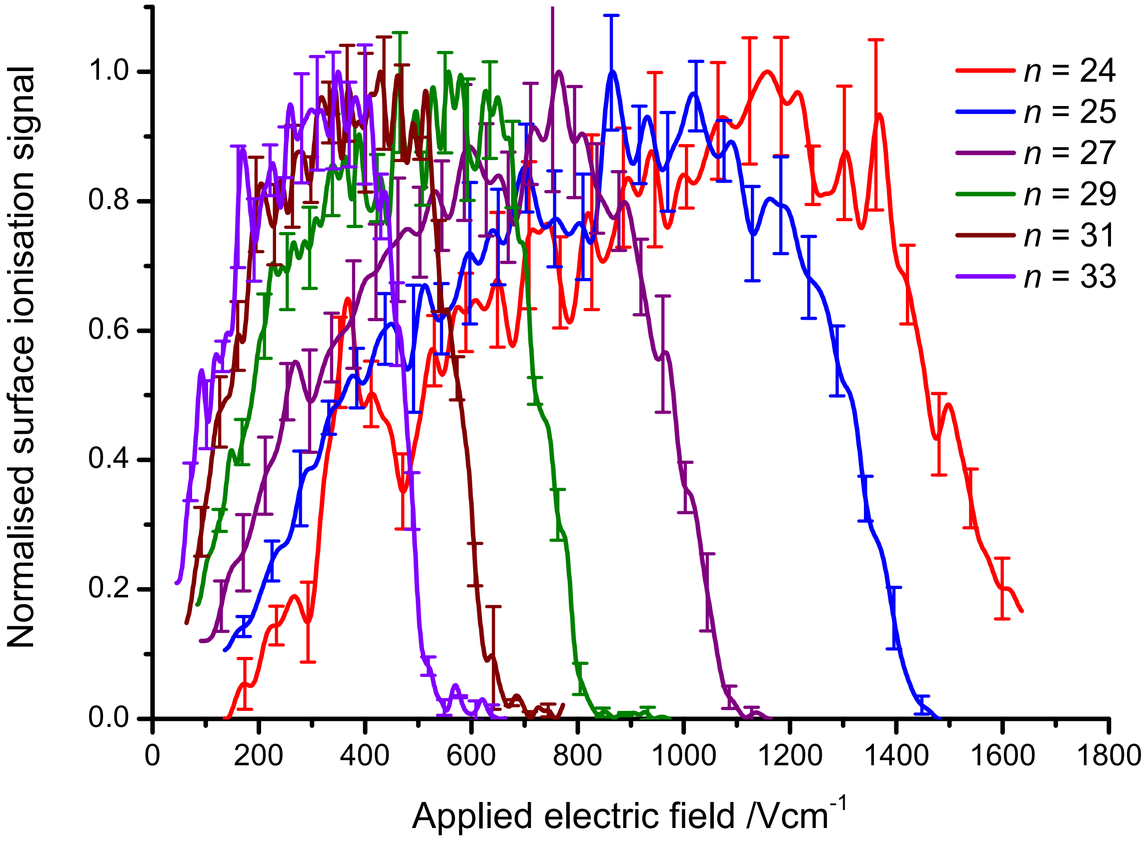

Figure 5.2: Integrated surface ionisation signal as a function of applied electric field for the most red shifted Stark states of a range of principal quantum numbers interacting with a monolayer gold nanoparticle surface (∅ 5 nm) at a collisional velocity of $v_\perp = 430\ m\,s^{-1}$. The signal follows the expected trends: the high field cut-off shifts towards lower fields with increasing quantum number and the detection efficiency decreases together with the electric field. However, the detection efficiency at low fields is increased, and the profiles spread over a wider range of fields compared to a bulk gold surface.

malised surface ionisation profiles of the most red-shift Stark states as a function of electric field. However, the applied electric field has been scaled to n^{-4} in accordance with Equation 2.10 in order to make profiles of different principal quantum number more comparable. These results confirm the first impression that surface ionisation can be detected at lower applied fields and the detection efficiency at these fields is surprisingly high. These observations thus indicate that for nanoparticle surfaces, ionisation occurs over a wider range of distances and typically starts at a greater distance from the surface compared to the bulk gold surface.

Ganeshalingham et al. recently investigated the interaction of Rydberg states with doped silicon wafers [74]. In these studies, an increase in detection efficiency at low fields similar to the results reported here was observed. In order to rule out that the results presented in this thesis are affected by the silicon wafer in the 'background', Figure 5.4 shows surface ionisation profiles for selected $k = -(n-1)$ Stark states measured with a nanoparticle surface, a bulk gold surface and a plain silicon wafer. For all principal quantum numbers presented here, the surface ionisation profiles measured at the nanoparticle surface possess a higher detection efficiency compared to the other two surfaces. This clearly shows, that the observed effect indeed originates from the gold nanoparticles.

It is of interest to note how the surface ionisation signal of the silicon wafer changes with principal quantum number. For lower n values both the bulk gold and the silicon wafer results are in very good agreement. With increasing principal quantum number however the detection efficiency of the surface ionisation signal as measured with the silicon wafer increases compared to the one measured with the gold surface (but is still lower compared to the nanoparticle surface). A similar observation was made by Ganeshalingham et al. and the observed effect thus is in good agreement with the results reported in [74].

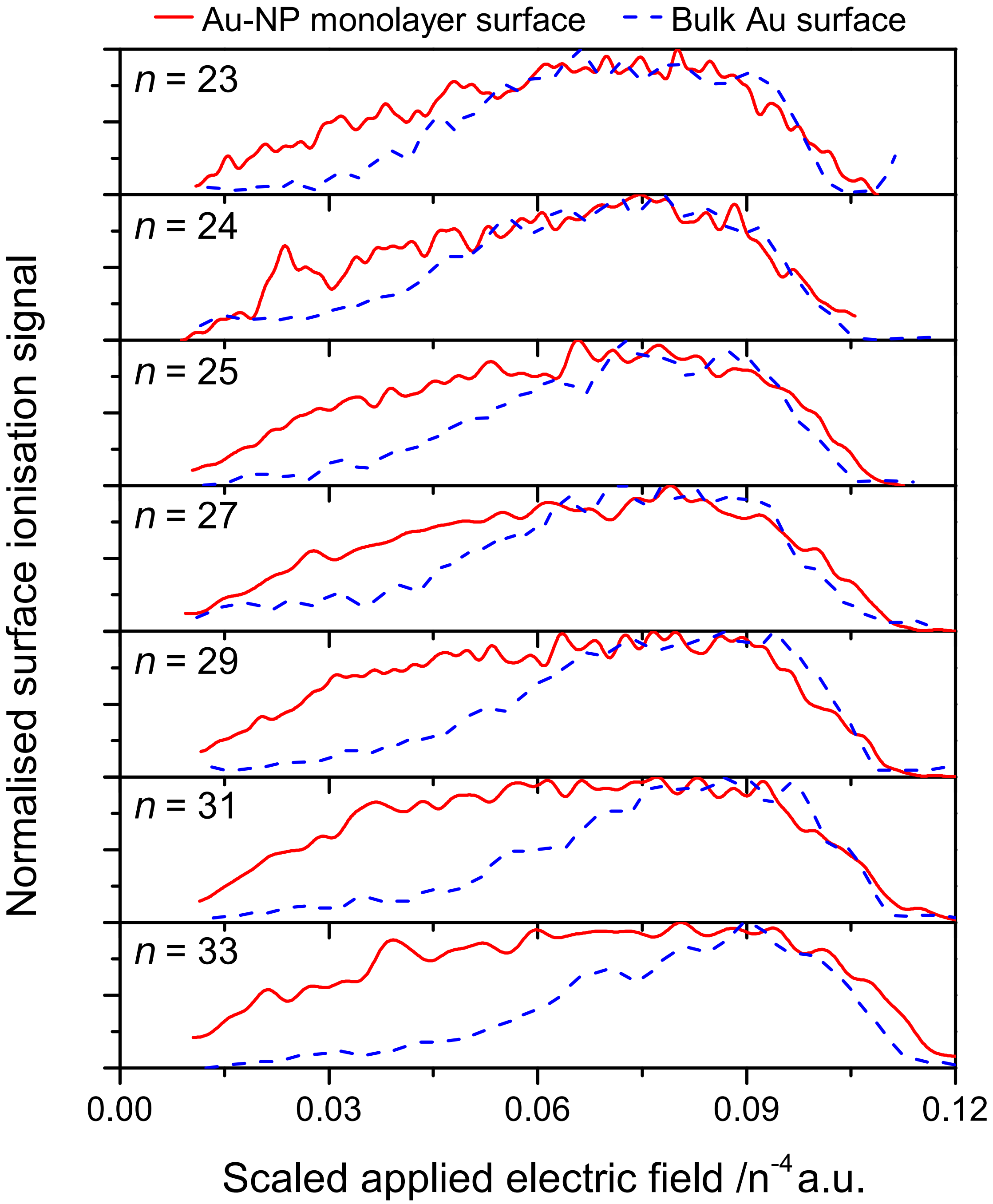

Figure 5.3: Integrated surface ionisation signal as a function of scaled applied electric field for the most red shifted Stark states of a range of principal quantum numbers, interacting with a monolayer gold nanoparticle surface ($\varnothing = 5$ nm) at a collisional velocity of $v_{\perp} = 430\ m\,s^{-1}$ (full blue lines). For comparison, according surface ionisation profiles measured with bulk gold surface are also shown (dashed red lines).

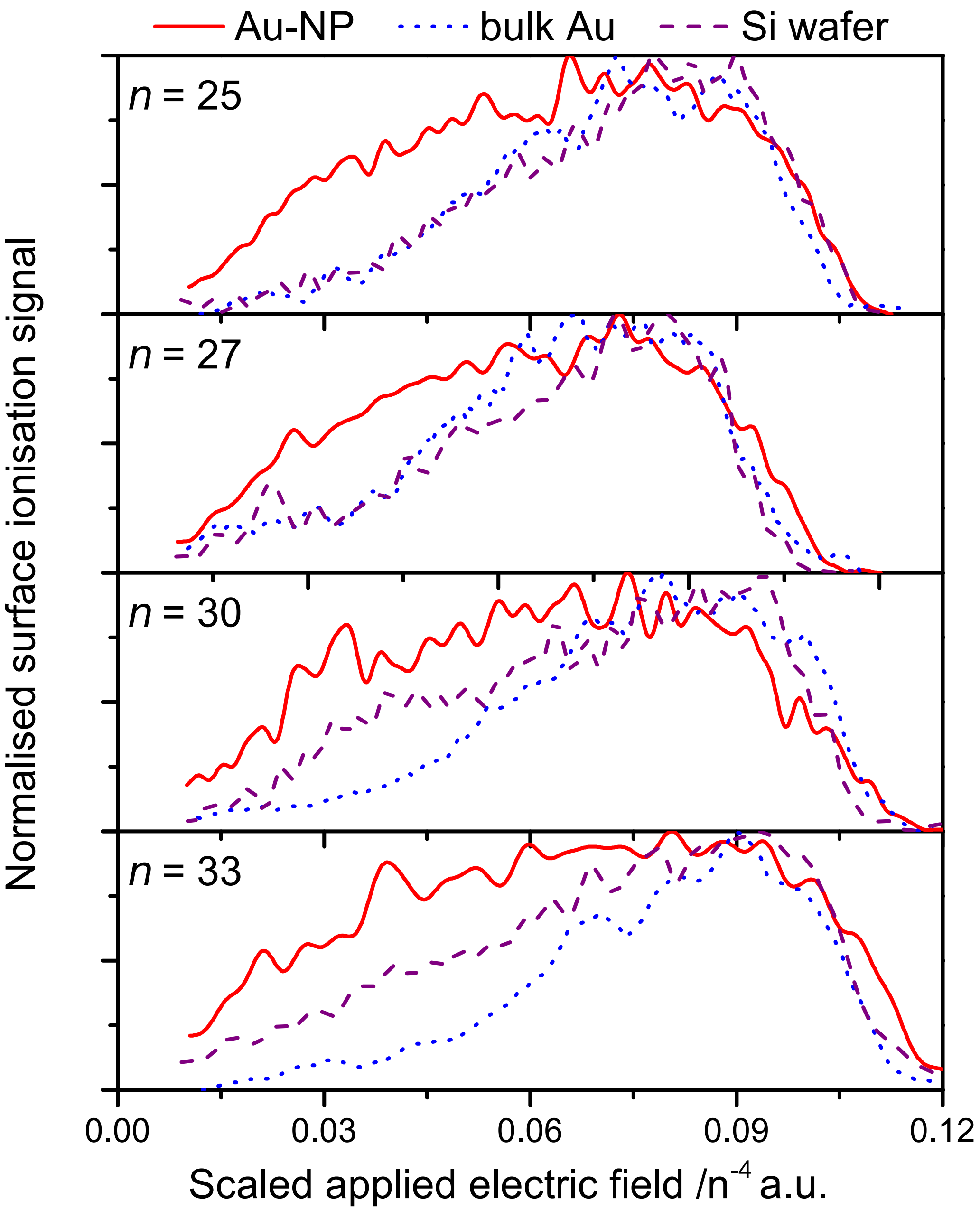

Figure 5.4: Comparison of the surface ionisation profiles of the most red shifted Stark states of the $n = 25, 27, 30, 33$ manifolds measured with a gold nanoparticle monolayer surface (full redlines), a bulk Au surface (dotted blue lines) and a silicon wafer (purple dashed line). The electric field is scaled by n^{-4}.

The question as to what causes this kind of increase of ionisation distance, is non trivial. Depositing nanoparticles on a silicon wafer obviously adds a degree of surface structure which is in some way analogous to the effect of roughness as considered in previous studies. It was recently shown by So et al. that surface roughness can alter the surface ionisation in a similar way, leading to an increase in and a spread of ionisation distance [37]. Figure 5.5 presents simulated surface ionisation profiles using the Monte-Carlo trajectory simulation method explained in Section 2.3.2, incorporating the effects of surface roughness as measured by AFM. From Figure 5.1 it can be seen that the surfaces are almost flat, in accordance with the experimental results reported in [99]. In order to estimate the surface roughness, the nanoparticle surfaces are thus simulated as round spheres with a height of 5 nm, set up in a closed-packed arrangement across the whole surface. This leads to a corrugation of the ionisation surface (the distance above every point of the surface at which ionisation occurs at a given field) which in turn leads to a spread and shift of ionisation distances. However, both the observed shift as well as the widening of the simulated profiles is rather small and can in no way explain the experimentally observed surface ionisation profile.

However, it was demonstrated in Chapter 4 that stray fields can have a great impact on the surface ionisation process and thus the observed profiles. Looking at the nature of the surface it seems likely that similar fields as those observed by Dunning and co-workers, and used in the simulations presented in the previous sections will be present near a nanoparticle surface. Therefore, combining the surface roughness calculations with the Monte-Carlo stray-field simulations might be able to explain the experimental results. As it was not possible to measure possible stray fields near the nanoparticle surfaces, the same fields as measured in [47] were used in the same way as explained in Section 2.3.3. Combining the two effects leads to an additional corrugation of the ionisation surface which in turn should lead to an increased spread and shift

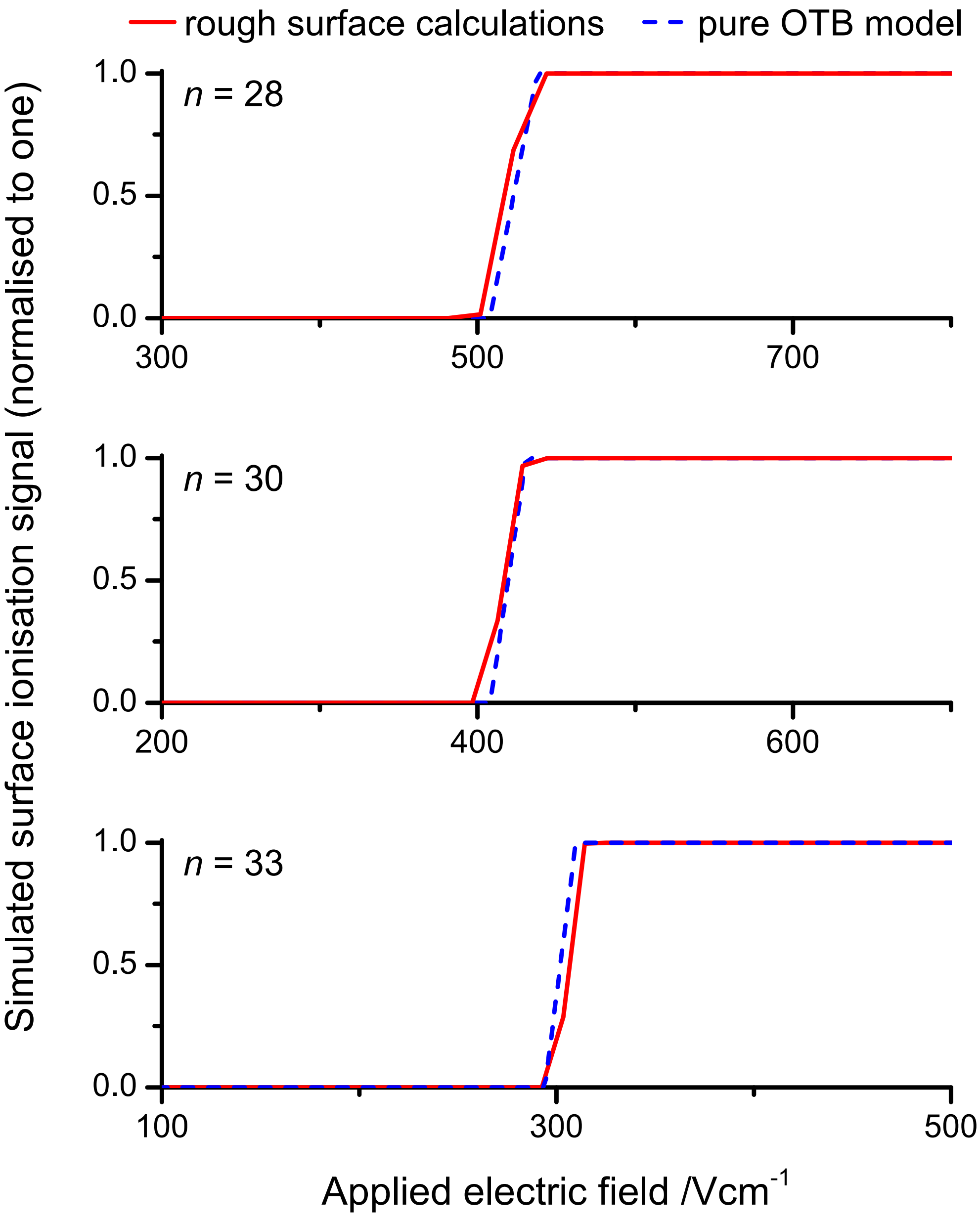

Figure 5.5: Simulated surface ionisation profiles for the most red-shifted states of the n = 28, 30 and 33 Stark manifolds using the Monte-Carlo simulation approach as described in Section 2.3.2. The full red lines represent calculations carried out taking into account the surface roughness introduced by depositing nanoparticles on the surface (see text for details). For comprison, Monte-Carlo trajectory simulations using a pure over-the-barrier ionisation approach are shown as blue dashed lines.

of ionisation distances. It needs to be noted that this assumption obviously only represents a very rough estimate. The different periodicity of the surfaces due to the regular arrangement of the 5 nm nanoparticles (in contrast Pu et al. measured a 1×1 μm square and repeated it periodically in 2 dimensions) compared to the domain sizes of the areas of different patch charges, is likely to likely to result in significant differences.

Figure 5.6 shows simulated surface ionisation profiles using the Monte-Carlo trajectory simulation for the $k = -n+1$ states of the $n = 28$, 30 and 33 Stark manifolds together with experimental data. The dashed red line corresponds to calculations including both the effect of stray fields and surface roughness induced by the nanoparticles while the dotted blue lines represent simulations including only the effect of stray fields. While the surface roughness does have a visible effect on the simulated surface ionisation profiles (mainly a shift to lower fields), these calculations once again fail to explain the shape of the experimentally observed data. It is thus possible to assume that the surface roughness does not lead to any significant change in the appearance of the detected surface ionisation profile, especially its width.

From the calculations presented above it can be concluded that the experimentally measured surface ionisation profiles are not purely caused by the surface roughness introduced by depositing nanoparticles on the surface. The exact reason for the observed width and onset are not yet understood and one possible explanation might be related to the electronic structure of the nanoparticles. With an individual size of 5 nm, these particles lie in a size region where the metal to insulator transition is expected to occur. Assuming, these particles still possess distinct energy levels, resonance effects could possibly be a reason for the observed ionisation behaviour. However, these effects do not necessarily lead to a more effective ionisation compared to bulk-gold and additional experiments are therefore needed to confirm (or to refute)

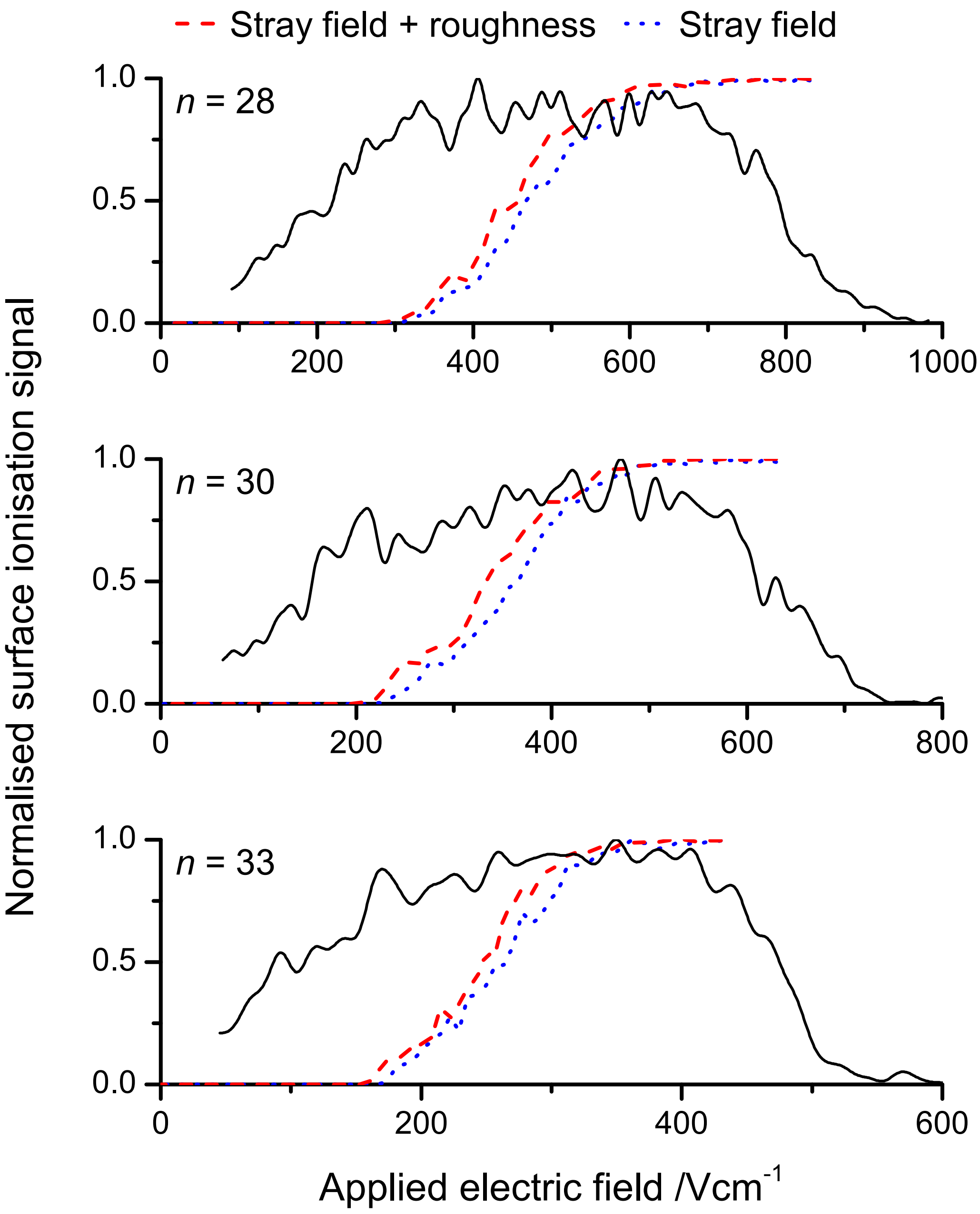

Figure 5.6: Simulated surface ionisation profiles of the most red-shifted Stark states of the $n = 28$, 30 and 33 Stark manifolds incident on a nanoparticle surface. The calculations were performed with the Monte-Carlo trajectory method described in Section 2.3.2 combining the surface roughness introduced by the nanoparticles with the effect of stray field as explained in the text (red dashed lines). For comparison the same calculations without the additional effect of surface roughness (blue dotted lines) and the experimentally measured surface ionisation profiles are also shown (full black lines).

this assumption.

5.1.2 Stark polarisation

Besides the orbital dimension of the Rydberg atom it might also be of interest to investigate how the surface ionisation process depends on the polarisation of the Rydberg electron wavefunction. Figure 5.7 shows surface ionisation profiles for different states of the $n = 29$ Stark manifold, with a collisional velocity of $v_\perp = 430\ \mathrm{m\,s^{-1}}$. The measured signal is normalised to the corresponding integrated field ionisation signal. Profiles of red-shifted states thereby show the expected behaviour of decreasing detection efficiency with increasing parabolic quantum number k. Blue shifted states however do not follow the usual trend but instead show an increasing detection efficiency with increasing k. For the most blue-shifted states, the measured detection efficiency even surpasses that of the most red-shifted state.

This unexpected observation is not exclusive to the $n = 29$ Stark manifold but can also be observed for other principal quantum numbers, for example the $n = 28$ Stark manifold shown in Figure 5.8. Once again, the detection efficiency for red shifted states decreases with increasing k but increases for blue-shifted states, with the $k = +27$ state once again surpassing the most red-shifted state.

One possible explanation for this unexpected observation could be coupling between red- and blue-shifted states of neighbouring manifolds at close proximity to the surface, leading to population transfer from a blue- to a red-shifted state. It should be possible to ‘test’ this assumption by comparing the surface ionisation profiles of the most blue-shifted Stark state of a principal quantum number n with the profile for the most red-shifted Stark state of the next principal quantum number manifold $(n+1)$. Figure 5.9 therefore presents surface ionisation profiles for two different combination of most red- and blue-shifted states of neighbouring manifolds ($n = 28/29$ and $n = 29/30$).

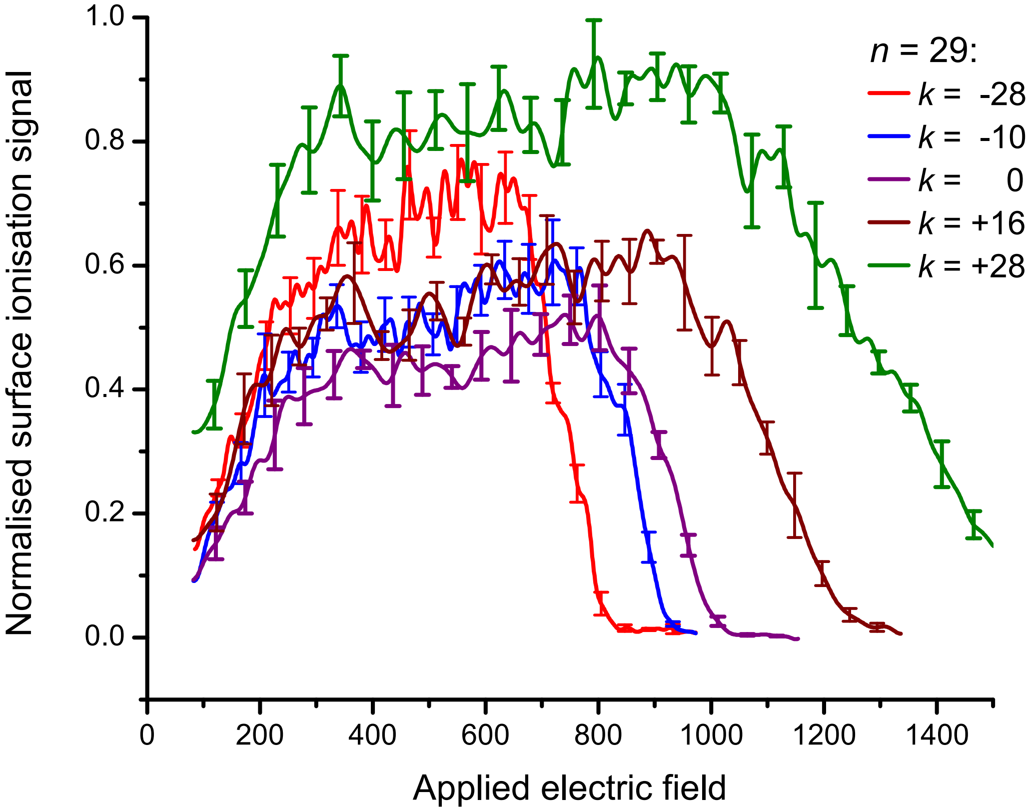

Figure 5.7: Surface ionisation signal as a function of applied electric field for selected Stark states of the $n = 29$ manifold normalised to the respective field ionisation signal. For red-shifted states the surface ionisation profiles follow the expected behaviour of reduced detection efficiency with increasing k. However, blue-shifted states show an increased detection efficiency, with the maximum at $k = +28$.

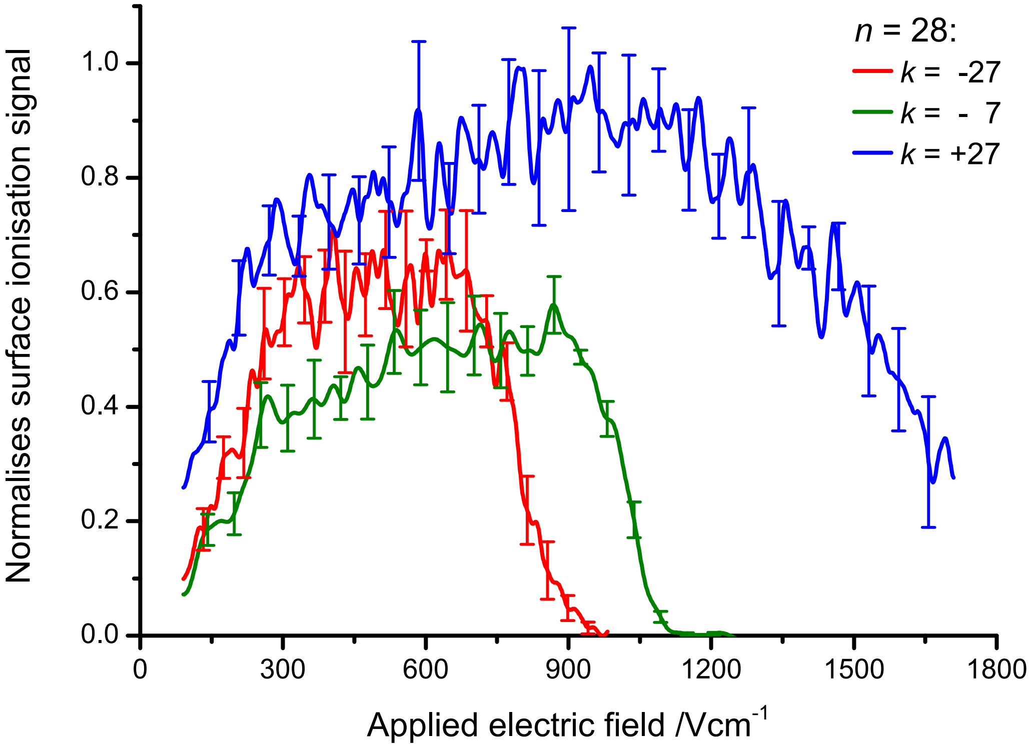

Figure 5.8: Surface ionisation signal as a function of applied electric field for selected Stark states of the $n = 28$ manifold normalised to the respective field ionisation signal. For red-shifted states the surface ionisation profiles follow the expected behaviour of reduced detection efficiency with increasing k. However, blue-shifted states show an increased detection efficiency, peaking for $k = +27$.

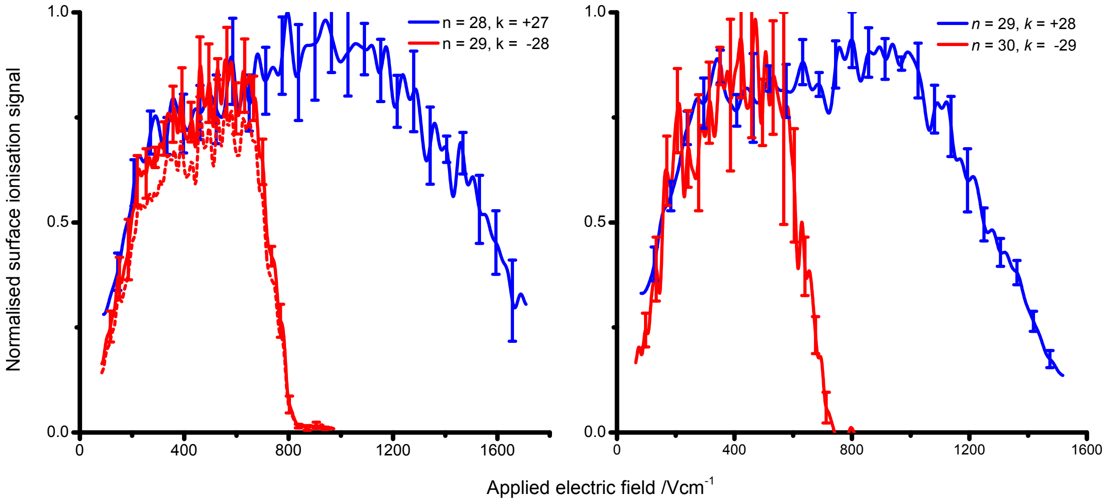

Figure 5.9: Surface ionisation signal as a function of applied electric field for selected red- and blue-shifted states of the $n = 28$, 29 and 30 Stark manifolds. A great amount of overlap between the surface ionisation profiles of neighboring blue- and red-shifted Stark states can be observed. The experimental results results of the $n = 29$, $k = -28$ state (dotted red line) were scaled by $\sim$ 10% (full red line).

For both cases a good degree of agreement between the the two surface ionisation profiles can be observed. It should be noted that in the left image of Figure 5.9 the surface ionisation profile of the $n = 29$, $k = -28$ state (red full line) is scaled by $\sim$ 10% in order to make the red- and the blue-shifted state overlap. But the two traces overlap, even without scaling, within their respective experimental errors (red dashed line).

Taking a closer look at the high-field cut off for all states investigated one can notice, that those still correspond to the theoretical predictions from Section 1.5. Given that field ionisation happens at too great a distance to be affected by the surface, this indicates that the population transfer (from blue- to red-shifted states) must occur at relatively small distances, further suggesting that the surface is involved in the observed effect.

The presence of avoided crossings has been observed before in surface scattering experiments with xenon and molecular hydrogen [66, 48]. But in those cases the origin of the avoided crossings was a loss of symmetry of the Rydberg states due to the finite size of the ion core. For H-atoms such crossings could only occur due to symmetry breaking by the surface. However, for the interaction of atomic hydrogen Rydberg states with a bulk metal surface this is not enough to lead to avoided crossings as has been shown in Chapter 4 of this thesis. For the interaction of Rydberg states with a monolayer nanoparticle surface however one can imagine a mechanism by which population transfer from blue- to red-shifted states is possible. While nanoparticles with a 5 nm diameter already possess strong bulk metal properties, a monolayer of such particles as used in the experiments presented here still possesses insulator type behaviour due to the alkanethiol used to stabilise the nanoparticle [117]. Therefore, two different mechanisms leading to the observed population transfer can be proposed.

Inhomogeneous fields are known to cause avoided crossings in Rydberg states. Due to the shape of the nanoparticles and the fact they are not yet completely bulk metal in nature, field perturbations might be present near the surface. Therefore electric field directions in close proximity to the surface do not run perpendicular away from the nanoparticle surface towards the extraction mesh opposite the surface but are rotated in direction by the nanoparticles. As the excited Stark state is polarised along the field lines, the eigenstate rotates with the field. Under these conditions, k is no longer a good quantum number and when red- and blue-shifted states of neighbouring quantum number coincide in energy, mixing between the states should be possible. The states thus probably track the field directions adiabatically except where there is a crossing. This mechanism of rotating k-states is demonstrated in Figure 5.10, which shows a sketch of the polarisation of the eigenstate along the field lines near a nanoparticle. Similar to experiments investigating the charge transfer of non-hydrogenic Rydberg atoms or molecules with metal surfaces, the observed surface ionisation dynamics would thus be dominated by that of the red-shifted state. However, as this population

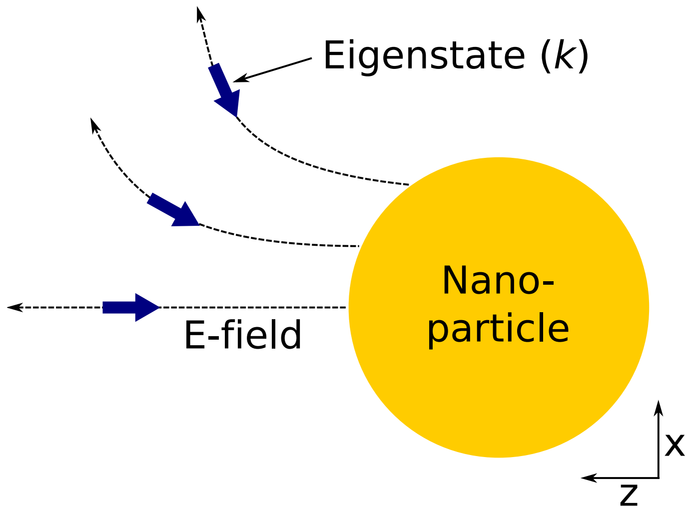

Figure 5.10: Sketch of the rotation of the k eigenstate of a Rydberg state near a nanoparticle due to rotation of the field lines. This rotation might allow population transfer from blue- to red-shifted states to occur.

transfer only occurs at small distances from the surface, the high-field cut-off of the recorded surface ionisation profile is not expected to be affected, which is in good agreement with the experimentally observed data.

Alternatively, should the energy of a crossing of red- and blue-shifted states be resonant with an energy state within a nanoparticle, population transfer from the blue state to the red state can be facilitated indirectly via the nanoparticle. In turn this would lead to ionisation at greater than expected distances from the surface (see Figure 5.11 for a schematic of this mechanism), once more explaining the observed results.

In order to confirm either of the suggested mechanisms a theoretical investigation of the interaction of Rydberg states with nanoparticle covered surfaces is needed. As explained in Section 2.2.1, static simulation approaches are unable to observe the effects described here and are thus unsuitable. The first wave-packet-propagation calculation investigations have recently been performed in the group of Prof. Softley at Oxford [118]. In these calculations it could be shown that coupling between Stark states and individual nanoparticle states is possible and population transfer (in both directions)

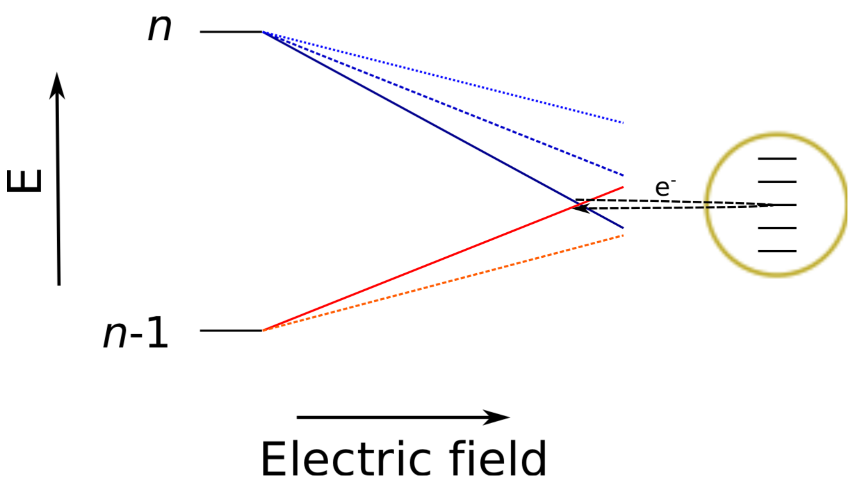

Figure 5.11: Schematic of the interaction of a blue-shifted Rydberg state with a gold nanoparticle ($\phi = 5$ nm) monolayer surface. The Figure demonstrates the proposed mechanism by which population transfer from blue- to red-shifted Stark states is facilitated via resonance effects with energy levels in the nanoparticle.

between the Rydberg state and the nanoparticle could be observed. Calculations were mainly performed for red-shifted states with a low principal quantum number and smaller nanoparticles than the once used in these experiments due to the great computational cost of these calculations as described in [37]. However, calculations are currently under way investigating interaction of blue-shifted states with low principal quantum number with nanoparticle surfaces, testing the general validity of the idea.

5.1.3 Ageing

The experiments presented in the previous section were all performed with a single nanoparticle monolayer surface. To test repeatability, the experiments were repeated about six months after the initial measurements using two other surfaces that had been produced at the same time and via the same method as the first one. Figure 5.12 shows surface ionisation profiles of the most red-shifted Stark states for a range of principal quantum numbers recorded with either of the two surfaces (blue full lines). For comparison, profiles recorded with the original surface (red full lines) as well as with a plain silicon wafer are also shown (black dashed lines). Looking at the new experimental data one notices right away the decreased detection efficiency at the low field parts of the profiles. Furthermore, comparing the results of the repeated measurements with results obtained with a plain silicon wafer, a surprising amount of agreement can be observed, raising the question of whether there are actually nanoparticles left on the surface after such an extended amount of time.

The surfaces were therefore once again investigated by an in-house surface analysis facility using a range of surface analysis techniques in order to gain a better understanding of observed experimental results. Figure 5.13 shows an x-ray photoelectron spectroscopy (XPS) spectrum of the surface (a) as well as a 5×5 μm AFM image (b). XPS is an element specific analytical method in which the surface is irradiated with x-rays of a specific energy and the kinetic energy of electrons freed from the surface is measured. As such this method is able to confirm (or rule out) the presence of gold on the surface but is unable to establish its arrangements. The measured spectrum indeed confirms the presence of gold on the surface, showing peaks corresponding to all the valence electrons, appearing roughly at the correct binding energies. AFM on the other hand allows for an in depth analysis of the physical structure of the surface and therefore can be seen as complimentary to XPS. The AFM image presented in Figure 5.13 (b) deviates significantly from the image obtained with a 'freshly' prepared surface (see Figure 5.1). It shows large clusters with sizes in the micrometer range and large height differences. These observations suggest that instead of retaining their monolayer shape, the nanoparticles start aggregating, probably leaving large parts of the surface uncovered in the process. This would explain the observed results of the repeat experiments. Whether these ageing effects are due to inappropriate storage of the surfaces or other reason might be the focus of future investigations.

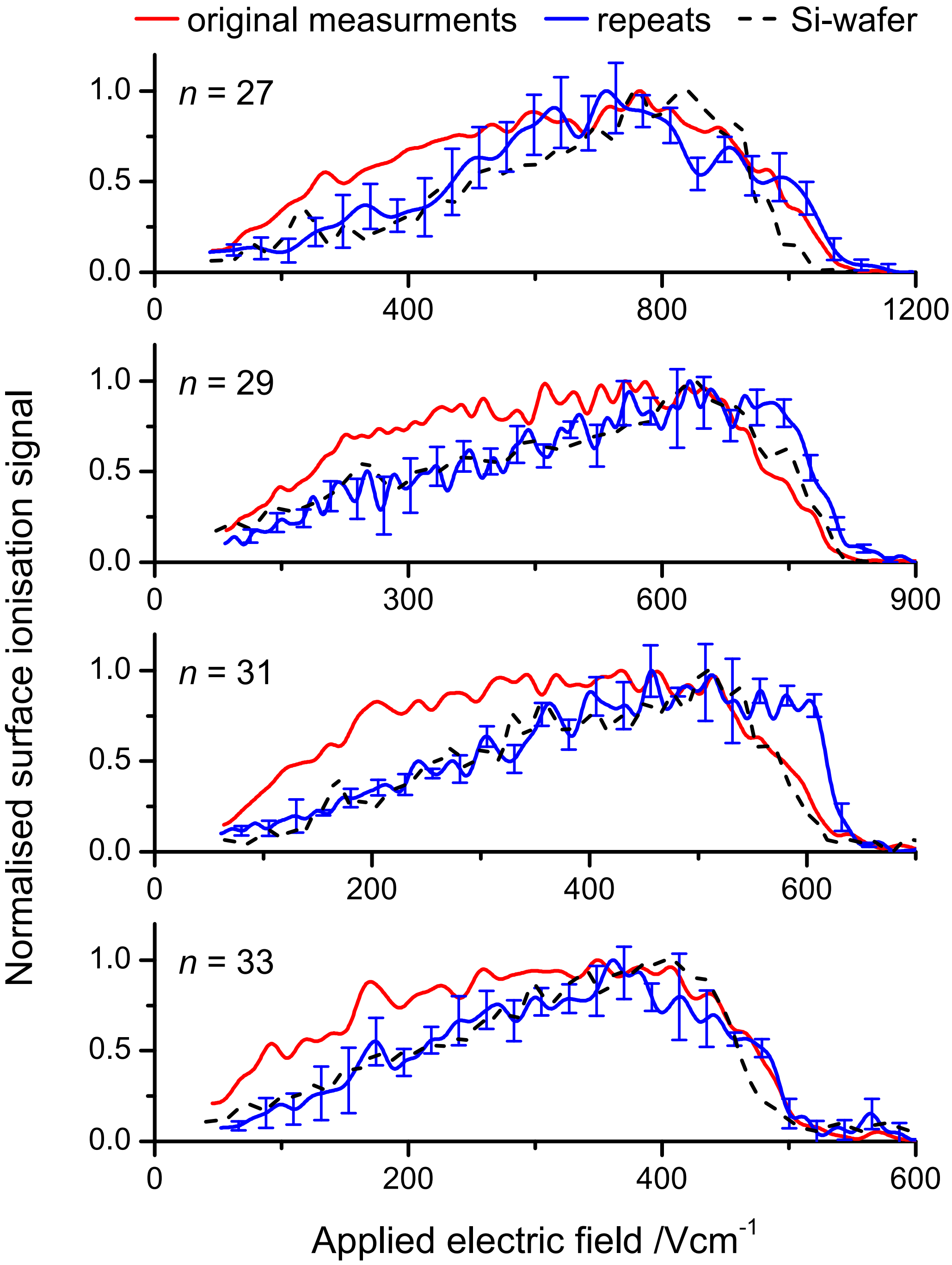

Figure 5.12: Integrated surface ionisation signal as a function of applied electric field for the most red-shifted Stark states ($k = -(n-1)$) for a range of principal quantum numbers n ($\angle_{\text{impact}} = 15°$, $v_{\perp} \approx 430\ m\,s^{-1}$). Red, full lines: experiments performed shortly after producion of the surface. Blue, full line: experiments performed approximately 6 months after production with two different surfaces. Black, dashed lines: results obtained with plain silicon wafer for comparison.

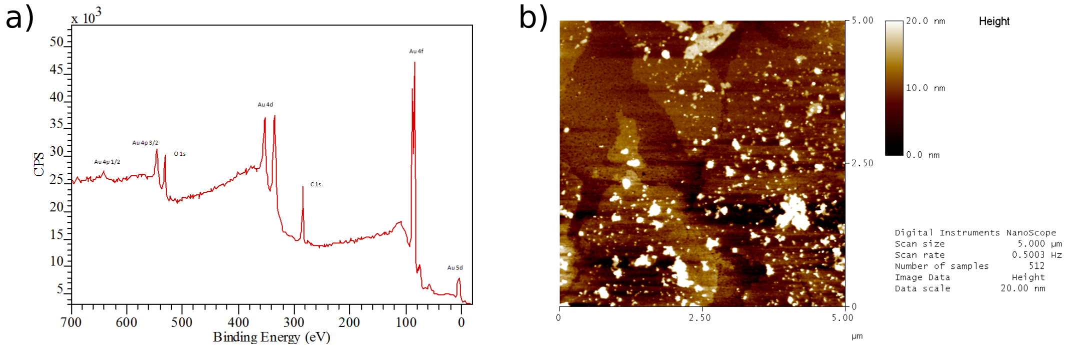

Figure 5.13: Surface analysis of a 5 nm nanoparticle monolayer surface 6 month after production. a) XPS spectrum of the surface confirming the presence of gold on the surface. b) AFM image of the surface, demonstrating the agglomeration of the nanoparticles to clusters of significantly larger size.

5.2 Effects of nanoparticle size and density

In the previous section the interaction of Rydberg states with a monolayer nanoparticle surface were discussed. This section deals with surfaces covered with a sub-monolayer coverage of nanoparticles of different sizes and particle densities. The surfaces were prepared within the group, using commercial nanoparticles, using the production method outlined in Section 3.3.

As mentioned before, it is difficult to deposit particles of different sizes at comparable densities. This is mostly due to the different concentrations of particles in the precursor solutions. It therefore proved impossible to investigate surfaces with a sub monolayer coverage of nanoparticles of different sizes with the same nanoparticle density. Figure 5.14 shows normalised surface ionisation profiles for Rydberg hydrogen atoms of a range of principal quantum numbers ($n = 29 - 34$), measured with surfaces covered by nanoparticles of different sizes and densities. Results obtained with a 20 nm gold nanoparticle surface with a density of approximately 160 nanoparticles per μm^2 surface ($\simeq 6.5\%$ of a monolayer, assuming cubic packing) are shown as full blue line while results obtained with a 80 nm particles at 15 particles per μm^2 surface ($\simeq 9.5\%$ of a monolayer) are shown as red full lines. It appears as if there is only minimal difference between the two different surfaces and these differences also lie well within experimental error. Most likely this is due to the rather low density of nanoparticles on the surface. It is therefore not possible to directly identify any effect of nanoparticle size and/or density from the surface ionisation profiles presented here.

It is more interesting to compare the results obtained using a nanoparticle surface with data obtained from a bulk gold (Figure 5.14, dotted black line) and an APTMS covered silicon wafer, the substrate used to deposit the nanoparticles (Figure 5.14, dashed black line). Comparing the results obtained for different principal quantum numbers reveals an interesting trend. Firstly, both nanoparticle covered and pure ATPMS covered surfaces possess a higher detection efficiency at the low field end of their respective surface ionisation profiles compared to the respective profiles measured with a bulk Au surface. However, nanoparticle covered surfaces and pure APTMS surfaces show different trends when varying the principal quantum number. At lower investigated principal quantum numbers ($n = 29,\ 30$) there is a distinct difference between surfaces covered with nanoparticles and the 'pure' APTMS surface with the nanoparticle surfaces possessing a significantly higher detection efficiency. However, with increasing n this effect gradually becomes smaller and it seems to have completely disappeared for the highest investigated principal quantum numbers ($n = 33,\ 34$).

In order to get a more quantitative understanding of the observed effect, Figure 5.15 presents the integrated surface ionisation profiles as a function of principal quantum number, n. The graph also includes data for a surface covered with 50 nm gold nanoparticles (37 nanoparticle per μm^2, $\simeq 9\%$ of a monolayer) which were omitted from Figure 5.14 as these results show essentially the same trend as the other two nanoparticle surfaces. Straight lines were fitted through the experimental data as a guidance for the eye of the reader and to emphasize the observed trends. The results confirm the qualitative observations made from Figure 5.14. At low principal quantum

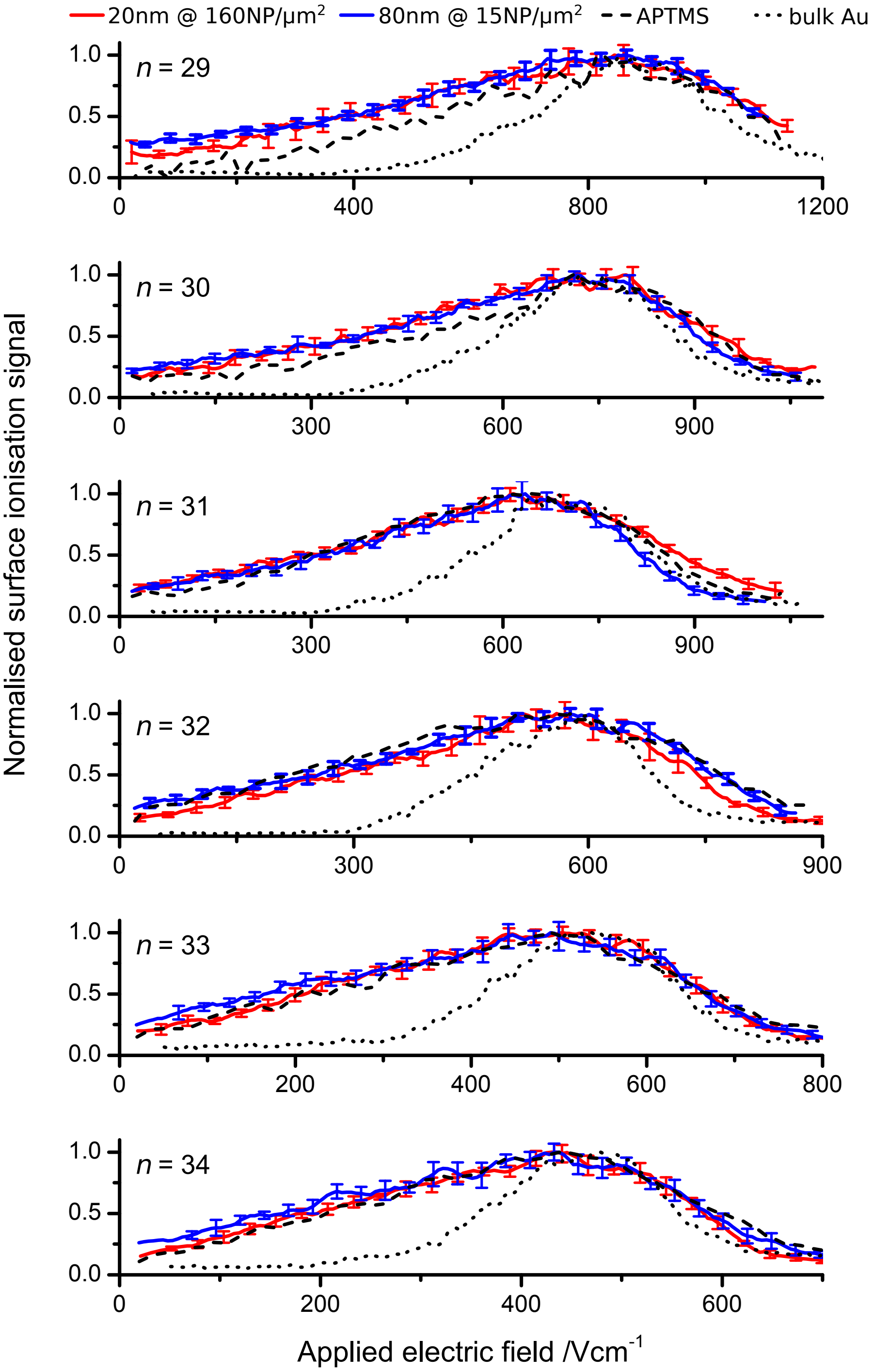

Figure 5.14: Surface ionisation signal as a function of applied electric field for Rydberg states in the range $n = 29 - 34$ ($\angle_{\text{impact}} = 15°$, $v_{\perp} \approx 430\ m\,s^{-1}$) measured at Au nanoparticle surfaces of varying sizes (20 nm particles @ 160 nanoparticles/μm^2, 80 nm particles @ 15 nanoparticles/μm^2). For comparison surface ionisation profiles for the same principal quantum numbers measured with bulk gold and ATPMS covered surfaces are also shown.

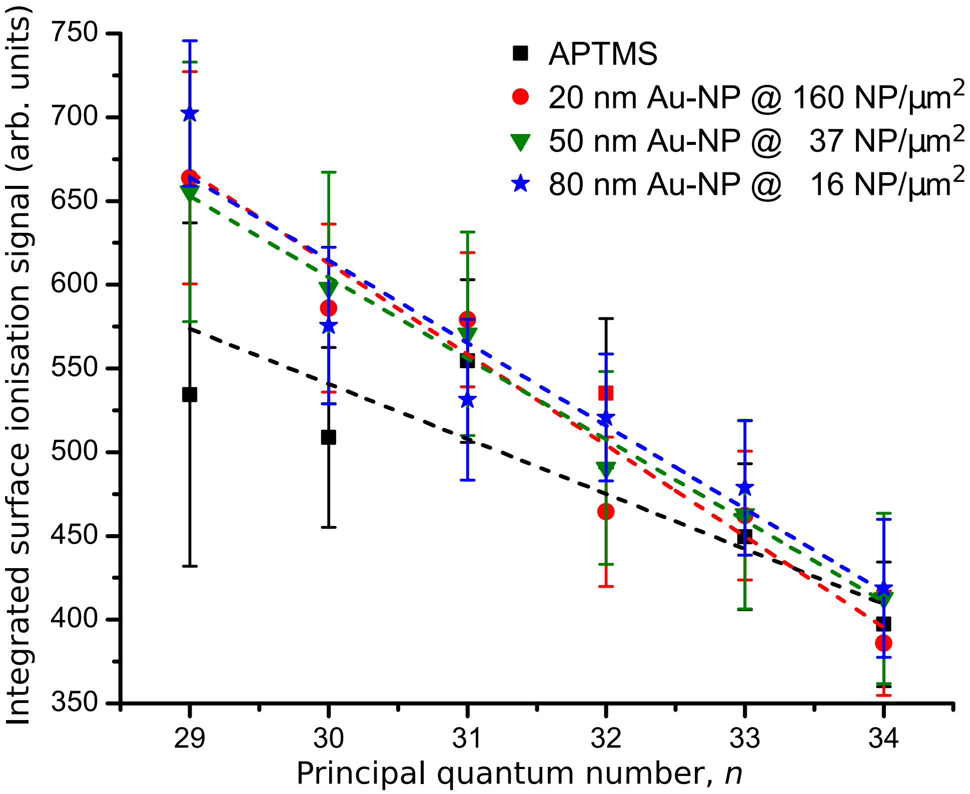

Figure 5.15: Integrated surface ionisation profiles of Rydberg states interacting with different nanoparticle (20, 50 and 80 nm) and APTMS covered surfaces. The dotted lines correspond to linear fits through the measured data points in order to emphasise the observed trends.

number, the detected signal is overall lower for the APTMS surface compared to the nanoparticle surfaces. However, the ‘gap’ between the two types of surfaces decreases with increasing quantum number and they are virtually identical for $n > 32$ (within their respective errors).

Keeping in mind that there is no significant difference between the different nanoparticle surfaces, the only variable in these experiments is the principal quantum number and thus the orbital size of the Rydberg atom (see Table 5.1 for n vs. size relationship). This therefore demonstrates that the sensitivity of Rydberg states to surface properties decreases with increasing size. The lowest principal quantum numbers investigated already correspond to a larger Rydberg orbital than the largest nanoparticles used in

Table 5.1: Comparison of principal quantum number and (classical) size of a Rydberg state ($d \sim n^2 a_0$).

n	Diameter /nm
13	17.89
20	42.34
25	66.15
29	89.01
30	95.26
31	101.71
32	108.38
33	115.26
34	122.35

the experiments presented here. Only (currently) experimentally inaccessibly small principal quantum numbers like $n = 12$ ($\phi \approx 18$ nm) would result in a small enough orbital radius to make Rydberg atoms and nanoparticles comparable in size. This perhaps explains why even for the $n = 29$ Rydberg state there is only a relatively small difference between a nanoparticle covered and a plain APTMS surface and this small difference disappears quickly with increasing n.

These results obviously only present a first glance into the interaction of Rydberg atoms with nanoparticle surfaces and further experimental work is needed. Possible improvements include better control of nanoparticle density, especially when comparing surfaces of different nanoparticle sizes and there is a need to improve the nanoparticle density in general to significant levels of coverage. This is not easily possible with the commercially available nanoparticles used for the work presented here and preliminary work is therefore being carried out in the group with the aim to produce nanoparticles of different sizes at sufficiently high concentration in-house. The according protocols are presented in Section 3.3 but no experiments using ‘homemade’ nanoparticles have been performed yet. The problem of Rydberg orbital size vs. nanoparticle size is even harder to overcome. Rydberg states with principal quantum numbers below $n = 20$

are inaccessible with the current experimental setup due to limitations in the extraction field that can be applied. However, those are the states needed in order reach an orbital radius below 50 nm. One might also consider increasing the nanoparticle size, but creating precursor solutions with a high enough concentration of large nanoparticles will be problematic.

5.3 Conclusions

The interaction of Rydberg states with 5 nm gold nanoparticles deposited on a silicon wafer in the form of a monolayer has been investigated experimentally. These results show clear deviations from data obtained with a bulk gold surface. When studying the effect of the size of the Rydberg state on the surface ionisation a much higher detection efficiency at the low-field end of the surface ionisation signal compared to a bulk gold surface or a silicon wafer can be observed indicating that ionisation is happening at greater than expected distances and also over a wider range of distances. It could be shown through Monte-Carlo trajectory simulations, that the observed results are not an effect of surface roughness introduced by the deposition of the nanoparticles. However, their exact origin stays unclear.

Further experiments were performed with the same nanoparticle monolayer surface, investigating the effect of the polarisation of the Rydberg orbital with respect to the surface. While red shifted states showed the expected behaviour of a decreasing detection efficiency when the parabolic quantum number k increases, the detection efficiency of blue-shifted states increased with increasing k . For the most blue-shifted state the detection efficiency reached levels comparable to those observed for red-shifted states. Plotting the surface ionisation profiles of the most red- and blue-shifted Stark states of neighbouring principal quantum number manifolds on top of each other revealed a surprising amount of overlap between profiles of the two states. It is therefore proposed that population transfer from the originally populated blue-shifted Stark state (n, $k = n - 1$) to the most red-shifted Stark state of the neighbouring principal quantum number manifold ($n + 1$, $k = -((n + 1) - 1)$ occurred, leading to ionisation at greater than expected distance from the surface. It is also important to note that the respective high-field cut-off still appeared at the predicted electric field for both states, indicating that the suggested population transfer happened at close distance from the surface.

Two different theories are proposed to explain these observations. First, the population transfer might be facilitated by rotating electric fields in close vicinity to the surface, leading to k not being a good quantum number any longer and thereby mixing blue- and red-shifted Stark states. Alternatively, the two energy levels might be coupled together via individual states within the 5 nm diameter nanoparticles once again leading to a population transfer from a blue- to a red-shifted state.

Furthermore, the interaction of red-shifted Stark states with nanoparticles of different sizes deposited at a sub-monolayer coverage on an APTMS coated silicon wafer was also studied. Comparing the obtained results of different nanoparticle surfaces with a pure APTMS surface only small differences can be seen. For the lower quantum numbers investigated in the work presented here ($n < 30$) the detection efficiency of the nanoparticle surfaces is clearly bigger than that of the APTMS surface but this difference quickly decreases with increasing quantum number. It is possible to understand this observation by comparing the size of the nanoparticles to the size of the Rydberg state. The biggest nanoparticles investigated possess a diameter of 80 nm while the lowest Rydberg state ($n = 29$) has a classical orbital radius of approximately 90 nm. For low quantum numbers the two sizes are on a similar scale but with increasing n the Rydberg atoms quickly ‘outgrow’ the nanoparticles. It can thus be inferred that the Rydberg states only ‘see’ and therefore interact with the nanoparticle for the lowest investigated quantum numbers. The observed difference between the different nanoparticle surfaces which possess different particle sizes and densities were negligible. This is probably due to the difficulties encountered in terms of generating surfaces with large nanoparticles at high enough particle density.

While the results presented here show that the charge transfer process of Rydberg states at nanoparticle surface depends on factors like size and polarisation of the Rydberg orbital, they only provide a first impression of the complex processes involved. For example, further studies with a better control of nanoparticle size and density and a higher range of principal quantum numbers of Rydberg states are needed in order to gain a better understanding of the effect of the relative size.

Chapter 6

H-Atom Rydberg states at a Cu(100) surface

In section 2.3.4 the work of So et al. investigating the interaction of hydrogen atom Rydberg states with single crystal Cu(100) surfaces were presented [37]. These results showed some evidence for the presence of resonant charge transfer from a hydrogen Rydberg atom to the surface via image states (see Figure 6.1). However, it also became evident that further experiments are needed to gain a deeper understanding of the ionisation process.

In this chapter new experimental results are presented with the aim to gain further insight into this charge transfer process. Instead of analysing ionisation profiles of Stark states of a range of n-manifolds at a constant impact velocity the experiments described here analyse the effect of varying the collisional velocity on the ionisation process.

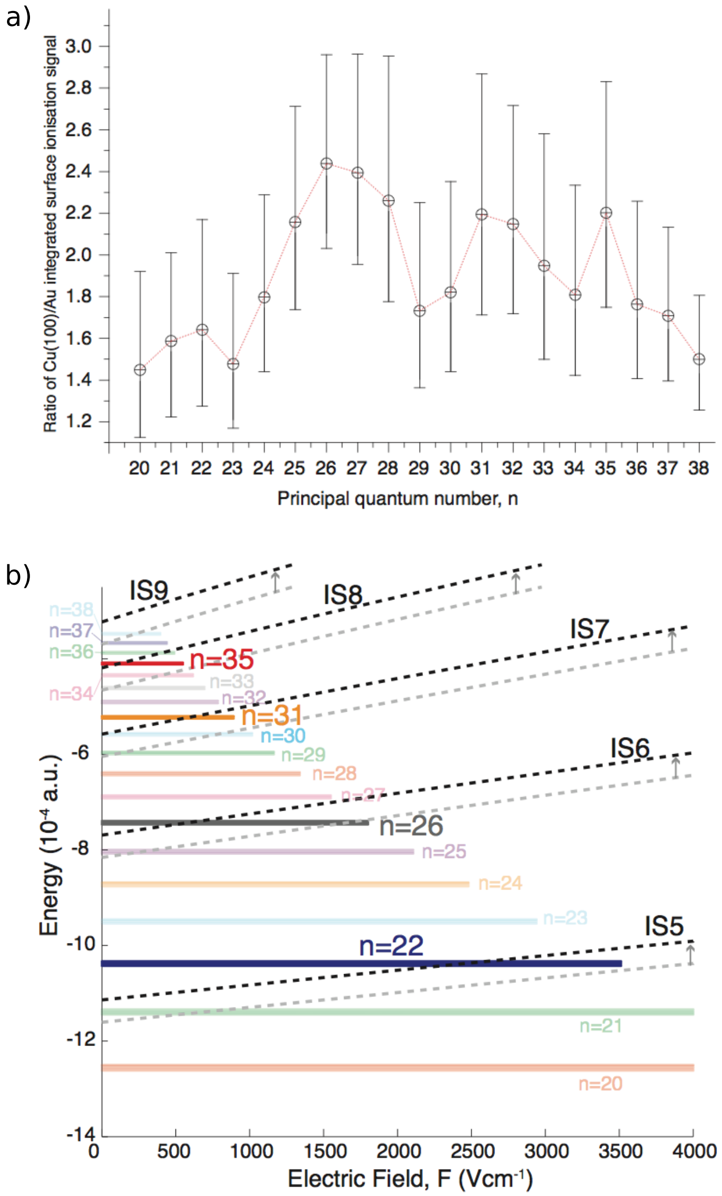

Figure 6.1: From [37]. a) ratio of the integrated surface ionisation profiles for the Cu(100) surface and a jellium type gold surface for mid-manifold Stark with principal quantum numbers in the range $n = 20 - 38$. b) Overlap of the energies of the image states of Cu(100) (grey, dotted lines) with the energy of mid-manifold Stark states ($k = 0$ or -1) in the range $n = 20 - 38$ (full coloured lines) as a function of electric field. The energies of the image states are shifted up by 5×10^{-5} a.u. to account for perturbation effects (black, dotted lines).

6.1 Interaction at constant velocities

As described in section 2.3.4, the interaction of Rydberg states with band-gap semiconductors is non-trivial due to the emergence of surface- and image-states within the band-gap. The otherwise hindered charge-transfer process at Rydberg state energies that lie within the band-gap region can be facilitated for states which are resonant in energy with those states. While previous studies of the interaction of atomic hydrogen Rydberg states with a Cu(100) surface showed some evidence for such resonance effects [37] it became evident that further investigations are needed to verify these predictions.

Figure 6.2 shows the detected surface ionisation signal as a function of applied electric field for the $k \simeq 0$ states of the $n = 25 - 34$ Stark manifolds with a collisional velocity of $v_\perp = 650\ \mathrm{m\,s^{-1}}$ (full red lines). For comparison, the corresponding surface ionisation profiles measured with a bulk gold surface are also shown (blue dashed lines). Analogous to the earlier results by So et al. there is an increased detection efficiency in the low-field part of the detected surface ionisation profiles for Cu(100). It should be noted that all the results presented in Figure 6.2 (Gold and Cu) are normalised to a maximum peak height of one to make them more comparable. However, when normalising the signal to the respective field ionisation signal, the surface ionisation signal measured with a Cu(100) surface is significantly smaller compared to a Au surface, as would be expected due to the Rydberg energy lying in the band-gap region. This effect is demonstrated in Figure 6.3 which shows surface ionisation profiles for the $n = 29$, $k = 0$ Stark states ($v_\perp \approx 430\ \mathrm{m\,s^{-1}}$) measured with a Cu(100) (full red line) and a bulk gold metal surface (blue dashed line).

For the most part, the obtained data is in good agreement with the results presented in [37]. This is demonstrated in Figure 6.4 which compares the two sets of results for a range of principal quantum numbers ($k \simeq 0$ and $v_\perp = 650\ \mathrm{m\,s^{-1}}$). The different

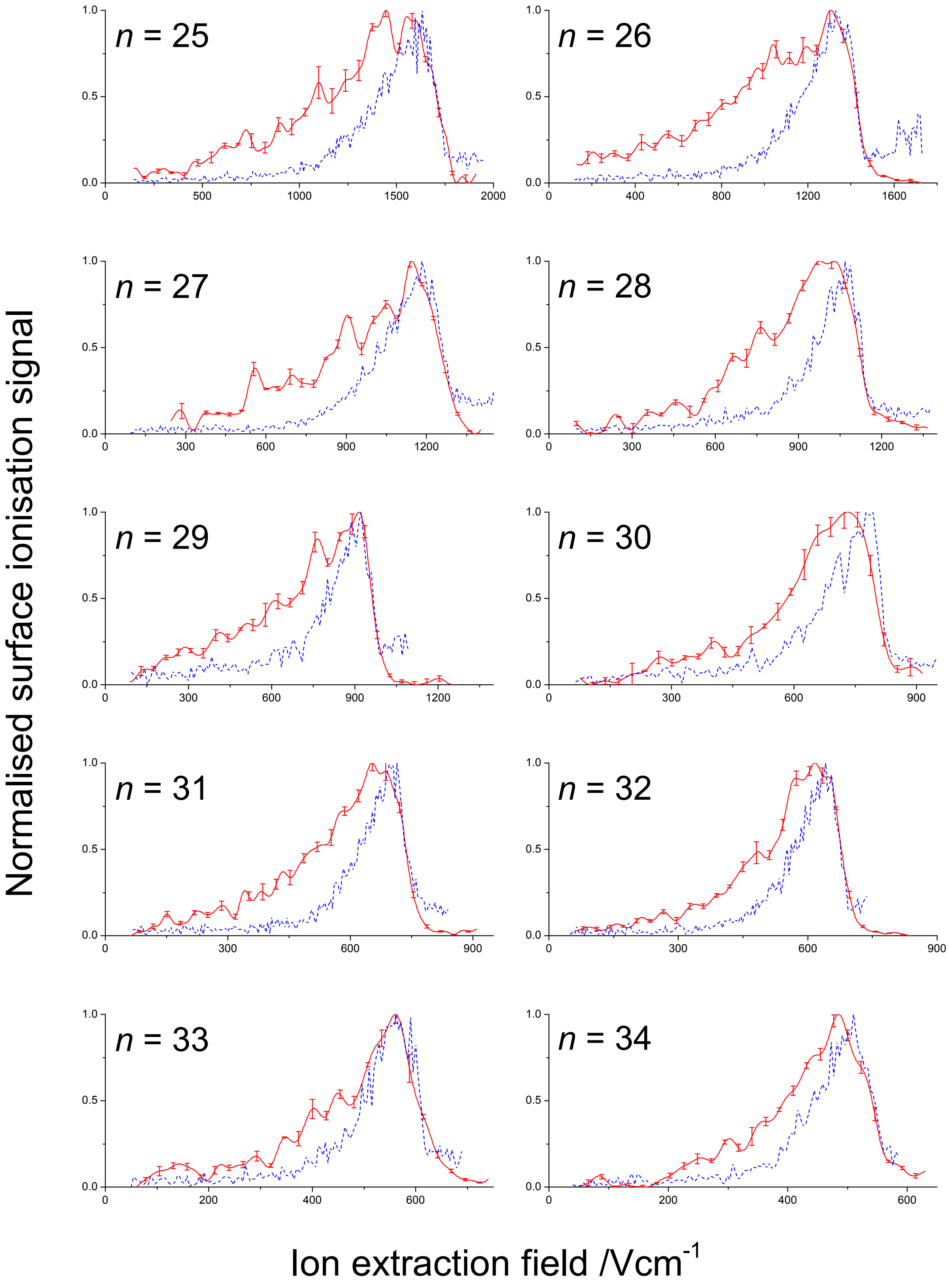

Figure 6.2: Integrated surface ionisation signal as a function of applied electric field for the $k \simeq 0$ states of the $n = 25 - 34$ Stark manifolds measured with a Cu(100) single crystal surface (full red lines) and a bulk Au surface (blue dashed lines). The collisional velocities for all shown profiles is set as $v_\perp = 650\ \mathrm{m\,s^{-1}}$ and the impact angle is 15°.

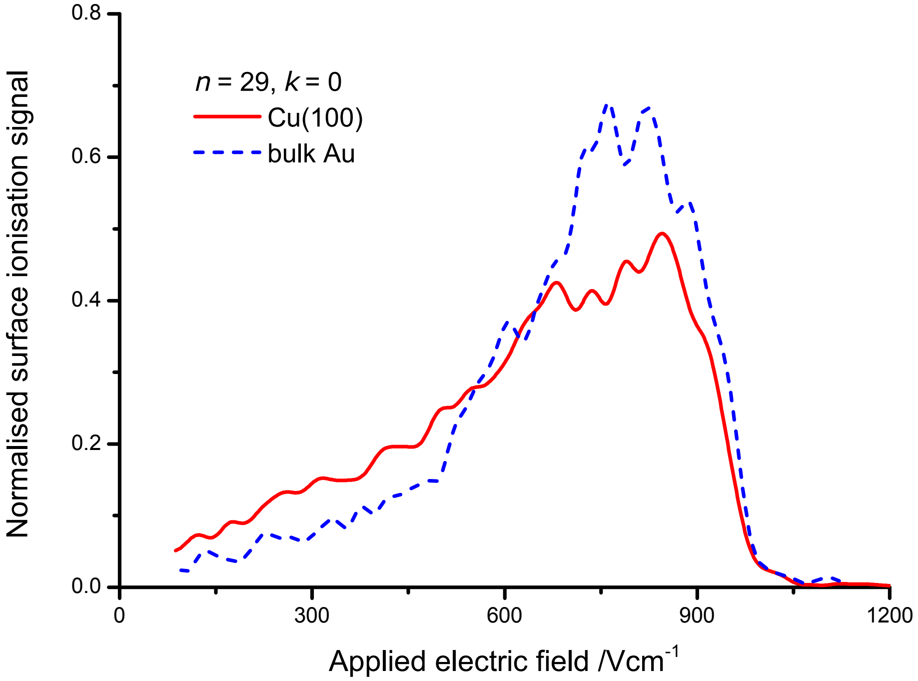

Figure 6.3: Integrated surface ionisation signal as a function of applied electric field for the $n = 29$, $k = 0$ Stark states measured with a Cu(100) (full red line) and a bulk Au (dashed blue line) surface ($v_\perp \approx 430$ m s^{-1}). Both profiles are normalised to the respective integrated field ionisation signal as measured at the beginning of the surface ionisation gate.

profiles show a high degree of agreement except for the higher principal quantum numbers, where the detection efficiency with the modified setup lies slightly below previous results. The reason for this small discrepancy is so far unknown.

In the work by So et al. results were analysed by comparing the surface ionisation profiles measured with a Cu(100) surface with those from an Au surface [37]. Both surface ionisation profiles were integrated and the bulk gold surface data was used to normalise the corresponding Cu(100) results. Figure 6.5 was generated in the same way, using the results measured for this thesis. It shows the ratio of the integrated surface ionisation profiles of Cu(100) to bulk gold as a function of principal quantum number ($n = 25 - 34$, $v_{\perp} \approx 650$ $\mathrm{m\,s^{-1}}$). The calculated ratios reach a maximum for $n = 26$ and $n = 31$ which is in good agreement with previous results (see Figure 6.1 a). As discussed previously, these peaks are attributed to resonances between the Rydberg state and an image state of the Cu(100) surface. The size of the error bars associated with the presented data also are on a similar scale as the ones reported by So et al., further showing the reliability and consistency of the data presented in [37].

6.2 Varying the collisional velocity

While the results from the previous section demonstrate the repeatability of earlier measurements they also suggest the need for a new way of investigating and analysing the interaction of Rydberg states with a Cu(100) surface. From Figure 6.1 it can be seen that resonance effects of a given Rydberg state with the surface Rydberg state possess a clear dependence on the applied electric field. Only over a small range of fields do the energies of the Rydberg state and the image state overlap, a prerequisite for resonance effects and distinct differences for electric fields at which resonant charge transfer is possible compared to non-resonant fields can be expected. It is therefore believed that by studying the surface ionisation process as a function of collisional

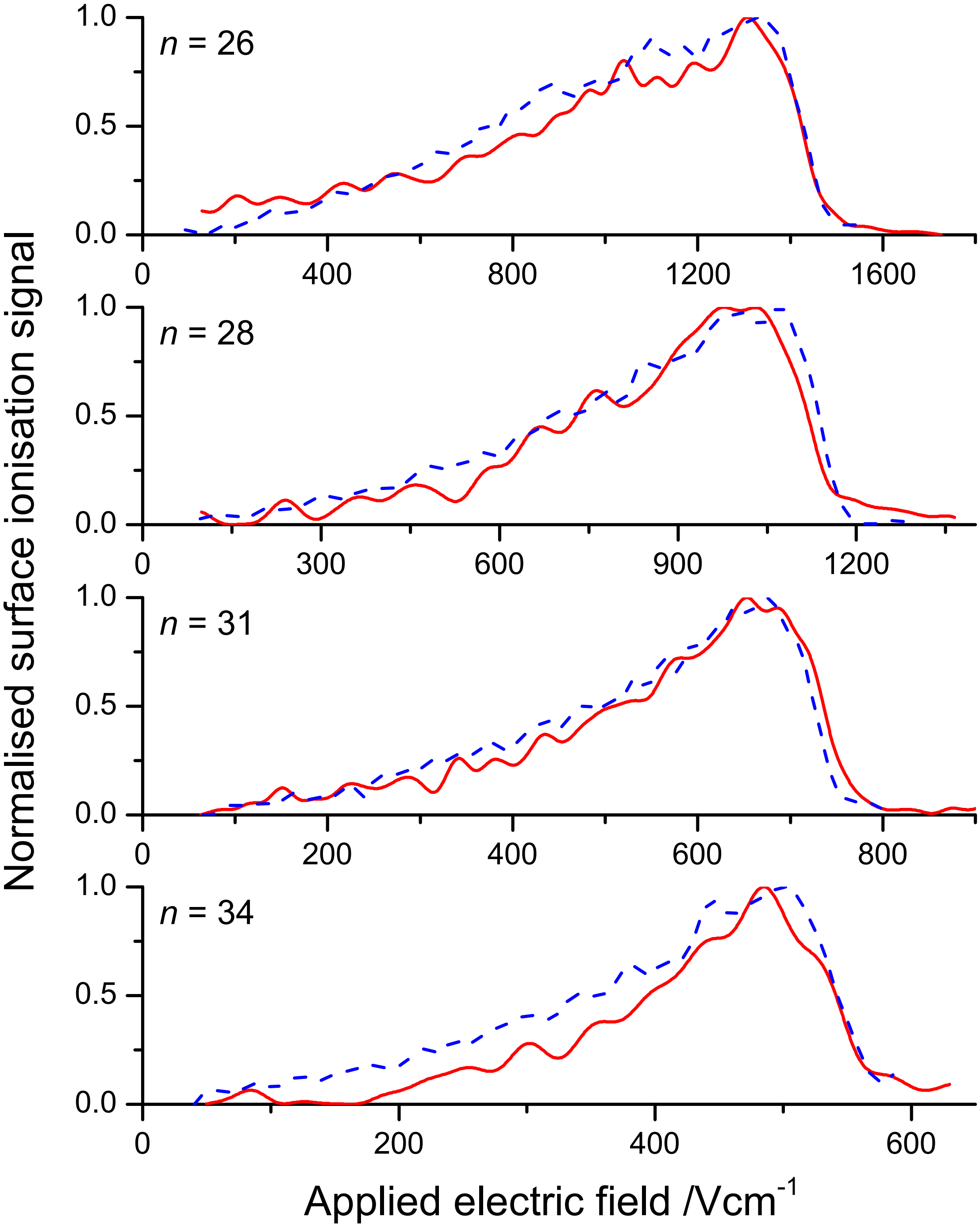

Figure 6.4: Integrated surface ionisation signal as a function of applied field for $k \simeq 0$ Stark states measured with a Cu(100) single crystal surface. For comparison, the results measured with the newly modified setup (full red lines) are shown together with the results acquired in earlier experiments [37] (blue dashed lines). For both sets of results the collisional velocity is chosen as $v_\perp = 650\ \mathrm{m\,s^{-1}}$ and the impact angle is 15°.

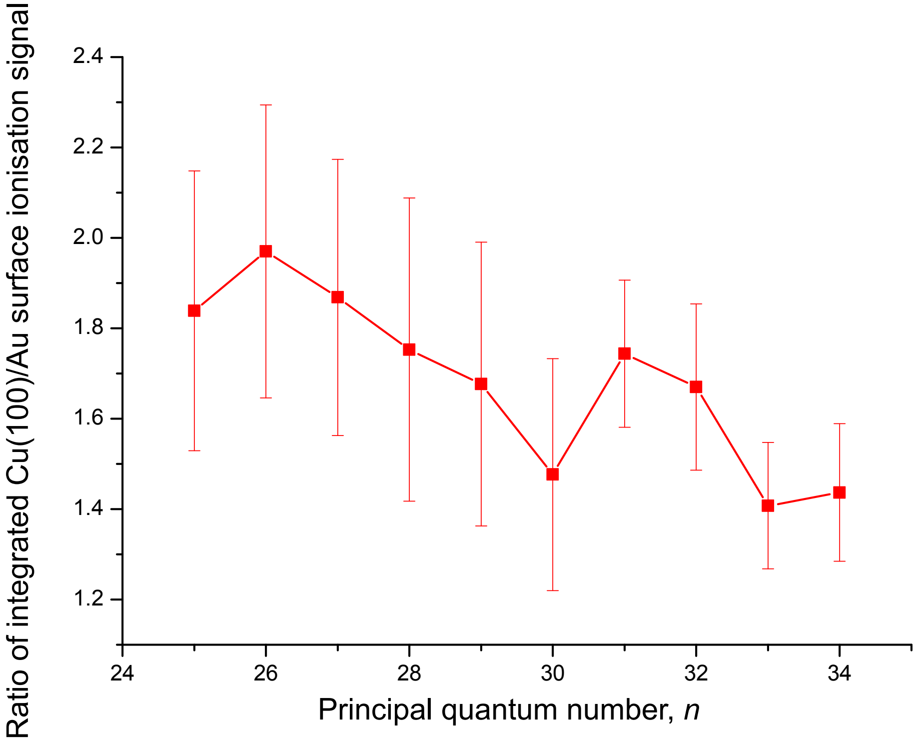

Figure 6.5: Ratio of the integrated surface ionisation profiles of H-atom Rydberg incident on Cu(100) and Au surfaces as a function of principal quantum number. The collisional velocity is set to $v_{\perp} = 650$,s^{-1}. The ratio peaks at $n = 26$ and 31 which is in good agreement with previous results measured by So et al. [37].

velocity of the Rydberg atom additional information about resonant effects can be obtained. Increasing the collisional velocity of the incoming Rydberg atom leads to a reduction of detection efficiency as greater fields are required to pull the ion away from the surface (see Section 2.2.2). In addition, an increase in velocity may also lead to ionisation happening over a wider range of distances. However, for resonant fields an increased ionisation rate and therefore increased detection efficiency can be expected even at relatively high collisional velocities.

In principle, there are two different ways of recording the data needed to analyse the velocity dependence of the surface ionisation process. One could either measure the surface ionisation as a function of applied electric field at a constant velocity for a range of velocities (essentially the same technique as used in the previous chapters) or one could measure the surface ionisation at a constant field while varying the collisional velocity. In both cases the collisional velocity can be controlled by varying the delay between the photodissociation laser and the two excitation lasers as described in Section 3.1.2. While both techniques should give the same results, instabilities in the signal for example caused by a change in laser power might lead to differences and it might therefore be of interest to compare results obtained with both methods. There is one difficulty in scanning the velocity at a given electric field, which is that the signal obtained at every data point recorded needs to be normalised individually to the field ionisation signal (this is due to the detection probability depending on the velocity as the time between excitation and extraction changes). When scanning the field at a fixed velocity on the other hand, one normalisation factor can be used for the whole surface ionisation profile. While both methods were used for the work presented in this chapter, most of the data was therefore collected by scanning the electric field at fixed velocity. As in the previous section, only the surface ionisation signal of mid-manifold Stark states ($k \simeq 0$) in the range $n = 25 - 34$ at a range of collisional velocities ($v_{\perp} = 320\ \mathrm{m\,s^{-1}} - 1000\ \mathrm{m\,s^{-1}}$) and electric fields was investigated to minimise the effect the field has on the energy of a selected Rydberg state (see Figure 2.13).

Figure 6.6 shows surface ionisation profiles recorded at a range of collisional velocities ($360\ \mathrm{m\,s^{-1}}$ - $870\ \mathrm{m\,s^{-1}}$) for $k \simeq 0$ Stark states over a range of principal quantum numbers. As expected, increasing detection efficiency can be observed for slower velocities both in terms of overall detection probability as well as the low-field tail of the profile. This effect appears to saturate at a velocity of about $360\ \mathrm{m\,s^{-1}}$ as no significant signal increase can be detected for slower velocities.

In order to compare different principal quantum numbers, it is useful to analyse the surface ionisation as a function of a scaled electric field. Equation 2.10 shows that the electric field is expected to scale with n^{-4}. However, it was shown by So et al. that there is a discrepancy from this behaviour [37]. The fields for the work presented here are therefore scaled by an empirical parameter of $n^{-3.8}$ instead, which is chosen in such a way that the high field cut-off of all the principal quantum numbers investigated appears at the same scaled electric field.

Figure 6.7 shows the surface ionisation signal of the $k \simeq 0$ Stark states in the range $n = 25 - 34$ as a function of scaled electric field ($n^{-3.8}$a.u.) for a range of collisional velocities. The surface ionisation signal is again normalised to the integrated field ionisation signal at the corresponding velocity and the traces follow the before observed behaviour of an increase in detected signal with decreasing collisional velocity. The high field cut-off's all roughly coincide at a value of approximately $0.071\, n^{-3.8}$, marked by a black dashed line.

When carrying out these experiments it was anticipated, that for those principal quantum numbers for which resonance effects with image states were expected, a different

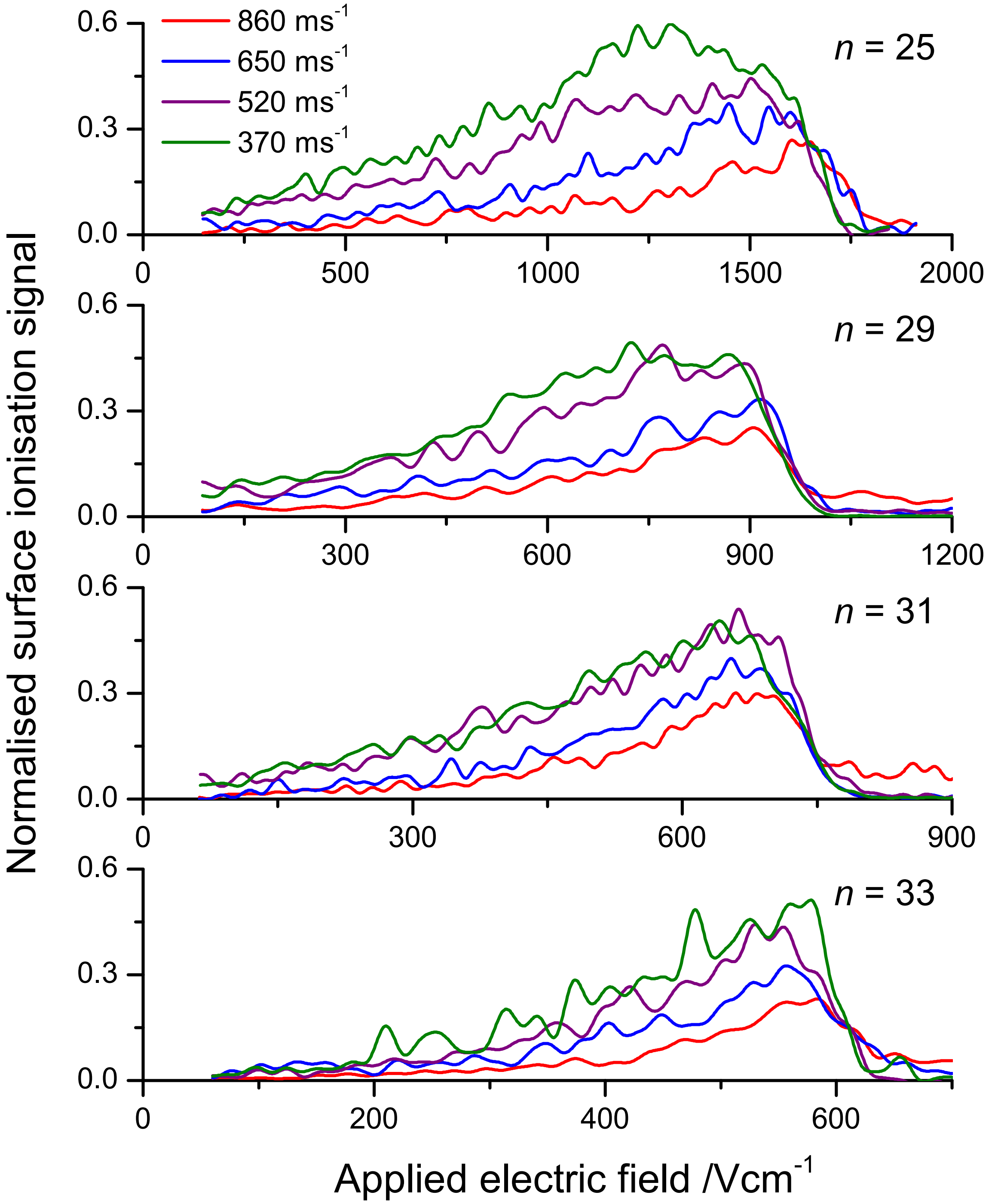

Figure 6.6: Surface ionisation signal as a function of applied electric field for H-atom Stark states impacting on a Cu(100) surface. Profiles were recorded for the centre-manifold states ($k \simeq 0$) for a range of principal quantum numbers. Collisional velocities range from 360 $\mathrm{m\,s^{-1}}$ to 870 $\mathrm{m\,s^{-1}}$.

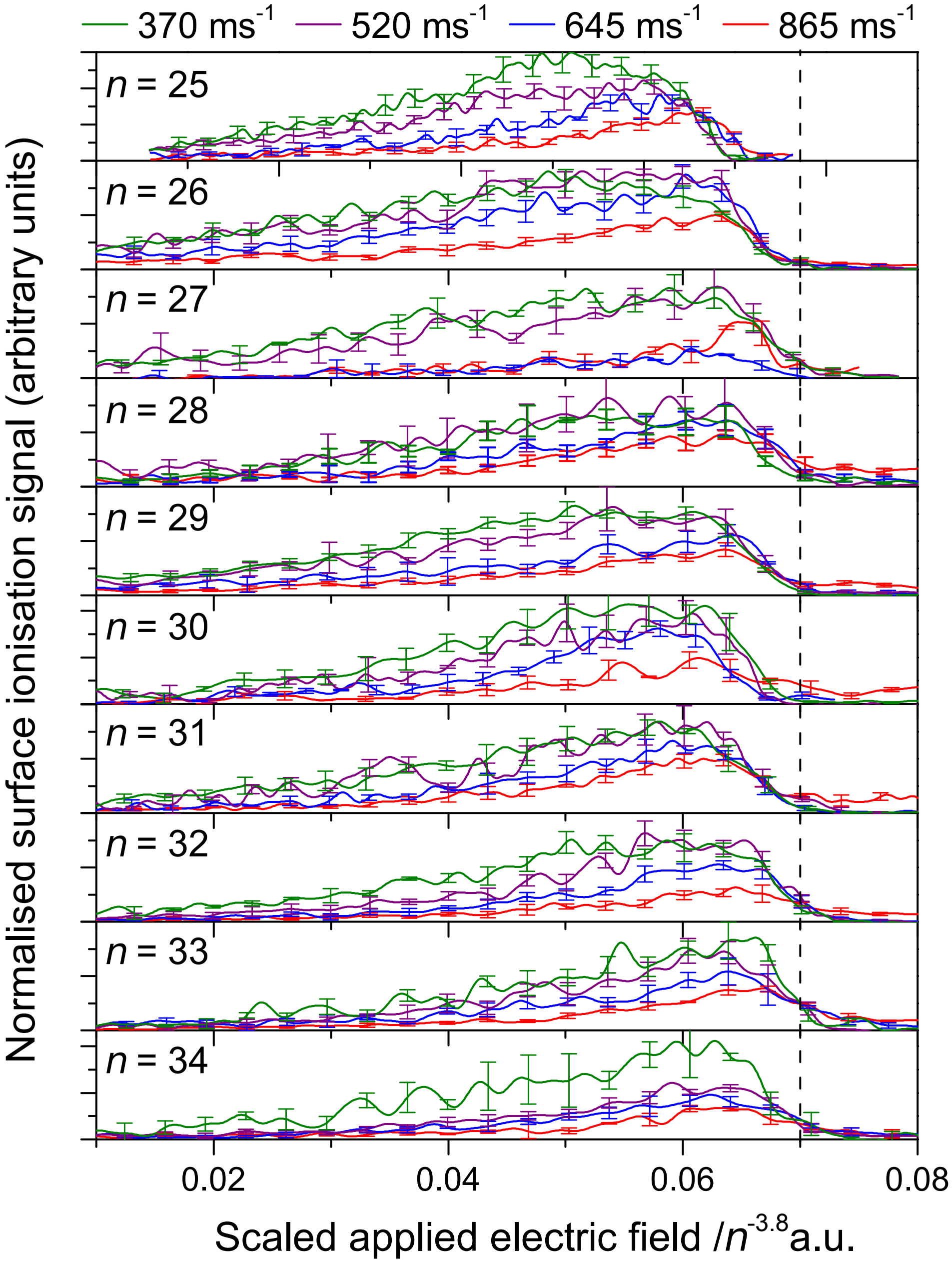

Figure 6.7: Surface ionisation signal (normalised by the field-ionisation signal) as a function of scaled electric field for $k \simeq 0$ Stark states in the range $n = 25-34$. For each principal quantum number four different velocities are shown: 370 $\mathrm{m\,s^{-1}}$ (green lines), 520 $\mathrm{m\,s^{-1}}$ (purple lines), 645 $\mathrm{m\,s^{-1}}$ (blue lines) and 865 $\mathrm{m\,s^{-1}}$ (red lines). The electric field is scaled by an empirical parameter of $n^{-3.8}$ as described in the text, leading to an almost constant high field cut-off of $\approx 0.071\ n^{-3.8}$a.u. (dashed black line).

comparative behaviour of the profiles as a function of velocity would be observed. However, analysing the different profiles individually does not lead to any stronger indication for the presence of resonance effects. Therefore a different approach to analysing the available data is needed. Figure 6.8 shows 3D contour plots of selected principal quantum numbers in which the normalised surface ionisation signal is plotted as a function of both applied field and velocity. These plots show the recorded surface ionisation profiles colour-coded (red = highest detection efficiency) plotted parallel to the y-axis for velocities in the range 325 $\mathrm{m\,s^{-1}}$ to 995 $\mathrm{m\,s^{-1}}$. While there are many data points along the field axis, profiles were only measured at ten different velocities and the signal between these points is thus interpolated.

In order to get an idea what an idealised contour plot (=no resonance effects) should look like, the semi-empirical over-the-barrier ionisation model (see Section 2.3.1) can be modified to roughly model the detected surface ionisation profiles. By replacing the principal quantum number n with an effective quantum number ν and adjusting ionisation width (σ) and shift of ionisation distance (δ) it is possible to get a relatively good qualitative fit of the detected surface ionisation profiles. The effective quantum number is chosen such that the high field cut-off of the theoretical and experimental curves coincide, while the other two parameters are then varied to give the best overall fit for the whole velocity range investigated. This is demonstrated in Figure 6.9 which presents the experimentally obtained profiles for the $n = 28$, $k = -1$ Rydberg state at collisional velocities of 325 $\mathrm{m\,s^{-1}}$ and 865 $\mathrm{m\,s^{-1}}$, a state for which no resonance with an image state is expected. For $n = 28$ the optimal parameters are $\nu = 26.8$, $\sigma = 4n^2 a_0$ and $\delta = 1.5n^2$. The two velocities shown in this figure present two extremes of the investigated velocity range and while the peak height of the model curves are overestimated at fast velocities and underestimated detection at low ones, they none the less give a decent estimate of the experimental results.

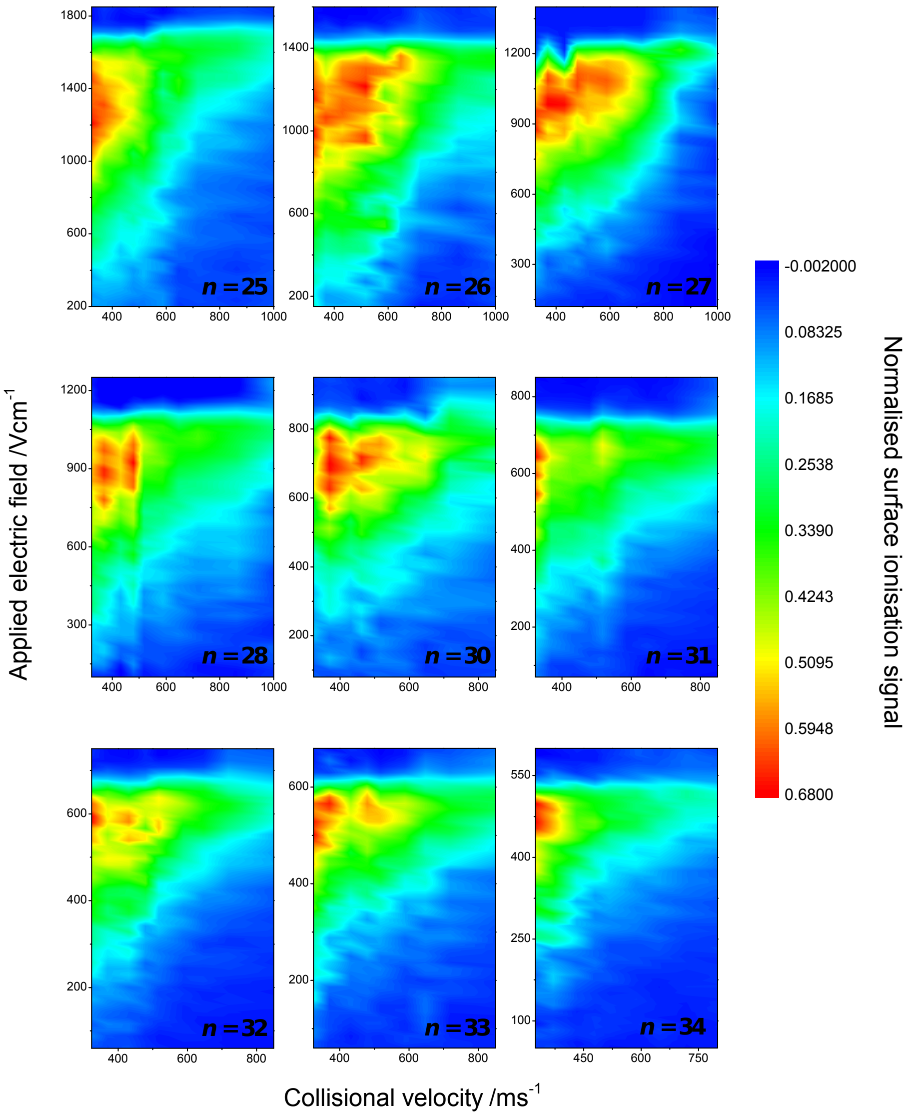

Figure 6.8: Contour plots showing surface ionisation profiles normalised by the field ionisation signal of selected mid-manifold Stark states in the range $n = 25 - 34$ measured at a Cu(100) as a function of both collsional velocity and applied field.

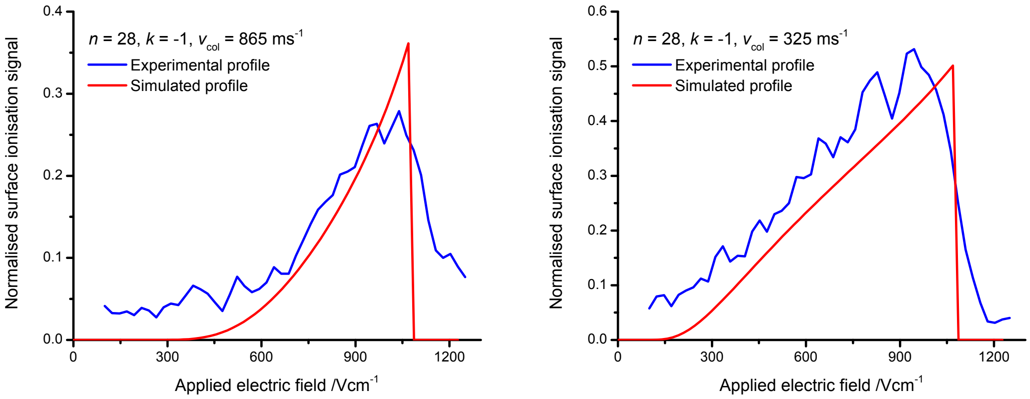

Figure 6.9: Simulated surface ionisation profiles (full red lines) of the $n = 28$, $k = -1$ Rydberg state at two different collisional velocities, $v_\perp = 865\ \mathrm{m\,s^{-1}}$ (left) and $v_\perp = 325\ \mathrm{m\,s^{-1}}$ (right). The fitting procedure is based on the OTB semi-empirical model and is explained in detail in the text. The fitting parameters used were $\nu = 26.8$, $\sigma = 4n^2a_0$ and $d = 1.5n^2$. Experimentally meassured surface ionisation profiles are also shown for comparison (full blue lines).

Subsequently, the simulated profiles can be converted into a 3D contour plot showing signal as a function of collisional velocity and applied electric field, analogous to the experimental data as demonstrated in Figure 6.10 a). Comparing the simulated contour plot with the experimental data in Figure 6.8 shows good overall agreement. The highest signal is detected at low velocity and high electric fields and the detection efficiency decreases with increasing field or velocity. While some deviation from this ideal behaviour can be seen in the experimental data, it is unclear whether these are an indication for resonance effects. The results presented by So et al. suggest that resonance effects should be observed for $n = 26$ and $n = 31$ [37]. Here, the contour plot for $n = 26$ shows clear deviation from the expected trend, as the detection efficiency stays surprisingly high with decreasing electric field until it suddenly drops at a field of approximately $900\ \mathrm{V\,cm^{-1}}$. However, this electric field does not correspond to the field position of the resonance, which is expected to be located somewhere around $500\ \mathrm{V\,cm^{-1}}$ (see Figure 6.1).

It is possible to relate an applied electric field to a minimum detectable ionisation

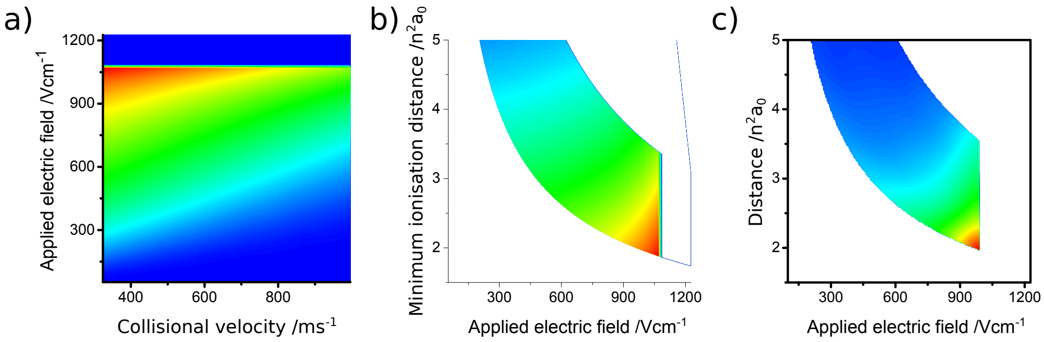

Figure 6.10: Calculated contour plots for signal as a function of a) collisional and applied electric field and b) applied electric field and distance. c) ionisation rate as a function of applied field and distance.

distance:

$$\vec{F}_{\min}(D_i, T_\perp) = Z_c \left[\frac{1}{2D_i} + \sqrt{\frac{T_\perp}{D_i}} \right]^2 . \tag{6.1}$$

From this relationship the electric field needed to repel an ion from the surface can be calculated [43] (see Section 1.7 for details). Using surface ionisation profiles recorded at different velocities it is now possible to decouple the applied electric field from the ionisation distance. The minimum detectable ionisation distance and thus the plots of signal vs field and velocity can be transformed into plots of signal vs field and minimum ionisation distance. Figure 6.11 shows 3D contour plots of the normalised measured surface ionisation signal as a function of applied electric field and ionisation distance for the same principal quantum numbers as presented in Figure 6.8. For comparison, Figure 6.10 (b) shows the same plot for the corresponding simulated profiles of the $n = 28$ Rydberg state. In general, the measured data in Figure 6.11 corresponds well with the simulation. As for Figure 6.8, the most prominent difference from the expected behaviour is observed for the $n = 26$, $k = -1$ state. For this state, there still is significant ionisation at large distances from the surface at electric fields near 600 V cm^{-1}. A similar observation can be made for $n = 25$ where an increased ionisation appears at even lower fields. For the $n = 31$ state, which should also possess a resonance the difference from the expected behaviour is less distinct. However, for this state the resonance effect would be harder to detect with the method described here as the resonance is expected to appear at an electric field of roughly 700 $\mathrm{V\,cm^{-1}}$, a field which is very close to the maximum of the surface ionisation signal and thus always possesses a relatively high detection efficiency.

In order to be able to observe resonance effects close to the peak position of a surface ionisation signal it might be advantageous to rather look at the ionisation rate instead. In this case, a resonance would reveal itself as an unusually high rate (at a certain field) at a surprisingly great distance from the surface. As the ionisation rate not only depends on the applied electric field, but also varies with collisional velocity, this is not straight forward. In the experiments presented here, the detected signal is normalised by the integrated field ionisation signal as measured at the beginning of the surface ionisation gate of the TOF trace thus representing an ionisation probability P. As described previously, the number of measurements along the collisional velocity axis is rather small (surface ionisation profiles for 10 different velocities were measured) and in order to get a meaningful 3D plot, these gaps were filled by interpolation.

Differentiating the ionisation probability (i.e. the probability that a given Rydberg H-atom has ionised by the time it reaches the minimum ionisation distance, D_{min}) with respect to the minimum ionisation distance at a constant electric field and subsequently multiplying by the collisional velocity results in an ionisation rate $\zeta_F(d)$ for every point of the plot:

$$\zeta_F(d) = \frac{\partial P}{\partial t} = \left(\frac{\partial P}{\partial D_{\mathrm{min}}}\right)_F \cdot v_\perp. \qquad (6.2)$$

Due to fluctuations in the detected signal this might result in negative rates for points when the detected ionisation profiles show a decrease in signal at an increase in field. As this is deemed infeasible, a 10 point nearest neighbour smoothing function is used

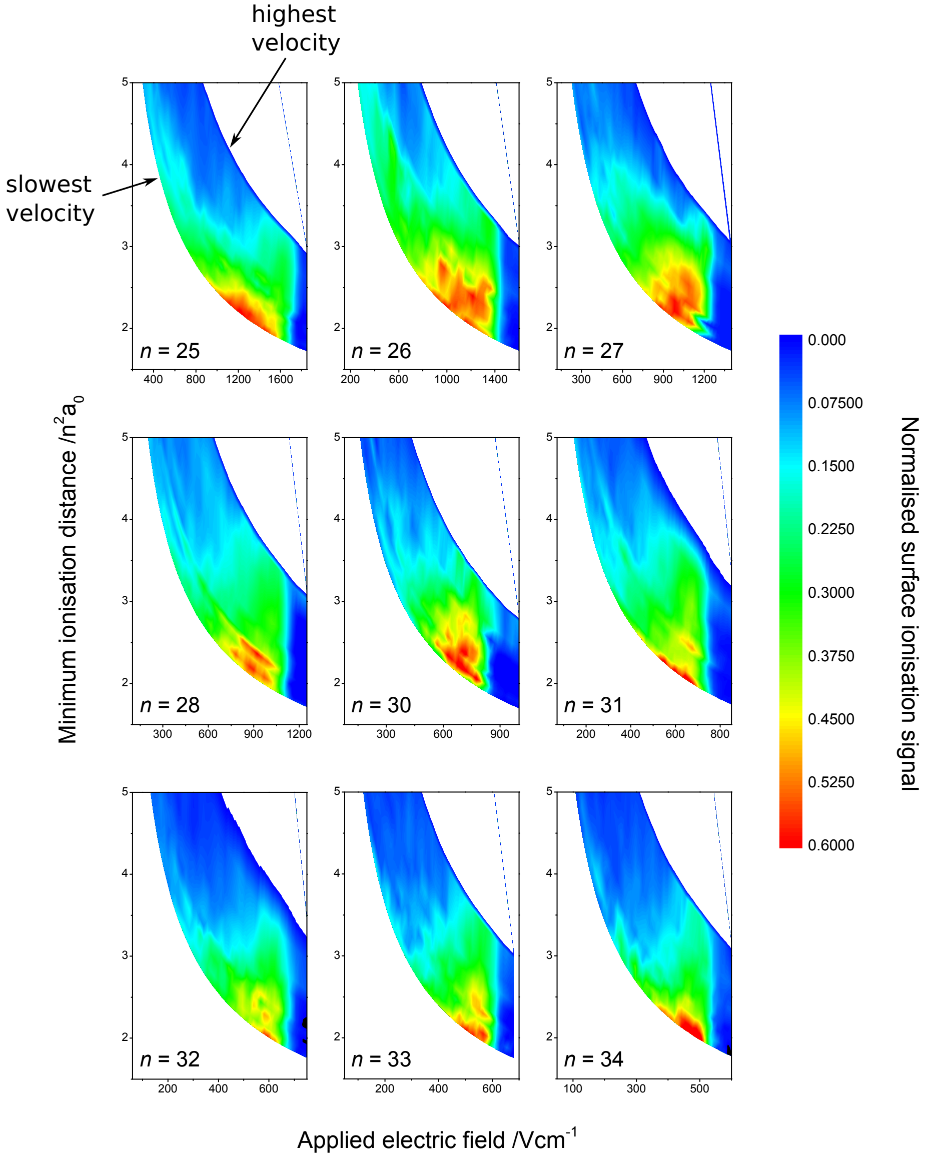

Figure 6.11: Contour plot showing normalised surface ionisation profiles as a function of applied electric field and minimum ionisation distance for selected mid-manifold Rydberg states in the range $n = 25 - 34$.

on the calculated ionisation rate in both dimensions and all residual negative values are replaced with an ionisation rate of $\zeta_F(d) = 0\,\mathrm{s}^{-1}$.

Figure 6.12 shows contour plots of ionisation rate plots calculated in this way, as a function of applied field and ionisation distance for Rydberg H-atoms interacting with a Cu(100) surface. Rates have also been calculated for the simulated data of the $n = 28$ state for comparison and the results for this are shown in Figure 6.10 (c). Comparing the experimental results with the simulated contour plots shows that most principal quantum numbers follow closely the trend of the theoretical model with the highest rate being observed near the bottom vertex of the plot. The rate increases both with increasing field and decreasing distance. One difference is that after the high field cut-off the rate immediately drops to $\zeta_F(d) = 0\,\mathrm{s}^{-1}$ for the simulated plots while the decrease is more gradual for the experimental data.

Close investigation of the experimental rates reveal three states which show the distinct feature of a high ionisation rate at a large distance from the surface, expected for resonantly enhanced surface ionisation. The $n = 26$, $k = -1$ state exhibits a very high ionisation rate at an applied electric field of approximately 500 $\mathrm{V\,cm^{-1}}$ and at a distance from the surface of approximately $4.25\,n^2\mathrm{a}_0$. This is in very good agreement with the expected field of the resonance as predicted by So et al. (see Figure 2.14) [37]. The neighbouring $n = 25$ Rydberg state also shows signs of a resonance, barely capturing this effect at a field of approximately 400 $\mathrm{V\,cm^{-1}}$, an observation not identified in previous experiments. In the work by So, the energy of the image-states of the copper surface were shifted upwards by a factor of 5×10^{-5} a.u. to reflect perturbation of these states by the Rydberg atom. However, this shift was mainly chosen to fit experimental observations and is not a result of theoretical calculations. Using the uncorrected energies instead, a resonance is indeed predicted for the $n = 25$, $k = 0$ Rydberg state of atomic hydrogen. By assuming that the introduced shift only

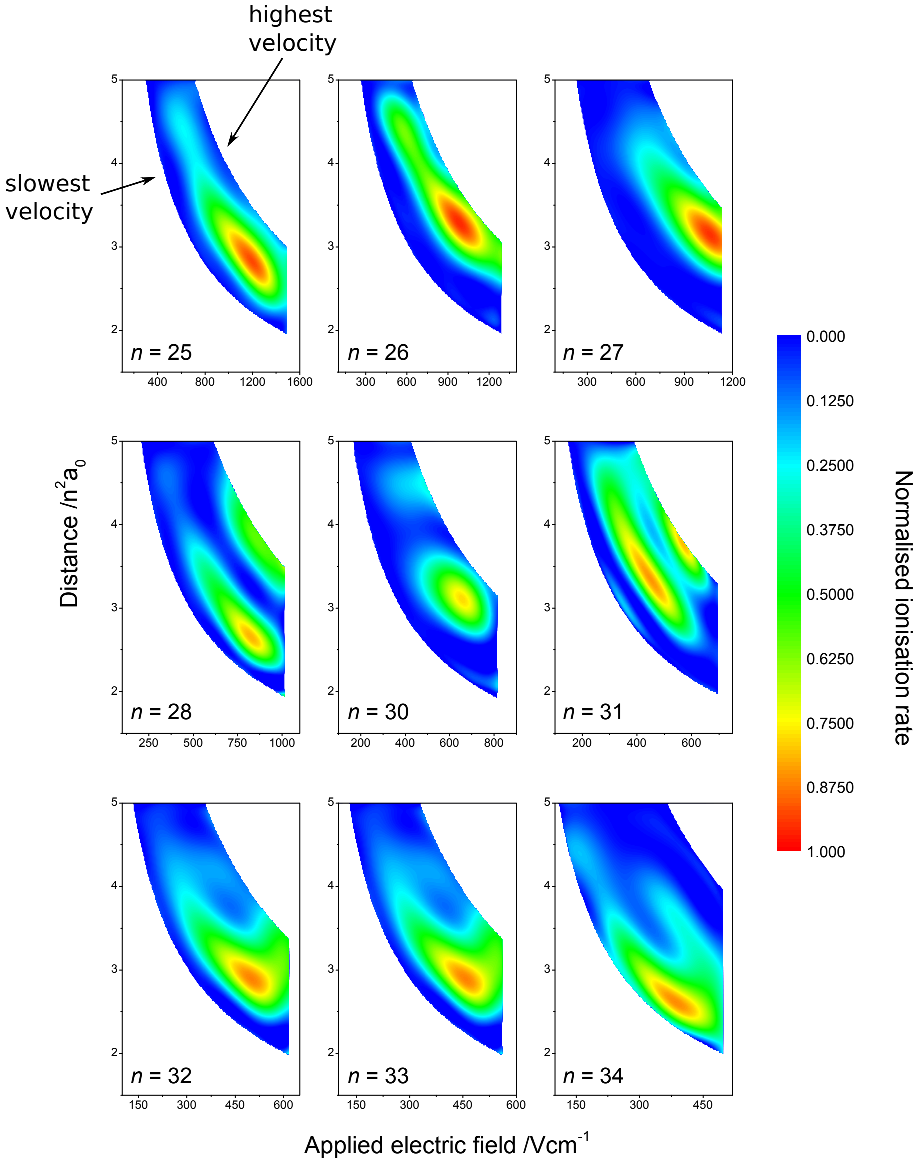

Figure 6.12: Contour plot showing the Ionisation rate ζ of mid-manifold Rydberg states in the range $n = 25 - 34$ near a Cu(100) surface as a function of applied electric field and minimum ionisation distance.

represents an upper limit to the perturbation of the Rydberg state and that these resonances thus possess a certain width, the experimental observation made for $n = 25$ can be explained.

The second state which is expected to show a resonance effect in the n-range investigated is $n = 31$. For this state, the resonance is supposed to be located at an electric field that coincides with the peak of the surface ionisation profiles (~ 600 V cm^{-1}). While the analysis methods discussed in the previous paragraphs were not sensitive in this field range, analysing the ionisation rate provides a way to overcome this problem. In the corresponding plot of Figure 6.12, the observed ionisation rate at the resonance field, does not decrease with increasing distance but stays high almost over the whole detectable range of distances, exactly the behaviour expected for resonance charge transfer to an image state.

Analysing the ionisation rate as a function of applied electric field and distance thus seems to confirm the occurrence of resonant charge transfer from the hydrogen Rydberg atom to image states of a single crystal Cu(100) surface. However, it would be advantageous to investigate a wider range of principal quantum numbers to test the wider applicability of this method. Experimental work is currently being carried out seeking signs of resonance effects in the range $n = 20 - 25$.

6.3 Conclusion

The interaction of H-atom Rydberg states with a Cu(100) band-gap semi-conductor has been investigated. At first, investigations were carried out with mid-manifold Stark states ($k \simeq 0$) of a range of principal quantum numbers at a single collisional velocity to test the repeatability of previous experimental results. The recorded data is analysed by integrating the surface ionisation profiles and scaling them with integrated profiles of the same states measured with a gold surface and subsequently plotting this ratio as a function of principal quantum number. Analogous to previous results by So et al., the scaled detection efficiency shows peaks for $n = 26$ and $n = 31$ [37].

In order to match experimental results with theoretical predictions the energies of the image and surface states in the energy range of the investigated atomic hydrogen Rydberg states need to be known. These energies have been calculated for low lying image states using the one-electron pseudo-potential devised by Chulkov et al. As they form a Rydberg series, it is straight forward to calculate their energies in the energy range of interest [95]. To explain the observed peaks in the Cu(100)/Au signal ratio, the calculated energies needed to be shifted by 5×10^{-5} a.u which can be interpreted as a perturbation of the image state energies by the Rydberg atom. However, as with the results of So et al., the relative errors of the observed detection efficiencies were too large as to clearly confirm the presence of resonance effects.

To improve the sensitivity for resonance effects, the detection probability was measured as a function of collisional velocity of the incoming Rydberg atom. Varying the collisional velocity offers the possibility to decouple the applied electric field from ionisation distance. By changing the collisional velocity, a given minimum surface ionisation distance corresponds to a different field and resonance effects are expected to lead to increased ionisation at greater than expected distances for resonant fields. Plotting detected signal as a function of applied electric field it is possible to identify resonances at fields that lie in the tail end of the corresponding surface ionisation profile. This was shown for the $n = 26$ Rydberg state which possesses a resonance with an image state at a field of $\sim 500\,\mathrm{V\,cm^{-1}}$.

This approach is not susceptible to resonance effects at fields that lie near the high field cut-off of the corresponding surface ionisation profile. However, it was demonstrated that this restriction could be overcome by converting the ionisation probability to an ionisation rate and plotting this rate as a function of applied field and ionisation distance. Similar to before, these plots show an increase in ionisation rate at large distances from the surface for resonant fields as could be observed for both the $n = 26$ as well as for the $n = 31$ Rydberg states of atomic hydrogen.

It was thus possible to successfully demonstrate the possibility to use Rydberg atoms to probe the electronic structure of a surface. The next step will be to increase the range of Rydberg states investigated to show that resonance effects can be detected experimentally over a wider range of principal quantum numbers.

Chapter 7

Towards hydrogen 2s Rydberg states

There are several reasons which might raise an interest in low-n Rydberg states. It was mentioned in Chapter 5 that in order to make Rydberg states and nanoparticles more comparable in size, a smaller classical orbital radius is needed. Another interesting experiment would be to investigate a phenomenon called quantum reflectivity, by which $2s$ states of atomic hydrogen can be scattered off a cold surface without undergoing ionisation [119]. As a first step on the road to such experiments, this chapter presents a novel approach to populating the $2s$ state of atomic hydrogen and demonstrates its experimental implementation.

The lowest energy excited state of atomic hydrogen is $n = 2$. While the $2p$ states ($^2\mathrm{P}_{\frac{3}{2}}$ and $^2\mathrm{P}_{\frac{1}{2}}$) are readily accessible by optical means via one colour excitation using Lyman-α radiation, they have a rather short lifetime of approximately 1.6 ns [120], making it nearly impossible to study their surface interaction. The $2s$ state ($^2\mathrm{S}_{\frac{1}{2}}$) on the other hand possesses an effectively infinite lifetime with respect to single-photon radiative decay due to parity requirements such that the lifetime is limited by a two-photon decay process ($\tau_{2\mathrm{s}} \approx {}^1\!/_8\,\mathrm{s}$ [121]). In principle it is possible to populate this state by a two-photon transition at twice the Lyman-α wavelength. However, this is a problematic approach because of the high likelihood of ionisation by the focused laser beam needed for this process.

It is possible to overcome this problem using an electric field. As mentioned in Section 1.4, in the presence of an electric field l no longer is a good quantum number and the $2s(^2\mathrm{S}_{\frac{1}{2}})$ and $2p(^2\mathrm{P}_{\frac{1}{2}})$ states are coupled together forming a hybrid Stark state where the coupling strength depends on the electric field strength. This leads to a (field dependent) reduction of the lifetime at low field of the $2s$ Rydberg state (the state with predominant $2s$ character) given by the following relationship [122]:

$$W_F = \alpha F^2 = 2780 F^2\, s^{-1} \tag{7.1}$$

where W_F is the decay rate and F the electric field in V cm^{-1}.

In 1959, Fite et al. experimentally measured the effect of applying an electric field on the lifetime of the $2s(^2\mathrm{S}_{\frac{1}{2}})$ state of atomic hydrogen [123]. This was done by exciting atomic hydrogen from the ground to the $2s(^2\mathrm{S}_{\frac{1}{2}})$ state by electron impact and subsequently detecting the photons emitted during the $2p(^2\mathrm{P}_{\frac{1}{2}})$ to $1s(^2\mathrm{S}_{\frac{1}{2}})$ relaxation process. A variable electric field could be applied in the detection region in order to control the amount of coupling between the $2s(^2\mathrm{S}_{\frac{1}{2}})$ and $2p(^2\mathrm{P}_{\frac{1}{2}})$ states and thus controlling the decay rate. This way, they measured a lifetime of approximately 2.4 ms. It was suggested that stray fields might be responsible for this relatively 'short' lifetime as electric fields of approximately 0.7 V cm^{-1} would be enough to lead to the observed lifetime.

In principle it should be possible to use a similar approach to populate the $2s(^2\mathrm{S}_{\frac{1}{2}})$ state in a one photon excitation. By applying a large enough electric field during the excitation process, a hybrid $2s$-$2p$ state will initially be populated. This state has a limited lifetime, of only a few nanoseconds, as given by Equation 7.1. Should it be possible to ramp down the electric field fast enough following excitation and thus decouple the 2*s* from the 2*p* state, a fraction of the excited H-atoms will be trapped in the metastable $2s(^2\mathrm{S}_{\frac{1}{2}})$ state. The other fraction, populating the $2p(^2\mathrm{P}_{\frac{1}{2}})$ state will decay away within a few nanoseconds.

There are two main experimental challenges to this project. In order to avoid loss of population due to limited lifetime of the 2*s*-2*p* hybrid state, the applied electric field needs to be ramped down from several hundred $\mathrm{V\,cm^{-1}}$ to 0 $\mathrm{V\,cm^{-1}}$ within a few nanoseconds. From equation 7.1, it can be deduced that a field of approximately 350 $\mathrm{V\,cm^{-1}}$ should be large enough to completely mix the two states. At this field, the calculated lifetime will be about twice that of the the 2*p* state, indicating an equal mixture. Second, the field needs to be ramped down at exactly the correct time at the end of the laser excitation pulse for the same reason and thus exact nanosecond control of the timing is needed. The experiments presented below were performed with a custom made, in-house built fast voltage pulser, which fulfils both of the aforementioned requirements.

The experimental setup used for these experiments is the same as in the previous chapters. The only difference is that the usually applied Stark field is replaced by a mixing-field of approximately 400 $\mathrm{V\,cm^{-1}}$ during the first step of the excitation process, which is ramped down within 5 ns synchronously with the excitation laser pulse. Subsequently, a 2nd laser pulse is fired at a variable delay, further exciting the hydrogen atom from the intermediate state to the $n = 34$ Rydberg state. After a further time delay of approximately $1 - 2$ µs an extraction field of approximately $+1000\ \mathrm{V\,cm^{-1}}$ is applied to field ionise the Rydberg atom and repel the resulting ions away from the surface towards the detector. In this way, the population of the $n = 2$ state can be determined as a function of the pump-probe delay.

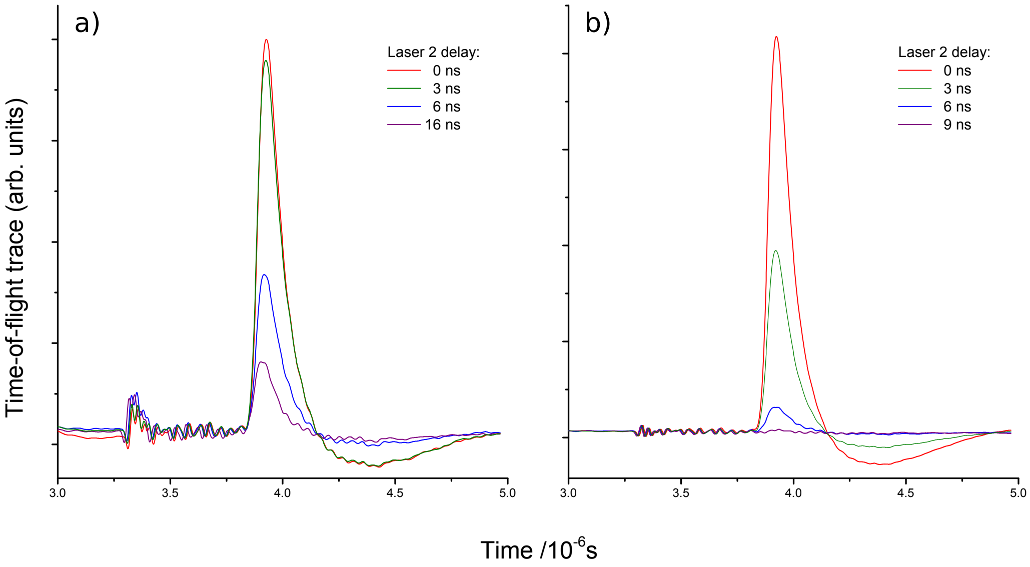

Figure 7.1: Experimental time-of-flight profiles showing the detected field ionisation signal. (a) traces recorded in the presence of a $2s$-$2p$ mixing field of approximately 400 V cm^{-1}. (b) traces recorded without a mixing field. TOF traces recorded at different delays between the two excitation lasers are shown in different colours. The exact excitation process is described in detail in the text.

Figure 7.1 shows the resulting time-of-flight traces, detected at a range of different delays between the two excitation lasers ($0 - 30$ ns), detected both with (left) and without the $2s$-$2p$ mixing field (right). While both images show a strong field ionisation peak for the $n = 34$ state at a delay of 0 ns, there are distinct differences once a delay between the two lasers is introduced. For the field-free case the detected signal rapidly disappears, in accordance with the short lifetime of the $2p$ state. The signal for excitation within the presence of the mixing field also drops off quickly but after about 5 ns settles at a peak height of $\sim 20 - 25\%$ of the original peak.

For a more quantitative analysis, the detected signal is integrated, normalised by the maximum signal at a delay of 0 ns and plotted as a function of laser 2 delay in Figure 7.2. These plots confirm the first visual impression. Without the mixing-field, the signal completely disappears for delays greater then ~ 5 ns, due to the short lifetime of the $2p$ intermediate state. This impression can be further confirmed by fitting the peak with a Gaussian function, using the well known half-life time of the 2*p* state of atomic hydrogen of $\tau_{2\mathrm{p}} = 1.6\,\mathrm{ns}$ (red dashed line). In the presence of the mixing field however, the signal does not disappear for greater delays but after the initial drop stabilises and it can be detected to delays up to approximately 40 ns, indicating that part of the population indeed ends up in the 2*s* state. Again, the detected signal can be modelled with a relatively high degree of accuracy, by using two Gaussian functions, each of which represents either the 2*s* and the 2*p* state. Assuming a 1:3 *s* to *p* mixing ratio and using a decay time of $\tau_{2\mathrm{p}} = 3.2\,\mathrm{ns}$ for the 2*p* state ($\sim 2\times$ of the field-free lifetime), this leads to lifetime of the 2*s* state of $\tau_{2\mathrm{s}} \approx 20\,\mathrm{ns}$. The mixing ratio is approximated in that not only is the $2p(^2\mathrm{P}_{\frac{1}{2}})$ state mixed with the $2s(^2\mathrm{S}_{\frac{1}{2}})$ state but the $2p(^2\mathrm{P}_{\frac{3}{2}})$ state also contributes to the hybrid state. It should be noted that there is an unusual sudden drop in signal after $\sim 20 - 25$ ns, the reason of which is not known. The origin of this observation is so far unknown but it is currently believed that this is due to a technical limitation of the experimental setup. For example, at such delays the experimental setup is operated close to its lower detection limit and the MCP voltage needs to be repeatedly adjusted, which might affect the normalisation process.

The measured lifetime of the 2*s* state is considerably shorter than expected. It can thus be assumed that there are other factors contributing to the observed lifetime, such as the hydrogen atoms moving out of the laser focus or the presence of stray fields. The incoming beam of atomic hydrogen has a velocity of approximately 2500 $\mathrm{m\,s^{-1}}$, or 0.0025 $\mathrm{mm\,ns^{-1}}$, indicating that after 40 ns, the atoms have travelled approximately 0.05 mm. While this should not affect the observed detection probability for two perfectly aligned lasers, it might at least contribute to the overall lifetime should one of the laser beams be aligned at the edge of the other laser. The effect of stray fields is harder to gauge. Equation 7.1 allows one to calculate the stray field needed to obtain the observed decay rate. A lifetime of 20 ns would thus relate to a stray field

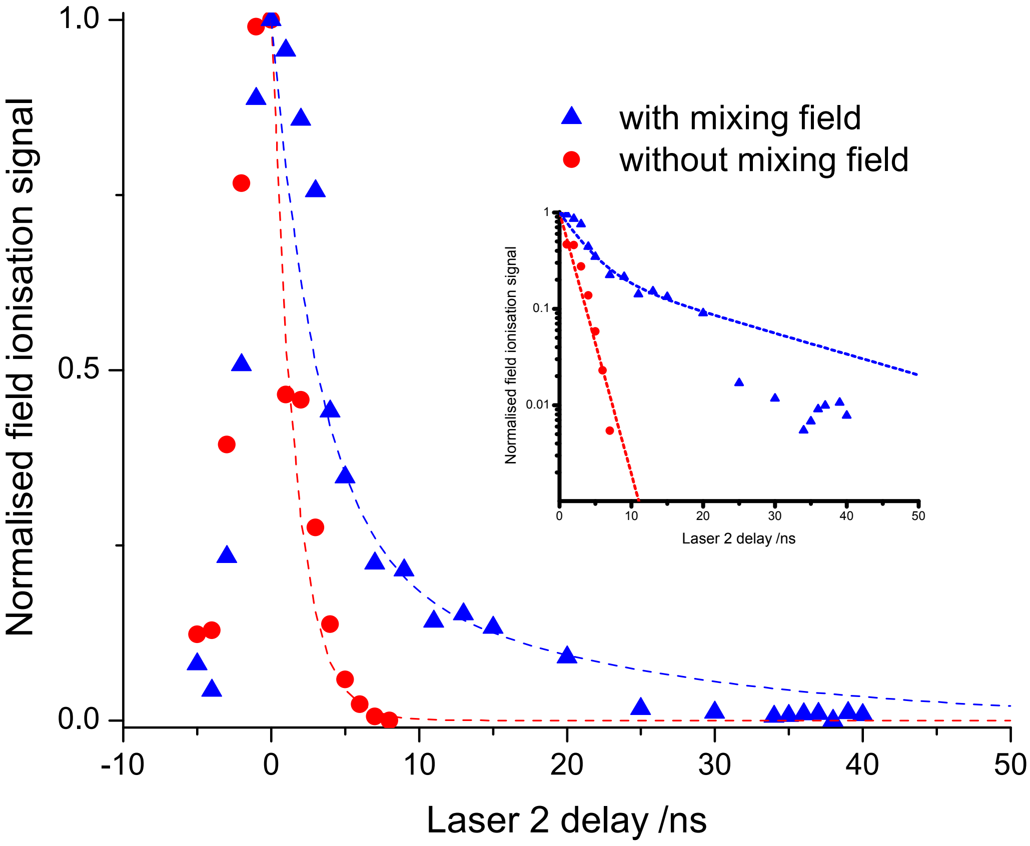

Figure 7.2: Integrated field ionisation signal as a function of delay between the two excitation lasers for both cases, with the mixing field present (blue triangles) and without the mixing field (red circles). Inset: same plot on a log-scale.

of approximately 130 $\mathrm{V\,cm^{-1}}$, an unrealistically high value. Therefore other possible reasons affecting the lifetime, such as the still rather slow ramp-down time, will have to be considered. Furthermore, it is assumed that as the field is ramped down the Stark levels are followed adiabatically, resulting in a statistical mix of $2s$ and $2p$ states. However, the possibility of forming a linear superposition cannot be ruled out.

These results are only the start of investigating the feasibility of exciting atomic hydrogen in the $2s$ Rydberg state. Work is currently being carried out with the aim to increase the fraction of hydrogen atoms in the $2s$ state by improving the different timings of the mixing-field and laser excitation as well as optimizing the mixing-field strength. Investigations are also under way, trying to identify the reason(s) behind the unexpectedly short lifetimes. Future work will be focused on designing experiments utilising the properties of the $2s$ state.

7.1 Conclusion

In this chapter, a new method to produce metastable $2p(^2\mathrm{P}_{\frac{1}{2}})$ atomic hydrogen Rydberg states has been proposed and first experiments confirming the feasibility of the method have been presented. Hydrogen atoms are excited into a $2s$-$2p$ hybrid state via a one photon resonant excitation process in the presence of an electric field. The field is subsequently ramped down to disentangle the $2s$ from the $2p$ state and to avoid decay of the hybrid state. A statistical number of hydrogen atoms therefore end up in the metastable $2s(^2\mathrm{S}_{\frac{1}{2}})$ state.

The proposed method was confirmed using in-house built equipment. By carefully adjusting the timing of laser excitation and ramping-down of the mixing field it was possible to demonstrate that hydrogen atoms in the desired $2s(^2\mathrm{S}_{\frac{1}{2}})$ states were created. The $2s$ states were then detected by using a second laser to further excite the

$n = 2$ states to the $n = 34$ Rydberg state and subsequent field-ionisation. To eliminate a contribution of the $2p$ intermediate state to the detected signal, the two lasers have a variable temporal gap allowing the $2p$ state to decay away before further excitation, meaning that at long enough delays the detected signal was purely due to hydrogen atoms in the $2s$ Rydberg state.

Some information about the lifetime of this state under current experimental conditions could be gained by measuring the detected signal as a function of delay between the two excitation lasers. Thereby a surprisingly short lifetime of the $2s$ state of about 20 ns was observed, the origin of which is not yet completely understood. In addition, this modelling approach suggested that states of different m_l might be mixed by the electric field, indicating either the presence of inhomogeneous fields or imperfect laser polarisation with respect to the electric field.

Chapter 8

Conclusion and future work

The interaction of Rydberg atoms or molecules with a wide range of surfaces has been studied in the past both experimentally and theoretically. In most of these studies, the surface was used as a tool to probe the electronic structure and dynamical behaviour of the excited atom or molecule. These investigations can be simplified by using Rydberg states of atomic hydrogen instead, providing a system that is theoretically tractable. In addition, this also allows for the experiment to be turned around, using the Rydberg atom as a probe of the electronic structure of the surface.

In this thesis, the charge-transfer of Rydberg states of atomic hydrogen with a range of different surfaces has been studied experimentally. Surfaces investigated include a bulk metal gold surface, a Cu(100) band-gap surface and nanoparticle surfaces of varying size and density. The work presented in this thesis thus represents the most in depth investigation to date, demonstrating the possibility to use these atoms as surface probes.

At first, the interaction of hydrogen Rydberg atoms with a gold metal surface was investigated. While similar experiments have been performed before, small but nonetheless significant discrepancies between experimental results and theoretical predictions were observed. This deviation from the predicted behaviour was believed to be due to limitations in the detection setup used. To overcome this problem, the experimental setup was modified and previous experiments were repeated.

The data obtained with this modified setup was analysed in the form of surface ionisation profiles, a plot of detection efficiency against applied electric field. In general, the results showed similar trends as observed in previous experiments. Recorded surface ionisation profiles for the most red-shifted Stark states of atomic hydrogen in the range $n = 25 - 35$ showed an increase in minimum ionisation distance which roughly scaled with n^2, in good agreement with previous experimental results. However, comparing the shape of the surface ionisation profiles observed in previous experiments to the ones presented in this thesis revealed distinct differences. The detected signal starts at roughly the same electric fields but the detection efficiency rises more quickly towards its maximum value and shows signs of plateauing, indicating that all created ions are detected and that ionisation occurs over a smaller range of ionisation distances than previously observed.

An empirical model, which was first presented by So et al., can be used to fit model curves to the experimentally obtained profiles. This model is based on a simple over-the-barrier ionisation model and uses two fitting parameters (ionisation width and shift of ionisation distance) to match the shape of the calculated curves onto experimental results. As can be expected from the different observed shapes, a new set of fitting parameters is needed to obtain a good fit of the experimental data. For the current results, the magnitude of the fitting parameters decreases overall, indicating a less distinct deviation from the ideal (classical) ionisation behaviour predicted by theory. This relatively simple model, does not specify any reason for the observed spread in ionisation distance. It was proposed by Dunning and co-workers that changes in the surface work function might lead to strong patch fields which might at least in parts explain the spread of ionisation distances. Patch fields were therefore included into Monte-Carlo trajectory simulations and theoretical surface ionisation profiles were calculated. These theoretical results showed good agreement with measured experimental data and therefore, bridge the gap between theory and experiment, demonstrating the possibility to use Rydberg states as a probe for surface fields.

The effect of changing the polarisation of the incoming Rydberg atom was also studied. The obtained results confirmed earlier observations, which showed a strong dependence of the ionisation distance on the polarisation of the Rydberg state. Via Equation 1.29 the electric field is coupled to a minimum ionisation distance, with a higher field corresponding to a smaller minimum ionisation distance. Most red-shifted states ionise at a scaled distance of approximately $3-5\,n^2\mathrm{a}_0$ while blue-shifted states ionise significantly closer to the surface ($2-3\,n^2\mathrm{a}_0$ for the $k=+16$, $n=29$ Stark state of atomic hydrogen).

The charge transfer between atomic hydrogen Rydberg states and gold nanoparticle surfaces was investigated to further explore the possibility of probing surface properties of finite size particles. Nanoparticles possess interesting properties like a size-dependent metal-to-insulator transition and a size that can be tuned to be either larger or smaller than the incoming Rydberg atom. At first, the charge transfer between the most red-shifted Stark states of atomic hydrogen with a monolayer surface of gold nanoparticles deposited on a silicon wafer was investigated. Comparing the obtained surface ionisation profiles with those obtained with a bulk gold surface showed an increase in the detection efficiency at the low field end of the profiles, indicating that surface ionisation starts at greater distances from the surface. In addition, the effect of the polarisation of the Rydberg orbital with respect to the surface was also studied. While red-shifted states showed the expected behaviour of an overall decrease of detection efficiency together with a shift of the high-field cut-off to higher applied fields with increasing parabolic quantum number, blue-shifted states revealed an interesting deviation from this trend: the detection efficiency started to increase again with increasing k and reached values similar to those observed for the most red-shifted Stark state. Comparing surface-ionisation-profiles of blue- and red-shifted states of neighbouring manifolds revealed a surprising amount of overlap, indicating the possibility of population transfer from the blue- to the red-shifted states. Two different mechanism are proposed to explain this observation. Rotating electric field lines near the nanoparticles might lead to rotation of the quantization direction of the k eigenstates thus inducing avoided crossings between red- and blue-shifted Stark states. Alternatively, these states might be coupled through energetically resonant states within the nanoparticle, that strongly overlap with the Rydberg wavefunction.

In addition, the interaction of Rydberg atoms with nanoparticles of different sizes (20 – 80 nm) were also investigated. By varying the size of the Rydberg orbital, it was possible to gain a first idea of how the relative size of Rydberg atom versus nanoparticle can influence the charge transfer process. Experiments were performed with a range of surfaces on which nanoparticles of different size and density were deposited. The observed results revealed that with an increase in principal quantum number and thus size of the Rydberg orbital, the difference between the nanoparticle covered surface and a bare comparison surface decreased and became undistinguishable for principal quantum numbers $n > 32$. These results suggest that the Rydberg atom is only able to interact with the nanoparticle if the two are comparable in size.

It is expected, that the charge transfer of atomic hydrogen Rydberg states with Cu(100) band-gap semiconductor surfaces should be dominated by resonance effects between image states on the surface-vacuum interface in the band-gap region and the Rydberg state. First investigations by So et al. showed evidence for this effect but further work was needed to confirm those results. Experiments were performed investigating the interaction of mid-manifold Stark states of atomic hydrogen with a Cu(100) surface at different collisional velocities. By varying the velocity of the incoming Rydberg state it was possible to decouple the applied electric field from the minimum ionisation distance, allowing for a new type of data analysis. Converting the detected ion signal into an ionisation rate and plotting this data as a function of applied electric field and distance from the surface revealed interesting facts about the surface ionisation process. These plots were then compared with theoretical data obtained from a modified version of the empirical model used to analyse the results in Chapter 4. It could be shown that for certain states of the principal quantum number range investigated ($n = 25 - 34$) an unusually high ionisation rate was observed at large distances from the surface with the electric field corresponding to theoretical predictions.

Finally, a new way of producing atomic hydrogen in the $2s$ Rydberg state using a one-photon excitation process has been proposed and demonstrated in Chapter 7. This usually forbidden transition is made possible when applying an electric field during the excitation process, effectively mixing the $2s$ with the $2p$ states. To overcome problems such as the limited lifetime of this hybrid state the mixing field was ramped down on a nanosecond time-scale, leaving a statistical amount of hydrogen atoms in the metastable $2s$ state. These atoms were then detected by delayed laser excitation to the $n = 34$ Rydberg state and subsequent field ionisation. While further experiments are needed to maximise the number of atoms in the $2s$ state and to understand the (surprisingly short) observed lifetime of the metastable atoms, a first proof of principle could be achieved.

Many possible future experiments investigating the interaction of hydrogen Rydberg atoms with surfaces can be envisioned, both with the aim to further improve the understanding of the charge-transfer process but also to further test the possibility to use these state to probe surface properties. While the experiments with nanoparticle surfaces revealed interesting results, more work on this topic might help to better understand the involved processes. For example, the experiments investigating the effect of relative size of nanoparticles and Rydberg orbital were hampered by a lack of control of nanoparticle density on the surface. Gaining greater control over the nanoparticle density would therefore allow for more in depth studies of the effects involved, maybe showing different behaviours for nanoparticles of different sizes. Another limitation of the studies involving nanoparticle surfaces presented in this thesis is the lack of theoretical investigations. While the first wave-packet propagation calculations have been carried out within the group, these results are limited to static systems, placing a low n hydrogen Rydberg atom at fixed distances from a small nanoparticle. Pushing forward these calculations to incorporate dynamic systems, could help explain the relatively wide spread of the observed surface ionisation profiles and might also be able to shed light on the observed population transfer from blue- to red-shifted Stark states of neighbouring principal quantum number manifolds. Regarding the copper band-gap surface experiments, it might be useful to extend the experiments to include lower principal quantum numbers making it possible to observe more resonant states (e.g. $n = 22$). This could further confirm that analysing the surface ionisation rate is indeed a valid method to detect resonance effects.

The first steps towards producing $2s$ Rydberg atoms in sufficiently high number states, presented in this thesis, open the door for a range of possible experiments. For example, it was proposed that these states should bounce off a cooled down gold surface ($T < 4\,\mathrm{K}$) in a process called quantum reflection and it would be interesting to test this prediction experimentally. A first hurdle has been overcome by successfully populating the $2s$ state of atomic hydrogen and the next step will be to investigate the possibility to cool down the surface to the temperatures required to observe the aforementioned effect. In addition, charge transfer experiments involving $2s$ hydrogen Rydberg states are also conceivable. While detecting the resulting positive ions will be a challenge due to the high electric fields required to repel them from the surface, it might be possible to detect electrons originating from the ionisation process by reversing the applied extraction field as was successfully shown recently [51]. Another interesting target for future studies are thin-film surfaces with a controllable thickness of a few monolayers (e.g. lead). Calculations predict that these materials show bulk-like behaviour along the surface, but possess discrete energy levels in the direction of the surface normal. Resonance effects somewhat similar to those observed with the Cu(100) surface can thus be expected should one of these states be in resonance with a Stark state of a Rydberg atom. The proposed experiments are experimentally challenging due to the instability of the thin-film surfaces and the surfaces will have to be prepared inside the same vacuum chamber in which the experiments will be performed. Other future work might be concerned with further decelerating the Rydberg atom on its way to the surface via an atom-chip Stark-decelerator as shown by Merkt et al. [124]. This would allow a more detailed investigation of how the Rydberg atom is affected by the surface, something which might be of interest for parts of the quantum computing community which among other methods uses Rydberg atoms trapped near surfaces.

In summary, the interaction of hydrogen Rydberg atoms with a range of different surfaces has been studied experimentally. Surfaces investigated included bulk gold, nanoparticle covered and band-gap semiconductor surfaces. The work presented in this thesis has demonstrated the possibility to use atomic hydrogen atoms excited to Rydberg states to probe different properties of these surfaces (e.g. stray fields, identification of discrete energy levels within the surface, etc.). In addition, a new method to produce hydrogen atoms in the long lived $2s$ quantum state has been demonstrated, setting the stage for surface scattering experiments with the aim to observe quantum effects such as quantum reflectivity.

References

[1] R. S. Mason, P. D. Miller, I. Mortimer, D. J. Mitchell, N. A. Dash, *Physical Review E* **68**, 016408 (2003).

[2] T. Sakurai, M. Toda, *Thin Solid Films* **374**, 157 (2000).

[3] N. Stolterfoht, D. Niemann, M. Grether, A. Spieler, A. Arnau, *Scanning Microscopy* **12**, 437 (1998).

[4] L. Holmlid, E. A. Manykin, *Journal of Experimental and Theoretical Physics* **84**, 875 (1997).

[5] L. Holmlid, *Chemical Physics* **237**, 11 (1998).

[6] L. Holmlid, *Journal of Physics-Condensed Matter* **14**, 13469 (2002).

[7] Y. N. Gnedin, *et al.*, *New Astranomy Reviews* **53**, 259 (2009).

[8] N. A. Nguyen, B. K. Dey, M. Shapiro, P. Brumer, *Journal of Physical Chemistry A* **108**, 7878 (2004).

[9] T. Breeden, H. Metcalf, *Physical Review Letters* **47**, 1726 (1981).

[10] E. Vliegen, F. Merkt, *Physical review letters* **97**, 33002 (2006).

[11] J. Mozley, *et al.*, *The European Physical Journal D-Atomic, Molecular, Optical and Plasma Physics* **35**, 43 (2005).

[12] M. Saffman, T. G. Walker, K. Mølmer, *Reviews of Modern Physics* **82**, 2313 (2010).

[13] H. Kübler, J. P. Shaffer, T. Baluktsian, R. Löw, T. Pfau, *Nature Photonics* **4**, 112 (2010).

[14] A. Tauschinsky, R. M. T. Thijssen, S. Whitlock, H. B. V. van den Heuvell, R. J. C. Spreeuw, *Physical Review A* **81**, 063411 (2010).

[15] E. Urban, *et al.*, *Nature Physics* **5**, 110 (2009).

[16] L. Isenhower, *et al.*, *Physical Review Letters* **104**, 10503 (2010).

[17] H. Goldstein, *American Journal of Physics* **44**, 1123 (1976).

[18] H. Bethe, S. E, *Quantum mechanics of one- and two-electron atoms* (Plenum Publishing Corporation, 1977).

[19] J. Burgdörfer, P. Lerner, F. W. Meyer, *Physical Review A* **44**, 5674 (1991).

[20] N. S. Simonovic, *Journal of Physics B: Atomic, Molecular and Optical Physics* **30**, 613 (1999).

[21] M. Inarrea, *et al.*, *Physical Review A* **76**, 052903 (2007).

[22] J. P. Salas, N. S. Simonovic, *Journal of Physics B: Atomic, Molecular and Optical Physics* **33**, 291 (2000).

[23] D. Wang, M. L. Du, S. Lin, *Journal of Physics B: Atomic, Molecular and Optical Physics* **39**, 3529 (2006).

[24] D. Wang, H. K, L. S, *European Physical Journal D* **54**, 379 (2009).

[25] G. J. W, *Surface Science* **6**, 133 (1967).

[26] M. Remy, *Journal of Chemical Physics* **53**, 2487 (1970).

[27] K. Ganesan, K. T. Taylor, *Journal of Physics B: Atomic, Molecular and Optical Physics* **29**, 1293 (1999).

[28] A. Borisov, D. Teillet-Billy, J. P. Gauyacq, *Nuclear Instruments and Methods in Physics Research Section B: Beam Interactions with Materials and Atoms* **78**, 49 (1993).

[29] P. Nordlander, J. C. Tully, *Physical Review B* **42**, 5564 (1990).

[30] P. Nordlander, *Physical Review B* **53**, 4125 (1996).

[31] J. Hanssen, C. F. Martin, P. Nordlander, *Surface Science* **423**, L271 (1999).

[32] P. Kürpick, U. Thumm, U. Wille, *Physical Review A* **1**, 543 (1997).

[33] P. Kürpick, U. Thumm, U. Wille, *Physical Review A* **57**, 1920 (1998).

[34] A. G. Borisov, A. K. Kazansky, J. P. Gauyacq, *Physical Review B* **59**, 10935 (1999).

[35] J. Sjakste, A. Borisov, J. Gauyacq, *Physical Review A* **73**, 042903 (2006).

[36] E. So, M. T. Bell, T. P. Softley, *Physical Review A* **79**, 012901 (2009).

[37] E. So, Interaction of rydberg hydrogen atoms with metal surfaces, Ph.D. thesis, Merton College, University of Oxford (2011).

[38] A. Anderson, S. Haroche, E. A. Hinds, W. Jhe, D. Meschede, *Physical Review A* **37**, 3594 (1988).

[39] V. Sandoghdar, C. I. Sukenik, S. Haroche, E. A. Hinds, *Physical Review A* **53**, 1919 (1996).

[40] C. Fabre, M. Gross, J. M. Raimond, S. Haroche, *Journal of Physics B: Atomic, Molecular and Optical Physics* **16**, L671 (1983).

[41] C. A. Kocher, C. R. Taylor, *Physics Letters A* **124**, 68 (1987).

[42] G. E. McCown, C. R. Taylor, C. A. Kocher, *Physical Review A* **38**, 3918 (1988).

[43] D. Gray, Z. Zheng, K. Smith, F. Dunning, *Physical Review A* **38**, 1601 (1988).

[44] S. B. Hill, C. B. Haich, Z. Zhou, P. Nordlander, F. B. Dunning, *Physical Review Letters* **85**, 5444 (2000).

[45] F. B. Dunning, S. Wethekam, H. R. Dunham, J. C. Lancaster, *Nuclear Instruments & Methods in Physics Research Section B - Beam Iinteractions with Materials and Atoms* **258**, 61 (2007).

[46] D. Neufeld, H. Dunham, S. Wethekam, J. Lancaster, F. Dunning, *Physical Review B* **78**, 115423 (2008).

[47] Y. Pu, D. Neufeld, F. Dunning, *Physical Review A* **81**, 042904 (2010).

[48] G. R. Lloyd, S. R. Procter, T. P. Softley, *Physical Review Letters* **95**, 133202 (2005).

[49] G. R. Lloyd, S. R. Procter, E. A. McCormack, T. P. Softley, *Journal of Chemical Physics* **126**, 184702 (2007).

[50] E. A. McCormack, M. S. Ford, T. P. Softley, *Journal of Physical Chemistry A* **114**, 11175 (2010). Reprinted with permission from ACS publications

[51] E. A. McCormack, S. E, M. Dethlefsen, M. S. Ford, T. P. Softley, *Journal of Physics B: Atomic, Molecular and Optical Physics* **45**, 015204 (2011).

[52] E. So, M. Dethlefsen, M. Ford, T. Softley, *Physical Review Letters* **107**, 093201 (2011).

[53] T. Gallagher, *Rydberg Atoms* (Cambridge University Press, 1994).

[54] T. P. Softley, *International Reviews in Physical Chemistry* **23**, 1 (2004).

[55] E. S. Chang, *Physical Review A* **31**, 495 (1985).

[56] T. F. Gallagher, W. E. Cooke, *Physical Review Letters* **42**, 835 (1979).

[57] I. I. Beterov, D. B. Tretyakov, I. I. Ryabtsev, A. Ekers, N. N. Bezuglov, *Physical Review A* **75**, 052720 (2007).

[58] I. L. Glukhov, E. A. Nekipelov, V. D. Ovsiannikov, *Journal of Physics B-Atomic Molecular and Optical Physics* **43**, 125002 (2010).

[59] X. X. Lu, Y. Sun, H. Metcalf, *Physical Review A* **84**, 033402 (2011).

[60] J. Stark, *Annalen der Physik* **348**, 965 (1914).

[61] J. D. Bekenstein, J. B. Krieger, *Physical Review* **188**, 130 (1969).

[62] N. Vanhaecke, U. Meier, M. Andrist, B. H. Meier, F. Merkt, *Physical Review A* **75**, 31402 (2007).

[63] S. D. Hogan, A. W. Wiederkehr, H. Schmutz, F. Merkt, *Physical Review Letters* **101**, 143001 (2008).

[64] R. J. Damburg, V. V. Kolosov, *Journal of Physics B: Atomic, Molecular and Optical Physics* **12**, 2637 (1979).

[65] R. O. Jones, P. J. Jennings, J. O, *Physical Review B* **29**, 6474 (1984).

[66] Z. Zhou, C. Oubre, S. B. Hill, P. Nordlander, F. Dunning, *Nuclear Instruments & Methods in Physics Research Section B-Beam Interactions with Materials and Atoms* **193**, 403 (2002).

[67] C. Oubre, P. Nordlander, F. B. Dunning, *Journal of Physical Chemistry B* **106**, 8338 (2002).

[68] F. B. Dunning, H. R. Dunham, C. Oubre, P. Nordlander, *Nuclear Instruments & Methods in Physics Research Section B-Beam Interactions with Materials and Atoms* **203**, 69 (2003). Reprinted with permission from Elsevier

[69] P. Nordlander, F. B. Dunning, *Nuclear Instruments & Methods in Physics Research Section B-Beam Interactions with Materials and Atoms* **125**, 300 (1997).

[70] S. Wethekam, H. Dunham, J. Lancaster, F. Dunning, *Physical Review A* **73**, 032903 (2006).

[71] E. A. McCormack, Ionisation of hydrogen rydberg molecules at surfaces, Ph.D. thesis, University of Oxford (2010).

[72] H. R. Dunham, S. Wethekam, J. C. Lancaster, F. B. Dunning, *Nuclear Instruments & Methods in Physics Research Section B-Beam Interactions with Materials and Atoms* **256**, 46 (2007).

[73] D. Neufeld, H. Dunham, S. Wethekam, J. Lancaster, F. Dunning, *Surface Science* **602**, 1306 (2008).

[74] S. Ganeshalingam, Charge transfer of rydberg hydrogen molecules and atoms at doped silicon surfaces, Ph.D. thesis, University of Oxford (2012).

[75] P. Nordlander, F. B. Dunning, *Physical Review B* **53**, 8083 (1996).

[76] P. Nordlander, N. D. Lang, *Physical Review B* **44**, 13681 (1991).

[77] M. Taylor, P. Nordlander, *Physical Review B* **64**, 115422 (2001).

[78] U. Wille, *Physical Review B* **50**, 1888 (1994).

[79] V. Sandoghdar, C. Sukenik, E. Hinds, S. Haroche, *Physical Review Letters* **68**, 3432 (1992).

[80] J. B. Camp, T. W. Darling, R. E. Brown, *Journal of Applied Physics* **69**, 7126 (1991).

[81] C. Speake, C. Trenkel, *Physical review letters* **90**, 160403 (2003).

[82] J. Carter, J. Martin, *Physical Review A* **83**, 032902 (2011).

[83] A. Borisov, R. Zimny, D. TeilletBilly, J. Gauyacq, *Physical Review A* **53**, 2457 (1996).

[84] C. Zener, *Proceedings of the Royal Society of London A* **137**, 696 (1932).

[85] T. Fabcic, J. Main, G. Wunner, *Physical Review A* **79**, 043416 (2009).

[86] W. Press, S. Teukolsky, B. Flannery, V. Vetterling, *Numerical Recipes in FORTRAN: The Art of Scientific Computing* (Camebridge University Press, New York, NY, USA, 1992).

[87] F. Merkt, R. Zare, *Journal of Chemical Physics* **101**, 3495 (1994).

[88] N. Gaillard, M. Gros-Jean, D. Mariolle, F. Bertin, A. Bsiesy, *Applied physics letters* **89**, 154101 (2006).

[89] E. V. Chulkov, V. M. Silkin, P. M. Echenique, *Surface Science* **437**, 330 (1999).

[90] I. E. Tamm, *Z. Physik* **76**, 849850 (1932).

[91] W. Shockley, *Phys. Rev.* **56** (1939).

[92] P. M. Echenique, J. B. Pendry, *Journal of Physics C: Solid State Physics* **11**, 2065 (2001).

[93] T. Klamroth, P. Saalfrank, U. Höfer, *Physical Review B* **64**, 035420 (2001).

[94] A. G. Borisov, J. P. Gauyacq, A. K. Kazansky, *Surface Science* **505**, 260 (2002).

[95] E. V. Chulkov, *et al.*, *Chemical Reviews-Columbus* **106**, 4160 (2006).

[96] S. Willitsch, J. M. Dyke, F. Merkt, *Helvetica Chimica Acta* **86**, 1152 (2003).

[97] S. Ganeshalingam, M. S. Ford, T. P. Softley, *The Journal of Chemical Physics* **138**, 114308 (2013).

[98] D. A. Dahl, *International Journal of Mass Spectrometry* **200**, 3 (2000).

[99] M. N. Martin, J. I. Basham, P. Chando, S. K. Eah, *Langmuir* **26**, 7410 (2010).

[100] M. Brust, M. Walker, D. Bethell, D. J. Schiffrin, R. Whyman, *J. Chem. Soc., Chem. Commun.* **7**, 801 (1994).

[101] W. Haiss, N. T. K. Thanh, J. Aveyard, D. G. Fernig, *Analytical chemistry* **79**, 4215 (2007).

[102] S. K. Eah, *Journal of Materials Chemistry* **21**, 16866 (2011).

[103] E. W. Kuipers, C. Laszlo, W. Wieldraaijer, *Catalysis Letters* **17**, 71 (1993).

[104] C. Doornkamp, C. Laszlo, W. Wieldraaijer, E. W. Kuipers, *Journal of Materials Research* **10**, 411 (1995).

[105] R. G. Freeman, *et al.*, *Science* **267**, 1629 (1995).

[106] A. Doron, E. Katz, I. Willner, *Langmuir* **11**, 1313 (1995).

[107] G. Schmid, S. Peschel, T. Sawitowski, *Zeitschrift Fur Anorganische und Allgemeine Chemie* **623**, 719 (1997).

[108] T. Sato, D. Brown, B. F. G. Johnson, *Chemical Communications* **11**, 1007 (1997).

[109] T. P. Bigioni, *et al.*, *Nature Materials* **5**, 265 (2006).

[110] J. Zhai, Y. Wang, Y. Zhai, S. Dong, *Nanotechnology* **20**, 055609 (2011).

[111] J. Turkevich, P. C. Stevenson, J. Hillier, *Discuss. Faraday Soc.* **11**, 55 (1951).

[112] K. C. Grabar, *et al.*, *Journal of the American Chemical Society* **118**, 1148 (1996).

[113] Y. K. Hong, *et al.*, *Applied Physics Letters* **80**, 844 (2002).

[114] G. Schmid, B. Corain, *European Journal of Inorganic Chemistry* **2003**, 3081 (2003).

[115] M. C. Daniel, D. Astruc, *Chemical Reviews-Columbus* **104**, 293 (2004).

[116] P. Zhang, T. K. Sham, *Physical Review Letters* **90**, 245502 (2003).

[117] A. Zabet-Khosousi, P. Trudeau, Y. Suganuma, A. Dhirani, B. Statt, *Physical Review Letters* **96**, 156403 (2006).

[118] J. Gibbard, The interaction of H-atoms with thin films and nanostructures, Master's thesis, University of Oxford, St. Hildas College (2011).

[119] H. Friedrich, A. Jurisch, *Physics Letters A* **335**, 43 (2005).

[120] W. S. Bickel, A. S. Goodman, *The Physical Review* **148**, 1 (1966).

[121] E. E. Salpeter, *Physical Review* **112**, 1642 (1958).

[122] H. Bethe, E. E. Salpeter, *Encyclopaedia of Physics*, vol. XXXV (Springer-Verlag, Berlin, 1957).

[123] W. L. Fite, R. T. Brackmann, D. G. Hummer, R. F. Stebbings, *Physical Review* **116**, 363 (1959).

[124] S. D. Hogan, P. Allmendinger, H. Saßmannshausen, H. Schmutz, F. Merkt, *Physical Review Letters* **108**, 063008 (2012).